Journal of the Serbian Chemical Society

VOLUME 78

No 5

BELGRADE 2013

CONTENTS

Available online at www.shd.org.rs/JSCS/

Modern Friedel–Crafts chemistry. Part 36. Facile synthesis of some new pyrido[3,2,1-*jk*]carbazoles *via* Friedel–Crafts cyclialkylations

HASSAN ABDOU KOTB ABD EL-AAL* and ALI ALI KHALAF

Chemistry Department, Faculty of Science, Assiut University, Assiut, 71516, Egypt

Abstract: An efficient methodology for the synthesis of novel substituted pyrido[3,2,1-*jk*]carbazoles *via* Friedel–Crafts cyclialkylations is reported. The methodology was realized by a three-step protocol involving the addition of carbazole to 3-methylcrotononitrile. The resulting nitrile was subjected to alcoholysis to the desired ester, followed by addition of Grignard reagents to afford tertiary alcohols and/or reacted directly with different Grignard reagents to form the desired ketones. The latter ketones were converted to both secondary and tertiary alcohols by reduction with lithium aluminum hydride (LAH) and addition of Grignard reagents, respectively. These alcohols were cyclialkylated under Friedel–Crafts conditions catalyzed by AlCl$_3$/CH$_3$NO$_2$, *p*-toluenesulfonic acid (PTSA) or polyphosphoric acid (PPA) to give tri- and tetra-substituted pyrido[3,2,1-*jk*]carbazoles.

Keywords: Friedel–Crafts cyclialkylation; pyrido[3,2,1-*jk*]carbazole; heteropolycycles; heteroarylalkanols; carbocations.

INTRODUCTION

Synthesis of heteropolycycles containing pyrido[3,2,1-*jk*]carbazole scaffold is of interest because they are the core subunit often found in the heterocyclic skeleton of many natural products,[1] optoelectronics applications,[2] dye-sensitized solar cells (DSCs),[3] photochromic dyes[4] and were designed as vital precursors in the synthesis of many biologically active carbazole alkaloids.[5] Moreover, some derivatives are of interest in biomedical and pharmacological applications.[6]

A limited number of synthetic methodologies have been developed for the synthesis of pyrido[3,2,1-*jk*]carbazole derivatives. Among these synthetic approaches described in literature are the thermal condensations of malonates with carbazole,[7] Diels–Alder reaction of vinylindoles,[8] photolysis of *N*-aryltetrahydroquinolines,[9] dimerization of *N*-vinylcarbazole,[10] Fisher reaction of tetrahydro-
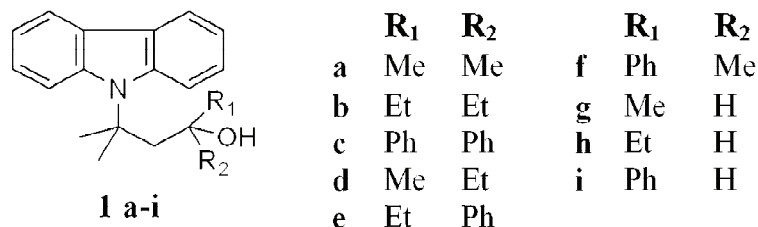
---

quinolines[11] and *via* intermolecular [4+2] cycloaddition of benzotriazoles with alkenes.[12]

Despite the numerous advances in the field of synthetic organic chemistry, the development of direct, concise and economic methods is currently a popular research area and has always been an attractive and challenging area for both medicinal and synthetic chemists. Among these methods, intramolecular Friedel–Crafts reaction (called cyclialkylations)[13–19] promoted by both Brönsted and Lewis acid catalysts is promising as a powerful tool offering considerable opportunities for synthetic manipulations.

In recent years, a part of our Friedel–Crafts research was devoted to the development of facile routes to approach the construction of novel bi- and higher heterocyclic systems. The previous paper of this series[19] described the synthesis of seven substituted nitrogen and nitrogen–sulfur polycycles containing fused carbazole, tetrahydrocarbazole, quinoline, tetrahydroquinoline, acridine, phenothiazine and indole moieties *via* Friedel–Crafts cyclialkylations of the corresponding heteroarylalkanols.

In connection with previous studies, herein the facile synthesis of nine unrecorded 5,6-dihydro-4*H*-pyrido[3,2,1-*jk*]carbazole derivatives *via* intramolecular cyclialkylations of suitable synthesized alcohols **1a**–**i** (Scheme 1) is described.

		R₁	**R₂**			**R₁**	**R₂**
	a	Me	Me	**f**		Ph	Me
	b	Et	Et	**g**		Me	H
	c	Ph	Ph	**h**		Et	H
	d	Me	Et	**i**		Ph	H
	e	Et	Ph				

Scheme 1. Heteroarylalkanols **1a**–**i**.

RESULTS AND DISCUSSION

Synthesis of the starting alcohols

The requisite precursor 3-(9*H*-carbazol-9-yl)-3-methylbutanenitrile (**4**) was readily obtained by refluxing a solution of 3-methylcrotononitrile (**3**) and carbazole (**2**) in dioxane in the presence of a catalytic amount of triton B. Ethanolysis of **4** gave ethyl 3-(9*H*-carbazol-9-yl)-3-methylbutanoate (**5**), which was converted to tertiary alcohols **1a**–**c**, by reaction with two equivalents of the corresponding Grignard reagent.[20]

Furthermore, reaction of **4** with one equivalent of Grignard afforded ketones **6a**–**c** which were successively converted to the respective tertiary alcohols **1d**–**f** by reaction with one equivalent of the corresponding Grignard reagent and to secondary alcohols **1g**–**i** by reduction with LAH[21] The structures of all new al-

cohols were appropriately established by the usual spectroscopic methods. The results are presented in Table I and Scheme 2.

TABLE I. Synthesis of heteroarylalkanols **1a**–**i**

Entry	Substrate	R_1	R_2	Conditions[a]	Product	m.p. / °C (n_D^{25})	Yield[b] %
1	**5**	Me	Me	MeMgI, Et$_2$O, rt, 10 h	**1a**	122	86
2	**5**	Et	Et	EtMgBr, Et$_2$O, rt, 12 h	**1b**	115	92
3	**5**	Ph	Ph	PhMgBr, Et$_2$O, 40 °C, 12 h	**1c**	(1.542)	84
7	**6a**	Me	Et	EtMgBr, Et$_2$O, rt, 5 h	**1d**	(1.558)	85
8	**6b**	Et	Ph	PhMgBr, Et$_2$O, rt, 8 h	**1e**	112	83
9	**6c**	Ph	Me	MeMgI, Et$_2$O, rt, 6 h	**1f**	(1.538)	85
10	**6a**	Me	H	LAH, Et$_2$O, rt, 3 h	**1g**	(1.533)	84
11	**6b**	Et	H	LAH, Et$_2$O, rt, 2 h	**1h**	(1.536)	91
12	**6c**	Ph	H	LAH, Et$_2$O, rt, 3 h	**1i**	(1.541)	88

[a]All reactions were performed using 0.1 equivalent excess of RMgX and LAH, then calculated; [b]isolated yield referred to substrate
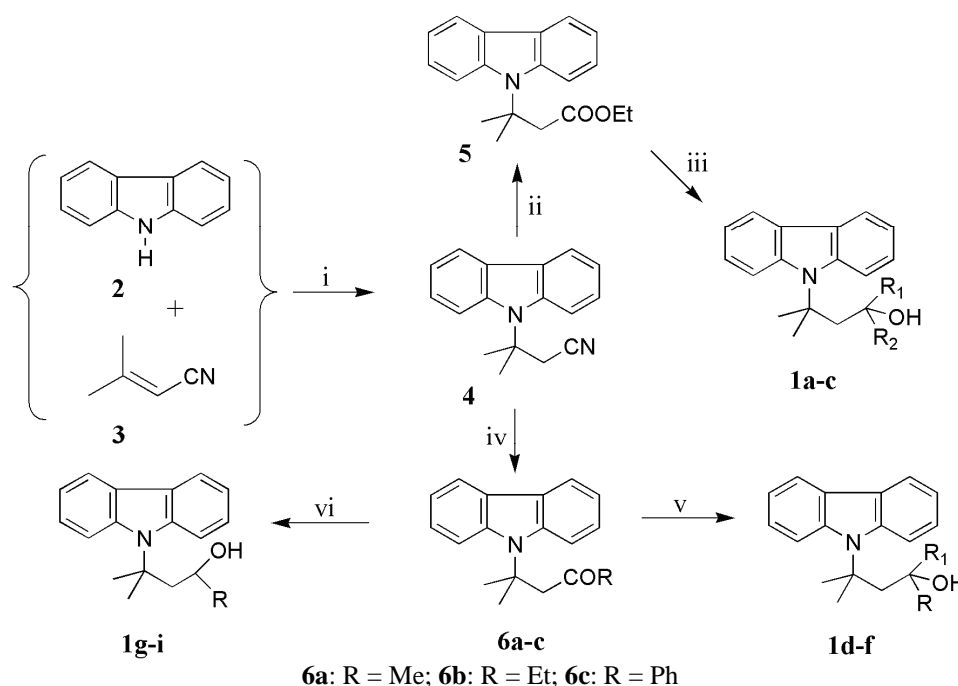
Scheme 2. Synthesis of heteroarylalkanols **1a**–**i**; reagents and conditions: i) BnMe$_3$NOH, dioxane, 90 °C, 4 h, yield: 92.5 %, ii) EtOH, H$_2$SO$_4$, reflux 10 h, yield: 85.7 %, iii) 2RMgX, Et$_2$O, NH$_4$Cl solution, iv) RMgX, THF/Et$_2$O, HCl solution, v) RMgX, Et$_2$O, NH$_4$Cl solution and vi) LAH, Et$_2$O, room temperature (Table I).

The ^{1}H-NMR data allowed an unambiguous confirmation of the formation of the heterocyclic alkanols. Thus, the ^{1}H-NMR spectrum for alcohol **1a** displayed signals in which aromatic protons appeared at δ 7.0–7.9 ppm. The *gem*-dimethyls at C-2 and C-4 appeared as two singlets at δ 1.1 and 1.6 ppm, respectively. The third singlet at δ 2.1 ppm was assigned to the downfield CH_2 protons. A broad singlet appearing at δ 2.8 ppm was assigned to OH group. In all IR spectra, the characteristic peaks of carbonyl groups were absent. The characterization data for the synthesized compounds are given in the Supplementary material to this paper.

Cyclialkylation of heteroaryl alcohols

Cyclialkylations of alcohols **1a**–**i** were performed in the presence of $AlCl_3$/CH_3NO_2, polyphosphoric acid (PPA) and *p*-toluenesulfonic acid (PTSA) catalysts under varying conditions. Cyclialkylations of carbinols **1a**, **1b** and **1d**–**f** proceeded smoothly in the presence of $AlCl_3$/CH_3NO_2 for 2 h at room temperature to give the substituted 5,6-dihydro-4*H*-pyrido[3,2,1-*jk*]carbazoles **8a**, **8b** and **8d**–**f**. The results are embedded in Table II and Scheme 3.

TABLE II. Cyclialkylation conditions and results for the heteroarylalkanols **1a**–**f**

Entry	Substrate	Catalyst	Product	Solvent	t / °C	Time, h	Yield[a], %
1	**1a**	$AlCl_3$/CH_3NO_2[b]	**8a**	DCM[c]	RT	2	82
2	**1a**	PPA[d]	**8a**	–	160	1	75
3	**1a**	PTSA[e]	**8a**	PhH	reflux	10	88
4	**1b**	$AlCl_3$/CH_3NO_2	**8b**	PE[f]	RT	2	81
5	**1b**	PPA	**8b**	–	160	1	73
6	**1c**	$AlCl_3$/CH_3NO_2	**8c**	DCM	RT	48	81
7	**1c**	PPA	**8c**	–	250	12	76
9	**1d**	$AlCl_3$/CH_3NO_2	**8d**	DCM	RT	2	79
10	**1d**	PPA	**8d**	–	160	2	74
11	**1e**	$AlCl_3$/CH_3NO_2	**8e**	PE	RT	2	84
12	**1e**	PPA	**8e**	–	160	2	74
13	**1e**	PTSA	**8e**	PhH	reflux	10	78
14	**1f**	$AlCl_3$/CH_3NO_2	**8f**	DCM	RT	4	80
15	**1f**	PPA	**8f**	–	160	4	76

[a]Isolated yield referred to substrate; [b]with $AlCl_3$/CH_3NO_2 catalyst reactant proportions were: alcohol (0.002 mol), $AlCl_3$ (0.0024 mol), CH_3NO_2 (0.024 mol), solvent (10 mL); [c]dichloromethane; [d]with PPA catalyst, the reactant proportions were: alcohol (0.5 g) and PPA (3 g); [e]with PTSA catalyst, the reactant proportions were: alcohol (0.5 g), PTSA (3 g) and solvent (10 mL); [f]petroleum ether (60–80 °C)

Intramolecular cyclization of alcohol **1c**, required more severe reaction conditions compared to its methyl-substituted analogs **1a**. Accordingly, the best results were *via* cyclialkylations of alcohol **1c** under more strenuous conditions in the presence of PPA for 12 h at 250 °C and with $AlCl_3$/CH_3NO_2 for 48 h in dichloromethane (DCM) solution at room temperature to yield 5,6-dihydro-

-6,6-dimethyl-4,4-diphenyl-4*H*-pyrido[3,2,1-*jk*]carbazole (**8c**) as the sole product (Scheme 3; Table II, Entries 6 and 7).
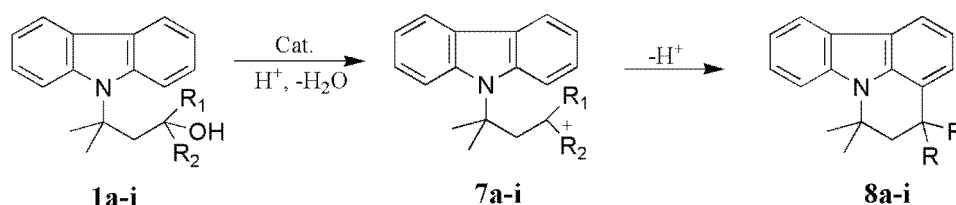
Scheme 3. Cyclialkylation of heteroarylalkanols **1a**–**i**.

Cyclialkylations of alcohols **1g**–**i** were performed in the presence of AlCl$_3$//CH$_3$NO$_2$, PPA and PTSA catalysts under different reaction conditions (Table III, Scheme 3). The closure step of the secondary alcohols required less strenuous reaction conditions than alcohol **1c**. Thus, upon treatment of such alcohols with acidic catalysts, the products were shown to be the tetracyclic amines **8g**–**i**.

TABLE III. Cyclialkylation conditions and results for heteroarylalkanols **1g**–**i**

Entry	Substrate	Catalyst	Product	Solvent	t / °C	Time, h	Yield, %
1	**1g**	AlCl$_3$/CH$_3$NO$_2$	**8g**	PE	RT	5	80
2	**1g**	PPA	**8g**	–	160	8	74
3	**1g**	PTSA	**8g**	PhH	reflux	15	83
4	**1h**	AlCl$_3$/CH$_3$NO$_2$	**8h**	DCM	RT	6	82
5	**1h**	PTSA	**8h**	PhH	reflux	15	80
6	**1h**	PPA	**8h**	–	160	8	75
7	**1i**	AlCl$_3$/CH$_3$NO$_2$	**8i**	PE	RT	4	79
8	**1i**	PPA	**8i**	–	160	6	76
9	**1i**	PTSA	**8i**	PhH	reflux	10	77

Examination of the data depicted in Tables II and III revealed the following significant points: *i*) most cyclialkylations could be easily achieved by AlCl$_3$//CH$_3$NO$_2$ in DCM and petroleum ether (60–80 °C) (PE) at room temperature, by PPA at 160 °C and by PTSA in benzene under reflux, *ii*) the only exception lies in the cyclialkylations of **1c** in which both R$_1$ and R$_2$ are phenyl groups. This reaction required much longer times with AlCl$_3$/CH$_3$NO$_2$ and much higher temperatures with PPA. Certainly, this is due to the development steric interactions exerted by both phenyls at the closure step. Similar steric observations were also noted in other reported cases.[13]

EXPERIMENTAL

Instrumentation

All reagents were purchased from Merck, Sigma or Aldrich Chemical Co. and were used without further purification. Melting points were measured on a digital Gallenkamp capillary melting point apparatus and are uncorrected. The IR spectra were recorded on a Shimadzu 470

infrared spectrophotometer using KBr wafer and thin film techniques. The ^{1}H-NMR spectra were recorded on Jeol LA 400 MHz FT-NMR (400 MHz) and Varian 90 MHz NMR spectrometers using $CDCl_3$ as the solvent with TMS as the internal standard. Elemental analyses were performed on a Perkin-Elmer 2400 Series II analyzer. The mass spectra were obtained using a JEOL JMS 600 spectrometer at an ionizing potential of 70 eV using the direct inlet system. Reactions were monitored by thin layer chromatography (TLC) using pre-coated silica plates and visualized with UV light. Flash column chromatography was performed on silica gel and basic alumina.

Synthesis of 3-(9H-carbazol-9-yl)-3-methylbutanenitrile (4)

An ice-cold solution of carbazole **2** (6.9 g, 40 mmol) and 3-methylcrotononitrile (**3**) (3.4 g, 42 mmol) in dioxane (30 mL) was treated with 0.7 ml of triton B. The reaction mixture was heated in a water bath for 5 h and then concentrated in *vacuo*. The pasty product was triturated with methanol (3×5 mL) and the resulting precipitate was filtered off, washed excessively with methanol and dried to yield 9.5 g (92.5 %) of the crude product. Crystallization from acetone gave (8.9 g, 86.6 %) of pure nitrile **4** in the form of white crystals.

Synthesis of ethyl 3-(9H-carbazol-9-yl)-3-methylbutanoate (5)

A mixture of 3-(9H-carbazol-9-yl)-3-methylbutanenitrile (**4**) (5 g, 20 mmol), absolute ethanol (40 mL) and 7 ml of concentrated sulfuric acid was refluxed for 10 h. Excess alcohol was then removed by distillation and the residue was diluted with cold water (50 mL), basified with Na_2CO_3 solution (20 mL, 30%) and extracted with ether (3×30 mL). The combined ethereal extracts were washed with water, dried over $MgSO_4$, filtered and finally concentrated to give 5 g (85.7 %) of crude oily ester. Purification by flash column chromatography (basic alumina, EtOAc/*n*-hexane, 2/3) gave 4.8 g (82.3 %) of pure **5** in the form of pale yellow oil.

General procedure for the synthesis of heteroaryl ketones 6a–c

A solution of nitrile **4** (2.5g, 10 mmol) in THF (20 mL) was added rapidly under stirring to an ice-cold Grignard reagent obtained as usual[20] from Mg turnings (0.3 g, 12 mmol) and alkyl or aryl halide (12 mmol) in diethyl ether (30 mL). After refluxing for 15 h, the mixture was poured into ice-cold hydrochloric acid (100 mL, 30 %) when the ketimine hydrochloride separated. The organic solvent was removed in *vacuo* and the cold aqueous mixture was filtered under suction. The resulting ketimine was then hydrolyzed by refluxing with a mixture of benzene, 20 mL; HCl, 10 mL; AcOH, 10 mL until the ketimine disappeared (7–9 h). The solution was cooled and the benzene layer was separated, while the aqueous layer was basified by addition of solid Na_2CO_3 under stirring and finally extracted with benzene (2×30 mL). The combined organic phases were washed with water, dried over anhydrous Na_2SO_4 and the solvent was evaporated *in vacuo* to afford the crude product that was purified by crystallization.

General procedure for the synthesis of heteroaryl alcohols 1a–f

To an ice-cold Grignard reagent solution obtained as usual[20] from Mg turnings (0.2 g, 8 mmol) and alkyl or aryl halide (8 mmol) in ether (25 mL), a solution of ester **5** (1.0 g, 3.6 mmol) and/or ketone **6a–c** (7.3 mmol) in ether (30 mL)was added. The reaction mixture was stirred at required temperature for appointed time (Table I) followed by decomposition with saturated NH_4Cl aqueous solution. The product was extracted with ether (3×20 mL) and combined organic phases were washed with water, dried over anhydrous Na_2SO_4 and the solvent was evaporated *in vacuo*. The residue was purified by flash column chromatography (basic alumina, EtOAc/*n*-hexane, 2/3), which gave the pure products **1a–f**.

*General procedure for the synthesis of heteroaryl alcohols **1g**–**i***

A solution of ketone **6a**–**c** (2.5 mmol) in anhydrous ether (15 mL) was added in 30 min to an ice-cold (0 °C) solution of LAH (0.10 g, 2.7 mmol)[21] in ether (15 mL). The reduction was complete after stirring for appointed time at defined temperature (Table I, TLC, 20% ethyl acetate/hexane). The cold reaction mixture was quenched at 0 °C by the sequential addition of water (2 mL), NaOH solution (10 mL, 20%) and water (10 mL). Then it was warmed to room temperature. Suction filtration removed the white precipitate of aluminum compounds, which were thoroughly triturated with ethyl acetate. The organic layer was separated, washed with water, dried over anhydrous Mg_2SO_4 and the solvent was evaporated *in vacuo* to afford crude alcohols **1g**–**i**. Purification of the crude products with flash column chromatography (basic alumina, EtOAc/*n*-hexane, 2/3) gave the pure products **1g**–**i**.

Friedel–Crafts cyclialkylations procedures

The procedures described earlier for cyclialkylation of heteroarylalkanols with $AlCl_3$/ /CH_3NO_2,[14] PTSA,[16] and PPA[19] were essentially followed and are mentioned below. In all reactions, the crude oily or solid products were purified by flash column chromatography (basic alumina, EtOAc/*n*-hexane, 1/1) giving the pure products **8a**–**i**. The conditions and yields for the products **8a**–**i** are presented in Tables II and III while the characterization data for the products are given in the Supplementary material to this paper.

Method A. Cyclialkylations using $AlCl_3/CH_3NO_2$ catalyst. To a solution of $AlCl_3$ (2.4 mmol) in CH_3NO_2 (24 mmol) was added a solution of alcohols **1a**–**i** (2.0 mmol) in DCM or PE (60–80 °C) (10 mL) dropwise under stirring over 10–15 min. The reaction mixture was further stirred for a certain time at room temperature and decomposed by careful addition of 10 % ice-cold hydrochloric acid solution (20 mL). The residue was extracted with diethyl ether (3×20 mL) and the combined organic phases were washed with 10 % Na_2CO_3, water and dried over anhydrous $MgSO_4$. The solvent was evaporated under reduced pressure to afford the crude products **8a**–**i**.

Method B. Cyclialkylations using PTSA catalyst. A solution of the carbinols **1a**, **1e** and **1g**–**i** (0.5 g) and PTSA (3 g) in dry benzene (10 ml) was refluxed for 10 h. After cooling to room temperature, the reaction mixture was diluted with ether (30 mL). The organic layer was separated, washed successively with a saturated solution of $NaHCO_3$, water and dried over $MgSO_4$. The solvent was evaporated under reduced pressure to afford the crude products **8a**, **8e** and **8g**–**i**.

Method C. Cyclialkylations using PPA catalyst. A stirred mixture of alcohols **1a**–**i** (0.5 g) and the PPA (3 g) was heated on an oil bath and kept at the required temperature for a certain time. Afterwards, the flask was cooled to room temperature and basified by addition of $NaHCO_3$ solution (25 ml, 30 %). The residue was extracted with diethyl ether (3×20 mL) and the combined organic phases were washed with water, dried over anhydrous Na_2SO_4 and the solvent was evaporated in *vacuo* to give the crude products **8a**–**i**.

CONCLUSIONS

In summary, a facile protocol was developed for the synthesis of nine new pyrido[3,2,1-*jk*]carbazole derivatives *via* the direct intramolecular Friedel–Crafts cyclization reaction of heteroarylalkanols (**1a**–**i**) catalyzed by $AlCl_3/CH_3NO_2$, PTSA or PPA. The simplicity of the processes, accessibility and moderate cost of the required substrates proved that Friedel–Crafts cyclialkylation could be considered as one of the most useful pathways to the synthesis of heteropolycycles.

SUPPLEMENTARY MATERIAL

Characterization data for the synthesized compounds are available electronically from http://www.shd.org.rs/JSCS/, or from the corresponding author on request.

И З В О Д

УНАПРЕЂЕНА ФРИДЕЛ–КРАФТСОВА РЕАКЦИЈА. ДЕО 36. ЛАКА СИНТЕЗА НОВИХ ПИРИДО[3,2,1-*jk*]КАРБАЗОЛА ФРИДЕЛ–КРАФТСОВИМ ЦИКЛИАЛКИЛОВАЊЕМ

HASSAN ABDOU KOTB ABD EL-AAL И ALI ALI KHALAF

Chemistry Department, Faculty of Science, Assiut University, Assiut, 71516, Egypt

Приказана је ефикасна методологија синтезе нових супституисаних пиридо[3,2,1--*jk*]карбазола Фридел–Крафтсовим циклиалкиловањем. Поступак је реализован протоколом од три корака који укључују адицију карбазола на 3-метилкротононитрил. Новодобијени нитрил је подвргнут алкохолизи до жељеног естра, након чека су употребом Грињаревог реагенса добијени терцијарни алкохоли. Другим Грињаревим реагенсима нитрил је трансформисан у жељене кетоне који су редукцијом помоћу LAH или другим Грињаревим реагенсима преведени у одговарајуће секундарне или терцијарне алкохоле. Алкохоли су подвргнути реакцији циклиалкиловања под Фридел–Крафтсовим условима у присуству $AlCl_3/CH_3NO_2$, PTSA и PPA чиме су добијени три- и тетра-субституисани пиридо[3,2,1-*jk*]карбазоли.

REFERENCES

1. a) T. R. Kasturi, L. Mathew, J. A. Sattigeri, *Indian J. Chem., B* **29** (1990) 1004; b) T. Ohmoto, K. Koike, *Chem. Pharm. Bull*. **33** (1985) 4901; c) S. Szpilfogel, J. Battegay, *Helv. Chem. Acta* **30** (1947) 366
2. a) I. Fitilis, M. Fakis, I. Polyzos, V. Giannetas, P. Persephonis, P. Vellis, *Chem. Phys. Lett.* **447** (2007) 300; b) V. Promarak, A. Pankvuang, S. Ruchirawat, *Tetrahedron Lett.* **48** (2007) 1151; c) Q. Peng, X. Liu, Y. Qin, J. Xu, M. Li, L. Dai, *J. Mater. Chem.* **21** (2011) 7714
3. a) Y. Ooyama, Y. Harima, *Eur. J. Org. Chem.* **18** (2009) 2903; b) C. Li, M. Liu, N. G. Pschirer, M. Baumgarten, K. Müllen, *Chem. Rev.* **110** (2010) 6817
4. a) R. Chen, X. Yang, H. Tian, L. Sun, *J. Photochem. Photobiol., A* **189** (2007) 295; b) N. Koumura, Z.-S. Wang, S. Mori, M. Miyashita, E. Suzuki, K. Hara, *J. Am. Chem. Soc.* **128** (2006) 14256; c) S. M. R. Billah, R. M. Christie, R. Shamey, *Color. Technol.* **124** (2008) 223; d) T. Cheng, T. Lin, R. Brady, X. Wang, *Fibers Polym.* **9** (2008) 521
5. a) E. Fattorusso, O. Taglialatela-Scafati, *Modern Alkaloids*, 8th ed., Wiley-VCH, Weinheim, 2008, p. 481; b) G. L. Gupta, S. S. Nigam, *Planta Med.* **19** (1970) 83; c) A. N. Kesari, R. K. Gupta, G. Watal, *J. Ethnopharmacol.* **97** (2005) 247; d) M. Fiebig, J. M. Pezzuto, D. D. Soejarto, A. D. Kinghorn, *Phytochemistry* **24** (1985) 3041
6. a) A. Broadbent, H. Thomas, S. Broadbent, *Curr. Med. Chem.* **5** (1998) 469; b) E. Ziegler, U. Rossmann, F. Litvan, H. Meier, *Monatsh. Chem.* **93** (1962) 26; c) M. Harfenist, E. Magnien, *J. Org. Chem.* **28** (1963) 538
7. a) W. Stadlbauer, H. V. Dang, B. Knobloch, *J. Heterocycl. Chem.* **48** (2011) 1039; b) H. V. Dang, B. Knobloch, N. S. Habib, T. Kappe, W. Stadlbauer, *J. Heterocycl. Chem.* **42** (2005) 85
8. J. H. Markgraf, M. Finkelstein, J. R. Cort, *Tetrahedron* **52** (1996) 461

9. C. Mortelmans, G. V. Binst, *Tetrahedron* **34** (1978) 363

10. a) S. G. Gorbachev, V. D. Filimonov, E. E. Sirotkina, *Vysokomol. Soedin., B* **21** (1979) 125; b) *CA* **90** (1979) 204558f

11. R. Fusco, F. Sannicolo, *Tetrahedron Lett.* (1975) 3351

12. A. R. Katritzky, G. Zhang, M. Qi, L. Xie, *Tetrahedron Lett*. (1997) 6959

13. a) R. M. Roberts, A. A. Khalaf, *Friedel–Crafts Alkylation Chemistry. A Century of Discovery*, Marcel Dekker, New York, 1984; b) G. A. Olah, R. Krishnamurti, G. K. S. Prakash, in *Comprehensive Organic Synthesis*, Vol. 3, B. M. Trost, I. Fleming, Eds., Pergamon Press, Oxford, 1991, p. 293; c) L. R. C. Barclay, in *Friedel–Crafts and Related Reactions*, Vol. II, G. A. Olah, Ed., Interscience, New York, 1964, Ch. 22 and references therein

14. A. A. Khalaf, R. M. Roberts, *J. Org. Chem.* **37** (1972) 4227 and references therein

15. A. A. Khalaf, I. M. Awad, T. I. El-Emary, H. A. K. Abd El-Aal, *J. Indian Chem. Soc*. **85** (2008) 300

16. A. A. Khalaf, I. M. Awad, T. I. El-Emary, H. A. K. Abd El-Aal, *J. Indian Chem. Soc*. **83** (2006) 1018

17. A. A. Khalaf, A. M. El-Khawaga, I. M. Awad, H. A. K. Abd El-Aal, *ARKIVOC* (2009) 314

18. A. A. Khalaf, I. M. Awad, T. I. El-Emary, H. A. K. Abd El-Aal, *J. Indian Chem. Soc*. **87** (2010) 595

19. A. A. Khalaf, A. M. El-Khawaga, I. M. Awad, H. A. K. Abd El-Aal, *ARKIVOC* (2010) 338

20. a) J. Cason, F. S. Prout, *J. Am. Chem. Soc*. **66** (1944) 46; b) G. W. Perold, A. P. Steyn, F. V. K. V. Reiche, *J. Am. Chem. Soc*. **79** (1957) 462

21. a) R. F. Nystrom, W. G. Brown, *J. Am. Chem. Soc*. **69** (1947) 2548; b) D. G. Drueckhammer, C. F. Barbas, K. Nozaki, C. Wong, *J. Org. Chem*. **53** (1988) 1607.

Modern Friedel–Crafts chemistry. Part 36. Facile synthesis of some new pyrido[3,2,1-*jk*]carbazoles *via* Friedel–Crafts cyclialkylations

HASSAN ABDOU KOTB ABD EL-AAL* and ALI ALI KHALAF

Chemistry Department, Faculty of Science, Assiut University, Assiut, 71516, Egypt

CHARACTERIZATION DATA FOR THE SYNTHESIZED COMPOUNDS

*4-(9*H-*Carbazol-9-yl)-2,4-dimethylpentan-2-ol (1a).* White crystals; m.p.: 122 °C (methanol); Anal. Calcd. for $C_{19}H_{23}NO$ (FW: 281): C, 81.13; H, 8.18; N, 4.98 %. Found: C, 80.86; H, 8.30; N, 5.20 %; IR (KBr, cm^{-1}): 3360, 3255, 3070, 2950, 2850, 1590, 1485, 1450, 1440, 1340, 1145, 750; ^{1}H-NMR (90 MHz, CDCl$_3$, δ / ppm): 1.10 (6H, *s*, 2CH$_3$), 1.60 (6H, *s*, 2CH$_3$), 2.10 (2H, *s*, CH$_2$) 2.80 (1H, *s*, OH exchangeable with D$_2$O), 7.00–7.90 (8H, *m*, Ar-H); MS (EI, 70 eV, *m/z* (%)): 281 (M$^+$, 10.7), 263 (82.4), 222 (100), 208 (43.5), 191 (25.0), 181 (62.5), 177 (20.2), 167 (5.3), 166 (4.8), 90 (7.3), 77 (4.6), 66 (2.5).

*5-(9*H-*Carbazol-9-yl)-3-ethyl-5-methylhexan-3-ol (1b).* Yellow needles; m.p.: 115 °C (benzene/PE 60–80 °C); Anal. Calcd. for $C_{21}H_{27}NO$ (FW: 309): C, 81.55; H, 8.73; N, 4.53 %. Found: C, 81.80; H, 8.54; N, 4.42 %; IR (KBr, cm^{-1}): 3370, 3060, 2960, 2850, 1590, 1480, 1460, 1450, 1345, 1220, 720; ^{1}H-NMR (90 MHz, CDCl$_3$, δ / ppm): 0.90 (6H, *t*, *J* = 7.5 Hz, 2CH$_3$), 1.30 (4H, *q*, *J* = 7.5 Hz, 2CH$_2$), 1.70 (6H, *s*, 2CH$_3$), 1.80 (2H, *s*, CH$_2$), 2.40 (1H, *s*, OH exchangeable with D$_2$O), 6.70–7.30 (8H, *m*, Ar-H); MS (EI, 70 eV, *m/z* (%)): 309 (M$^+$, 14.5), 291 (100), 222 (85.3), 208 (38.2), 190 (22.4), 180 (55.2), 178 (11.2), 167 (3.2), 91 (17.5), 77 (3.5).

*3-(9*H-*Carbazol-9-yl)-3-methyl-1,1-diphenylbutan-1-ol (1c).* Reddish viscous oil; n_D^{25}: 1.542; Anal. Calcd. for $C_{29}H_{27}NO$ (FW: 405): C, 85.92; H, 6.66; N, 3.45 %. Found; C, 85.67; H, 6.35; N, 3.71 %; IR (film, cm^{-1}): 3380, 3060, 2990, 1585, 1555, 1445, 1370, 1220, 1130, 725; ^{1}H-NMR (90 MHz, CDCl$_3$, δ / ppm): 1.60 (6H, *s*, 2CH$_3$), 2.30 (2H, *s*, CH$_2$), 4.20 (1H, *s*, OH exchangeable with D$_2$O), 6.70–7.30 (8H, *m*, Ar-H); MS (EI, 70 eV, (*m/z* (%)): 405 (M$^+$, 5.5),

* Corresponding author. E-mail: hassankotb33@yahoo.com

387 (100), 310 (40.5), 233 (29.5), 222 (61.4), 207 (31.4), 191 (28.5), 180 (41.5), 177 (15.0), 91 (9.5), 77 (4.2).

*5-(9*H-*Carbazol-9-yl)-3,5-dimethylhexan-3-ol* (***1d***). Yellowish viscous oil; n_D^{25}: 1.558; IR (film, cm^{-1}): 3530, 3050, 2990, 1600, 1465, 1445, 1340, 1190, 920, 740, 695; ^{1}H NMR (90 MHz, CDCl$_3$, δ / ppm): 0.90 (3H, *t*, *J* = 9 Hz, CH$_3$), 1.20 (3H, *s*, CH$_3$), 1.50 (2H, *q*, *J* = 9 Hz, CH$_2$), 1.70 (6H, *s*, 2CH$_3$), 1.80 (2H, *s*, CH$_2$), 2.90 (1H, *s*, OH exchangeable with D$_2$O), 7.00–7.70 (8H, *m*, Ar-H); MS (EI, 70 eV, *m/z* (%)): 295 (M$^+$, 1.5), 208 (4.8), 277 (100), 251 (6.4), 222 (53.2), 208 (65.2), 190 (19.7), 182 (28.5), 178 (11.3), 90 (6.3), 77 (3.6). Anal. Calcd. for C$_{20}$H$_{25}$NO (295): C, 81.35; H, 8.47; N, 4.74. Found: C, 81.55; H, 8.24; N, 4.90.

*5-(9*H-*Carbazol-9-yl)-5-methyl-3-phenylhexan-3-ol* (***1e***). Cream plates; m.p.: 112 °C (benzene); Anal. Calcd. for C$_{25}$H$_{27}$NO (FW: 357): C, 84.03; H, 7.56; N, 3.92 %. Found: C, 84.26; H, 7.48; N, 3.85 %; IR (KBr, cm^{-1}): 3450, 3054, 2975, 1600, 1486, 1440, 1370, 1210, 1180, 740, 695; ^{1}H-NMR (90 MHz, CDCl$_3$, δ / / ppm): 0.90 (3H, *t*, *J* = 9 Hz, CH$_3$), 1.20 (1H, *s*, OH exchangeable with D$_2$O), 1.60 (6H, *s*, 2CH$_3$), 1.80 (2H, *q*, *J* = 9 Hz, CH$_2$), 2.20 (2H, *s*, CH$_2$), 7.10–7.60 (13H, *m*, Ar-H); MS (EI, 70 eV, *m/z* (%)): 357 (M$^+$, 2.7), 339 (72.3), 280 (11.5), 222 (100), 208 (32.4), 190 (22.8), 180 (37.6), 178 (25.3), 91 (7.5), 77 (3.8).

*4-(9*H-*Carbazol-9-yl)-4-methyl-2-phenylpentan-2-ol* (***1f***). Yellow viscous oil; n_D^{25}: 1.538; Anal. Calcd. for C$_{24}$H$_{25}$NO (FW: 343): C, 83.96; H, 7.28; N, 4.08 %. Found: C, 84.25; H, 7.18; N, 3.85 %; IR (film, cm^{-1}): 3375, 3120, 2980, 1610, 1550, 1520, 1480, 1365, 1145, 950, 740, 680; ^{1}H-NMR (90 MHz, CDCl$_3$, δ / ppm): 1.50 (3H, *s*, CH$_3$), 1.65 (6H, *s*, 2CH$_3$), 2.20 (2H, *s*, CH$_2$), 2.80 (1H, *s*, OH exchangeable with D$_2$O), 6.70–7.40 (13H, *m*, Ar-H); MS (EI, 70 eV, *m/z* (%)): 343 (M$^+$, 2.4), 325 (92.4), 266 (12.5), 222 (100), 208 (41.2), 190 (18.4), 177 (22.5), 90 (16.3), 77 (2.6).

*4-(9*H-*Carbazol-9-yl)-4-methylpentan-2-ol* (***1g***). Pale yellow viscous oil; n_D^{25}: 1.533; Anal. Calcd. for C$_{18}$H$_{21}$NO (FW: 267): C, 80.89; H, 7.86; N, 5.24 %. Found: C, 81.32; H, 7.51; N, 5.10 %; IR (film, cm^{-1}): 3355, 3055, 2980, 1610, 1470, 1450, 1370, 1210, 740, 690; ^{1}H-NMR (90 MHz, CDCl$_3$, δ / ppm): 1.30 (3H, *d*, *J* = 7.5 Hz, CH$_3$), 1.60 (6H, *s*, 2CH$_3$), 1.80 (2H, *d*, *J* = 7.5 Hz, CH$_2$), 2.40 (1H, *s*, OH exchangeable with D$_2$O), 3.30 (1H, *m*, CH), 6.90–7.40 (8H, *m*, Ar-H); MS (EI, 70 eV, *m/z* (%)): 249 (M$^+$–H$_2$O, 100), 252 (9.4), 222 (65.2), 208 (32.4), 190 (18.2), 180 (33.5), 178 (11.4), 166 (5.7), 91 (4.3), 77 (4.6).

*5-(9*H-*Carbazol-9-yl)-5-methylhexan-3-ol* (***1h***). Reddish viscous oil; n_D^{25}: 1.536; Anal. Calcd. for C$_{19}$H$_{23}$NO (FW: 281): C, 81.13; H, 8.18; N, 4.98 %. Found: C, 80.77; H, 8.05; N, 4.82 %; IR (film, cm^{-1}): 3620, 3060, 2995, 1595, 1460, 1450, 1370, 1220, 1175, 740, 695; ^{1}H-NMR (90 MHz, CDCl$_3$, δ / ppm): 0.90 (3H, *t*, *J* = 7.5 Hz, CH$_3$), 1.42 (2H, *q*, *J* = 7.5 Hz, CH$_2$), 1.55 (6H, *s*, 2CH$_3$), 1.80 (2H, *d*, *J* = 7.5 Hz, CH$_2$), 3.20 (1H, *m*, CH), 3.80 (1H, *s*, OH exchangeable with D$_2$O), 6.80–7.50 (8H, *m*, Ar-H); MS (EI, 70 eV, *m/z* (%)): 281 (M$^+$, 1.2),

263 (M$^+$–H$_2$O, 100), 204 (7.5), 222 (41.5), 208 (39.0), 191 (38.5), 180 (10.2), 177 (8.4), 167 (6.3), 91 (4.9).

*3-(9*H-*Carbazol-9-yl)-3-methyl-1-phenylbutan-1-ol (1i)*. Yellowish viscous oil; n_D^{25}: 1.541; Anal. Calcd. for C$_{23}$H$_{23}$NO (FW: 329): C, 83.89; H, 6.99; N, 4.25 %. Found: C, 83.80; H, 7.10; N, 4.45 %; IR (film, cm^{-1}):3450, 3085, 2975, 1600, 1475, 1450, 1370, 1210, 1180, 740, 695; ^{1}H-NMR (90 MHz, CDCl$_3$, δ / / ppm): 1.60 (6H, *s*, 2CH$_3$), 2.20 (2H, *m*, CH$_2$), 3.30 (1H, *s*, OH exchangeable with D$_2$O), 4.30 (1H, *m*, CH), 6.90–7.40 (13H, *m*, Ar-H); MS (EI, 70 eV, *m/z* (%)): 329 (M$^+$, 3.5), 311 (M$^+$–H$_2$O, 100), 252 (15.4), 223 (6.9), 222 (22.7), 208 (52.9), 191 (12.6), 182 (16.3), 177 (27.0), 166 (7.4), 90 (10.4), 77 (3.2).

*3-(9*H-*Carbazol-9-yl)-3-methylbutanenitrile (4)*. Yield: 86.6 %, white crystals; m.p.: 122 °C (acetone); Anal. Calcd. for C$_{17}$H$_{16}$N$_2$ (FW: 248): C, 82.25; H, 6.45; N, 11.29. Found; C, 82.47; H, 6.62; N, 10.92; IR (KBr, cm^{-1}): 3060, 2970, 2250, 1595, 1480, 1455, 1330, 1170, 745; ^{1}H-NMR (90 MHz, CDCl$_3$, δ / ppm): 1.70 (6H, *s*, 2CH$_3$), 2.80 (2H, *s*, CH$_2$), 7.10–7.90 (8H, *m*, Ar-H); MS (EI, 70 eV) *m/z* (%): 248 (M$^+$, 4.2), 221 (M$^+$–HCN, 32.4), 208 (100), 204 (14.2), 191 (14.3), 177 (6.4), 166 (3.3), 91 (4.1), 77 (6.4), 66 (2.8).

*Ethyl 3-(9*H-*carbazol-9-yl)-3-methylbutanoate (5)*. Yield: 85.7 %; n_D^{25}: 1.5722; Anal. Calcd. for C$_{19}$H$_{21}$NO$_2$ (FW: 295): C, 77.28; H, 7.11; N, 4.74 %. Found: C, 77.15; H, 6.85; N, 5.10 %; IR (film, cm^{-1}): 3040, 2995, 1740, 1600, 1580, 1480, 1450, 1320, 1170, 740; ^{1}H-NMR (90 MHz, CDCl$_3$, δ / ppm): 1.30 (3H, *t*, *J* = 9 Hz, CH$_3$), 1.60 (6H, *s*, 2CH$_3$), 2.60 (2H, *s*, CH$_2$), 4.10 (2H, *q*, *J* = 9 Hz, CH$_2$), 6.90–7.90 ppm (8H, *m*, Ar-H); MS (EI, 70 eV, *m/z* (%)): 296 (M$^+$+1, 4.7), 295 (M$^+$, 32.5), 250 (M$^+$–OC$_2$H$_5$, 100), 222 (21.6), 208 (52.4), 191 (20.4), 177 (6.5), 166 (3.2), 91 (5.6), 77 (4.4), 66 (2.7).

*4-(9*H-*Carbazol-9-yl)-4-methylpentan-2-one (6a)*. Yield: 75 %; m.p.: 92 °C (acetone); Anal. Calcd. for C$_{18}$H$_{19}$NO (FW: 265): C, 81.51; H, 7.16; N, 5.28 %. Found; C, 81.90; H, 6.75 ; N, 5.17 %; IR (KBr, cm^{-1}): 3070, 2985, 1715, 1585, 1480, 1440, 1375, 1275, 1060, 1020, 740, 690; ^{1}H-NMR (90 MHz, CDCl$_3$, δ / / ppm): 1.40 (2H, *s*, 2CH$_3$), 2.10 (3H, *s*, CH$_3$), 2.70 (2H, *s*, CH$_2$), 7.10–8.20 (8H, *m*, Ar-H); MS (EI, 70 eV, *m/z* (%)): 265 (M$^+$, 28.4), 250 (100), 222 (72.5), 207 (13.7), 192 (19.7), 177 (6.3), 167 (4.2), 166 (4.8), 91 (3.5), 77 (2.3), 66 (3.0).

*5-(9*H-*Carbazol-9-yl)-5-methylhexan-3-one (6b)*. Yield: 77 %; m.p.: 85 °C (methanol); Anal. Calcd. for C$_{19}$H$_{21}$NO (FW: 279): C, 81.72; H, 7.52; N, 5.01 %. Found: C, 81.69; H, 7.63; N, 5.18 %; IR (KBr, cm^{-1}): 3050, 2990, 2910, 1718, 1580, 1470, 1450, 1370, 1260, 1060, 1030, 735, 680; ^{1}H-NMR (90 MHz, CDCl$_3$, δ / ppm): 1.0 (3H, *t*, *J* = 7.5 Hz, CH$_3$), 1.60 (6H, *s*, 2CH$_3$), 2.35 (2H, *q*, *J* = 7.5 Hz, CH$_2$), 2.80 (2H, *s*, CH$_2$), 6.80–7.50 (8H, *m*, Ar-H); MS (EI, 70 eV, *m/z* (%)): 279 (M$^+$, 24.6), 250 (100), 222 (72.5), 207 (68.5), 191 (29.7), 178 (12.5), 167 (9.2), 166 (7.3), 91 (5.9), 77 (6.4).

*3-(9*H*-Carbazol-9-yl)-3-methyl-1-phenylbutan-1-one (**6c**)*. Yield: 71 %; m.p.: 122 °C (acetone); Anal. Calcd. for $C_{23}H_{21}NO$ (FW: 327): C, 84.40; H, 6.42; N, 4.28 %. Found: C, 84.65; H, 6.25; N, 4.44 %; IR (KBr, cm^{-1}): 3055, 3010, 2980, 1725, 1580, 1480, 1450, 1375, 1275, 1060, 1020, 740, 690; ^{1}H-NMR (90 MHz, CDCl$_3$, δ / ppm): 1.60 (6H, *s*, 2CH$_3$), 2.90 (2H, *s*, CH$_2$), 6.90–8.00 (13H, *m*, Ar-H): MS (EI, 70 eV, *m/z* (%)): 327 (M$^+$, 45.8), 250 (68.4), 222 (100), 209 (43.6), 191 (10.7), 178 (7.6), 166 (5.4), 90 (5.7), 77 (4.1), 68 (20.5).

*5,6-Dihydro-4,4,6,6-tetramethyl-4*H*-pyrido[3,2,1*-jk*]carbazole (**8a**)*. Yellow plates; R_f: 0.47 (1:3, EtOAc/hexane); m.p.: 105 °C (benzene); Anal. Calcd. for $C_{19}H_{21}N$ (FW: 263): C, 86.69; H, 7.98; N, 5.32 %. Found: C, 86.50; H, 7.65; N, 5.52 %; IR (KBr, cm^{-1}): 3060, 2980, 1610, 1570, 1490, 1445, 1430, 1330, 1060; ^{1}H-NMR (400 MHz, CDCl$_3$, δ / ppm): 1.22 (6H, *s*, 2CH$_3$), 1.71 (6H, *s*, 2CH$_3$), 1.94 (6H, *s*, CH$_2$), 6.85–7.40 (7H, *m*, Ar-H); MS (EI, 70 eV, *m/z* (%)): 263 (M$^+$, 55.6), 248 (M$^+$–CH$_3$, 100), 233 (10.8), 232 (M$^+$–2CH$_3$–H, 22.8), 218 (8.3), 204 (6.2), 190 (4.7), 177 (6.4), 166 (11.3), 151 (1.6), 109 (3.3), 90 (2.3), 77 (6.1), 66 (1.2).

*4,4-Diethyl-5,6-dihydro-6,6-dimethyl-4*H*-pyrido[3,2,1*-jk*]carbazole* (**8b**). Brownish viscous oil; R_f: 0.53 (1:3, EtOAc/hexane); n_D^{25}: 1.635; Anal. Calcd. for $C_{21}H_{25}N$ (FW: 291): C, 86.59; H, 8.59; N, 4.81 %. Found: C, 86.33; H, 8.82; N, 5.12 %; IR (film, cm^{-1}): 3070, 2990, 1610, 1560, 1450, 1445, 1330, 745; ^{1}H--NMR (400 MHz, CDCl$_3$, δ / ppm): 0.90 (6H, *t*, *J* = 9 Hz, 2CH$_3$), 1.50 (4H, *q*, *J* = 9 Hz, 2CH$_2$), 1.70 (6H, *s*, 2CH$_3$), 1.93 (2H, *s*, CH$_2$), 6.61–7.41 (7H, *m*, Ar-H); MS (EI, 70 eV, *m/z* (%)): 291 (M$^+$, 35.6), 290 (M$^+$–H, 100), 276 (4.2), 262 (M$^+$––C$_2$H$_5$ 15.8), 261 (4.2), 247 (M$^+$–CH$_3$–C$_2$H$_5$, 18.4), 233 (4.8), 217 (6.3), 203 (4.1), 190 (2.5), 177 (3.4), 166 (1.7), 151 (2.7), 109 (1.3), 90 (5.3), 77 (6.7), 66 (3.6).

*5,6-Dihydro-6,6-dimethyl-4,4-diphenyl-4*H*-pyrido[3,2,1*-jk*]carbazole* (**8c**). Pale brown solid; R_f: 0.28 (1:3, EtOAc/hexane); m.p.: 125 °C (methanol); Anal. Calcd. for $C_{29}H_{25}N$ (FW: 387): C, 89.92; H, 6.46; N, 3.61 %. Found: C, 89.90; H, 6.52; N, 3.42 %; IR (KBr, cm^{-1}): 3090, 2920, 1610, 1475, 1450, 1315, 745; ^{1}H-NMR (400 MHz, CDCl$_3$, δ / ppm): 1.72 (6H, *s*, 2CH$_3$), 2.61 (2H, *s*, CH$_2$), 6.63–7.37 (17H, *m*, Ar-H); MS (EI, 70 eV, *m/z* (%)): 388 (M$^+$+1, 7.3), 387 (M$^+$, 15.5), 371 (M$^+$–CH$_3$–H, 100), 357 (M$^+$–2CH$_3$, 33.2), 309 (M$^+$–Ph–H, 8.9), 295 (81.5), 280 (77.2), 233 (2.5), 218 (1.6), 203 (2.4), 190 (7.5), 177 (5.4), 166 (4.6), 151 (6.4), 109 (0.3), 90 (3.3), 77 (3.5), 66 (2.6)..

*4-Ethyl-5,6-dihydro-4,6,6-trimethyl-4*H*-pyrido[3,2,1*-jk*]carbazole* (**8d**). Reddish viscous oil; R_f: 0.6 (1:3, EtOAc/hexane); n_D^{25}: 1.605; Anal. Calcd. for $C_{20}H_{23}N$ (FW: 277): C, 86.64; H, 8.3; N, 5.05 %. Found: C, 86.4; H, 8.45; N, 5.12 %; IR (film, cm^{-1}): 3095, 2920, 1620, 1565, 1490, 1445, 1365, 1070, 745, 690; ^{1}H-NMR (400 MHz, CDCl$_3$, δ / ppm): 0.87 (3H, *t*, *J* = 9 Hz, CH$_3$), 1.35 (3H, *s*, CH$_3$), 1.52 (2H, *q*, *J* = 9 Hz, CH$_2$), 1.73 (6H, *s*, 2CH$_3$), 2.15 (2H, *m*,

CH$_2$), 6.83–7.35 (7H, *m*, Ar–H); MS (EI, 70 eV, *m/z* (%)): 278 (M$^+$+1, 3.3), 277 (M$^+$, 15.5), 262 (M$^+$–CH$_3$, 62.4), 261 (18.4), 248 (42.1), 247 (M$^+$–2CH$_3$, 100), 233 (4.6), 218 (7.6), 203 (7.4), 190 (6.4), 177 (2.1), 166 (6.4), 151 (3.0), 109 (1.5), 91 (2.5), 77 (1.3), 66 (3.6).

*4-Ethyl-5,6-dihydro-6,6-dimethyl-4-phenyl-4*H-*pyrido[3,2,1*-jk]*carbazole (8e)*. Brown crystals; R_f: 0.38 (1:3, EtOAc/hexane); m.p.: 82 °C (methanol); Anal. Calcd. for C$_{25}$H$_{25}$N (FW: 339): C, 88.49; H, 7.37; N, 4.13 %. Found: C, 88.57; H, 7.42; N, 3.84 %; IR (KBr, cm^{-1}): 3065, 2965, 1600, 1568, 1465, 1440, 1360, 1070, 740, 695; ^{1}H-NMR (400 MHz, CDCl$_3$, *δ* / ppm): 0.93 (3H, *t*, *J* = 7.5 Hz, CH$_3$), 1.55 (6H, *s*, 2CH$_3$), 1.82 (2H, *q*, *J* = 7.5 Hz, CH$_2$), 2.36 (2H, *m*, CH$_2$), 6.94–7.43 (12H, *m*, Ar-H); MS (EI, 70 eV, *m/z* (%)): 339 (M$^+$, 7.3), 323 (M$^+$––CH$_3$–H, 100), 309 (M$^+$–2CH$_3$, 40.4), 295 (60.2), 280 (20.4), 262 (4.1), 247 (M$^+$–CH$_3$–Ph, 11.4), 232 (2.6), 218 (5.6), 203 (1.4), 190 (6.4), 177 (2.4), 168 (15.4), 154 (0.5), 109 (2.5), 90 (4.2), 77 (2.1), 66 (1.4)..

*5,6-Dihydro-4,6,6-trimethyl-4-phenyl-4*H-*pyrido[3,2,1*-jk]*carbazole   (8f)*. Buff crystals; R_f: 0.35 (1:3, EtOAc/hexane); m.p.: 115 °C (benzene); Anal. Calcd. for C$_{24}$H$_{23}$N (FW: 325): C, 88.61; H, 7.07; N, 4.30 %. Found: C, 88.70; H, 7.22; N, 4.06 %; IR (KBr, cm^{-1}): 3075, 2950, 1610, 1558, 1482, 1443, 1360, 1073, 745, 690; ^{1}H-NMR (400 MHz, CDCl$_3$, *δ* / ppm): 1.62 (6H, *s*, 2CH$_3$), 1.75 (3H, *s*, CH$_3$), 2.25 (2H, *m*, CH$_2$), 6.93–7.51 (12H, *m*, Ar-H); MS (EI, 70 eV, *m/z* (%)): 326 (M$^+$+H, 7.3), 325 (M$^+$–CH$_3$–H, 100), 310 (M$^+$–2CH$_3$, 22.4), 295 (14.5), 280 (3.7), 248 (M$^+$–Ph, 7.4), 233 (4.2), 218 (2.2), 203 (0.7), 190 (3.4), 177 (4.3), 168 (18.2), 154 (2.3), 109 (1.6), 90 (3.7), 77 (1.3), 66 (1.8)..

*5,6-Dihydro-4,6,6-trimethyl-4*H-*pyrido[3,2,1*-jk]*carbazole   (8g)*. Reddish viscous oil; R_f: 0.57 (1:3, EtOAc/hexane); n_{D}^{25}: 1.624; Anal. Calcd. for C$_{18}$H$_{19}$N (FW: 249): C, 86.74; H, 7.63; N, 5.62 %. Found: C, 87.10; H, 7.44; N, 5.47 %; IR (film, cm^{-1}): 3072, 2984, 1620, 1585, 1480, 1440, 1370, 1065, 750, 685; ^{1}H--NMR (400 MHz, CDCl$_3$, *δ* / ppm): 1.25 (3H, *d*, *J* = 7.5 Hz, CH$_3$), 1.60 (6H, *s*, 2CH$_3$), 2.05 (2H, *m*, CH$_2$), 2.85 (1H, *m*, CH), 6.85–7.40 (7H, *m*, Ar-H); MS (EI, 70 eV, *m/z* (%)): 249 (M$^+$, 11.4), 234 (M$^+$–CH$_3$, 55.2), 218 (M$^+$–CH$_3$–H, 100), 204 (M$^+$–3CH$_3$, 44.5), 219 (6.9), 190 (32.5), 177 (11.7), 167 (9.4), 166 (6.5), 91 (5.3), 77 (14.2), 66 (3.7).

*4-Ethyl-5,6-dihydro-6,6-dimethyl-4*H-*pyrido[3,2,1*-jk]*carbazole (8h)*. Reddish viscous oil; R_f: 0.63 (1:3, EtOAc/hexane); n_{D}^{25}: 1.594; Anal. Calcd. for C$_{19}$H$_{21}$N (FW: 263): C, 86.7; H, 7.90; N, 5.32 %. Found: C, 86.84; H, 7.62; N, 5.35 %; IR (film, cm^{-1}): 3066, 2935, 1605, 1562, 1475, 1455, 1346, 1065, 740, 695; ^{1}H-NMR (400 MHz, CDCl$_3$, *δ* / ppm): 0.92 (3H, *s*, CH$_3$), 1.57 (2H, *m*, *J* = 9 Hz, CH$_2$), 1.64 (6H, *s*, 2CH$_3$), 2.10 (2H, *m*, CH$_2$), 2.65 (1H, *m*, CH), 6.80–7.41 (7H, *m*, Ar-H); MS (EI, 70 eV, *m/z* (%)): 264 (M$^+$+1, 18.4), 263 (M$^+$, 86.8), 248 (M$^+$–CH$_3$, 100), 234 (11.5), 232 (M$^+$–2CH$_3$–H, 15.3), 219 (6.5), 217 (7.9), 204 (4.2), 192 (30.4), 177 (5.3), 167 (3.7), 166 (5.2), 91 (6.8), 77 (5.4), 66 (2.1).

*5,6-Dihydro-6,6-dimethyl-4-phenyl-4*H-*pyrido[3,2,1-*jk*]carbazole (8i):* Yellowish viscous oil; Anal. Calcd. for $C_{23}H_{21}N$ (311): C, 88.74; H, 6.75; N, 4.5. Found: C, 88.75; H, 6.84; N, 4.25; R_f 0.45 (1:3, EtOAc/hexane); n_D^{25}: 1.615; IR (film, cm^{-1}): 3060, 2970, 1600, 1568, 1480, 1440, 1360, 1070, 740, 695 cm^{-1}; ^{1}H NMR (400 MHz, CDCl$_3$, δ / ppm): 1.63 (6H, *s*, 2CH$_3$), 2.30 (2H, *m*, CH$_2$), 3.83 (1H, *m*, CH), 6.70–7.35 (12H, *m*, Ar-H); MS (EI, 70 eV), *m/z* (%): 312 (M$^+$+1, 16.9), 311 (M$^+$, 41.5), 296 (M$^+$–CH$_3$, 12.5), 281 (M$^+$–2CH$_3$, 100), 234 (17.9), 219 (21.2), 204 (3.5), 191 (22.4), 177 (6.2), 168 (11.2), 166 (2.7), 91 (4.3), 77 (6.2), 66 (2.1).

Synthesis of quinolone substituted 2-azetidinone derivatives

UDAY C. MASHELKAR*, MUKESH S. JHA** and BEENA U. MASHELKAR

Organic Research Laboratory, S. S. and L. S. Patkar College, Goregaon (West), Mumbai 400 062, India

Abstract: Acetanilide was converted into 2-chloro-3-formylquinoline by reaction with DMF–POCl$_3$ at 80–90 °C and then condensed with aromatic primary amines to give Schiff bases **3a**–**c**. These Schiff bases were then reacted with acid chlorides in toluene in the presence of a base to give 1,3,4-trisubstituted-2-azetidinones.

Keywords: acetanilide; 2-chloro-3-formylquinoline; aromatic amine; acid chloride; tributylamine; 2-azetidinone.

INTRODUCTION

Malaria is one of the most widespread diseases in the world besides tuberculosis and AIDS. The World Health Organization estimates that about 40 % of the world's population presently lives under malarial threat and approximately 300–500 million cases of malaria occur annually, leading to 1–3 million deaths. Mortality is particularly high in children under the age of five, accounting for about 25 % of childhood deaths in Africa.[1,2] Malaria is caused by different species of *Plasmodium*, of which *Plasmodium falciparum* is the most virulent human malarial parasite and the others include *P. vivax*, *P. malariae* and *P. ovale*. A major reason for the continued severity of the worldwide malarial problem is the increasing resistance of malarial parasites to the available antimalarial drugs, such as chloroquine. Although continued attempts to develop a vaccine for malaria are ongoing, drugs remain the only available treatment option.

Quinoline-containing compounds have long been used for the treatment of malaria, beginning with quinine. The systematic modification of quinine led to the potent and inexpensive 4-aminoquinoline drug, chloroquine, and other related drugs. After worldwide development of drug resistance to chloroquine, the ratio-

---

*·** Corresponding authors. E-mails: (*)ucmashelkar@rediffmail.com;
(**)Jhamukesh1@rediffmail.com

621

nal approach in chemistry and screening efforts produced mefloquine, another quinoline-containing compound that was highly active against the chloroquine resistant strains of *P. falciparum*.

Since the development of mefloquine, there have been several reports of new potent quinoline compounds. Most of these contain the 7-chloroquinoline nucleus of chloroquine and vary in the length and nature of their basic amine side chain. Currently, compounds such as amodiaquine are promising leads for the development of new drugs.

The *β*-lactam class of compounds has served an important and highly successful role in the pharmaceutical industry. Miracle drugs such as penicillins and cephalosporins have significantly improved human health and life expectancy. Although most penicillin- and cephalosporin-like compounds have been obtained by biosynthesis, chemical modification of intermediates for bioassay of antibacterial activity has become important because of the growing resistance of bacteria to penicillin and cephalosporin-like compounds and the need for medicines with more specific antibacterial activity.[3,4] Developments in the field of *β*-lactams[5–8] during the last decades indicate that the only essential feature for the antibacterial activity in these compounds is the presence of the *β*-lactam (2-azetidinone) ring. Azetidinone derivatives have also been recognized as TNF-alpha converting enzyme (TACE) inhibitors[9] and agents with new biological activities, such as anticancer,[10] anticoccidial,[11] cardiovascular,[12] antiviral,[13] mutagenic,[14] anticonvulsant and anti-inflammatory.[15,16]

Bearing this in mind, it was decided to synthesize 2-azetidinones that have the quinoline moiety at position 3.

RESULTS AND DISCUSSION

2-Chloro-3-formylquinoline (**2**) was prepared according to a procedure reported[17] in literature by reacting acetanilide (**1**) with DMF–POCl$_3$ at 80–90 °C and characterized by its physical and spectral data, which were in accordance with the literature. The IR spectrum of compound **2** showed a band for one carbonyl group at 1726 cm^{-1} and the ^{1}H-NMR spectrum indicated the presence of an aldehyde proton at δ 10.60 ppm. 2-Chloro-3-formylquinoline (**2**) was condensed with various aromatic amines to yield Schiff bases **3a**–**c**. The reactions were monitored by TLC. After completion of the reactions, the products were filtered and dried to afford the Schiff bases **3a**–**c**, which were characterized by their physical and spectral data. In general their IR spectra showed the absence of a carbonyl band and the appearance of a band for –CH=N– at 1612 cm^{-1}. Other bands were present at 1501 & 1593 cm^{-1}. The ^{1}H-NMR spectra showed the absence of an aldehyde proton and presence of a –CH=N– (azomethine) proton at δ 9.0 ppm.

These Schiff bases **3a**–**c** were then reacted with acid chlorides in the presence of a base to yield the 1,3,4-trisubstituted-2-azetidinones **4a**–**h**. The IR spectra of compounds **4a**–**h** showed the absorption for one carbonyl. In the ^{1}H-NMR spectra, two doublets for C_3-H and C_4-H were present. The envisaged reaction sequence is depicted in Scheme 1.
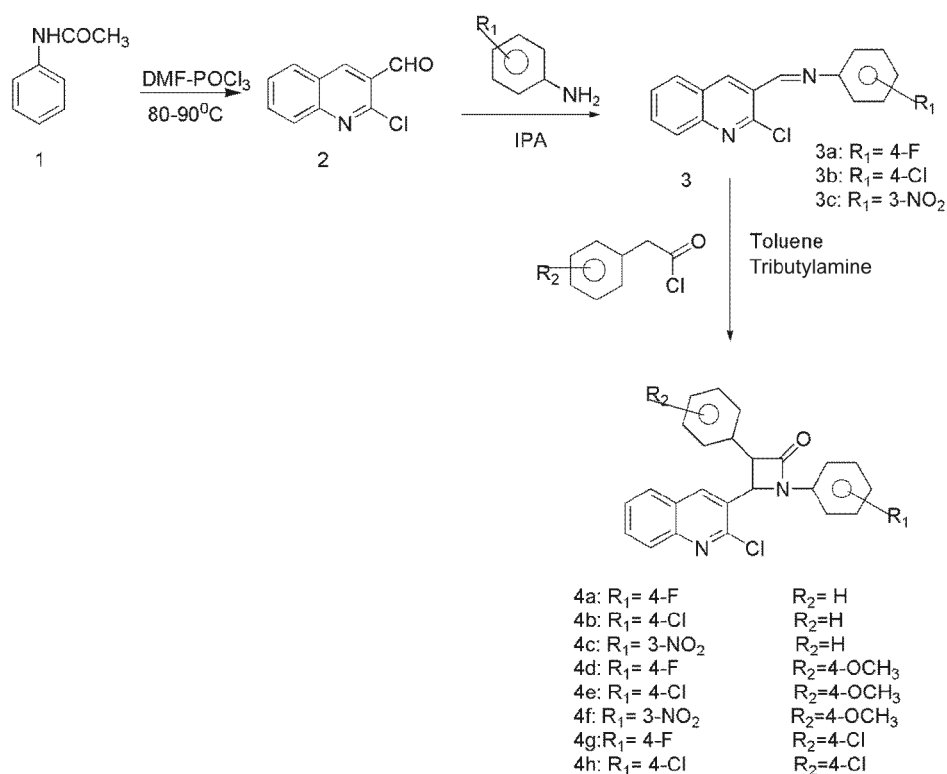
Scheme 1. The reaction sequence.

The structures of compounds **4a**–**h** were established based on their IR and ^{1}H-NMR spectra. As reported in the literature, *cis*-isomer shows higher values of the coupling constant than the *trans*-isomer.[18] The majority of the isolated compounds showed lower values of the coupling constant, confirming the *trans*-azetidinone. However, a few of them showed a mixture of both, in which the *trans*-azetidinones contained small amounts of *cis*-azetidinone (Table I).

EXPERIMENTAL

All the compounds were identified by examination of their spectral data and physical properties. The reported yields refer to the isolated yields of the desired products. Melting points were determined on Buchi-545 melting point apparatus and are uncorrected. The progress of the reaction was monitored by TLC. The IR spectra were recorded on a Perkin

Elmer Spectrum-1 (FTIR) instrument using KBr discs, The ^{1}H- and ^{13}C-NMR spectra were recorded in CDCl$_3$ using an Avance 400 MHz Bruker spectrometer with TMS as the internal standard. The mass spectra were recorded on a Thermo Finigan Ion Trap GCMS Polaris Q instrument. The dry reactions were performed under nitrogen with magnetic/mechanical stirring. The analytical and spectral data of the synthesized compounds are given in the Supplementary material to this paper.

TABLE I. Stereochemistry of compounds **4a**–**h**

Compound	R1	R2	Isolated isomer
4a	4-F	H	*Trans*
4b	4-Cl	H	*Trans:cis* (86:14)
4c	3-NO$_2$	H	*Trans*
4d	4-F	4-OCH$_3$	*Trans:cis* (78: 22)
4e	4-Cl	4-OCH$_3$	*Trans*
4f	3-NO$_2$	4-OCH$_3$	*Trans*
4g	4-F	4-Cl	*Trans*
4h	4-Cl	4-Cl	*Trans*

Synthesis of 2-chloro-3-formylquinoline (2)

To a stirred solution of acetanilide (6.75 g, 50.0 mmol) in dry DMF (10.95 g, 150.0 mmol) at 0–5 °C, POCl$_3$ (92.1 g, 600 mmol) was added dropwise and the mixture was stirred at 80–90 °C for a time ranging between 4–16 h. The mixture was then poured onto crushed ice, stirred for 5 min and the resulting solid was filtered, washed well with water and dried. The compounds were purified by recrystallisation from either ethyl acetate or acetonitrile.

General procedure for the synthesis of N-[(2-chloroquinolin-3-yl)methylene]benzenamine derivatives (3a–c)

An intimate mixture of 2-chloro-3-formylquinoline (**2**) (10 mmol) and the corresponding aromatic primary amine (11 mmol) was refluxed in 2-propanol (25 mL) for 6–7 h. The progress of the reaction was monitored by TLC. After completion of the reaction, the reaction mass was cooled to 10 °C and the product was filtered and washed with cold 2-propanol to obtain the solid products.

General procedure for the synthesis of 1,3,4-trisubstituted-2-azetidinones (4a–h)

A mixture of an *N*-((2-chloroquinolin-3-yl)methylene)benzenamine derivative (10 mmol) (**3a–c**), acid chlorides (20 mmol) and tri-*n*-butylamine (30 mmol) in toluene (50 mL) was refluxed for 3–4 h. The progress of the reaction was monitored by TLC. After completion of the reaction, the reaction mixture was then cooled to room temperature and 1:1 HCl (40–50 mL) was added. The organic layer was separated and washed with water, followed by NaHCO$_3$ solution and finally with water and dried over anhydrous sodium sulfate before the solvent was removed under reduced pressure. The required compound was isolated using column chromatography (*n*-hexane:ethyl acetate = 90:10) and thereafter it was crystallized from ethanol.

CONCLUSION

In conclusion, novel 4-(2-chloroquinolin-3-yl)-1,3-diphenylazetidin-2-ones were synthesized under mild condition starting from acetanilide.

SUPPLEMENTARY MATERIAL

Analytical and spectral data for the synthesized compounds are available electronically from http://www.shd.org.rs/JSCS/, or from the corresponding author on request.

И З В О Д

СИНТЕЗА ХИНОЛИЛ-СУПСТИТУИСАНИХ 2-АЗЕТИДИНОНА

UDAY C. MASHELKAR, MUKESH S. JHA и BEENA U. MASHELKAR

Organic Research Laboratory, S. S. and L. S. Patkar College, Goregaon (West), Mumbai 400 062, India

Ацетанилид је преведен у 2-хлор-3-формилхинолин помоћу DMF–POCl₃ загревањем на 80–90 °C, а кондензацијом са примарним аминима производ је преведен у Шифове базе **3a–c**. Шифове базе реакцијом са хлоридима карбоксилних киселина у присуству базе, у толуену, као производ дају 1,3,4-трисупституисане 2-азетидине.

(Примљено 17. јуна, ревидирано 30. јула 2012)

REFFERENCES

1. R. W. Snow, C. A. Guerra, A. M. Noor, H. Y. Myint, S. I. Hay, *Nature* **434** *(*2005) 214
2. I. Bathurst, C. Hentschel, *Trends Parasitol.* **22** (2006) 301
3. A. Upadhyay, S. K. Srivastava, S. D. Srivastava, R. Yadav, *Proc. Natl. Acad. Sci. India* **80** (2010) 131
4. Y. Ikee, K. Hashimoto, M. Nakashima, K. Hayashi, S. Sano, M. Shiro, Y. Nagao, *Bioorg. Med. Chem. Lett.* **17** (2007) 942
5. S. D. Sharma, U. Mehra, *J. Sci. Ind. Res.* **47** (1988) 451
6. L. R. Verma, C. S. Narayanan, *Indian J. Chem., B* **30** (1991) 676
7. E. Grochowski, K. Pupek, *Tetrahedron* **47** (1991) 6759
8. M. S. Manhas, D. R. Wagle, J. Ciang, A. K. Bose, *Heterocycles* **27** (1988) 1755
9. B. G. Rao, U. K. Bandarage, T. Wang, J. H. Come, E. Perola, Y. W. S.-K. Tian, J. O. Saunders, *Bioorg. Med. Chem. Lett.* **17** (2007) 2250
10. B. K. Banik, I. Banik, F. F. Becker, *Bioorg. Med. Chem.* **13** (2005) 3611
11. G.-B. Liang, X. Qian, D. Feng, M. Fisher, T. Crumley, S. J. Darkin-Rattray, P. M. Dulski, A. Gurnett, P. S. Leavitt, P. A. Liberator, A. S. Misura, S. Samaras, T. Tamas, D. M. Schmatz, M. Wyvratta, T. Biftu, *Bioorg. Med. Chem. Lett.* **18** (2008) 2019
12. S. Takai, D. Jin, M. Muramatsu, Y. Okamoto, M. Miyazaki, *Eur. J. Pharmacol.* **501** (2004) 1
13. W. W. Ogilvie, C. Yoakim, F. Do, B. Hache, L. Lagace, J. Naud, J. A. Omeara, R. Deziel, *Bioorg. Med. Chem.* **7** (1999) 1521
14. H. Valette, F. Dolle, M. Bottlaender, F. Hinnen, D. Marzin, *Nucl. Med. Biol.* **29** (2002) 849
15. P. Kohli, S. D. Srivastava, S. K. Srivastava, *J. Indian Chem. Soc.* **85** (2008) 326
16. S. K. Srivastava, S. Srivastava, S. D. Srivastava, *Indian J. Chem., B* **38** (1999) 183
17. A. Srivastava, R. M. Singh, *Indian J. Chem., B* **44** (2005) 1868
18. M. Browne, D. A. Burnett, M. A. Caplen, L.-Y. Chen, J. W. Clader, M. Domalski, S. Dugar, P. Pushpavanam, R. Sher, W. Vaccaro, M. Viziano, H. Zhao, *Tetrahedron Lett.* **36** (1995) 2555.

Synthesis of quinolone substituted 2-azetidinone derivatives

UDAY C. MASHELKAR*, MUKESH S. JHA** and BEENA U. MASHELKAR

Organic Research Laboratory, S. S. and L. S. Patkar College, Goregaon (West), Mumbai 400 062, India

2-Chloro-3-formylquinoline (2). White crystals; Yield: 82 %; m.p.: 149 °C; Anal. Calcd. for $C_{10}H_6ClNO$: C, 62.68; H, 3.16; N, 7.31 %. Found: C, 62.82; H, 3.37; N, 7.45 %; IR (KBr, cm^{-1}): 3050, 1726, 1610, 1555, 1448; ^{1}H-NMR (400 MHz, CDCl$_3$, δ / ppm): 7.7–8.8 (5H, *m*, Ar-H), 10.5 (1H, *s*, –CHO); ^{13}C-NMR (100.622 MHz, CDCl$_3$, δ / ppm): 127.7, 128.3, 129.4, 131.3, 134.1, 143.9, 147.4, 148.9, 151.2, 189.1; mass (*m/z*): 191 [M$^+$].

N-[(2-Chloroquinolin-3-yl)methylene]-4-fluorobenzenamine (3a). Yellow solid; Yield: 84 %; m.p.: 232–234 °C; Anal. Calcd. for $C_{16}H_{10}ClFN_2$: C, 67.50; H, 3.54; N, 9.84 %. Found: C, 67.68; H, 3.40; N, 9.99 %; IR (KBr, cm^{-1}): 3071, 1612, 1593, 1501, 1489, 1455; ^{1}H-NMR (400 MHz, CDCl$_3$, δ / ppm): 9.0 (1H, *s*, –CH=N–), 6.88–9.06 (9H, *m*, Ar-H); ^{13}C-NMR (100.622 MHz, CDCl$_3$, δ / ppm): 117.8, 124.2, 128.8, 127.2, 127.6, 128.5, 131.4, 137.8, 143.4, 148.6, 151.3, 155.6, 159.8, 163.8; mass (*m/z*): 284 [M$^+$].

4-Chloro-N-[(2-chloroquinolin-3-yl)methylene]benzenamine (3b). Yellow Solid; Yield: 87 %; m.p.: 227–228 °C; Anal. Calcd. for $C_{16}H_{10}Cl_2N_2$: C, 63.81; H, 3.35; N, 9.30 %. Found: C, 63.88; H, 3.55; N, 9.59 %; IR (KBr, cm^{-1}): 3073, 1618, 1598, 1504, 1495, 1452; ^{1}H-NMR (400 MHz, CDCl$_3$, δ / ppm): 9.0 (1H, *s*, –CH=N–), 6.88–9.06 (9H, *m*, Ar-H); ^{13}C-NMR (100.622 MHz, CDCl$_3$, δ / ppm): 117.6, 124.3, 128.9, 127.4, 127.6, 128.5, 131.3, 137.6, 142.8, 148.6, 151.2, 155.6, 159.8, 163.8; mass (*m/z*): 300 [M$^+$].

N-[(2-Chloroquinolin-3-yl)methylene]-3-nitrobenzenamine (3c). Yellow Solid; Yield: 82 %; m.p.: 212–214 °C; Anal. Calcd. for $C_{16}H_{10}ClN_3O_2$: C, 61.65; H, 3.23; N, 13.48 %. Found: C, 61.84; H, 3.49; N, 13.61 %; IR (KBr, cm^{-1}): 3068, 1616, 1591, 1514, 1502, 1444; ^{1}H-NMR (400 MHz, CDCl$_3$, δ / ppm): 9.0 (1H, *s*, –CH=N–), 6.88–9.06 (9H, *m*, Ar-H); ^{13}C-NMR (100.622 MHz, CDCl$_3$, δ

*,** Corresponding authors. E-mails: (*)ucmashelkar@rediffmail.com;
(**)Jhamukesh1@rediffmail.com

/ ppm): 116.8, 117.8, 119.6, 124.3, 127.5, 127.6,128.6, 128.9,131.5, 137.6, 142.9, 148.6, 151.3, 155.8, 158.8, 163.8; mass (m/z): 311 [M$^+$].

4-(2-Chloroquinolin-3-yl)-1-(4-fluorophenyl)-3-phenylazetidin-2-one   **(4a)**. White solid; Yield: 48 %; m.p.: 165–166 °C; Anal. Calcd. for $C_{24}H_{16}ClFN_2O$: C, 71.55; H, 4.00; N, 6.95 %. Found: C, 71.44; H, 3.92; N, 7.01 %; IR (KBr, cm^{-1}): 3064, 2959, 1760, 1602, 1497, 1410; ^{1}H-NMR (400 MHz, CDCl$_3$, δ / ppm): 4.33 (1H, *d*, *J* = 2.4 Hz, >CH–C=O), 5.55 (1H, *d*, *J* = 2.4 Hz, >CH–N<), 7.04–8.08 (14H, *m*, Ar-H); ^{13}C-NMR (100.622 MHz, CDCl$_3$, δ / ppm): 60.0, 65.5, 118.4, 126.9, 127.6, 128.0, 128.3, 128.4, 128.8, 128.9, 129.1, 129.6, 129.9, 131.3, 134.0, 135.3, 135.4, 147.5, 148.8, 165.2; mass (m/z): 402 [M$^+$].

1-(4-Chlorophenyl)-4-(2-chloroquinolin-3-yl)-3-phenylazetidin-2-one   **(4b)**. White solid; Yield: 42 %; m.p.: 174–175 °C; Anal. Calcd. for $C_{24}H_{16}Cl_2N_2O$: C, 68.75; H, 3.85; N, 6.68 %. Found: C, 68.80; H, 3.79; N, 6.74 %; IR (KBr, cm^{-1}): 3067, 1763, 1589, 1508, 1456; ^{1}H-NMR (400 MHz, CDCl$_3$, δ / ppm): 4.33 (1H, *d*, *J* = 2.4 Hz, >CH–C=O), 5.55 (1H, *d*, *J* = 2.4 Hz, >CH–N<), 7.16–8.06 (14H, *m*, Ar-H); ^{13}C-NMR (100.622 MHz, CDCl$_3$, δ / ppm): 60.0, 65.5, 118.4, 126.9, 127.7, 128.0, 128.3, 128.4, 128.7, 128.9, 129.1, 129.6,129.8, 131.3, 134.0, 135.3, 135.4, 147.4, 148.8, 165.2; mass (m/z): 418 [M$^+$].

4-(2-Chloroquinolin-3-yl)-1-(3-nitrophenyl)-3-phenylazetidin-2-one   **(4c)**. Off white solid; Yield: 46 %; m.p.: 147 °C; Anal. Calcd. for $C_{24}H_{16}ClN_3O_3$: C, 67.06; H, 3.75; N, 9.78 %. Found: C, 67.12; H, 3.83; N, 9.85 %; IR (KBr, cm^{-1}): 3062, 2956, 1757, 1595, 1566, 1493; ^{1}H-NMR (400 MHz, CDCl$_3$), δ / ppm: 4.43 (1H, *d*, *J* = 2.4 Hz, >CH–C=O), 5.65 (1H, *d*, *J* = 2.4 Hz, >CH–N<), 7.43–8.29 (14H, *m*, Ar-H); ^{13}C-NMR (100.622 MHz, CDCl$_3$, δ / ppm): 60.0, 65.5, 118.6, 127.0, 127.5, 128.1, 128.3, 128.4, 128.6, 128.9, 129.3, 129.7, 129.9, 131.3, 134.5, 135.3, 135.4, 136.5, 138.8, 147.6, 148.8, 165.2; mass (m/z): 429 [M$^+$].

4-(2-Chloroquinolin-3-yl)-1-(4-fluorophenyl)-3-(4-methoxyphenyl)azetidin--2-one **(4d)**. Off white solid; Yield: 44 %; m.p.: 241 °C; Anal. Calcd. for $C_{25}H_{18}ClFN_2O_2$: C, 69.37; H, 4.19; N, 6.47 %. Found: C, 69.31; H, 4.13; N, 6.52 %; IR (KBr, cm^{-1}): 3071, 2956, 1751, 1611, 1506, 1460; ^{1}H-NMR (400 MHz, CDCl$_3$, δ / ppm): 3.65 (3H, *s*, –OCH$_3$), 4.25 (1H, *d*, *J* = 2.4 Hz, >CH––C=O), 5.45 (1H, *d*, *J* = 4.0 Hz, >CH–N<), 6.91–8.05 (13H, *m*, Ar-H); ^{13}C-NMR (100.622 MHz, CDCl$_3$, δ / ppm): 43.8, 60.0, 65.5, 118.4, 126.9, 127.7, 128.1, 128.3, 128.4, 128.7, 128.9,, 129.2, 129.6, 129.8, 131.3, 134.1, 135.3, 135.4, 147.4, 148.8, 165.3; mass (m/z): 432 [M$^+$].

1-(4-Chlorophenyl)-4-(2-chloroquinolin-3-yl)-3-(4-methoxyphenyl)azetidin--2-one **(4e)**. Off white solid; Yield: 47 %; m.p.: 181–183 °C; Anal. Calcd. for $C_{25}H_{18}Cl_2N_2O_2$: C, 66.83; H, 4.04; N, 6.23 %. Found: C, 66.76; H, 4.11; N, 6.32 %; IR (KBr, cm^{-1}): 3060, 2958, 1753, 1594, 1514, 1458; ^{1}H-NMR (400 MHz, CDCl$_3$, δ / ppm): 3.81 (3H, *s*, –OCH$_3$), 4.28 (1H, *d*, *J* = 2.4 Hz, >CH–C=O), 5.48 (1H, *d*, *J* = 2.4 Hz, >CH–N<), 6.94–8.06 (13H, *m*, Ar-H); ^{13}C-NMR (100.622

MHz, CDCl$_3$, δ / ppm): 43.8, 60.0, 65.5, 118.4, 126.9, 127.6, 128.2, 128.3, 128.4, 128.7, 128.9, 129.3, 129.6, 129.9, 131.3, 134.1, 135.3, 135.5, 147.4, 148.8, 165.2; mass (*m/z*): 448 [M$^+$].

4-(2-Chloroquinolin-3-yl)-3-(4-methoxyphenyl)-1-(3-nitrophenyl)azetidin--2-one (4f). Off white solid; Yield: 52 %; m.p.: 197–198 °C; Anal. Calcd. for C$_{25}$H$_{18}$ClN$_3$O$_4$: C, 65.29; H, 3.95; N, 9.14 %. Found: C, 65.18; H, 3.84; N, 9.23 %; IR (KBr, cm^{-1}): 3068, 2931, 1762, 1592, 1532, 1462; ^{1}H-NMR (400 MHz, CDCl$_3$, δ / ppm): 3.85 (3H, *s*, –OCH$_3$), 4.37 (1H, *d*, *J* = 2.8 Hz, >CH–C=O), 5.58 (1H, *d*, *J* = 2.8 Hz, >CH–N<), 6.95–8.28 (13H, *m*, Ar-H); ^{13}C-NMR (100.622 MHz, CDCl$_3$, δ / ppm): 43.8, 60.0, 65.5, 116.5, 118.9, 126.8, 127.6, 128.1, 128.2, 128.4, 128.7, 128.9, 129.1, 129.3, 129.6, 129.8, 131.3, 131.4, 134.1, 135.5, 147.4, 148.9, 165.2; mass (*m/z*): 459 [M$^+$].

3-(4-Chlorophenyl)-4-(2-chloroquinolin-3-yl)-1-(4-fluorophenyl)azetidin-2--one (4g). Off white solid; Yield: 46 %; m.p.: 188–189 °C; Anal. Calcd. for C$_{24}$H$_{15}$Cl$_2$FN$_2$O: C, 65.92; H, 3.46; N, 6.41 %. Found: C, 66.0; H, 3.56; N, 6.33 %; IR (KBr, cm^{-1}): 3063, 2955, 1758, 1592, 1454, 1407; ^{1}H-NMR (400 MHz, CDCl$_3$), δ / ppm: 4.30 (*d*, 1H, *J* = 2.4 Hz, >CH–C=O), 5.50 (*d*, 1H, *J* = 2.4 Hz, >CH–N<), 7.04–8.07 (*m*, 13H, Ar-H); ^{13}C-NMR (100.622 MHz, CDCl3, δ / / ppm): 60.0, 65.5, 118.4, 126.9, 127.6, 128.1, 128.3, 128.5, 128.7,128.9, 129.2, 129.7, 129.8, 131.3, 134.0, 135.3, 135.5, 147.4, 148.8, 165.2; mass (*m/z*): 436 [M$^+$].

1,3-Bis(4-chlorophenyl)-4-(2-chloroquinolin-3-yl)azetidin-2-one (4h). Off white solid; Yield: 45 %; m.p.: 212–213 °C; Anal. Calcd. for C$_{24}$H$_{15}$Cl$_3$N$_2$O: C, 63.53; H, 3.33; N, 6.17 %. Found: C, 63.63; H, 3.42; N, 6.30 %; IR (KBr, cm^{-1}): 3058, 2943, 1759, 1594, 1567, 1491; ^{1}H-NMR (400 MHz, CDCl$_3$, δ / ppm): 4.30 (1H, *d*, *J* = 2.4 Hz, >CH–C=O), 5.50 (1H, *d*, *J* = 2.4 Hz, >CH–N<), 7.31–8.09 (13H, *m*, Ar-H); ^{13}C-NMR (100.622 MHz, CDCl$_3$, δ / ppm): 60.0, 65.5, 118.5, 126.8, 127.7, 128.1, 128.3, 128.5, 128.7, 128.9, 129.2, 129.7, 129.8, 131.3, 134.0, 135.3, 135.5, 147.5, 148.8, 165.3; mass (*m/z*): 452 [M$^+$].

Journal of the Serbian Chemical Society

Solvent effects on the absorption spectra of potentially pharmacologically active 5-alkyl-5-arylhydantoins: a structure–property relationship study

SLEEM F. HMUDA, NEBOJŠA R. BANJAC, NEMANJA P. TRIŠOVIĆ[#],
BOJAN Đ. BOŽIĆ[#], NATAŠA V. VALENTIĆ[#] and GORDANA S. UŠĆUMLIĆ[#*]

Department of Organic Chemistry, Faculty of Technology and Metallurgy, University of Belgrade, Karnegijeva 4, 11120 Belgrade, Serbia

Abstract: To obtain insight into the interactions of potential anticonvulsant drugs with their surrounding, two series of 5-methyl-5-aryl- and 5-ethyl-5-arylhydantoins were synthesized and their absorption spectra were recorded in the region from 200 to 400 nm in a set of selected solvents. The effects of solvent dipolarity/polarizability and solvent–solute hydrogen bonding interactions on the absorption maxima shifts were analyzed by means of the linear solvation energy relationship (LSER) concept of Kamlet and Taft. The ratio of the contributions of specific and non-specific solvent–solute interactions were correlated with the corresponding absorption, distribution, metabolism, and excretion (ADME) properties of the studied compounds. The correlation equations were combined with different physicochemical parameters to generate new equations, which demonstrate the reasonable relationships between the solvent–solute interactions and the structure–activity parameters.

Keywords: hydantoin derivatives; Kamlet–Taft Equation; human intestinal absorption; lipophilicity, binding affinity.

INTRODUCTION

Hydantoin (imidazolidine-2,4-dione) is the core structure of different biologically active compounds, such as antibacterial[1] and antifungal agents,[2] free radical scavengers[3] and serotonin and fibrinogen receptor antagonists.[4] 5-Phenylhydantoins are commonly used in the treatment of epilepsy and related disorders. Phenytoin (5,5-diphenylhydantoin) is one of the oldest non-sedative anticonvulsant drugs,[5] whereas mephenytoin (3-methyl-5-ethyl-5-phenylhydantoin) is considered only after other less toxic anticonvulsants have failed.[6] Nirvanol, the 3-demethylated metabolite of mephenytoin, was the first hydantoin derivative used

---

briefly in the treatment of chorea, but it was abandoned due to its hypnotic–sedative effect.[7] Anticonvulsant drugs require long-term application and should have only minor unfavourable effects. For this reason, the synthesis and modelling of the behaviour of new hydantoin derivatives significantly contributes to a rational search for new anticonvulsant drugs.

The anticonvulsant activity of hydantoin derivatives is mediated by their interaction with and inhibition of the brain Na^+ channels.[8] Their common pharmacophore core contains at least one aromatic ring at C5, which forms aromatic–aromatic interactions, and a polar imide group, which interacts with the receptor site through a low-energy amino–aromatic hydrogen bond. Poupaert *et al.* tested a limited series of compounds structurally related to phenytoin and observed that the anticonvulsant activity decreased with a reduction in their ability to form hydrogen bonds.[9] Brouillette *et al.* demonstrated that 5-alkyl-5-phenylhydantoins have an affinity for Na^+ channels comparable to that of phenytoin, with the optimal length of the aliphatic chain corresponding to pentyl, hexyl or heptyl.[10,11] In this context, it was proposed that the structure–activity and structure–property relationships of hydantoin anticonvulsants have molecular size and hydrogen bonding as their primary determinants.[12–14]

Since most drug candidates fail in preclinical and clinical trials because of their unfavourable ADME (absorption, distribution, metabolism and excretion) properties, ADME modelling has attracted significant attention over the last two decades. The lipophilicity of drugs, as expressed by their octanol–water partitioning coefficient (log P), has been proven to be the most important parameter in the study of transport phenomena *in vivo* and through biological membranes. Insufficient lipophilicity results in poor membrane permeability of a drug, whereas excessive lipophilicity is a common cause of poor solubility that could lead to incomplete absorption following oral administration.[15] Concerning central nervous system (CNS) active drugs, the ideal candidates must be able to penetrate the blood–brain barrier (BBB) effectively. It was suggested that the optimum log P value for diffusion into the brain is around 2.[16]

In this work, two series of 5-methyl-5-aryl- and 5-ethyl-5-arylhydantoins were assembled (Fig. 1) as a part of a larger investigation on the contribution of hydrogen bonding to the pharmacologically relevant properties of hydantoin derivatives and their potential application as anticonvulsant drugs. Kleinpeter *et al.* estimated the lipophilicities of a representative number of hydantoins using RP-HPLC[17] and concluded that some of the derivatives studied in this work (**1**, **5**, **6**, **7**, **9**, **10** and **11**) are expected to interact with and penetrate native membranes and be bioactive.

A first insight into the interactions of the investigated molecules with their surrounding can be derived from solvatochromic studies in which specific and non-specific interactions can be separated.[18] Hereto, their absorption spectra

have been recorded in the region 200–400 nm in twelve solvents. The effects of solvent dipolarity/polarizabilty (non-specific solvent–solute interactions) and hydrogen bonding (specific solvent–solute interactions) on the absorption spectra shifts were interpreted using the Kamlet–Taft equation[19] in the form:

$$v = v_0 + s\pi^* + b\beta + a\alpha \qquad (1)$$

where v is the wavenumber π^* is an index of the solvent dipolarity/polarizabilty, β is a measure of the solvent hydrogen bonding acceptor (HBA) basicity, α is a measure of the solvent hydrogen bonding donor (HBD) acidity and v_0 is the regression value of this solute property in cyclohexane as the reference solvent. The regression coefficients s, b and a in Eq. (1) measure the relative suscepti-bilities of the absorption maxima shift to the indicated solvent parameters.

1:	R = Me, X = H		**7:**	R = Et, X = H
2:	R = Me, X = OH		**8:**	R = Et, X = OH
3:	R = Me, X = Me		**9:**	R = Et, X = Me
4:	R = Me, X = MeO		**10:**	R = Et, X = MeO
5:	R = Me, X = Cl		**11:**	R = Et, X = Cl
6:	R = Me, X = Br		**12:**	R = Et, X = Br
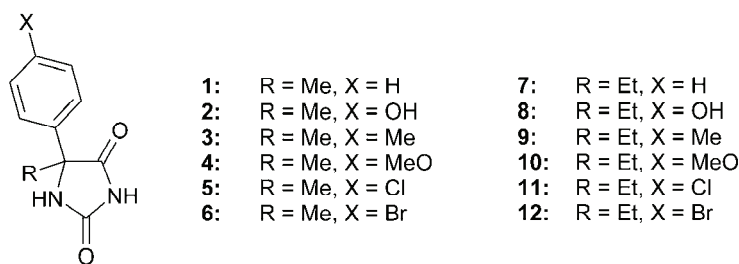
Fig. 1. Structures of the investigated 5-methyl-5-(4-substituted phenyl)- and 5-ethyl-5-(4-substituted phenyl)hydantoins.

To analyze the role of hydrogen bonding in their ADME properties, octanol––water partitioning coefficient (log P), human intestinal absorption (*Abs*) and protein binding affinity (k_A) data have been correlated with the regression coef-ficients from Eq. (1). The obtained correlation equations demonstrate reasonable relationships between solvent–solute interactions and structure–property parame-ters.

<div align="center">EXPERIMENTAL</div>

Synthesis of the investigated compounds

All of the investigated 5-methyl-5-aryl- and 5-ethyl-5-arylhydantoins were synthesized by a modification of the method of Bucherer[20] (Scheme 1). The appropriate ketone (0.020 mol) was dissolved in 50 % ethanol (50 cm³) and ammonium carbonate (7.70 g, 80.0 mmol) plus potassium cyanide (2.60 g, 40.0 mmol) were added. This mixture was warmed under a condenser at 60 °C for 15 h, after which the solution was concentrated to approximately two-thirds of its initial volume and chilled in an ice-bath. The mass was filtered on a Büchner fun-nel. The product was dissolved in 5 % sodium hydroxide solution, filtered from unreacted ketone and reprecipitated by acidification with hydrochloric acid. Recrystallization of the white solid from 60 % ethanol yielded a crystalline product. The ketones used in these prepa-rations were commercially available (Fluka). The chemical structure and the purities of the synthesized compounds were confirmed by their melting points and ¹H-NMR, ¹³C-NMR, FT-IR and UV spectra.
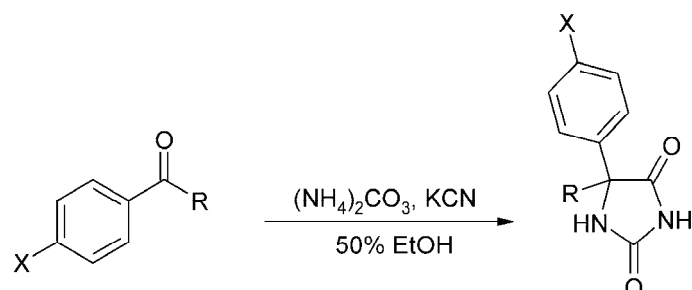
Scheme 1. Synthetic route to the investigated 5-alkyl-5-(4-substituted phenyl)hydantoins.

Spectroscopic measurements

The ^{1}H- and ^{13}C-NMR spectra were recorded on a Bruker AC 250 spectrometer at 200 MHz for the ^{1}H-NMR and 50 MHz for the ^{13}C-NMR spectra. The spectra were recorded at room temperature in DMSO-d_6. The chemical shifts are expressed in ppm referred to TMS ($\delta_H = 0$ ppm) in the ^{1}H-NMR and the residual solvent signal ($\delta_H = 39.5$ ppm) in the ^{13}C-NMR spectra. The FT-IR spectra were recorded on a Bomem MB 100 spectrometer. The absorption spectra were measured in spectroquality solvents (Fluka) at 10^{-5} mol dm^{-3} concentration using a Shimadzu 1700 spectrophotometer. All melting points are uncorrected and are presented in °C. Mass spectra were obtained on Agilent technologies 6210 TOF LC/MS (HRMS) instrument (LC: series 1200). Elemental analysis was performed using a Vario EL III elemental analyzer.

Physicochemical characterization of the investigated compounds

The physicochemical characterization of compounds **1**–**6** has already been reported,[21] whereas the yields and the characterization of compounds **7**–**12** are given in the Supplementary material to this paper.

Methods of calculation

The correlation analysis was realised using Microsoft Excel 2003, which considers the 95% confidence level. The goodness-of-fit is discussed using the correlation coefficient (*R*), standard error of the estimate (*S*) and the Fisher's criterion (*F*).

In the absence of appropriate experimental data in the literature, computer methods were used to predict the ADME properties of the investigated hydantoin derivatives. Their lipophilicity was estimated by calculation of their log *P* values with Advanced Chemistry Development (ACD) software Solaris, v. 4.67. The human intestinal absorption data (*Abs*) and protein binding values (f_b) were obtained with the ChemSilico program.[23]

The corresponding physicochemical characteristics and ADME data of the investigated molecules are collected in Table I.

TABLE I. Physicochemical properties and ADME data of the investigated molecules

No.	R	X	σ_I^a	σ_R^b	log P^c	Abs^d / %	f_b^d / %	log k_A^e
1	Me	H	0	0	0.999	91.8	37.435	2.71
2	Me	OH	0.24	–0.43	0.263	89.4	40.823	2.85
3	Me	Me	–0.01	–0.13	1.459	93.3	67.904	3.97
4	Me	MeO	0.3	–0.43	0.914	89.4	52.849	3.33
5	Me	Cl	0.47	–0.16	1.594	93.7	69.988	4.07

TABLE I. Continued

No.	R	X	σ_I[a]	σ_R[b]	log P[c]	Abs[d] / %	f_b[d] / %	log k_A[e]
6	Me	Br	0.47	–0.16	1.771	94.0	75.079	4.32
7	Et	H	0	0	1.530	92.8	48.188	3.15
8	Et	OH	0.24	–0.43	0.794	91.0	49.223	3.19
9	Et	Me	–0.01	–0.13	1.991	93.9	74.736	4.30
10	Et	MeO	0.3	–0.43	1.446	90.8	61.883	3.70
11	Et	Cl	0.47	–0.16	2.126	94.3	76.844	4.42
12	Et	Br	0.47	–0.16	2.302	94.4	80.989	4.67

[a]Inductive substituent parameter;[24] [b]resonance substituent parameter;[24] [c]calculated with ACD Solaris, v. 4.67; [d]calculated with ChemSilico; [e]the protein binding affinities were obtained by Eq. (3)

RESULTS AND DISCUSSION

Absorption spectra of the investigated molecules were recorded in twelve solvents of different polarities and the corresponding absorption maxima are presented in Table II. The absorption spectra were characterized by one band with a weak low-energy shoulder, which is typical for 5-phenylhydantoins. The main absorptions resulted from an intramolecular charge transfer (ICT), corresponding to a migration of electron density from the hydantoin moiety to the phenyl ring. The bathochromic shift of the absorption bands with increasing solvent dipolarity/polarizability is in accordance with previously published data.[12–14]

TABLE II. Absorption maxima of the investigated molecules in the set of selected solvents

Compound/ Solvent	$\nu_{max} \times 10^{-3}$ / cm^{-1}											
	1	**2**	**3**	**4**	**5**	**6**	**7**	**8**	**9**	**10**	**11**	**12**
Methanol	47.89	44.56	45.80	44.80	45.21	44.96	46.51	43.63	45.83	44.17	45.00	44.76
Ethanol	47.48	44.52	45.66	44.76	45.16	44.92	47.13	44.44	45.75	45.21	45.33	45.04
1-Propanol	47.50	44.62	45.45	45.00	44.88	45.51	47.08	44.60	45.87	45.21	44.68	44.56
2-Propanol	47.94	44.90	46.21	44.80	45.00	44.82	48.17	45.70	47.57	46.59	45.21	45.05
1-Butanol	47.60	44.85	46.00	45.44	46.00	45.33	47.04	44.96	45.83	45.45	45.63	44.13
Diethyl ether	40.62	40.42	40.91	40.52	40.55	40.52	40.88	40.75	40.72	40.45	40.49	40.39
Disopropyl ether	41.77	39.03	41.28	40.25	41.28	41.18	41.77	41.67	41.74	41.70	41.18	41.02
Tetrahydro-furan	39.18	38.79	39.15	39.09	39.12	39.06	39.43	39.31	39.28	39.34	39.28	39.25
Dimethyl sulfoxide	37.45	36.05	36.76	36.39	37.26	37.20	37.48	36.37	36.74	36.98	37.28	37.34
Ethyl acetate	38.58	36.39	38.66	36.60	38.46	38.28	39.62	36.51	39.28	36.88	38.76	38.32
N,N-Dimethyl-formamide	37.79	36.20	37.73	37.51	37.76	37.70	37.65	36.18	36.79	36.39	37.31	38.71
N,N-Dimethyl-acetamide	37.12	36.07	36.79	36.41	37.7	37.37	37.57	36.18	37.15	36.50	37.25	37.43

The effects of the solvent dipolarity/polarizability and hydrogen bonding on the absorption maxima shifts were evaluated by multiple regression analysis using the solvent parameter set of Kamlet and Taft (Table III). It was found that

absorption maxima of the investigated molecules in selected solvents show a satisfactory correlation with the π^*, β and α parameters. The fitted regression values of v_0, s, b and a at the 95 % confidence level are presented in Table IV. The success degree of Eq. (1) is shown in Fig. 2 by means of a plot of v_{max} calculated *versus* v_{max} observed in different solvents ($R = 0.991$, $S = 0.50$, $F = 8048$).

TABLE III. Solvent parameters[19]

Solvent	π^*	β	α
Methanol	0.60	0.62	0.93
Ethanol	0.54	0.77	0.83
1-Propanol	0.52	0.83	0.78
2-Propanol	0.48	0.95	0.76
1-Butanol	0.47	0.88	0.79
Diethyl ether	0.27	0.47	0.00
Diisopropyl ether	0.27	0.49	0.00
Tetrahydrofuran	0.58	0.55	0.00
Dimethyl sulfoxide	1.00	0.76	0.00
Ethyl acetate	0.55	0.45	0.00
N,N-Dimethylformamide	0.88	0.69	0.00
N,N-Dimethylacetamide	0.88	0.76	0.00
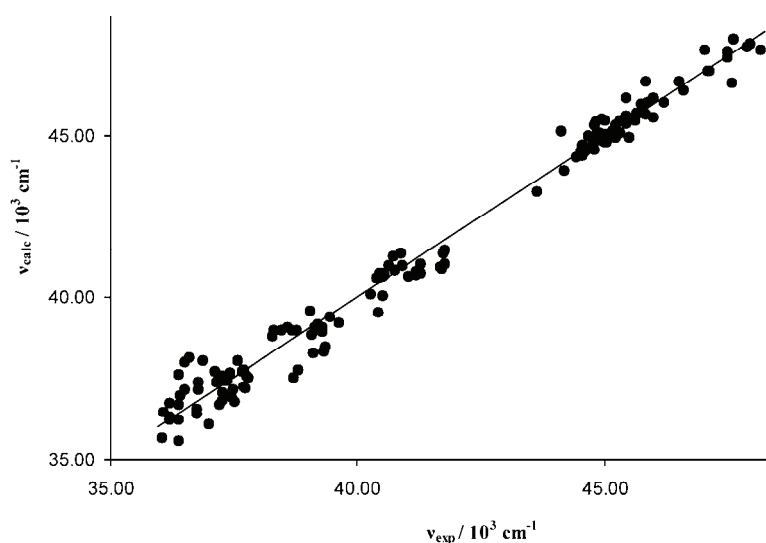
Fig. 2. Experimental *vs*. calculated values of v from Eq. (1).

The investigated compounds showed positive solvatochromism with regards to π^* (as indicated by the negative s coefficients in Table IV), which indicates that the dipole moment of the excited state is higher than in the ground state. Thus, considerable differences between the dipole moments in the ground and excited state are characteristic for ICT processes. The positive a and b coeffi-

cients indicate hypsochromic shifts of absorption maxima with increasing solvent hydrogen bond acidity and basicity (Table IV). This can be explained by the hydrogen bond formation between protic solvents and the hydantoin carbonyl moieties, which reduced their electron density and thus decreased the ICT character of the chromophoric system. On the other hand, the interactions of the NH groups played only a minor role, which is represented by the small percentage contribution of the b coefficient compared to those of a and s (Table V). These results are also in accordance with the preferred existence of the investigated molecules in their imido tautomer.

TABLE IV. Regression fits to the solvatochromic parameters

No.	R	X	$v_0 \times 10^{-3}$ / cm^{-1}	$s \times 10^{-3}$ / cm^{-1}	$b \times 10^{-3}$ / cm^{-1}	$a \times 10^{-3}$ / cm^{-1}	R[a]	S[b]	F[c]
1	Me	H	41.51(±0.68)	−6.51(±0.80)	2.59(±1.34)	9.15(±0.52)	0.996	0.48	351
2	Me	OH	39.80(±1.02)	−6.56(±1.20)	3.22(±2.01)	6.99(±0.78)	0.988	0.72	106
3	Me	Me	41.85(±0.49)	−6.88(±0.58)	2.11(±0.97)	7.16(±0.74)	0.997	0.34	463
4	Me	MeO	40.29(±1.08)	−6.55(±1.26)	3.28(±2.11)	6.65(±0.82)	0.985	0.76	89
5	Me	Cl	41.22(±0.54)	−5.89(±0.63)	2.30(±1.06)	6.41(±0.41)	0.998	0.38	310
6	Me	Br	41.18(±0.61)	−6.45(±0.72)	2.60(±1.06)	6.36(±0.46)	0.994	0.43	238
7	Et	H	41.43(±0.63)	−7.43(±0.74)	4.16(±1.24)	7.65(±0.48)	0.996	0.44	346
8	Et	OH	40.47(±1.13)	−9.67(±1.32)	6.34(±2.22)	5.04(±0.86)	0.984	0.79	83
9	Et	Me	41.79(±0.89)	−8.06(±0.95)	3.57(±1.59)	6.96(±0.62)	0.993	0.57	187
10	Et	MeO	39.96(±1.11)	−9.14(±1.30)	6.94(±2.19)	5.53(±0.85)	0.986	0.78	92
11	Et	Cl	41.49(±0.47)	−6.13(±0.55)	1.98(±0.93)	6.45(±0.36)	0.997	0.33	409
12	Et	Br	41.29(±0.40)	−5.73(±0.47)	1.88(±0.79)	6.19(±0.31)	0.997	0.28	505

[a]Correlation coefficient; [b]standard error; [c]Fisher's test

Table V. Percentage contribution of the solvatochromic effects

No.	R	X	P_{π^*} / %	P_β / %	P_α / %
1	Me	H	35.67	14.19	50.14
2	Me	OH	39.12	19.20	41.68
3	Me	Me	42.60	13.07	44.33
4	Me	MeO	39.75	19.90	40.35
5	Me	Cl	40.30	15.76	43.93
6	Me	Br	41.86	16.87	41.27
7	Et	H	38.62	21.62	39.76
8	Et	OH	45.94	30.12	23.94
9	Et	Me	43.36	19.20	37.44
10	Et	MeO	42.30	32.11	25.59
11	Et	Cl	42.10	13.60	44.30
12	Et	Br	41.52	13.62	44.86

To investigate the importance of various types of interactions in determining the anticonvulsant potencies of the investigated compounds, a multiple regression approach was applied to analyze the factors which govern their ADME properties. ADME data, whether experimentally measured or computationally pre-

dicted, provide key insights into how a drug will ultimately be treated or accepted by the body.

The evidence for solvent effects on the structure–property relationships of the investigated molecules was first demonstrated by plotting the calculated human intestinal absorption (HIA) values against the ratio $a/|s|$ as a convenient measure of the relative contributions of the dominant modes of solvation (Fig. 3). The HIA values (*Abs*) calculated by the ChemSilico program are expressed as the percentage of a drug absorbed by the intestine (Table I). The plot of the *Abs* values *versus* $a/|s|$ reveals that the molecules, where OH and MeO are attached to the phenyl ring (**2**, **4**, **8** and **10**), behave differently and their intestinal absorption percentages when compared to the others are somewhat lower. This can be expected, because these substituents may act as an additional site for hydrogen-bonding with the surrounding solvent molecules.
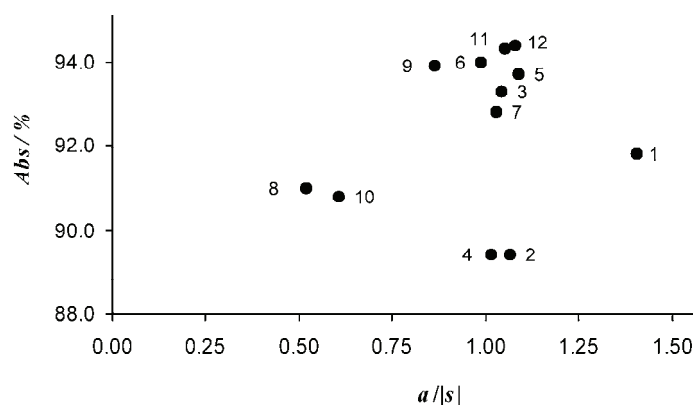
Fig. 3. Correlation between the *Abs* values and the ratio of the contributions of the specific and non-specific solvent–solute interactions ($a/|s|$).

The improved correlation, which includes all of the investigated molecules, was derived through the additional inclusion of the resonance (σ_R) and inductive (σ_I) constants of substituents in *para* position of the phenyl group (Eq. 2):

$$Abs = 98.05(\pm1.65) - 3.94(\pm1.38)a/|s| + 4.68(\pm1.28)\sigma_I + 13.45(\pm2.02)\sigma_R \quad (2)$$
$$(R = 0.928, S = 0.81, F = 16, n = 12)$$

It can be seen that Eq. (2) has a meaning similar to the corresponding model of Abraham,[25] when one realizes that the *a* and *s* coefficients refer to the hydrogen bond basicity and dipolarity/polarizability of the investigated molecules, respectively. The Abraham approach is based on the theoretical cavity model of solvent–solute interactions and successfully correlates different physicochemical properties of solutes.[26] Eq. (2) shows that the hydrogen bond basicity of the investigated molecules decreases intestinal absorption, whereas the dipolarity/po-

larizability enhances it. Generally, substituents on the phenyl ring at C5 exhibit two opposing effects: the conjugative electron donation, which decreases drug intestinal absorption, and the inductive electron withdrawal, which acts in the opposite direction.

Furthermore, the same approach was applied in the analysis of factors that determine octanol–water partitioning (log P) and protein binding affinity (k_A). The log P parameter, calculated with Advanced Chemistry Development (ACD) software Solaris, v. 4.67 (Table I), is a solvational characteristic, since it is directly related to the change in the Gibbs energy of solvation of a drug between octanol and water.[27] The protein binding values (f_b, fraction bound) are given as the percentage of the total plasma concentration of a drug that is bound to all plasma proteins (Table I). Human serum albumin (HSA), the most abundant protein in blood plasma (concentration 0.53–0.75 mM), has multiple hydrophobic binding sites and binds diverse drugs.[28] The percentage data were converted into an equivalent binding affinity k_A using the following formula (Eq. (3)) derived from the mass law. k_A is the binding affinity to HSA under the assumption that binding occurs exclusively to HSA, a binary complex is formed, and an excess of albumin (concentration 0.6 mM, [HSA]) is present compared to the concentration of the drug:[29]

$$\log k_A = \log \frac{[f_b]}{1 - [f_b]} - \log[\text{HSA}] \tag{3}$$

Reasonable statistics were obtained for 10 compounds with the exclusion of compounds **3** and **9** bearing substituents with electron-donating inductive effect (Eqs. (4) and (5)):

$$\log P = 2.56(\pm 0.75) - 1.08(\pm 0.58)a/|s| + 2.34(\pm 0.61)\sigma_I + 3.43(\pm 0.84)\sigma_R \tag{4}$$
$$(R = 0.907,\ S = 0.33,\ F = 9,\ n = 10)$$
$$\log k_A = 3.88(\pm 0.51) - 0.79(\pm 0.40)a/|s| + 3.60(\pm 0.41)\sigma_I + 2.21(\pm 0.57)\sigma_R \tag{5}$$
$$(R = 0.965,\ S = 0.22,\ F = 27,\ n = 10)$$

Evidently, all equations ((2), (4) and (5)) show clear similarities. It should be pointed out that parameters $a/|s|$, σ_I and σ_R are not normalized to each other, so the regression coefficients in these equations do not provide adequate measures of the relative contributions of the indicated types of solvent–solute interactions and substituent effects to the analyzed ADME properties. On the other hand, they all interpret the contribution of the hydrogen bond basicity and dipolarity/polarizability to the lipophilicity and intestinal absorption of the investigated molecules in the same manner as the Abraham models.[26,30] The obtained correlations also suggest that the introduction of an electron-withdrawing substituent at the *para* position of the phenyl group at C5 may produce derivatives with improved pharmacokinetic properties.

CONCLUSIONS

The reasonable correlations of absorption maxima of 5-methyl-5-aryl- and 5-ethyl-5-arylhydantoins with the solvent parameter set of Kamlet and Taft indicated that the selected model interpreted their LSER correctly. In this case, where both solvent and solute are hydrogen bond donors and acceptors, it was quite difficult to quantitatively estimate and separate the overall solvent effect into the contributions of specific and non-specific interactions. However, such a separation provided further possibility to establish the structure–property relationships of the investigated molecules. The obtained models represented how various types of interactions and electronic effects of substituents on the phenyl ring at C5 influenced their biological partitioning and binding to plasma proteins. The approach proposed in this work provided the means to analyze pharmacokinetic properties of hydantoin derivatives, not yet pharmacologically tested, which are difficult to determine experimentally.

SUPPLEMENTARY MATERIAL

Physical and spectral data for compounds **7**–**12** are available electronically from http://www.shd.org.rs/JSCS/, or from the corresponding author on request.

И З В О Д

УТИЦАЈ РАСТВАРАЧА НА АПСОРПЦИОНЕ СПЕКТРЕ ПОТЕНЦИЈАЛНО ФАРМАКОЛОШКИ АКТИВНИХ 5-АЛКИЛ-5-АРИЛХИДАНТОИНА: ПРОУЧАВАЊЕ ОДНОСА СТРУКТУРЕ И СВОЈСТАВА

SLEEM F. HMUDA, НЕБОЈША Р. БАЊАЦ, НЕМАЊА П. ТРИШОВИЋ, БОЈАН Ђ. БОЖИЋ, НАТАША В. ВАЛЕНТИЋ и ГОРДАНА С. УШЋУМЛИЋ

Катедра за органску хемију, Технолошко–металуршки факултет, Универзитет у Београду, Карнегијева 4, 11120 Београд

Да би се проценио начин на који потенцијални антиконвулзивни лекови интерагују са својим окружењем, две серије 5-метил-5-(4-супституисаних фенил)- и 5-етил-5-(4-супституисаних фенил)хидантоина су синтетисане и њихови апсорпциони спектри су снимљени у интервалу таласних дужина од 200 до 400 nm у сету изабраних растварача. Ефекти диполарности/поларизабилности растварача и водоничног везивања између молекула растварача и растворене супстанце на померање апсорпционих максимума анализирани су применом метода линеарне корелације енергије солватације (LSER), односно Камлет–Тафтовом једначином. Однос доприноса специфичних и неспецифичних интеракција између молекула растварача и растворене супстанце корелисани су са одговарајућим АДМЕ својствима проучаваних једињења. Корелационе једначине су даље комбиноване са различитим физичко–хемијским параметрима при чему су добијене нове једначине које на задовољавајући начин описују односе између интеракција између молекула растварача и растворене супстанце и својстава која одређују њихову активност у организму.

(Примљено 19. јула, ревидирано 22. октобра 2012)

REFERENCES

1. K. Kieć-Kononowicz, E. Szymańska, *Farmaco* **57** (2002) 909
2. R. Rautela, P. C. Joshi, *Asian. J. Chem.* **7** (1995) 151
3. B. Dundar, O. Bozdar-Dundar, B. Can-Eke, T. Coban, M. Iscan, E. Buyukbingol, *Pharmazie* **57** (2002) 436
4. G. P. Moloney, G. R. Martin, N. Mathews, A. Milne, H. Hobbs, S. Dodsworth, P. Y. Sang, C. Knight, M. Williams, M. Maxwell, R. C. Glen, *J. Med. Chem.* **42** (1999) 2504
5. Y. Yaari, M. E. Selzer, J. H. Pincus, *Ann. Neurol.* **20** (1986) 171
6. A. Küpfer, G. M. Brilis, J. T. Watson, T. M. Harris, *Drug Metab. Dispos.* **8** (1980) 1
7. F. A. Ellis, *South. Med. J.* **36** (1943) 575
8. G. M. Lipkind, H. A. Fozzard, *Mol. Pharmacol.* **78** (2010) 631
9. J. H. Poupaert, D. Vandervorst, P. Guiot, M. M. M. Moustafa, P. Dumont, *J. Med. Chem.* **27** (1984) 76
10. W. J. Brouillette, V. P. Jestkov, M. L. Brown, M. S. Akhtar, T. M. DeLorey, G. B. Brown, *J. Med. Chem.* **37** (1997) 3289
11. M. L. Brown, G. B. Brown, W. J. Brouillette, *J. Med. Chem.* **40** (1999) 602
12. S. F. Hmuda, N. P. Trišović, N. V. Valentić, G. S. Ušćumlić, *J. Solution Chem.* **40** (2011) 307
13. N. Trišović, N. Valentić, M. Erović, T. Đaković-Sekulić, G. Ušćumlić, I. Juranić, *Monatsh. Chem.* **142** (2011) 1227
14. N. Trišović, N. Valentić, G. Ušćumlić, *Chem. Cent. J.* **5** (2011) 62
15. D. A. Smith, H. van de Waterbeemd, W. D. Walker, *Pharmacokinetics and metabolism in drug design*, Wiley-VCH, Weinheim, Germany, 2006, pp. 13–15
16. V. A. Levin, *J. Med. Chem.* **23** (1980) 682
17. S. Scholl, A. Koch, D. Henning, G. Kempter, E. Kleinpeter, *Struct. Chem.* **10** (1999) 355
18. M. Bauer, S. Spange, *Eur. J. Org. Chem.* (2010) 259
19. M. J. Kamlet, J. L. M. Abboud, M. H. Abraham, R. W. Taft, *J. Org. Chem.* **48** (1983) 2877
20. H. T. Bucherer, V. A. Lieb, *J. Prakt. Chem. / Chem-Ztg.* **141** (1934) 5
21. N. D. Divjak, N. R. Banjac, N. V. Valentić, G. S. Ušćumlić, *J. Serb. Chem. Soc.* **47** (2009) 1195
22. R. G. Murray, D. M. Whitehead, F. Le Strat, S. Conway, *Org. Biomol. Chem.* **6** (2008) 988
23. ChemSilico LLC, http://chemsilico.com (Accessed 10 July 2012)
24. M. Charton, *J. Org. Chem.* **49** (1984) 1997
25. Y. H. Zhao, J. Le, M. H. Abraham, A. Hersey, P. J. Eddershaw, C. N. Luscombe, D. Boutina, G. Beck, B. Sherborne, I. Cooper, J. A. Platts, *J. Pharm. Sci.* **90** (2001) 749
26. M. H. Abraham, A. Ibrahim, A. M. Zissimos, Y. H. Zhao, J. Comer, D. P. Reznolds, *Drug Discovery Today* **7** (2002) 1056
27. F. Reymond, P.-A. Carrupt, B. Testa, H. H. Girault, *Chem. Eur. J.* **5** (1999) 39
28. F. Yang, C. Bian, L. Zhu, G. Zhao, Z. Huang, M. Huang, *J. Struct. Biol.* **152** (2007) 348
29. N. A. Kratochwil, W. Huber, F. Müller, M. Kansy, P. R. Gerber, *Biochem. Pharmacol.* **64** (2002) 1355
30. M. H. Abraham, W. R. Lieb, N. P. Franks, *J. Pharm. Sci.* **80** (1991) 719.

Solvent effects on the absorption spectra of potentially pharmacologically active 5-alkyl-5-arylhydantoins: a structure–property relationship study

SLEEM F. HMUDA, NEBOJŠA R. BANJAC, NEMANJA P. TRIŠOVIĆ,
BOJAN Đ. BOŽIĆ, NATAŠA V. VALENTIĆ and GORDANA S. UŠĆUMLIĆ*

Department of Organic Chemistry, Faculty of Technology and Metallurgy, University of Belgrade, Karnegijeva 4, 11120 Belgrade, Serbia

PHYSICAL AND SPECTRAL DATA FOR COMPOUNDS **7–12**

5-Ethyl-5-phenylhydantoin (7). Yield: 76 %; m.p.: 198–199 °C (lit**. 194–196 °C); IR (KBr, cm^{-1}): 3285 (NH), 3214 (NH), 1771 (C=O), 1737 (C=O); ^{1}H--NMR (200 MHz, DMSO-d_6, δ / ppm): 0.83 (3H, t, J = 7.3 Hz, CH$_3$), 1.82–2.18 (2H, m, CH$_2$), 7.28–7.55 (5H, m, Ph), 8.67 (1H, s, N1),10.80 (1H, s, N3); ^{13}C--NMR (50 MHz, DMSO-d_6, δ / ppm): 8.2, 31.4, 68.3, 125.7, 128.0, 128.7, 139.4, 157.0, 176.6.

5-Ethyl-5-(4-hydroxyphenyl)hydantoin (8). Yield: 48 %; m.p.: 265–267 °C; Anal. Calcd. for C$_{11}$H$_{12}$N$_2$O$_3$: C, 59.99; H, 5.49; N, 12.72 %. Found: C, 60.10; H, 5.36; N, 12.70 %; IR (KBr, cm^{-1}): 3420 (OH), 3269 (NH), 3148 (NH), 1753 (C=O), 1728 (C=O); ^{1}H-NMR (200 MHz, DMSO-d_6, δ / ppm): 0.81 (3H, t, J = = 7.1 Hz, CH$_3$), 1.76–2.13 (2H, m, CH$_2$), 6.78 (2H, d, J = 8.4 Hz, Ar-H), 7.29 (2H, d, J = 8.4 Hz, Ar-H), 8.51 (1H, s, N1), 10.11 (1H, bs, N3), 10.08 (1H, bs, **H**O–C$_6$H$_4$) (signal at 10.11 is partly covered by the signal at 10.08); ^{13}C-NMR (50 MHz, DMSO-d_6, δ / ppm): 8.3, 31.2, 67.9, 115.4, 127.0, 129.6, 157.1, 157.3, 177.1; HRMS (*m/z*): 221.0924, corresponding to the molecular formula C$_{11}$H$_{12}$N$_2$O$_3$H$^+$ (error in ppm: 1.32).

5-Ethyl-5-(4-methylphenyl)hydantoin (9). Yield: 58 %; m.p.: 196–198 °C; Anal. Calcd. for C$_{12}$H$_{14}$N$_2$O$_2$: C, 66.04; H, 6.47; N, 12.84 %. Found: C, 66.12; H, 6.42; N, 12.78 %; IR (KBr, cm^{-1}): 3268 (NH), 3206 (NH), 1779 (C=O), 1746 (C=O); ^{1}H-NMR (200 MHz, DMSO-d_6, δ / ppm): 0.92 (3H, t, J = 7.1 Hz, CH$_3$), 1.90–2.26 (2H, m, CH$_2$), 2.39 (3H, s, **CH**$_3$–C$_6$H$_4$), 7.30 (2H, d, J = 8.0 Hz, Ar-H), 7.50 (2H, d, J = 8.4 Hz, Ar-H), 8.72 (1H, s, N1), 10.82 (1H, bs, N3); ^{13}C-NMR

---

* Corresponding author. E-mail: goca@tmf.bg.ac.rs
** R. G. Murray, D. M. Whitehead, F. Le Strat, S. Conway, *Org. Biomol. Chem.* **6** (2008) 988.

(50 MHz, DMSO-d_6, δ / ppm): 8.2, 20.8, 31.3, 68.1, 125.6, 129.3, 136.5, 137.3, 157.0, 176.8; HRMS (m/z): 219.1124, corresponding to the molecular formula $C_{12}H_{14}N_2O_2H^+$ (error in ppm: –1.68).

*5-Ethyl-5-(4-methoxyphenyl)hydantoin (**10**)*. Yield: 44 %; m.p.: 210–212 °C; Anal. Calcd. for $C_{12}H_{14}N_2O_3$: C, 61.53; H, 6.02; N, 11.96 %. Found: C, 61.55; H, 6.00; N, 11.92 %; IR (KBr, cm^{-1}): 3277 (NH), 3202 (NH), 1772 (C=O), 1721 (C=O); ^{1}H-NMR (200 MHz, DMSO-d_6, δ / ppm): 0.81 (3H, t, J = 7.3 Hz, CH$_3$), 1.78–2.11 (2H, m, CH$_2$), 3.71 (1H, s, CH$_3$O–C$_6$H$_4$), 6.96 (2H, d, J = 8.4 Hz, Ar-H), 7.42 (2H, d, J = 9.0 Hz, Ar-H), 8.61 (1H, s, N1), 10.74 (1H, s, N3); ^{13}C-NMR (50 MHz, DMSO-d_6, δ / ppm): 8.2, 31.3, 55.4, 67.9, 114.1, 126.9, 131.3, 157.0, 159.1, 176.9; HRMS (m/z): 235.1075 corresponding to the molecular formula $C_{12}H_{14}N_2O_3H^+$ (error in ppm: –0.76).

*5-(4-Chlorophenyl)-5-ethylhydantoin (**11**)*. Yield: 72 %; m.p.: 213–215 °C; Anal. Calcd. for $C_{11}H_{11}ClN_2O_2$: C, 55.36; H, 4.65; N, 11.74 %. Found: C, 55.42; H, 4.58; N, 11.72 %; IR (KBr, cm^{-1}): 3282 (NH), 3204 (NH), 1772 (C=O), 1730 (C=O); ^{1}H-NMR (200 MHz, DMSO-d_6, δ / ppm): 0.83 (3H, t, J = 7.3 Hz, CH$_3$), 1.81–2.16 (2H, m, CH$_2$), 7.47 (2H, d, J = 8.4 Hz, Ar-H), 7.55 (2H, d, J = 9.0 Hz, Ar-H), 8.69 (1H, s, N1), 10.95 (1H, s, N3); ^{13}C-NMR (50 MHz, DMSO-d_6, δ / / ppm): 8.2, 31.5, 68.0, 127.7, 128.7, 132.9, 138.5, 157.3, 176.6; HRMS (m/z): 239.0583 corresponding to the molecular formula $C_{11}H_{11}ClN_2O_2H^+$ (error in ppm: 0.39).

*5-(4-Bromophenyl)-5-ethylhydantoin (**12**)*. Yield: 68 %; m.p.: 222–224 °C; Anal. Calcd. for $C_{11}H_{11}BrN_2O_2$: C, 46.67; H, 3.92; N, 9.89 %. Found: C, 46.55; H, 3.88; N, 9.82 %; IR (KBr, cm^{-1}) 3252 (NH), 3222 (NH), 1772 (C=O), 1733 (C=O); ^{1}H-NMR (200 MHz, DMSO-d_6, δ / ppm): 0.82 (3H, t, J = 7.1 Hz, CH$_3$), 1.80–2.16 (2H, m, CH$_2$), 7.47 (2H, d, J = 9.0 Hz, Ar-H), 7.62 (2H, d, J = 8.6 Hz, Ar-H), 8.73 (1H, s, N1), 10.87 (1H, s, N3); ^{13}C-NMR (50 MHz, DMSO-d_6, δ / / ppm): 8.2, 31.5, 68.0, 121.5, 130.1, 132.0, 138.8, 156.8, 176.2; HRMS (m/z): 283.0080 corresponding to the molecular formula $C_{11}H_{11}BrN_2O_2H^+$ (error in ppm: 1.20).

Journal of the Serbian Chemical Society

Influence of rhamnolipids, produced by *Pseudomonas aeruginosa* NCAIM(P), B001380 on their Cr(VI) removal capacity in liquid medium

NATAŠA S. AVRAMOVIĆ[1]*, SNEŽANA D. NIKOLIĆ-MANDIĆ[2#]
and IVANKA M. KARADŽIĆ[1]**#

[1]*School of Medicine, Department of Chemistry, University of Belgrade, Višegradska 26, Belgrade, Serbia and* [2]*Faculty of Chemistry, University of Belgrade, Studentski trg 12–16, Belgrade, Serbia*

Abstract: *Pseudomonas aeruginosa* NCAIM(P), B001380, a propitious bacterial strain isolated from mineral cutting oil, was identified to be chromium tolerant and a producer of the biosurfactant rhamnolipid (RL) with potential application in heavy metal bioremediation. Culture growth, RL production and Cr(VI) removal capacity of the strain in the presence of 50 mg L^{-1} Cr(VI) (**I**) and 100 mg L^{-1} Cr(VI) (**II**) were studied. The maximums of RL production were found in the late-stationary phase at 72 h for both Cr(VI)-amended cultures: **I** (236 mg L^{-1}) and **II** (160 mg L^{-1}), as well as the maximums of the Cr(VI) removal capacity: 70 % (**I**) and 57 % (**II**). The amount of Cr in RL preparation **II** was 22 μg mg^{-1}, determined by flame atomic absorption spectroscopy (FAAS). Appearance of a new band at 914 cm^{-1} in infrared (IR) spectrum of RL (**II**) indicated significant proof for a possible coordination of CrO$_4^{2-}$ with RL. The effect of Cr(VI) on monorhamnolipids (RL1) and dirhamnolipids (RL2) distribution and their ratio were studied by electrospray ionization mass spectrometry (ESI-MS). An increase was observed in the RL2/RL1 ratio for **II** compared to the control.

Keywords: rhamnolipids; chromium(VI); *Pseudomonas*; bioremediation.

INTRODUCTION

Their potential to metabolize chemical pollutants in the environment makes *Pseudomonas* species suitable for use as bioremediation agents capable of removing heavy metal pollutants and numerous toxic organic compounds.[1–4] *Pseu-*

---

domonas produces and excretes small secondary metabolite rhamnolipids (RL), natural biosurfactants that could have unique metal binding capacities and selectivities to complex heavy metal ions.[1] Biosurfactants are a diverse group of surface-active substances divided based on molecular weight into low molecular-mass biosurfactants (glycolipids, phospholipids and lipopeptides) and high molecular-mass biosurfactants (polysaccharides, proteins, lipopolysaccharides and lipoproteins).[2] Rhamnolipids belong to the low-molecular mass molecules and, based on their chemical composition, the principal rhamnolipids are mono-rhamno-di-lipidic congeners (RL1) and di-rhamno-di-lipidic congeners (RL2).[2]

In comparison to their chemically synthesized equivalents, biosurfactants have many advantages. They are eco-friendly, biodegradable, less toxic and non-hazardous, with better foaming properties and higher selectivity.[5,6] Due to their potential advantages, special attention has been paid to the use of rhamnolipid biosurfactants in different aspects of environmental biotechnology.[2] Juwarkar *et al.* reported that di-rhamnolipid biosurfactant produced by *Pseudomonas aeruginosa* BS2 was used in the remediation of metals from multi-metal contaminated soil, confirming removal selectivity of metals in the order Cd = Cr > Pb = Cu > > Ni.[3] Removal of heavy metals from sediments could also be enhanced by the use of a solution of rhamnolipid.[4] On the other hand, application of rhamnolipid foam increases the efficiency and allows a higher percentage of removal of heavy metals in comparison to the use of rhamnolipid solution.[7,8]

While the complexation of RL with metal contaminants initiated numerous investigations on the potential use of RL as environmentally compatible soil washing agents, only a few publications were dedicated to the influence of heavy metal ions on the microbial production of RL.[9] Elevated concentrations of some divalent cations were shown to inhibit RL production, while iron limitations were correlated with the overexpression of the rhlI system.[10,11] A recent investigation on *P. aeruginosa* IGB83 evaluated a significant increase in the ratio of dirhamnolipids (RL2) to monorhamnolipids (RL1) congeners produced by cultures grown in the presence of Cd^{2+}.[12] In addition, it was demonstrated that environmental and growth conditions influence both RL production and quorum sensing (QS) or the cell-to-cell communication system.[11]

High solubility, rapid transport through the biological membranes and complexation with intracellular polymers, such as proteins and nucleic acids, imply high toxicity of Cr(VI) compounds for humans and microorganisms. Some microorganisms, however, can tolerate Cr(VI) using several distinct strategies: the plasmid mediated efflux system, absorbing heavy metals to their cell wall, by precipitation (including reductive precipitation) in the form of insoluble salts and binding metal ions to biological complexing agents, such as exopolymers and biosurfactants.[13–19] To date, a few chromium resistant *Pseudomonas* strains have been reported and their use in bioremediation of Cr(VI) suggested.[20–26] A re-

cently published proteomics study of chromium resistant *Pseudomonas aeruginosa*, indicated the existence of several resistance mechanisms as reasonable responses to Cr(VI) stress.[25]

P aeruginosa NCAIM(P), B001380 (earlier labeled as *P. aeruginosa* san ai) was isolated from mineral cutting oil used as a metal working fluid in the metal industry.[27] It was expected that *P. aeruginosa* NCAIM(P), B001380 isolated from such extreme conditions, could be a possible candidate for remediation of an environment polluted by the extremely toxic chromium. Therefore, the purpose of this study was to evaluate the chromium tolerance of the strain and to study the influence of their naturally produced rhamnolipids on their Cr(VI) removal capacity with aim of providing potential applications of the strain and its biosurfactants in bioremediation.

EXPERIMENTAL

Bacterial growth and chromium removal ability

The Cr(VI) tolerance of the bacterial strain was determined using 100 mL of nutrient Luria broth (LB) medium (0.5 % NaCl, 0.5 % yeast extract and 1 % tryptone) in 500 mL Erlenmeyer flasks, inoculated with 5 vol. % of a 24-h pre-culture and agitated at 250 cycles min^{-1} on a horizontal Kuhner shaker, Switzerland.[27] The inoculated medium was supplemented by two concentrations of Cr(VI): 50 (**I**), and 100 (**II**) mg L^{-1} at pH 7.2. A stock solution of chromium was prepared by dilution of $K_2Cr_2O_7$ to a final concentration of 10 g L^{-1} chromium. Samples were taken at regular intervals, centrifuged at 10000 rpm for 20 min (Sorvall, Rotor SS-1, New Town, Conn., USA) and analyzed for chromium removal. Controls were non-inoculated LB with 50 and 100 mg L^{-1} of Cr(VI). The chromium concentrations of samples **I** and **II** were calculated and compared to the controls. All determinations were performed in triplicate.

Growth of bacterial strains

Bacterial growth of the control (LB inoculated, without Cr(VI)) and Cr(VI)-amended cultures (**I** – 50 and **II** – 100 mg L^{-1}) were monitored as the change in optical density (*OD*) at 580 nm, using sterile LB medium as the control. The determination of the *OD* was performed in triplicate.

Evaluation of the chromium resistance

The minimal inhibitory concentration (*MIC*) was determined in LB medium supplemented with Cr(VI) concentrations ranging from 0.5–20 mM. Tubes containing the growth medium and various concentrations of Cr(VI) were inoculated with a 24-h culture to obtain an initial optical density of 0.06. Turbidity measurements were recorded after 24 h of growth. The minimum concentration of the metal inhibiting complete growth was taken as the *MIC*.[26]

Chromate reductase activity assay

Chromate reductase was assayed at 30 °C in 0.5 mL reaction mixture containing 0.05 mM K_2CrO_4 in 50 mM Tris–HCl pH 7.1, supplemented with 0.1 mM NADPH and 0.5 mL of enzyme preparation. The concentration of the residual Cr(VI) was determined spectrophotometrically at 540 nm using diphenylcarbazide.[28]

Determination of chromium(VI) in the culture broth

During the incubation period, a 3 mL sample of culture broths of **I** and **II** was taken from each flask. Samples were centrifuged at 10000 rpm for 5 min to precipitate the biomass. The concentration of chromium in the supernatant (c_{Cr}) was determined spectrophotometrically at 540 nm using diphenylcarbazide reagent in acidic solution as the complexing agent for Cr(VI).[24,29]

Total chromium determination

Total chromium was quantified by reducing air acetylene flame atomic absorption spectroscopy (FAAS) using a Perkin Elmer Model 2380 instrument at 359.3 nm after digestion of the samples with HNO_3 and H_2O_2 in a DS-6 digester, Tecator, Sweden.

Isolation and purification of rhamnolipids

A mixture of RL was isolated from the fermentation broth after separation of the bacterial cells by centrifugation. A crude preparation of RL was obtained by acidic precipitation using 1 M HCl (final pH 2). The precipitate was collected by centrifugation at 5000 rpm for 10 min (Sorvall, Rotor SS-1, UK) and the RL were dissolved in a mixture of chloroform and methanol (2:1). The clear supernatant obtained after centrifugation at 5000 rpm for 10 minutes (Janetzki T32c, Germany) was evaporated to dryness under vacuum and used for MS analysis and total chromium determination.[30] Further purification of crude preparation was performed by normal-phase column chromatography on silica gel (Kiesel gel 100, 70–230 mesh ASTM, Merck) as was demonstrated previously.[30] The purified samples were analyzed by FTIR and ^{1}H-NMR spectroscopy.

Rhamnolipid determination

The orcinol assay for determination of amount of methyl pentose was used for quantification of RL in the culture supernatants of the controls, and samples **I** and **II**. A 150 μL aliquot of supernatant was diluted with water to attain a volume of 300 μL, which was extracted twice with 600 μL of diethyl ether. The pooled ether fractions were evaporated to dryness, the residue was dissolved in 100 μL of distilled water and mixed with 100 μL of 1.6 % orcinol and 800 μL of 60 % sulfuric acid. After heating at 80 °C for 30 min in a water bath, the absorbance at 421 nm was measured. The content of rhamnose in the samples was determined by comparing the absorption with those of rhamnose standards with defined concentrations (0.075–0.020 g L^{-1}). The RL concentration (c_{rl}) was calculated based on the assumption that 1 μg of rhamose corresponds to 2.5 μg of rhamnolipids.[31]

FTIR analysis of RL

Purified and dried RL samples of the control and sample **II** (1 mg) were dispersed in 100 mg of anhydrous KBr and pressed to a pellet. The FT-IR spectra were recorded at room temperature in the wave number range of 400–4000 cm^{-1} using a Perkin-Elmer 31725 X FTIR spectrophotometer.

NMR analysis of RL

The ^{1}H-NMR spectra of RL of the control and sample **II** were recorded in D_2O at room temperature using a Gemini 200 spectrometer at 200 MHz.

ESI-MS analysis of RL

Mass spectra of RL from the diethyl ether extracts of the culture filtrates of the control and sample **II** were recorded on MS system consisting of an HPLC (Agilent 1200 Series, Agilent Technologies) and a 6210 Time-of-Flight LC/MS (Agilent Technologies), using Zor-

bax Eclipse Plus C18 column and a DAD detector. The mobile phase was a mixture of solvent A (0.2 % formic acid in water) and B (acetonitrile) in a gradient mode: 0–1.5 min 95 % A, 1.5–12 min 95–5% A, 12–15 min 5 % A, 15–16 min 5–95 % A. The data were processed by means of a Mass Hunter Workstation. The relative abundance of the RL congeners was calculated from the mass spectral abundance (counts) of the observed ions. The dirhamnolipids (RL2)/monorhamnolipids (RL1) ratio represents the sum of all RL2 congeners divided by the sum of all RL1 congeners present in a given sample.

RESULTS AND DISCUSSION

Cr(VI) removal capacity and RL production

The *MIC* of Cr(VI) for *P. aeruginosa* NCAIM(P), B001380 strain was 5 mM, similarly to *P. putida* as a model organism for Cr-bioremediation.[26] However, preliminary experiments suggested that sub-lethal concentrations of Cr(VI) of 50 (**I**) and 100 mg L^{-1} (**II**) had significant effects on RL production, so they were selected to monitor growth, *OD*, RL production, c_{rl}, and the concentration of Cr(VI), c_{Cr}, in the culture broth of *P. aeruginosa* NCAIM(P), B001380 (Fig. 1).

As Fig. 1a shows, Cr(VI)-amended cultures (**I** and **II**) had a slightly lower *OD* and a delay in growth phases compared to those of the control. The RL production c_{rl} in the control, **I** and **II** was observed in the stationary phase, when it was sustained on a high level until the late-stationary phase (Fig. 1b). A similar delay in c_{rl} induced by Cr(VI) was observed with the Cd-amended culture of *P. aeruginosa* IGB83.[12] The maximum RL concentrations, c_{rl}, were found in the late-stationary phase at 48 h in the control (310 mg L^{-1}), at 72 h in **I** (236 mg L^{-1}) and **II** (160 mg L^{-1}), Figs. 1a and 1b. Elevated concentrations of divalent cations, such as zinc, copper, and cadmium, were shown to inhibit c_{rl} but the correlation between Cr(VI) and RL production has not been evaluated yet.[12] In the current study, it was found that amount of Cr(VI) in the fermentation broth, c_{Cr}, (Fig. 1c) slowly decreased from the log to the late-stationary phase (Fig. 1a), along with enhancement of the RL production, c_{rl}, (Fig. 1b), reaching the maximum Cr(VI) removal capacity of 70 % (**I**) and 57 % (**II**) in the late-stationary phase at 72 h, which coincides with the maximum of c_{rl} for both Cr(VI)-amended cultures. This fact is in a good agreement with the observation that extra-cellular RL influences the bioavailability of heavy metals.[12] Namely, it was hypothesized that as the RL production increased, the content of Cd^{2+} was reduced due to complexation with the extra-cellular RL present in culture medium, similarly to the present observation that the amount of Cr(VI) slowly decreased with increasing RL production.[12] On the contrary, Kiliç *et al.* showed that a *P. aeruginosa* strain, isolated from tannery effluents, had the highest Cr(VI) removal (94.3 %) at 50 mg L^{-1} Cr(VI) at the end of a 96-h of incubation, which correlated with the maximum production of exo-polysaccharide, and that *Micrococcus* sp., from a media containing 100 mg L^{-1} Cr(VI), removed the heavy metal with a yield of 35.5 % after incubation for 72 h.[24]

(a)

(b)

(c)
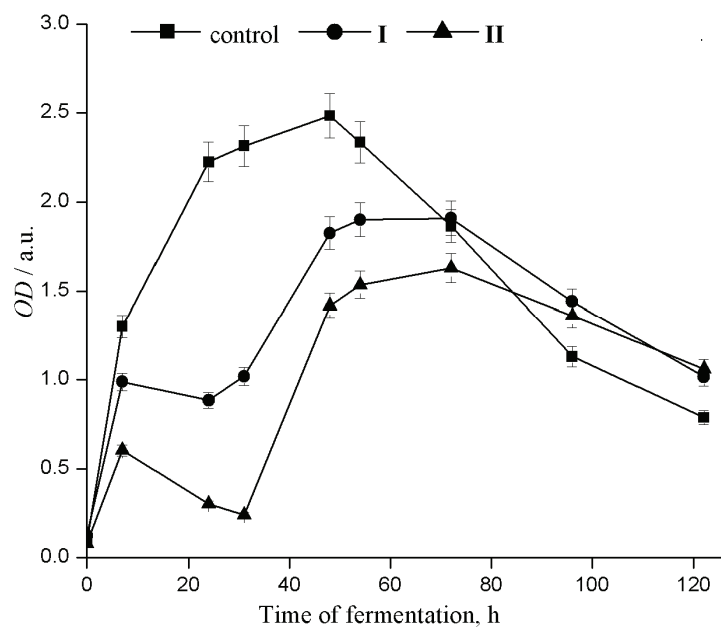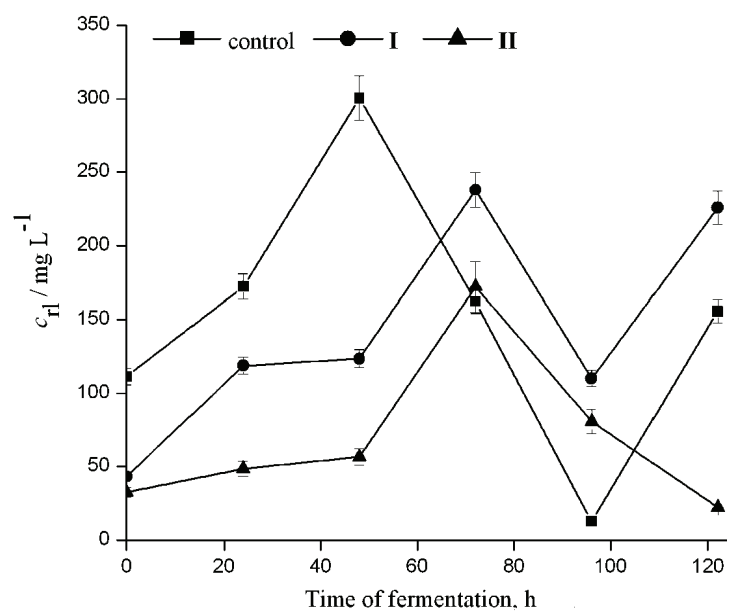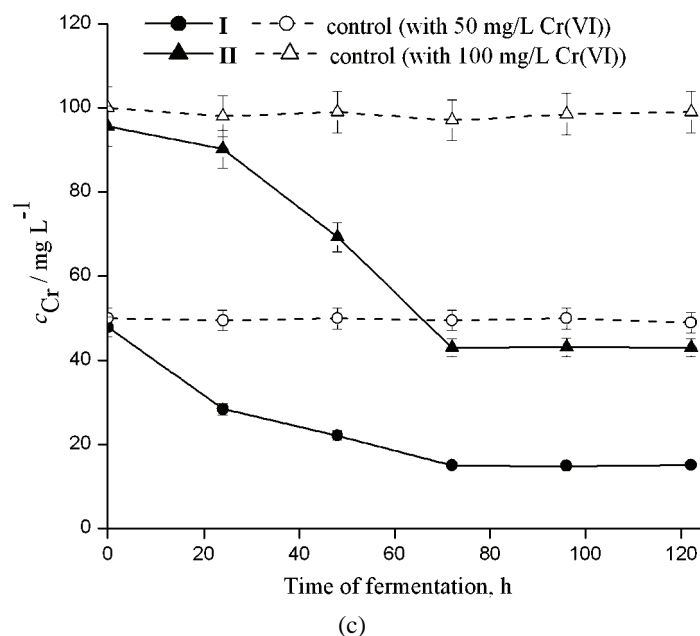
Fig. 1. a) Dynamics of the *OD* growth and RL production by *P. aeruginosa* NCAIM(P) as c_{rl} (b); B001380 grown in LB (control) and Cr(VI) supplemented LB medium with 50 (**I**) and 100 mg L^{-1} of Cr(VI) (**II**); c) concentration of Cr(VI) c_{Cr} in the culture broth of *P. aeruginosa* NCAIM(P), B001380 in the controls (non-inoculated LB mediums with 50 and 100 mg L^{-1} of Cr(VI)) and Cr(VI) supplemented LB mediums **I** and **II**. The symbols represent the average values of triplicate data and the error bars are standard errors.

With regard to the hypothesis that complexation with extracellular RL occurs, total chromium was determined in the RL samples by flame absorption atomic spectroscopy (FAAS) and it was found that amount of Cr in the RL preparation isolated from the culture filtrate of *P. aeruginosa* NCAIM(P), B001380 grown in LB with 100 mg of Cr(VI) (II), was 22 μg of Cr per mg of RL. Interestingly, the same amount of 22 μg of heavy metal Cd^{2+} per mg of RL was found to be complexed.[1] Actually, from the culture filtrate of **II**, it was confirmed that 57 % of total added Cr(VI) was absorbed. The amount of Cr measured in the RL preparation suggested that less than 5 % of total added Cr(VI), that is about 10 % of overall absorbed Cr(VI), was bound to RL, while all remaining chromium was found in the biomass, indicating absorption of Cr on exopolymers (EPS) on the surface of cells, as previously reported.[24] Aside from absorption, the strain *P. aeruginosa* NCAIM(P), B001380 can reduce Cr(VI) by chromate reductase, which was found to be an intracellular, soluble, non-inducible enzyme, with a specific activity of 40 μg Cr(VI) h^{-1} mg^{-1} proteins, as was expected.[28] Based on the given data, at least two mechanisms are proposed by

which *P. aeruginosa* NCAIM(P), B001380 controls the amount of toxic Cr(VI): reduction to Cr(III) and its efficient efflux, accompanied with biological complexing of Cr(VI) to RL and EPS.

Structural elucidation of RL–Cr(VI) adduct/complex

Heavy metals efficiently form complexes with RL obtained by *P. aeruginosa*, but structural details of complexes are lacking.[12,32,33] The coordination chemistry of Cr(VI) as a ligand is mainly the chemistry of anions as chromates, dichromates and polychromates with T_d symmetry.[34] RL–Cr(VI) interaction could be based on binding of CrO_4^{2-} as a ligand for protonated carboxylate groups of fatty acids residues of RL in complexes $(RL–COOH_2^+)_2CrO_4^{2-}$. RL preparations obtained by *P. aeruginosa* NCAIM(P), B001380 without (control) and with Cr(VI) (**II**) were analyzed by FT-IR, EI-MS and NMR spectroscopy to find and elucidate the structural relationship between RL and Cr(VI).

FT-IR spectroscopy of RL

The FT-IR spectra of purified RL of the control and Cr(VI)-amended sample **II** were recorded at room temperature in the wavenumber range of 400–4000 cm^{-1} and compared in Fig. 2. Both IR spectra showed characteristic bands for mono- and di-rhamnolipids, as reported by Leitermann *et al.*[35]

Broader and red shifted O–H band at 3288 cm^{-1} of **II** compared to control at 3450 cm^{-1} (Fig. 2), might be the first indication for protonation of the COOH group of RL in complex with CrO_4^{2-}. The red shift of 59 cm^{-1} for the C=O stretching band of **II** (1650 cm^{-1}) compared to the control (1709 cm^{-1}) is a further indication for a possible coordination of CrO_4^{2-} and hence weaker C=O bond. The red shift of the deformation C–OH band at 1399 cm^{-1} and the blue shift of O–C–O symmetric band at 1072 cm^{-1} for **II** compared to the control (1459 and 1043 cm^{-1}) could also be explained by coordination of the CrO_4^{2-}, as an anion ligand, with the protonated $COOH_2^+$ group of the fatty acid residue of RL.

In addition, another significant difference in spectrum of **II** is appearance of a new, weak and sharp band at 914 cm^{-1} (Fig. 2). This observation might be crucial proof for the coordination of CrO_4^{2-} to RL in **II** because it is known that when the chromate ion is coordinated, it shows a new, weak band of the Cr=O vibration at about 900 cm^{-1}.[36,37]

^{1}H-NMR spectra of RL

The ^{1}H-NMR spectra of RL of the control and **II** gave characteristic proton signals of rhamnose 1 and rhamnose 2 from monorhamnolipids (RL1) and dirhamnolipids (RL2) and signals of lipid components of RL.[30] The NMR results indicate that the products of the RLs of the control and **II** were a mixture of RL1 and RL2, but without any significant difference in their spectra. Many of their proton signals are overlapped, especially chemical shift of –CH$_2$–COO$^-$ protons

at 2.48–2.57 ppm, where a difference was expected between the control and **II**, due to the interaction of CrO_4^{2-} and RL of **II**, as it was evidenced by the IR spectra.
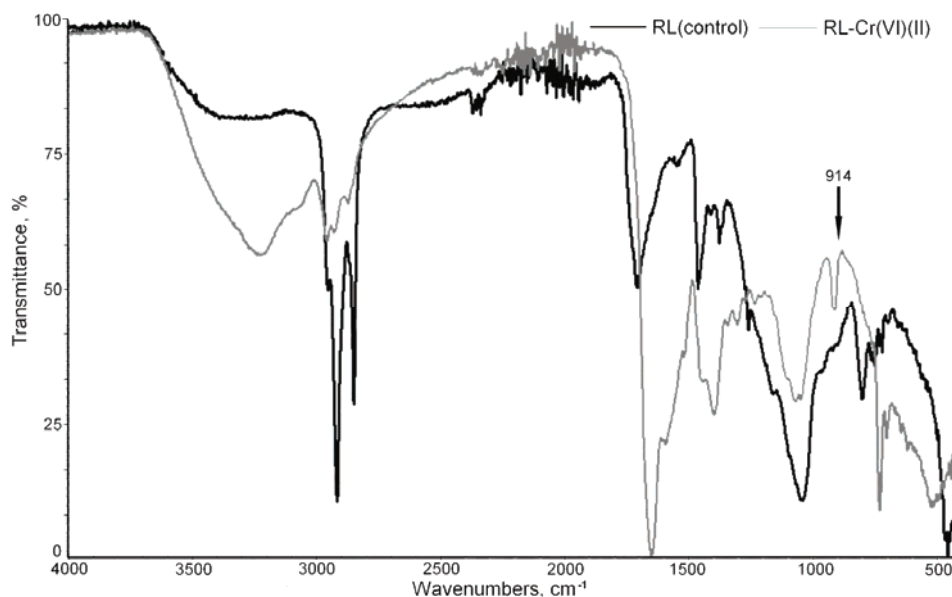
Fig. 2. Comparison of rhamnolipids IR spectra of the control and Cr(VI)-amended sample **II** (100 mg L^{-1}) obtained by *P. aeruginosa* NCAIM(P), B001380 grown in LB medium.

Influence of Cr(VI) on the distribution of RL congeners

RLs were isolated from the culture broths of the control and sample **II** at the time of its maximum yield (48 and 72 h, respectively), and they were analyzed by electrospray ionization mass spectrometry ESI/MS.[38,39] In the negative ESI mode, only negatively charged molecules can be observed. Under such conditions, the RLs, as molecules with an acidic function, show an intense [M–H]$^-$ peak without the occurrence of fragmentation. The effect of Cr(VI) on the distribution of the RL congeners is presented in Table I.

The mono-rhamnolipid (RL1) congeners **1**–**7** were observed in both samples, except **3**, which was detected only in the control (Table I). All of the di-rhamnolipid (RL2) congeners **8**–**12** were observed in both samples, except **12**, which was present only in sample **II** (Table I). Obviously, the slight difference between the control and the Cr(VI)-amended culture (**II**) comes from the minor congeners.

While the major RL congeners were the same in both cultures, the ratio of RL2 to RL1 was changed. The Cr(VI) treatment (**II**) resulted in a RL2/RL1 ratio

of 1.11, while in control, the RL2/RL1 ratio was 0.56. Similarly, it was reported that the ratio was significantly higher for a Cd-amended culture.[12]

TABLE I. List of rhamnolipid RL1 (**1**–**7**) and RL2 (**8**–**12**) congeners obtained in the control and Cr(VI)-amended sample **II** (100 mg L^{-1}), by *P. aeruginosa* NCAIM(P), B001380 grown in LB medium, with molecular formula, molecular weight, elution time and ratio of relative ion abundance control/Cr(VI)-amended culture (**II**), observed by ESI/MS

No	RL congener	Molecular formula	Molecular weight, g mol^{-1}	Elution time, min	Ratio of the relative ion abundance[a] control/**II**
1	Rha–C8	$C_{14}H_{26}O_7$	306.35	9.48	0.9/0.5
2	Rha–C10	$C_{16}H_{30}O_7$	334.41	8.95	0.4/0.5
3	Rha–C12	$C_{18}H_{34}O_7$	362.23	11.12	0.2/–[b]
4	Rha–C10–C10 / Rha–C8–C12 / Rha–C12–C8	$C_{26}H_{48}O_9$	504.65	11.43	28.8/37.6
5	Rha–C10–C12 / Rha–C12–C10	$C_{28}H_{52}O_9$	532.36	12.49	22.9/4.5
6	Rha–C10–C12:1 / Rha–C12:1–C10	$C_{28}H_{50}O_9$	530.69	12.06	9.8/3.3
7	Rha–C10–C10–CH3	$C_{27}H_{50}O_9$	518.68	11.97	1.0/0.9
8	Rha–Rha–C10–C10	$C_{32}H_{58}O_{13}$	650.79	10.74	20.1/30.9
9	Rha–Rha–C10–C12 / Rha–Rha–C12–C10	$C_{34}H_{62}O_{13}$	678.84	11.80	8.8/11.1
10	Rha–Rha–C10–C12:1 / Rha–Rha–C12:1–C10	$C_{34}H_{60}O_{13}$	676.40	11.36	5.5/3.5
11	Rha–Rha–C10–C10–CH$_3$	$C_{33}H_{60}O_{13}$	664.40	11.26	1.6/5.8
12	Rha–Rha–C10–C14:1/ Rha–Rha–C12–C12:1/ Rha–Rha–C12:1–C12	$C_{36}H_{64}O_{13}$	704.43	12.38	–[b]/1.4

[a]Abundance taken as the count number of the observed molecular ions. The relative ion abundance was calculated as the abundance of a given RL congener divided by the sum of abundances of all observed RLs; [b]Congener was not detected

The relative ion abundance (%) of the most abundant RL1 (**4**–**7**) and RL2 (**8**–**11**) congeners in the control and sample **II** are shown in Fig. 3. Monorhamnolipids **4**–**7** showed a higher relative abundance in the control, except **4** and even 5- and 3-fold increases for **5** and **6** in the expression ratio compared to those in **II** (Fig. 3, Table I). The dirhamnolipids congeners **8**–**11** were slightly more present in **II**, except for **10**. This resulted in the increase in the RL2/RL1 ratio of 1.11 for **II** compared to that of the control (0.56). This observation clearly shows that the presence of Cr(VI) influenced the rhamnolipid profile produced by *Pseudomonas*. This in turn would impact the bioavailability of the metal.
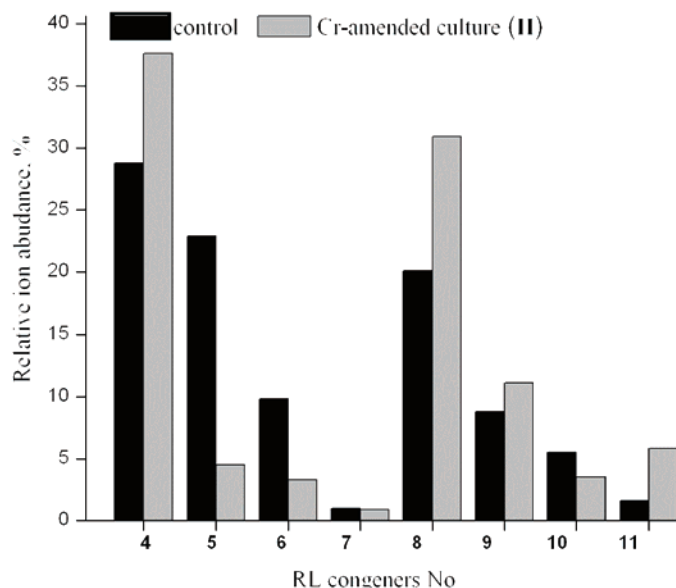
Fig. 3. Relative ion abundances (%) of the most abundant RL1 (**4**–**7**) and RL2 (**8**–**11**)
congeners obtained in the control and Cr(VI)-amended sample **II** (100 mg L^{-1}),
by *P. aeruginosa* NCAIM(P), B001380 grown in LB mediums.

CONCLUSIONS

This work confirmed the potential of *Pseudomonas aeruginosa* NCAIM(P), B001380 for application in bioremediation. The effect of different sub-lethal concentrations of Cr(VI) ion (**I** – 50 mg L^{-1} and **II** – 100 mg L^{-1}) on the growth and production of RL by strain was investigated. Cr(VI) was shown to inhibit RL production slightly, but the maximum of RL production was found in the late-stationary phase at 72 h for both Cr(VI)-amended cultures: **I** (236 mg L^{-1}) and **II** (160 mg L^{-1}). The relationship between RL production and Cr(VI) removal capacity was closely observed, showing that the maximum of the Cr(VI) removal capacity: 70 % (**I**) and 57 % (**II**) was reached with the maximum RL production. Although the amount of Cr measured in the RL preparation (22 μg mg^{-1}) indicated that less than 5 % of the total added Cr(VI) was bound to RL, in a further investigation, the yield could be enhanced in a two-phases experiment with first the production of rhamnolipids and then treatment with Cr(VI). Structural proof for RL–Cr(VI) interaction, which might have a pronounced impact on chromium bioremediation, was established by FTIR spectroscopy. An increase in a RL2/RL1 ratio to 1.11 for **II** compared to the control (0.56) was observed by ESI-MS, which also supports the finding that the presence of Cr(VI) may influence the rhamnolipid congeners produced by *Pseudomonas*, which in turn would impact the bioavailability of the metal.

ИЗВОД

УТИЦАЈ РАМНОЛИПИДА ДОБИЈЕНИХ ПОМОЋУ *Pseudomonas aeruginosa* NCAIM(P), B001380 НА КАПАЦИТЕТ ЗА УКЛАЊАЊЕ Cr(VI) ПРИ РАСТУ У ТЕЧНОЈ ПОДЛОЗИ

НАТАША С. АВРАМОВИЋ[1], СНЕЖАНА Д. НИКОЛИЋ-МАНДИЋ[2] и ИВАНКА М. КАРАЏИЋ[1]

[1]Медицински факултет, Институт за хемију, Универзитет у Београду, Вишеградска 26, Београд и [2]Хемијски факултет, Универзитет у Београду, Студентски трг 12–16, Београд

Утврђено је да бактерија *Pseudomonas aeruginosa* NCAIM(P), B001380, изолована из минералног уља за сечење метала, има високу толеранцију на хром и да производи био-сурфактант рамнолипид који има потенцијал за примену у биоремедијацији тешких метала. Испитан је раст културе, продукција рамнолипида и капацитет за уклањање Cr(VI) у присуству 50 (**I**) и 100 mg L^{-1} Cr(VI) (**II**) у течној подлози. Утврђен је максимум продукције рамнолипида у касној стационарној фази при расту бактерије у присуству Cr(VI): **I** (236 mg L^{-1}) и **II** (160 mg L^{-1}), при чему је уклоњен максимум Cr(VI): 70 % (**I**) и 57 % (**II**). Атомском апсорпционом спектроскопијом је утврђено присуство Cr у препарату екстрацелуларног рамнолипида **II** у концентрацији од 22 μg mg^{-1}. Појављивање нове траке на 914 cm^{-1} у инфрацрвеном спектру рамнолипида **II** се може узети као значајна индикација могуће координације јона CrO$_4^{2-}$ са рамнолипидом. Ефекат Cr(VI) на расподелу и однос ди- и моно- рамнолипида је испитан помоћу електроспреј-јонизационе масене спектрометрије (ESI–MS), при чему је, у поређењу са контролом, уочено повећање односа ди-/моно-рамнолипида у узорку **II.**

(Примљено 31. августа, ревидирано 29. октобра 2012)

REFERENCES

1. P. Singh, S. S. Cameotra, *Biochem. Biophys. Res. Commun.* **319** (2004) 291
2. M. Pacwa-Plocinicizak, G. A. Plaza, Z. Piotrowska-Seget, S. S. Cameotra, *Int. J. Mol. Sci.* **12** (2011) 633
3. A. A. Juwarkar, K. V. Dubey, A. Nair, S. K. Singh, *Indian J. Microbiol.* **48** (2008) 142
4. B. Dahrazma, C. N. Mulligan, *Chemosphere* **69** (2007) 705
5. C. N. Mulligan, *Environ. Pollut.* **133** (2005) 183
6. L. Di Palma, O. Gonzini, R. Mecozzi, *Chem. Ecol.* **27** (2011) 97
7. S. Wang, C. N. Mulligan, *Water Air Soil Pollut.* **157** (2004) 315
8. S. Wang, C. N. Mulligan, *Process Biochem.* **44** (2009) 296
9. Y. Asci, M. Nurbas, Y. S. Acikel, *J. Hazard. Mater.* **154** (2008) 663
10. E. Déziel, F. Lépine, S. Milot, R. Villemur, *Microbiology* **149** (2003) 2005
11. K. Duan, M. G. Surette, *J. Bacteriol.* **189** (2007) 4827
12. J. W. Neilson, L. Zhang, T. A. Veres-Schalnat, K. B. Chandler, C. H. Neilson, J. D. Crispin, J. E. Pemberton, R. Maier, *Appl. Microbiol. Biotechnol.* **88** (2010) 953
13. A. A. Juwarkar, A. Nair, K. V. Dubey, S. K. Singh, S. Devotta, *Chemosphere* **68** (2007) 1996
14. C. Kantar, H. Demiray, N. M. Dogan, C. J. Dodge, *Chemosphere* **82** (2011) 1489
15. C. Kantar, H. Demiray, N. M. Dogan, *Chemosphere* **82** (2011) 1496

16. S. Silver, *Gene* **179** (1996) 9
17. L. Garavaglia, S. B. Cerdeira, D. L. Vullo, *J. Hazard. Mater.* **175** (2010) 104
18. M. I. Ramírez-Díaz, C. Díaz-Pérez, E. Vargas, H. Riveros-Rosas, J. Campos-García, C. Cervantes, *Biometals* **21** (2008) 321
19. U. Thacker, R. Parikh, Y. Shouche, D. Madamwar, *Bioresour. Technol.* **98** (2007) 1541
20. M. W. Ali Khan, M. Ahmad, *J. Environ. Sci. Heal., A* **41** (2006) 659
21. D. Canovas, I. Cases, V. De Lorenzo, *Environ. Microbiol.* **5** (2003) 1242
22. A. Gupta, M. Kumar, R. Goel, *Biol. Trace Elem. Res.* **99** (2004) 269
23. N. Koçberber, G. Dönmez, *Bioresour. Technol.* **98** (2007) 2178
24. N. K., Kiliç, G. Dönmez, *J. Hazard. Mater.* **154** (2008) 1019
25. N. K. Kiliç, A. Stensballe, D. E. Otzen, G. Dönmez, *Bioresour. Technol.* **101** (2010) 2134
26. D. K. Thompson, K. Chourey, G. S. Wickham, S. B. Thieman, N. C. VerBerkmoes, B. Zhang, A. T. McCarthy, M. A. Rudisill, M. Shah, R. L. Hettich, *BMC Genomics* **11** (2010) 311
27. I. Karadzic, A. Masui, L. I. Zivkovic, N. Fujiwara, *J. Biosci. Bioeng.* **102** (2006) 82
28. C. H. Park, M. Keyhan, B. Wielinga, S. Fendorf, A. Matin, *Appl. Environ. Microb.* **66** (2000) 1788
29. F. D. Snell, C. T. Snell, *Colorimetric Methods of Analysis*, D. van Nostrand company, Inc., New York, USA, 1959, pp. 267–278
30. M. Heyd, A. Kohnert, T. H. Tan, M. Nusser, F. Kirschhöfer, G. Brenner-Weiss, M. Franzreb, S. Berensmeier, *Anal. Bioanal. Chem.* **391** (2008) 1579
31. S. Wilhelm, A. Gdynia, P. Tielen, F. Rosenau, K.-E. Jaeger, *J. Bacteriol.* **189** (2007) 6695
32. C. Mulligan, S. Wang, *Eng. Geol.* **85** (2006) 75
33. C. N. Mulligan, *Curr. Opin. Colloid Interface Sci.* **14** (2009) 372
34. P. Gili, P. A. Lorenzo-Luis, *Coord. Chem. Rev.* **193–195** (1999) 747
35. F. Leitermann, C. Syldatk, R. Hausmann, *J. Biol. Eng.* **2** (2008) 13
36. B. Volesky, *Sorption and Biosorption*, BV. Sorbex, Inc., Montreal, Canada, 2003, p. 52
37. Y. G. Ko, U. S. Choi, T. Y. Kim, D. J. Ahn, Y. J. Chun, *Macromol. Rapid Commun.* **23** (2002) 535
38. E. Déziel, F. Lépine, S. Milot, R. Villemur, *Biochim. Biophys. Acta* **1485** (2000) 145
39. A. P. Rooney, N. P. Price, K. J. Ray, T. M. Kuo, *FEMS Microbiol. Lett.* **295** (2009) 82.

Prediction of the electric conductivity of ionic liquids by two chemometrics methods

YU CAO[1], JIA YU[1], HANG SONG[1], XIANLONG WANG[2,3] and SHUN YAO[1]*

[1]Department of Pharmaceutical and Biological Engineering, Sichuan University, Chengdu 610065, China, [2]School of Life Science and Technology, University of Electronic Science and Technology of China, Chengdu 610054, China and [3]Department of Chemistry, Bryn Mawr College, 101 N Merion Ave, Bryn Mawr, PA 19010, USA

Abstract: In recent years, the study of the properties of ionic liquids (ILs) and their structures has developed largely. Among the common physicochemical properties of pure ILs, electric conductivity (*EC*) is of crucial importance for both practical and fundamental viewpoint. In order to develop effective models for predicting the *EC* value of various ILs, the relationship between the structural descriptors and the *EC* of thirty-five ionic liquids at different temperatures was investigated by multi-linear regression (MLR) and a back propagation artificial neural network (ANN). As a result, a three layer ANN with four variables selected by the MLR model as input nodes was successfully set up. The descriptors selected by MLR were suitable and significant to be the input nodes of the ANN model in this study. Moreover, the ionic conductivities calculated by the ANN model, having a high correlation coefficient and low root mean squared error, were quantitatively in good agreement with the experimental values. The ANN model was proved to be better than the MLR model.

Keywords: electroconductibility; ionic liquids; multi-linear regression; artificial neural network.

INTRODUCTION

In the last decades, ionic liquids (ILs) have attracted increasing interest in countless fields of physical and chemical sciences as "designer solvents".[1] Their properties, such as high chemical and thermal stability, low vapor pressure and high ionic conductivity, drive their popular application as useful media for synthesis, catalysis, extraction and separation processes.[2–6] Among the common properties of pure ILs, conductivity is of crucial importance for both practical and fundamental viewpoints.[7] The study of the conductivity of ILs was fully reviewed by Galinski *et al*.[8] In recent years, methods to investigate the properties of ILs

---

have been developed to a great extent. Especially with the development of chemometrics, the computational method has been widely used in fundamental research of ILs.[9,10] The early theoretical methods were summarized in a paper by Picálek *et al.*,[11] which included quantum calculations, molecular dynamics (MD) simulation and some Monte Carlo simulations. Zhao *et al.*[12] reported a model based on the conventional hole theory to study the conductivity and the calculated values were successfully fitted to the experimental data. However, the model was weak in predicting the conductivity of new ionic liquids. Matsuda and his coworkers[13] developed a method using computer-aided reverse design for ionic liquids. The conductivity of ionic liquids was conveniently predicted by computer-aided reverse design, but the model required complex parameters to fit. As for MD simulation, the presented studies on calculating the conductivity of ionic liquids were usually limited to one type of ionic liquids.[9,11,14] Recently, some researchers attempted to adopt simple models to predict the conductivity of different ILs at different temperatures, *e.g.*, the study of Eiden *et al.*[15] Moreover, the quantitative structure–property relationships (QSPR) method was popularly used to study the properties of ionic liquids and Zheng *et al.*[16] reviewed these meaningful studies. The back-propagation artificial neural network (BP ANN) method has been widely used by QSPR models in the study of other properties of ILs and good results were obtained.[17–19] To the best of our knowledge, the BP ANN method has not been reported in the study of the conductivity of ILs. This study aimed to explore multi-linear regression (MLR) and BP ANN methods to fit and predict the conductivity of ILs. The BP ANN was proved to have a better fitting and prediction capability than the MLR model. Furthermore, the developed ANN model has only four input nodes, which make it simpler than the other models.[12,13] The structures of the ionic liquids investigated in this study included the cations and anions given in Fig. 1, which represent the common anion–cation compositions of ILs.

<div align="center">COMPUTATIONAL DETAILS</div>

Dataset

Thirty-five ionic liquids (Table I) with 364 electric conductivity (*EC*) data at different temperatures from the Ionic Liquid Database (ILD)[20] were collected to investigate the relationship between the structure and conductivity of ILs. The 3D structural coordinates of the cations and anions[21-30] of these ILs were obtained from the Cambridge Structural Database (CSD).[31] All 364 data were divided into three data sets that contained a training set, a validation set and a test set with the percentage of 55, 18 and 27 %, respectively. In order to reflect the prediction capability of model, the data points of the same structural ILs were not divided into different datasets.

Descriptors

All the structures of the cations and anions were separately optimized at the B3LYP[32,33] level of calculation, using the 6-31G(d) basis set. These calculations were performed using the

Gaussian03 program.[34] Quantum mechanics descriptors of cations and anions were collected, which included total molecular energy (E), volume (V), the highest occupied molecular orbital energy (E_{HOMO}), the lowest unoccupied molecular orbital energy (E_{LUMO}), dipole moment (μ) etc. (Table II).
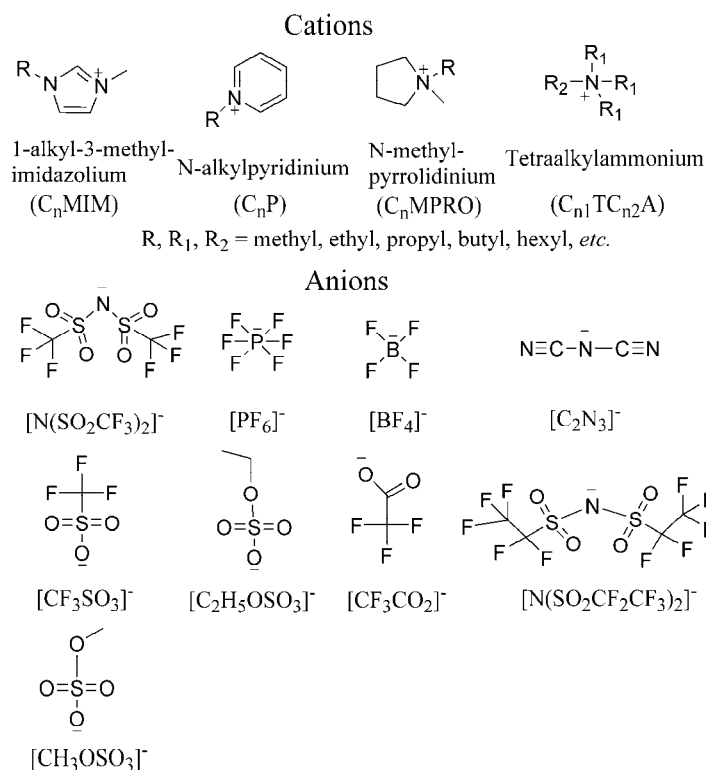
Fig. 1. The optimized cations and anions of the investigated ionic liquids.

TABLE I. The studied ionic liquids and data sets; training set: entries 1–18, validation set: entries 19–26, test set: entries 27–35

Entry	ILs	Temperature range, K	Data points
1	$[BP]^+[N(SO_2CF_3)_2]^-$	263.1–373.1	10
2	$[BMIM]^+[PF_6]^-$	268.15–468.15	21
3	$[HMIM]^+[BF_4]^-$	238.1–468.1	24
4	$[BMIM]^+[N(SO_2CF_2CF_3)_2]^-$	263.1–373.1	10
5	$[BTMA]^+[N(SO_2CF_3)_2]^-$	263.1–373.1	10
6	$[HMIM]^+[PF_6]^-$	295.1	1
7	$[OMIM]^+[PF_6]^-$	273.22–353.17	17
8	$[BMIM]^+[CF_3SO_3]^-$	268.15–468.15	21
9	$[MMIM]^+[N(SO_2CF_3)_2]^-$	263.15–373.15	12
10	$[EMIM]^+[C_2H_5OSO_3]^-$	258.1–433.1	36
11	$[HepTMA]^+[N(SO_2CF_3)_2]^-$	298.1	1
12	$[HTEA]^+[N(SO_2CF_3)_2]^-$	298.1	1

TABLE I. Continued

Entry	ILs	Temperature range, K	Data points
13	$[PMIM]^+[BF_4]^-$	298.1	1
14	$[HTBA]^+[N(SO_2CF_3)_2]^-$	298.1	1
15	$[OTBA]^+[CF_3SO_3]^-$	298.1	1
16	$[DMIM]^+[N(SO_2CF_3)_2]^-$	295.1	1
17	$[BMPRO]^+[N(SO_2CF_3)_2]^-$	263.1–373.1	10
18	$[BMIM]^+[C_2N_3]^-$	248.15–468.15	23
19	$[BMIM]^+[BF_4]^-$	238.1–468.1	24
20	$[HTMA]^+[N(SO_2CF_3)_2]^-$	298.1	1
21	$[HMIM]^+[N(SO_2CF_3)_2]^-$	263.15–373.15	12
22	$[BMIM]^+[N(SO_2CF_3)_2]^-$	263.15–373.15	12
23	$[OTEA]^+[N(SO_2CF_3)_2]^-$	298.1	1
24	$[HepTBA]^+[N(SO_2CF_3)_2]^-$	298.1	1
25	$[PMPRO]^+[N(SO_2CF_3)_2]^-$	298.1	1
26	$[BMIM]^+[CF_3CO_2]^-$	248.15–368.15	13
27	$[OMIM]^+[BF_4]^-$	238.1–468.1	24
28	$[OTMA]^+[N(SO_2CF_3)_2]^-$	298.1	1
29	$[EMIM]^+[N(SO_2CF_3)_2]^-$	248.15–353.15	12
30	$[HepTEA]^+[N(SO_2CF_3)_2]^-$	298.1	1
31	$[OTBA]^+[N(SO_2CF_3)_2]^-$	298.1	1
32	$[EMIM]^+[C_2N_3]^-$	238.15–353.15	13
33	$[BMIM]^+[CH_3OSO_3]^-$	303.2–353.2	11
34	$[OMIM]^+[N(SO_2CF_3)_2]^-$	263.15–373.15	12
35	$[EMIM]^+[BF_4]^-$	248.1–468.1	23

TABLE II. Data on the calculated quantum mechanics descriptors of the cations and anions

Ion	E / Hartree	E_{HOMO} / eV	E_{LUMO} / eV	M / D	V / cm^3 mol^{-1}
$[N(SO_2CF_3)_2]^-$	–1827.204081	–0.13542	0.17532	5.4169	127.003
$[PF_6]^-$	–940.6433857	–0.15668	0.281	0.0039	60.874
$[BF_4]^-$	–424.4990828	–0.11504	0.45846	0.0056	39.883
$[CF_3SO_3]^-$	–961.4979779	–0.07422	0.27653	4.4049	66.57
$[C_2H_5OSO_3]^-$	–778.313977	–0.06373	0.23851	4.9715	102.525
$[CF_3CO_2]^-$	–526.2375255	–0.03684	0.23386	4.7109	52.332
$[C_2N_3]^-$	–240.4860307	–0.0356	0.24231	0.8802	52.9
$[CH_3OSO_3]^-$	–738.9948944	–0.06002	0.25643	3.7771	72.761
$[N(SO_2CF_2CF_3)_2]^-$	–2302.767629	–0.14171	0.14446	6.3196	152.803
$[BP]^+$	–405.9244466	–0.45036	–0.23699	4.654	125.055
$[BMIM]^+$	–423.1786802	–0.42798	–0.17697	4.7649	131.637
$[HMIM]^+$	–501.8072113	–0.407	–0.17572	10.7448	176.128
$[OMIM]^+$	–580.4349008	–0.37963	–0.17545	16.0574	166.481
$[BTMA]^+$	–332.1108499	–0.45713	–0.11563	5.1609	124.465
$[MMIM]^+$	–305.2307599	–0.43626	–0.18467	0.7255	79.19
$[HTMA]^+$	–410.739132	–0.41514	–0.11419	10.015	151.489
$[EMIM]^+$	–344.5497093	–0.43158	–0.1805	1.6718	91.159
$[HepTMA]^+$	–450.0530362	–0.40016	–0.11389	12.6447	124.016
$[OTMA]^+$	–489.3668758	–0.38626	–0.11367	15.3359	175.687

TABLE II. Continued

Ion	E / Hartree	E_{HOMO} / eV	E_{LUMO} / eV	μ / D	V / cm^3 mol^{-1}
[HTEA]$^+$	–528.6795481	–0.41196	–0.08612	7.3707	192.29
[PMIM]$^+$	–383.8648154	–0.42903	–0.17839	3.5943	98.59
[HepTEA]$^+$	–567.9934591	–0.39697	–0.0858	9.6601	197.391
[OTEA]$^+$	–607.3072645	–0.38367	–0.08561	12.0649	211.196
[HTBA]$^+$	–764.5659048	–0.4091	–0.07486	3.6835	286.142
[HepTBA]$^+$	–803.879782	–0.39416	–0.07472	5.3987	318.19
[OTBA]$^+$	–843.1935931	–0.38139	–0.07462	7.3244	263.86
[DMIM]$^+$	–659.0624362	–0.36004	–0.17544	21.6069	181.37
[PMPRO]$^+$	–370.2219501	–0.48125	–0.10628	1.4382	115.118
[BMPRO]$^+$	–409.5364044	–0.45239	–0.10493	3.3716	140.102

Moreover, the molecular connectivity index is a term that reflects the relative accessibility of each bond to encounter other bonds of the same molecule in a milieu. The essence of molecular connectivity is the encoding of structure in a non-empirical way, which is thought to be helpful in the investigation of the physical properties.[35] Molecular connectivity index used in this study contained a chi index of zero order (^0X), first order (^1X) and second order (^2X). Eleven functions, such as linear, multinomial, exponent, logarithm and power function *etc.*, were explored to fit the relationship between each descriptor and conductivity. $^0X_{cation}$ was found to have a good S function relationship with the conductivity of ILs.

To predict the conductivity of ionic liquids at different temperatures, the temperature (T) must be considered as a variable in the models. In addition, the temperature and EC had a good quadratic polynomial relationship. Thus, the temperature (T), the S function of $^0X_{cation}$ (S) and the square of temperature (T^2) were also explored in this study. To decrease the redundancy existing in the descriptor data matrix, the descriptors correlation with each other and with the conductivity of the ILs were examined and collinear descriptors (*i.e.*, $r^2 > 0.9$) were detected.[36] Among the collinear descriptors, the one with the highest correlation with the conductivity was retained and the others were removed from the data matrix.

Prediction models

The prediction models for the conductivity of ILs were obtained by correlating the selected descriptors with the conductivity of corresponding ILs by the MLR and BP ANN methods. For a comparison of the different results from the MLR and BP ANN models, the training set and validation set were combined as one data set (called the construction set in the following text) and regressed to construct the MLR model, and the test set was used to evaluate the prediction capability of the models. The linear model was found with MLR method by the statistical package of the Social Sciences (SPSS) software. The model which had the highest squared correlation coefficient (R^2) was selected as the MLR prediction model to investigate the conductivities of the ILs. The descriptors determined in the linear model were selected as the input node of the ANN, and the conductivity of the ILs was considered as the output node. All parameters were first normalized to a scale of zero to one prior to use as the training, validation or testing data to avoid numerical overflows during the ANN process. The initial weights of the training network and momentum factor were random numbers. Then different training times, learning rates and number of neurons in the hidden layer were inputted to calculate the conductivity of ILs in training sets by means of the BP ANN method. The ANN algorithms were implemented in MATLAB programming language.

RESULTS AND DISCUSSION

The relationship between the descriptors and EC

Twenty-eight ionic liquids having conductivity data at 298.1K were used to investigate the relationship between the descriptors and conductivity. Eleven common functions were explored to fit each descriptor and conductivity. The EC was found to have a good S-function relationship with $^0X_{cation}$ (*S*), and the S function between $^0X_{cation}$ and the *EC* is shown in Fig. 2.
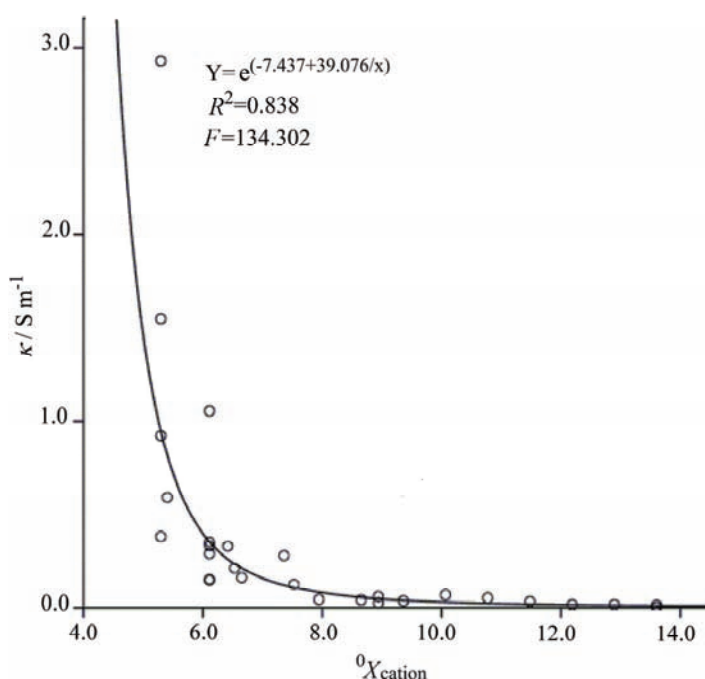
Fig. 2. The S-function relationship between $^0X_{cation}$ and electric conductivities.

The effect of temperature (*T*) was also studied. The relationship between the temperature and *EC* of the ionic liquids having more than one data point was all investigated. The rule was found that the temperature had quadratic polynomial relationship with *EC* for all the studied ionic liquids and had R^2 values higher than 0.98.

MLR Study

The descriptors were potential variables for the MLR model, which were chosen through correlation analysis. The linear relationship between these descriptors and *EC* was set up using the MLR model using SPSS software. The good correlations with experimental conductivity were selected based on R^2. Then, those descriptors without notable influence on R^2 were deleted and the model

with least number of descriptors and a high R^2 was founded. The correlation obtained for 364 data points of ILs conductivity is presented by the four-parameter equation as following:

$$EC = 14.577\,E_{\text{HOMO-anion}} - 0.117\,\mu_{\text{anion}} + 0.422\,S + (5.751\text{E}{-}5)\,T^2 - 2.941 \quad (1)$$

$$R^2 = 0.836,\ F = 331.818,\ sig = 0.000 \text{ (for all variables and the model)}$$

In the SPSS software, a *sig* value smaller than 0.05 indicates that the MLR model is of obvious statistical significance. In order to evaluate the model better, two aspects were compared concerning the prediction capability for different ionic liquids and the prediction capability for the same kind of ionic liquid but at different temperatures.

To illustrate the capability for different ionic liquids, the *EC* in the middle point of the temperature range for every ionic liquid was collected and analyzed. The calculated results for different ILs in the construction set and test set by MLR model are listed in Table III.

TABLE III. The conductivities of ILs predicted by the MLR and ANN models

Entry	T / K	κ_{exp} / S m^{-1}	κ_{MLR} / S m^{-1}	κ_{ANN} / S m^{-1}	ΔD (MLR)	ΔD (ANN)
1	298.10	0.33	–0.33	0.25	0.66	0.08
2	368.15	1.825	2.718	1.853	0.893	0.028
3	348.10	0.926	2.395	0.933	1.469	0.007
4	298.10	0.15	–0.49	0.15	0.64	0.00
5	298.10	0.21	–0.34	0.24	0.55	0.03
6	295.10	0.11	–0.17	0.04	0.28	0.07
7	313.15	0.06553	0.43389	0.06880	0.36836	0.00327
8	368.15	2.16	3.41	2.21	1.25	0.05
9	313.15	1.374	1.335	1.364	0.039	0.010
10	343.10	1.747	2.717	1.735	0.97	0.012
11	298.10	0.04	–0.42	0.18	0.46	0.14
12	298.10	0.067	–0.426	0.169	0.493	0.102
13	298.10	0.59	0.84	0.59	0.25	0.00
14	298.10	0.016	–0.432	0.164	0.448	0.148
15	298.10	0.0017	0.5767	0.1352	0.5750	0.1335
16	295.10	0.13	–0.53	0.14	0.66	0.01
17	298.10	0.28	–0.39	0.20	0.67	0.08
18	358.15	4.69	3.96	4.70	0.73	0.01
19	348.10	2.00	2.50	1.94	0.50	0.06
20	298.10	0.043	–0.404	0.187	0.447	0.144
21	313.15	0.3964	0.1355	0.3789	0.2609	0.0175
22	313.15	0.6575	0.2396	0.5115	0.4179	0.1460
23	298.10	0.033	–0.431	0.165	0.464	0.132
24	298.10	0.016	–0.433	0.163	0.449	0.147
25	298.10	0.16	–0.35	0.23	0.51	0.07
26	308.15	0.504	1.581	0.469	1.077	0.035
27	348.1	0.512	2.370	0.740	1.858	0.228
28	298.1	0.035	–0.422	0.172	0.457	0.137

TABLE III. Continued

Entry	T / K	κ_{exp} / S m^{-1}	κ_{MLR} / S m^{-1}	κ_{ANN} / S m^{-1}	ΔD (MLR)	ΔD (ANN)
29	298.1	0.921	–0.038	0.381	0.959	0.540
30	298.1	0.051	–0.429	0.167	0.480	0.116
31	298.1	0.013	–0.434	0.162	0.447	0.149
32	298.15	2.9281	1.9481	2.9390	0.9800	0.0109
33	328.2	0.626	2.086	0.688	1.460	0.062
34	313.15	0.2465	0.1105	0.3437	0.1360	0.0972
35	358.1	6.2	3.2	4.7	3.0	1.5

The results of the construction set reflected the fitting capability of the models. The remaining data, which did not construct the model, were collected as the test set to evaluate the prediction capability of the related models. For MLR model, the predicted conductivity of ILs in test set was calculated according to Eq. (1). The results in Table III suggested a minimum absolute error of 0.039, a maximum absolute error of 1.469 for the construction set, and a minimum error of 0.136 and a maximum error of 3.0 for the test set. The differences between the actual and estimated values were measured by the root mean squared error (*RMSE*), which is calculated as:

$$RMSE = \sqrt{\frac{\sum_{i=1}^{n}\left(y_i^{exp} - y_i^{cal}\right)^2}{n}} \tag{2}$$

where i represents the ith sample, y_i^{exp} is the experimental values, and y_i^{cal} is the predicted value by the model, n is the number of samples in the data set.[37] The *RMSE* of MLR model was 0.674 for construction set and 1.380 for test set, respectively. Fig. 3 shows the plots of the calculated electric conductivities by MLR model *versus* the experimental ones, with $R^2 = 0.8044$ for construction set and 0.5264 for test set. The fitting and prediction capabilities for the same kind of ionic liquid at different temperatures of MLR model were indicated by the *RMSE* of each kind of ILs in construction set and test set, respectively (Table IV).

The values of *RMSE* and R^2 for the MLR model suggested that the fitting and prediction capability of the MLR model were not good, especially of the latter. This means that the relationship between the structure and the conductivity of ionic liquids is not perfectly linear. However, compared with other methods used for the selection of descriptors, the MLR method is always faster and easier to implement.

BP ANN study

For the training, validation and test data sets, their ANN models were established by BP ANN analysis based on their descriptors obtained by the MLR model. The employed neural network in this modeling problem had four input

nodes, corresponding to the four operating variables, *i.e.*, $E_{\text{HOMO-anion}}$, μ_{anion}, S and T^2. The experimental data of the conductivity was the output node of the BP ANN. After optimization, a three-layer BP ANN was set up. The number of neurons in the hidden layers was 16, and the learning rate was 0.01. A log-sigmoid transfer function within the hidden layer and a linear transfer function within the output layer were used for the ANN model. According to the literature,[36,38] a validation set was employed to avoid over-fitting and optimize the weight value in this study. As the initial weights were random numbers produced by the computer, the weights may be converged on a local optimal. In order to avoid local optimal results, the ANN was calculated many times with different initial weights to obtain the global optimal result. Finally, the obtained ANN model was selected as a prediction model of the conductivity of ILs, which achieved the goal of training set and had good performance for validation set.

Fig. 3. The plots of the electric conductivities calculated by the MLR model *vs.* the experimental ones, the dotted line represents *y = x*.

Similar to the MLR model, the ANN prediction model was evaluated from two aspects. The experimental values and calculated values of conductivity by ANN model for different ionic liquids are given in Table III, showing that the minimum errors of the training set, validation set and test set achieved by the ANN model were 0.00, 0.0175 and 0.0109, respectively. The maximum error of the training set, validation set and test set were 0.148, 0.147 and 1.5, respectively. The *RMSE* values of the training set, validation set and test set obtained the ANN model were 0.072, 0.107 and 0.544, respectively. Furthermore, plots of the elec-

tric conductivities calculated by the ANN model *vs*. the experimental ones are shown in Fig. 4, with R^2 values of 0.9966, 0.9803 and 0.9703 for the training set, validation set and test set, respectively.

TABLE IV. The *RMSE* of the ionic liquids by MLR and ANN models

Entry	*RMSE* (MLR)	*RMSE* (ANN)	Data points
1	0.795	0.106	10
2	0.613	0.017	21
3	1.324	0.013	24
4	0.914	0.011	10
5	0.800	0.120	10
6	0.282	0.073	1
7	0.859	0.007	17
8	0.946	0.055	21
9	0.297	0.012	12
10	0.632	0.029	36
11	0.455	0.138	1
12	0.493	0.102	1
13	0.246	0.003	1
14	0.448	0.148	1
15	0.575	0.134	1
16	0.660	0.015	1
17	0.832	0.069	10
18	2.574	0.066	23
19	1.111	0.089	24
20	0.447	0.144	1
21	0.778	0.088	12
22	0.704	0.147	12
23	0.464	0.132	1
24	0.449	0.147	1
25	0.510	0.075	1
26	1.042	0.058	13
27	2.234	0.610	24
28	0.457	0.137	1
29	1.154	0.808	12
30	0.480	0.116	1
31	0.447	0.149	1
32	2.053	0.866	13
33	1.387	0.087	11
34	0.896	0.303	12
35	5.338	1.762	23

Similarly, the fitting and prediction capabilities for the same ionic liquids at different temperatures are given in Table IV. It could be concluded from Table III and Fig. 4 that the conductivities of the ionic liquids were mostly well predicted by the ANN model, and the results proved the good fitting and prediction capabilities of the constructed ANN model for these samples. Compared with the MLR

model, the ANN model had larger R^2 and smaller *RMSE* values than those of the MLR model. Moreover, the *RMSE* of the ionic liquids calculated by the ANN in Table IV were all smaller than those calculated by the MLR model. Based on above analysis, the prediction precision of this ANN model was high, and better than that of MLR model. In addition, the descriptors selected by the MLR model as the input node of the ANN model performed well in fitting and predicting the experimental data.
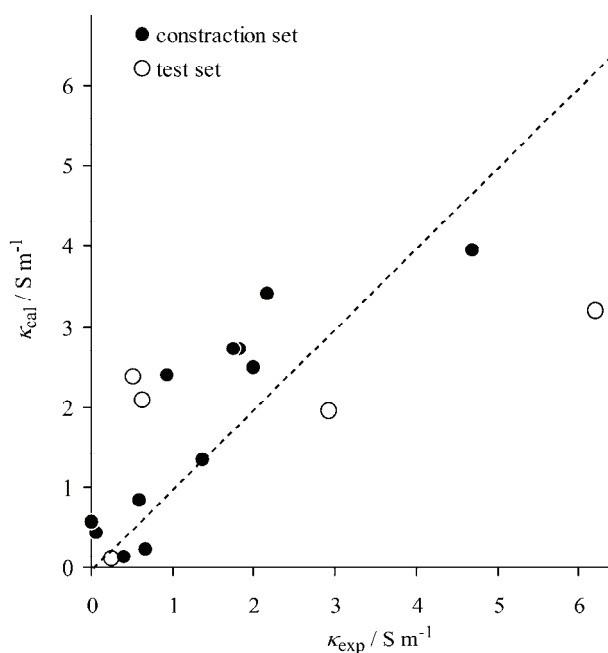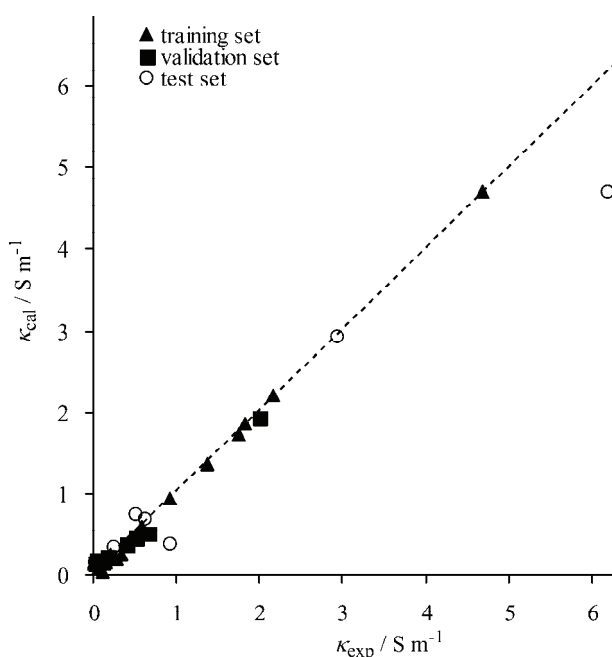

Fig. 4. The plots of the electric conductivities calculated by the ANN model *vs*. the experimental ones, the dotted line represents *y = x*.

On the other hand, both Tables III and IV suggested that the results for the test set were worse than those for the construction set. It was discussed in MLR study section that the ANN model had a much stronger fitting capability and better prediction precision than the MLR model. However, the results showed that some ionic liquids in the test set were not predicted well by ANN. For instance, the ionic liquid **29** was not predicted well, so all the ionic liquids with the same structural type as **29** were analyzed. The number of data points for this type of IL was 49, but only 13 data were in training test. In addition, the conductivity of ionic liquid **4** with ten data points in training set was very different from the others. For example, its conductivity was over 4 S m^{-1} at 373.15 K, while the others were all smaller than 3 S m^{-1}. Above all, the lack of experimental data for the training set may be the reason for the large deviation of IL **29**. Moreover, in the region of ionic conductivities lower than 0.1 S m^{-1}, a decrease in the prediction accuracy was found. It was noteworthy that the same phenomenon also

emerged in another study.[13] However, compared with the results in the previous study, the range of prediction accuracy was extended from 0.6 to 0.1 S m^{-1} in the present model. The ANN model was proved to be a relatively accurate prediction model and much better than the MLR model.

Analysis of the variables

The four descriptors employed in the MLR and ANN models were $E_{\text{HOMO-anion}}$, μ_{anion}, S and T^2. Multi-co-linearity between the four descriptors was detected by calculating their variation inflation factor (*VIF*) as:

$$VIF = \frac{1}{1-r^2} \quad (3)$$

where r is the correlation coefficient of the multiple regression equation between one descriptor and the others. If *VIF* equals one, no inter-correlation exists between each of the descriptors; if *VIF* is within the range 1.0–5.0, the corresponding model is acceptable; if *VIF* is larger than 10.0, the corresponding model is unstable.[37,39] The r^2 values for the four employed descriptors were 0.047, 0.164, 0.102 and 0.090, respectively. Accordingly, their *VIF* values were 1.049, 1.196, 1.136 and 1.099, respectively. Thus, the *VIF* values were less than five for each descriptor, which indicated that the constructed model was of obvious statistical significance.[37] To analyze the influence of descriptors on the EC values, the weights between input layer and hidden layer (shown in Table V) were studied.

The results given in Table V suggested that temperature, which is a thermodynamics variable, was the most important influencing factor for the *EC* of the ILs. Except temperature, the other three descriptors reflected the relationship between the structural characteristics and the *EC* of the ILs. According to previous analysis presented above, $^0X_{\text{cation}}$ is a good S function of *EC* at 298.1 K. Among the three variables, S founction of $^0X_{\text{cation}}$, which is related to the structural character of the cation, had the largest total weight value. $^0X_{\text{cation}}$ is the molecular connectivity index of a cation and it could represent information of structural characteristics containing size, number of valence electrons and the number of hydrogen atom attached to non-hydrogen atoms in the molecule.[40] The meaning of $^0X_{\text{cation}}$ and its total weight value analysis suggested that *EC* was related to the structural type of the cation, which was also proved by Matsuda *et al.*[13] in another model. μ_{anion} and $E_{\text{HOMO-anion}}$ are both related to the activity of anion. Affirmatively, different E_{HOMO}–E_{LUMO} gaps will lead to different conductivities. If the HOMO energy is lower, the electron work function will increase and electron transfer becomes more difficult. Dipole moment can reflect polarizability and is closely related with the capacity to conduct electricity. This indicated that the *EC* of the ionic liquid in this study might be determined by the

kind of the cation to a great degree and simultaneously influenced by the activity characteristics of the anion.

TABLE V. The weights between input layer and hidden layer

Neurons No.	Weight (absolute value)			
	μ_{anion}	$E_{HOMO\text{-}anion}$	S	T^2
1	0.1045	0.1650	8.8672	5.5500
2	2.7061	4.9088	5.5977	5.0415
3	4.6532	4.1600	5.5167	6.2565
4	10.1419	1.8552	3.8925	2.5628
5	3.4325	6.9361	8.4247	3.7612
6	4.9101	0.5836	10.7555	4.5674
7	5.9070	5.4873	7.9757	0.4859
8	6.6151	0.5055	1.3238	4.8877
9	1.1565	0.5655	0.9835	7.2336
10	6.0981	8.4227	1.2909	5.1381
11	1.5735	1.6982	5.0830	10.6385
12	10.2083	2.4696	9.5344	1.4208
13	4.1750	0.6770	4.6322	10.1808
14	6.1998	3.5529	6.1921	6.4718
15	8.4252	7.4568	0.2939	0.8942
16	1.3254	6.6955	1.5020	8.7378
Total	77.6322	56.1397	81.8658	83.8286

CONCLUSIONS

In this study, linear and ANN models were established based on the MLR and BP ANN methods to fit and predict the conductivity of ILs. 364 experimental conductivity data of the ILs were used to establish the models and test their predictive capability. The ANN model with $R^2 = 0.9966$ and *RMSE* = 0.072 for training set showed good fitting capability. The predictive capability of the ANN model was also reflected by its $R^2 = 0.9703$ and *RMSE* = 0.544 for the test set. The two models were found stable by *VIF* analysis. The R^2 and *RMSE* values of two models proved the ANN model was better than the MLR model. The results indicated the non-linear modeling might be more rational for the prediction of conductivity. It is worth mentioning that the descriptors selected by MLR were suitable and significant to be the input nodes of the ANN model in this study. The weights between the input layer and hidden layer were also analyzed, which indicated the conductivity of ionic liquid in this study might be determined to a great degree by the kind of cation and influenced by the activity characteristics of the anion. In summary, the developed ANN model proved itself to be promising for the prediction of the conductivity of various kinds of ionic liquids at different temperatures.

ИЗВОД

ПРЕДВИЂАЊЕ ЕЛЕКТРИЧНЕ ПРОВОДЉИВОСТИ ЈОНСКИХ ТЕЧНОСТИ ДВЕМА ХЕМОМЕТРИЈСКИМ МЕТОДАМА

YU CAO[1], JIA YU[1], HANG SONG[1], XIANLONG WANG[2,3] и SHUN YAO[1]

¹ Sichuan University, Chengdu, China, ² University of Electronic Science and Technology, Chengdu, China и ³ Bryn Mawr College, Bryn Mawr, PA, USA

У последњих неколико година постигнут је знатан напредак у проучавању особина јонских течности (ILs) и њихове структуре. Од обичних физичко–хемијских особина чистих ILs, електрична проводљивост (EC) је од битне важности како са практичног, тако и са фундаменталног аспекта. Да бисмо развили ефикасне моделе за предвиђање EC разних ILs, испитана је зависност између разних структурних дескриптора и EC за 35 IL на различитим температурама. То је учињено помоћу мултилинеарне регресије (MLR) и методом неуронских мрежа (ANN). Нађено је да је MLR модел одређен тростепеном ANN методом са 4 променљиве био успешан. Јонска проводљивост одређена ANN моделом има висок коефицијент корелације и малу средњу квадратну грешку и добро се слаже са експерименталним вредностима. ANN модел се показао бољим од MLR модела.

(Примљено 7. марта, ревидирано 12. јуна 2012)

REFERENCES

1. S. K. Tang, G. A. Baker, H. Zhao, *Chem. Soc. Rev.* **41** (2012) 4030
2. J. M. Lu, F. Yan, J. Texter, *Prog. Polym. Sci.* **34** (2009) 431
3. P. Kubisa, *Prog. Polym. Sci.* **34** (2009) 1333
4. X. S. Zhou, J. B. Liu, W. F. Luo, Y. W. Zhang, H. Song, *J. Serb. Chem. Soc.* **76** (2011) 1607
5. Z. Yang, W. B. Pan, *Enzyme Microb. Tech.* **37** (2005) 19
6. C. F. Poole, S. K. Poole, *J. Chromatogr., A* **1217** (2010) 2268
7. I. Bandres, D. F. Montano, I. Gascon, P. Cea, C. Lafuente, *Electrochim. Acta* **55** (2010) 2252
8. M. Galinski, A. Lewandowski, I. Stepniak, *Electrochim. Acta* **51** (2006) 5567
9. O. Borodin, *J. Phys. Chem., B* **113** (2009) 11463
10. M. G. Benavides-Garcia, M. Monroe, *Chem. Phys. Lett.* **479** (2009) 238
11. J. Picálek, J. Kolafa, *J. Mol. Liq.* **134** (2007) 29
12. H. Zhao, Z. C. Liang, F. Li, *J. Mol. Liq.* **149** (2009) 55
13. H. Matsuda, H. Yamamoto, K. Kurihara, K. Tochigi, *Fluid Phase Equilibr.* **261** (2007) 434
14. S. U. Lee, J. Jung, Y. K. Han, *Chem. Phys. Lett.* **406** (2005) 332
15. P. Eiden, S. Bulut, T. Kochner, C. Friedrich, T. Schubert, I. Krossing, *J. Phys. Chem., B* **115** (2011) 300
16. Y. S. Zheng, Q. Mo, Z. M. Liu, *Chin. J. Prog. Chem.* **21** (2009) 1772
17. J. Palomar, J. S. Torrecilla, V. R. Ferro, F. Rodríguez, *Ind. Eng. Chem. Res.* **47** (2008) 4523
18. C. Q. Yan, M. J. Han, H. Wan, G. F. Guan, *Fluid Phase Equilibr.* **292** (2010) 104

19. F. Nami, F. Deyhimi, *J. Chem. Thermodyn.* **43** (2011) 22
20. Ionic Liquids Database (IL Thermo), http://ilthermo.boulder.nist.gov/ILThermo/ pure-prp.uix.do (accessed in April, 2013)
21. A. R. Choudhury, N. Winterton, A. Steiner, A. I. Cooper, K. A. Johnson, *J. Am. Chem. Soc.* **127** (2005) 16792
22. K. Matsumoto, R. Hagiwara, Z. Mazej, P. Benkic, B. Zemva, *Solid State Sci.* **8** (2006) 1250
23. J. D. Holbrey, W. M. Reichert, R. P. Swatloski, G. A. Broker, W. R. Pitner, K. R. Seddon, R. D. Rogers, *Green Chem.* **4** (2002) 407
24. S. G. Raj, G. R. Kumar, R. Mohan, R. Jayavel, *Acta Crystallogr., E* **62** (2006) o5
25. S. Konar, S. Dalai, J. Ribas, M. G. B. Drew, E. Zangrando, N. R. Chaudhuri, *Inorg. Chim. Acta* **357** (2004) 4208
26. S. M. Dibrov, J. K. Kochi, *Acta Crystallogr., C* **62** (2009) o19
27. P. Nockemann, B. Thijs, S. Pittois, J. Thoen, C. Glorieux, K. Van Hecke, L. Van Meervelt, B. Krichner, K. Binnemans, *J. Phys. Chem., B* **110** (2006) 20978
28. J. Lachwa, I. Bento, M.T. Duarte, J. N. C. Lopes, L. P. N. Rebelo, *Chem. Commun.* **23** (2006) 2445
29. J. J. Jodry, K. Mikami, *Tetrahedron Lett.* **45** (2004) 4429
30. W. A. Henderson, M. Herstedt, V. G. Young Junior, S. Passerini, H. C. De Long, P.C. Trulove, *Inorg. Chem.* **45** (2006) 1412
31. F. H. Allen, *Acta Crystallogr., B* **58** (2002) 380
32. C. Lee, W. Yang, R.G. Parr, *Phys. Rev., B* **37** (1988) 785
33. A.D. Becke, *J. Chem. Phys.* **98** (1993) 5648.
34. Gaussian 03, revision C.02, Gaussian, Inc., Wallingford, CT, 2004
35. L. B. Kier, L. H. Hall, *Croat. Chem. Acta* **75** (2002) 371
36. M. Goodarzi, T. Chen, M. P. Freitas, *Chemometr. Intell. Lab.* **104** (2010) 260
37. L. Xi, H. Sun, J. Li , H. Liu, X. Yao, P. Gramatica, *Chem. Eng. J.* **163** (2010) 195
38. H. Yoon, Y. J. Hyun, K. K. Lee, *J. Hydrol.* **335** (2007) 68
39. R. F. George, A. P. Carl, Y. W. Leland, *J. Phys. Org. Chem.* **5** (1992) 395
40. X. Y. Zhang, H. W. Zhu, L. Li, G. Z. Li, Z. W. Wang, *Prog. Chem.* **15** (2003) 351.

New cholesteryl-containing bent core liquid crystals

COSMIN-CONSTANTIN HUZUM, IRINA CARLESCU, GABRIELA LISA
and DAN SCUTARU*

Faculty of Chemical Engineering and Environmental Protection, Gheorghe Asachi Technical University of Iasi, 71 D. Mangeron St., 700050 – Iasi, Romania

Abstract: The paper presents the synthesis and mesomorphic behavior of two new series of bent core liquid crystalline compounds based on a 1,3-dihydroxybezene core and containing a cholesteryl 6-oxyhexanoate wing. The two series were obtained by esterification of the cholesteryl 6-(3-hydroxyphenoxy)hexanoate core with some 4-{[4-(*n*-alkyloxy)phenyl]azo}benzoic acids (*n*-alkyl = *n*-hexyl – *n*-dodecyl) or 4-{[4-(*n*-alkyloxy)benzoyl]oxy}benzoic acids (*n*-alkyl = *n*-hexyl – *n*-decyl). The esterification reactions were performed *via* the corresponding acyl chlorides or with the dicyclohexylcarbodiimide/4--(*N,N*-dimethylamino)pyridine (DCC/DMAP) system. All the synthesized compounds evidenced enantiotropic liquid crystalline properties with smectic type textures when investigated by differential scanning calorimetry and polarized optical microscopy. Isotropization and isotropic to liquid crystal transitions occurred at relatively low temperatures (between 89 and 146 °C). The compounds containing the azo-aromatic linking group presented the largest range of stability of the mesophases (between 42 and 87 °C). All the investigated compounds were thermally stable in the range of the existence of mesophases.

Keywords: liquid crystals; banana shaped; cholesterol; resorcinol.

INTRODUCTION

Liquid crystals have been intensively investigated for the last six decades, resulting in the discovery of many applications in modern technologies. Cholesteric liquid crystals (CLCs) are compounds with liquid crystalline properties that contain at least one chiral carbon atom in their molecule. They are so-called because such properties were first observed in cholesteric esters.[1]

Due to their unique optical properties, such as selective reflection of circular polarized light, high optical rotatory power and circular dichroism, CLCs have attracted the attention of chemists and physicists.[2,3]

669

Liquid crystalline compounds containing two identical or non-identical mesogens united through a flexible spacer of varying length and parity are among the large variety of non-conventional liquid crystals reported to date.[4] Since the discovery of cholesteryl benzoate, the first liquid crystal,[5] more than 3300 monomers, oligomers and polymers with cholesterol have been synthesized and characterized.[6]

Chiral dimesogenic compounds consisting of two different mesogenic units with at least one containing a cholesteryl unit interlinked through a spacer are a relatively new class of liquid crystalline compounds that still require more research in order to establish the relationship between their structure and their liquid crystalline properties.[7] Unsymmetric dimesogenic compounds containing a cholesteryl esteric moiety and azobenzene mesogenic groups may be suitable for use in liquid crystalline displays and optical–electric functional devices.[8,9] Molecules containing azo groups show reversible *trans*/*cis* isomerization upon UV––Vis irradiation.[10,11] Tamaoki and Mallia reported the synthesis of dimesogenic compounds containing the cholesteryl-azobenzene moiety linked by a flexible alkyl chain of 6 to 14 carbon atoms in length, the majority of these compounds exhibited only the cholesteric mesophase.[12]

Very characteristic for liquid crystals with strong chiral pro-mesogenic units (as in the case of cholesterol with 8 chiral centers) are the blue phases (BP I, BP II, BP III). They appear between the isotropic and chiral nematic or smectic textures, within a narrow temperature range[13,14] and the twist grain boundary phase (TGBA, TGBC, TGBC*), observed at the phase transition from isotropic liquid or chiral nematic to the smectic A or chiral smectic C phases.[13]

TGB and BP phases are examples of frustrated mesophases and derive from an antagonistic situation when the molecules are trying to form a helical structure with the chiral nematic helix axis perpendicular on the long axes of the molecules simultaneously with their tendency to form a lamellar structure.[15] The discovery of these types of new mesophases raises up the interest for future practical applications of liquid crystals containing chiral groups in their molecules.[16]

The new field of bent core liquid crystals has also tried to exploit the properties that may be induced by the presence of a cholesteric moiety. Generally, the synthesized structures are quite complex, two typical rigid mesogenic groups being attached to the core molecule while the cholesteryl part acts more as a terminal chain.[6]

In order to develop the class of cholesterol-containing bent core liquid crystals, this paper presents the synthesis, structural characterization and mesomorphic properties of two new series of chiral liquid crystals based on a resorcinol core. In order to obtain as simple as possible bent core liquid crystalline compounds containing cholesteric units, the synthesized compounds possess only one typical mesogenic wing, formed by two aromatic rings, connected *via* ester or

azo linking groups, and containing alkyloxy terminal flexible chains. The other arm is formed by a cholesteryl unit linked by a pentamethylen flexible spacer to the core molecule.

EXPERIMENTAL

Materials, instruments and methods

All reagents and solvents were purchased from Aldrich or Merck and were used without further purification unless otherwise noted. Cholesteryl 6-bromohexanoate was synthesized accordingly to a literature procedure.[17] The 4-{[4-(alkyloxy)phenyl]azo}benzoic acids[18] and the 4-[4-(alkyloxy)benzoyloxy]benzoic acids[19] were obtained by adapting literature data. All reactions involving dicyclohexylcarbodiimide (DCC) and 4-(*N*,*N*-dimethylamino)pyridine (DMAP) were performed in anhydrous dichloromethane, under a dry nitrogen atmosphere. Silica gel 60 (Merck) was used for column chromatography.

Nuclear magnetic resonance (NMR) spectra were recorded on a Bruker® Avance DRX 400 MHz spectrometer. Chemical shifts were reported in ppm relative to tetramethylsilane (TMS) as an internal standard. The infrared (IR) spectra were recorded using a Nicolet® Magna 550 FT-IR spectrometer (NaCl crystal window). The mass spectra were recorded on a quadrupole–time of flight mass spectrometer equipped with an electrospray ion source (Agilent® 6520 Accurate Mass Q-TOF LC/MS). The transition temperatures were determined using a Linkam heating stage and Linksys 32 temperature control unit in conjunction with an Axioscop 40 Zeiss polarizing optical microscope and Qimaging/Retiga-1000R camera for image capture. The transitions were confirmed by DSC analysis (Mettler Toledo DSC1). Heating and cooling cycles were run at rates of 10 °C min^{-1} under a nitrogen atmosphere. The samples were measured in closed lid aluminum pans. Mesophase type was assigned by visual comparison (under the microscope) with known phase standards.[20]

All the thermal gravimetric analyses were performed on 2.5–4.5 mg samples on a Mettler-Toledo® TGA SDTA851^e instrument under a dynamic N_2 atmosphere, flow rate of 20 ml min^{-1}, at a heating rate of 10 K min^{-1} from 25 to 900 °C. In order to obtain comparable data, constant operational parameters were employed for all samples.

The melting points were recorded using a melting point meter Krüss Optotronic KSPI – N and are uncorrected.

Synthesis of cholesteryl 6-(3-hydroxyphenoxy)hexanoate (1)

A mixture of resorcinol (0.91 g, 8.25 mmol) and K_2CO_3 (4.55 g, 33 mmol) in 2-butanone (40 mL) was stirred at reflux temperature for 30 min and then cholesteryl 6-bromohexanoate (3.1 g, 5.5 mmol) dissolved in 2-butanone (10 mL) was added dropwise with a syringe. The reaction mixture was kept over night at reflux temperature, cooled down to room temperature, filtrated and concentrated under vacuum. Purification by column chromatography on silica gel using a mixture of hexane : ethyl acetate 3:1 as eluent afforded **1** as a pure substance. The physical and spectral data for **1** are given in the Supplementary material to this paper.

General method for the synthesis of compounds 4a–f

Acyl chlorides **2a**–**f** were prepared from the corresponding acids by reaction with thionyl chloride and were used immediately for the synthesis of **4a**–**f**. A mixture of one equivalent of **1**, 1.08 equivalents of 4-{[4-(alkyloxy)phenyl]azo}benzoyl chloride **2** and tetrabutylammonium hydrogensulfate (TBAHS) in dichloromethane (40 mL) and 1.28 equivalents of potassium carbonate in water (10 mL) were vigorously stirred for 24 h at room temperature. The organic layer was separated, washed several times with distilled water, dried over anhydrous

magnesium sulfate and concentrated on a rotary evaporator. Compounds **4a**–**f** were purified by column chromatography on silica gel using a mixture of dichloromethane : ethyl acetate 20:1 as eluent.

*3-{[6-(cholesteryloxy)-6-oxohexyl]oxy}phenyl 4-{[4-(hexyloxy)phenyl]azo}benzoate (**4a**)*

Quantities: compound **1** (0.21 g, 0.35 mmol), 4-{[4-(hexyloxy)phenyl]azo}benzoyl chloride (0.130 g, 0.38 mmol) and TBAHS (5.7 mg, 0.017 mmol) in dichloromethane (40 mL), and K$_2$CO$_3$ (0.48 g, 0.45 mmol) in water (10 mL).

*3-{[6-(cholesteryloxy)-6-oxohexyl]oxy}phenyl 4-{[4-(heptyloxy)phenyl]azo}benzoate (**4b**)*

Quantities: compound **1** (0.21 g, 0.35 mmol), 4-{[4-(heptyloxy)phenyl]azo}benzoyl chloride (0.135 g, 0.38 mmol) and TBAHS (5.7 mg, 0.017 mmol) in dichloromethane (40 mL), and K$_2$CO$_3$ (0.48 g, 0.45 mmol) in water (10 mL),

*3-{[6-(cholesteryloxy)-6-oxohexyl]oxy}phenyl 4-{[4-(octyloxy)phenyl]azo}benzoate (**4c**)*

Quantities: compound **1** (0.21 g, 0.35 mmol), 4{[4-(octyloxy)phenyl]azo}benzoyl chloride (0.141 g, 0.38 mmol) and TBAHS (5.7 mg, 0.017 mmol) in dichloromethane (40 mL), and K$_2$CO$_3$ (0.48 g, 0.45 mmol) in water (10 mL).

*3-{[6-(cholesteryloxy)-6-oxohexyl]oxy}phenyl 4-{[4-(nonyloxy)phenyl]azo}benzoate (**4d**)*

Quantities: compound **1** (0.21 g, 0.35 mmol), 4-{[4-(nonyloxy)phenyl]azo}benzoyl chloride (0.146 g, 0.38 mmol) and TBAHS (5.7 mg, 0.017 mmol) in dichloromethane (40 mL), and K$_2$CO$_3$ (0.48 g, 0.45 mmol) in water (10 mL).

*3-{[6-(cholesteryloxy)-6-oxohexyl]oxy}phenyl 4-{[4-(decyloxy)phenyl]azo}benzoate (**4e**)*

Quantities: compound **1** (0.21 g, 0.35 mmol), 4-{[4-(decyloxy)phenyl]azo}benzoyl chloride (0.151 g, 0.38 mmol) and TBAHS (5.7 mg, 0.017 mmol) in dichloromethane (40 mL), and K$_2$CO$_3$ (0.48 g, 0.45 mmol) in water (10 mL).

*3-{[6-(cholesteryloxy)-6-oxohexyl]oxy}phenyl 4-{[4-(dodecyloxy)phenyl]azo}benzoate (**4f**)*

Quantities: compound **1** (0.21 g, 0.35 mmol), 4-{[4-(dodecyloxy)phenyl]azo}benzoyl chloride (0.162 g, 0.38 mmol) and TBAHS (5.7 mg, 0.017 mmol) in dichloromethane (40 mL) and K$_2$CO$_3$ (0.48 g, 0.45 mmol) in water (10 mL). The physical and spectral data for **4a**–**f** are given in the Supplementary material to this paper.

*General method for the synthesis of compounds **5a**–**e***

A mixture of 1 equivalent of **1**, 1.1 equivalents of 4-{[4-(alkyloxy)benzoyl]oxy}benzoic acid and 0.2 equivalents of DMAP dissolved in dry dichloromethane was stirred for a 15–20 min at room temperature, cooled to 0 °C on an ice bath and then 1.2 equivalents of DCC dissolved in dry dichloromethane were added dropwise. After 30 min, the ice bath was removed and the reaction mixture was stirred for 48 h at room temperature after which the precipitated *N*,*N*′-dicyclohexylurea (DCU) was filtered off. The solvent was evaporated in vacuum and the solid residue was chromatographed on silica gel using a 3:1 mixture of hexane:ethyl acetate as eluent. White products were obtained.

*4-{[3-((6-(cholesteryloxy)-6-oxohexyl)oxy)phenoxy]carbonyl}phenyl 4-(hexyloxy)benzoate (**5a**)*

Quantities: compound **1** (0.20 g, 0.35 mmol), 4-{[4-(hexyloxy)benzoyl]oxy}benzoic acid (0.134 g, 0.39 mmol), DCC (0.087 g, 0.42 mmol), DMAP (0.0085 g, 0.07 mmol), dry dichloromethane (40 mL).

*4-{[3-((6-(cholesteryloxy)-6-oxohexyl)oxy)phenoxy]carbonyl}phenyl 4-(heptyloxy)benzoate (**5b**)*

Quantities: compound **1** (0.20 g, 0.35 mmol), 4-{[4-(heptyloxy)benzoyl]oxy}benzoic acid (0.140 g, 0.39 mmol), DCC (0.085 g; 0.41 mmol), DMAP (0.0085 g, 0.07 mmol), dry dichloromethane (40 mL).

4-{[3-((6-(cholesteryloxy)-6-oxohexyl)oxy)phenoxy]carbonyl}phenyl 4-(octyloxy)benzoate (5c)

Quantities: compound **1** (0.20 g, 0.35 mmol), 4-{[4-(octyloxy)benzoyl]oxy}benzoic acid (0.145 g, 0.39 mmol), DCC (0.085 g, 0.41 mmol), DMAP (0.0085 g, 0.07 mmol), dry dichloromethane (40 mL).

4-{[3-((6-(cholesteryloxy)-6-oxohexyl)oxy)phenoxy]carbonyl}phenyl 4-(nonyloxy)benzoate (5d)

Quantities: compound **1** (0.20 g, 0.35 mmol), 4-{[4-(nonyloxy)benzoyl]oxy}benzoic acid (0.150 g, 0.39 mmol), DCC (0.085 g, 0.41 mmol), DMAP (0.0085 g, 0.07 mmol), dry dichloromethane (40 mL).

4-{[3-((6-(cholesteryloxy)-6-oxohexyl)oxy)phenoxy]carbonyl}phenyl 4-(decyloxy)benzoate (5e)

Quantities: compound **1** (0.20 g, 0.35 mmol), 4-{[4-(decyloxy)benzoyl]oxy}benzoic acid (0.155 g, 0.39 mmol), DCC (0.085 g, 0.41 mmol), DMAP (0.0085 g, 0.07 mmol), dry dichloromethane (40 mL).

RESULTS AND DISCUSSION

A two-step reaction was necessary to obtain the desired compounds (Scheme 1). In the first step, cholesteryl 6-(3-hydroxyphenoxy)hexanoate (**1**) was obtained by refluxing cholesteryl 6-bromohexanoate and resorcinol (in a 1:1.5 molar ratio) in 2-butanone, in the presence of potassium carbonate.[17] In the second step, the free phenolic group of **1** was esterified with two series of mesogenic acids containing two aromatic rings, connected *via* an azo or an ester linking group and containing alkyloxy ending chains. For the esterification reactions, two methods were used. In the case of the **4a**–**f** series, poor results were obtained when the more convenient DCC/DMAP system was used. In this case, the esterification reactions were realized with the corresponding acid chlorides in aqueous K_2CO_3/ /dichloromethane at room temperature for 24 h, using tetrabutylammonium hydrogen sulfate (TBAHS) as a phase transfer catalyst.[21] In the case of **5a**–**e** series, the esterification was performed with DCC and DMAP in dry dichloromethane at room temperature for 48 h.[19] All the obtained compounds were purified by column chromatography using dichloromethane:ethyl acetate (20:1) or hexane:ethyl acetate (3:1) as eluents. The yields were similar for both series (around 50 %). The structure and purity of the obtained final compounds were checked and confirmed by ^{1}H-NMR, ^{13}C-NMR, FT-IR and mass spectrometry (data given in the Supplementary material to this paper).

Taking into consideration the importance of thermal stability for the whole interval of the existence of the mesophase, thermogravimetric studies were performed for both the **4a**–**f** and **5a**–**e** series. Thermogravimetric data evidenced very good thermal stability for all the compounds, the T_{onset} values (temperatures at which the degradation processes begin) being more than 150 °C higher than the isotropization values (T_{onset} values in Tables I and II). These values are comparable with those other classes of bent core compounds containing azo or ester linking groups.[18,22]
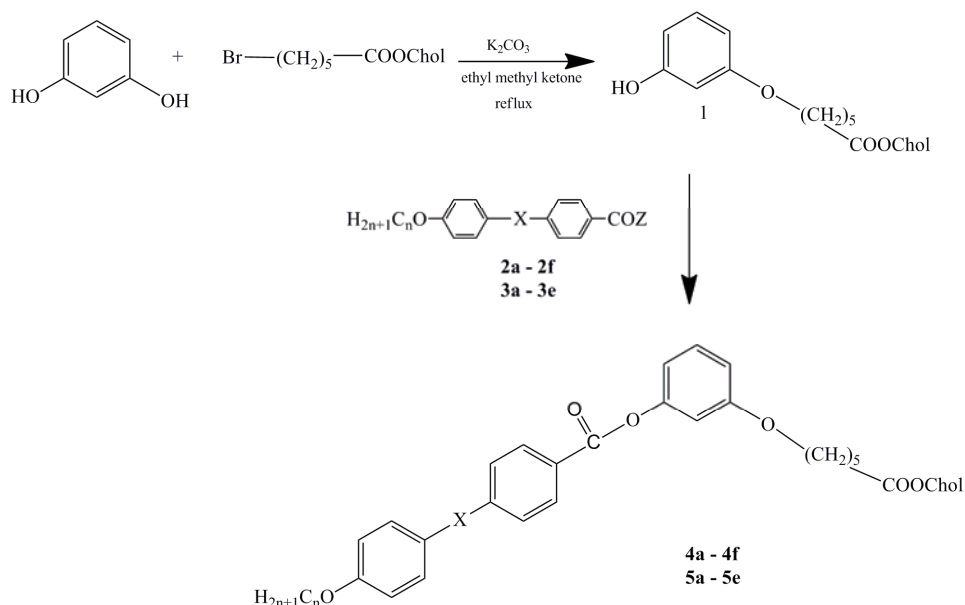
Scheme 1. Synthesis of the cholesteric liquid crystals; **2a–f**, X = –N=N–, Z = –Cl, *n* = 6–10, 12, aq. K$_2$CO$_3$, TBAHS, 24 h; **3a–e**, X = –COO–, Z = – OH, *n* = 6–10, DCC, DMAP, CH$_2$Cl$_2$, 48 h; **4a–f**, X = –N=N–, *n* = 6–10, 12; **5a–e**, X = –COO–, *n* = 6–10; Chol = cholesteryl.

TABLE I. Transition temperatures (°C), and associated transition enthalpies (J g^{-1}) for compounds **4a–f**; abbreviations: Cr, crystalline; LC, liquid crystal; I, isotropic; t_{onset}: the initial temperature at which the degradations processes begin

	T / °C [ΔH / J g^{-1}]						t_{onset} °C
Cmpd.	Heating			Cooling			
	Cr/LC	LC/I	Mesophase interval, °C	I/LC	LC/Cr	Mesophase interval, °C	
4a	59 [–24.94]	146 [–2.45]	87	131 [1.57]	–	–	327
4b	83 [–25.66]	142 [–1.89]	59	118 [3.21]	–	–	326
4c	77 [–22.66]	133 [–6.28]	56	130 [5.28]	–	–	329
4d	78 [–35.58]	133 [–3.66]	55	125 [4.02]	8 [1.26]	117	318
4e	80 [–36.05]	122 [–2.55]	42	115 [2.37]	34 [19.38]	71	326
4f	82 [–39.45]	97 [–1.12]	15	89 [0.55]	43 [15.08]	46	329

The phase transition temperatures and the associated enthalpies for **4a–f** are presented in Table I. During the DSC investigations, compounds **4a–f** showed

TABLE II. Transition temperatures (°C), and associated transition enthalpies (J g⁻¹) for compounds **5a–e**; abbreviations: Cr, crystalline; LC, liquid crystal; I, isotropic; t_{onset} the initial temperature at which the degradations processes begin

T / °C [ΔH / J g^{-1}]

Cmpd.	Heating						Cooling					t_{onset} °C
	Cr$_1$/Cr$_2$	Cr$_2$/Cr$_3$	Cr$_3$/LC$_1$	LC$_1$/LC$_2$	LC$_2$/I	Mesophase interval, °C	I/LC$_1$	LC$_1$/LC$_2$	LC$_2$/LC$_3$	LC$_3$/Cr	Mesophase interval, °C	
5a	33 [-21.5]	52 [-8.11]	91 [-37.24]	109 [-1.08]	115 [-0.27]	24	114 [0.49]	107 [1.75]	91 [0.19]	–	–	328
5b	50 [-24.0]	70 [-18.97]	87 [-0.11]	102 [-1.19]	109 [-0.41]	22	108 [0.74]	100 [1.15]	86 [0.18]	–	–	338
5c	–	78 [-27.56]	91 [-0.13]	102 [-1.38]	110 [-0.55]	19	109 [0.75]	100 [1.23]	90 [0.16]	–	–	342
5d	20 [-0.08]	41 [-0.12]	90 [-0.17]	99 [-1.17]	107 [-0.72]	17	106 [0.86]	97 [1.08]	90 [0.11]	18 [0.10]	88	330
5e	24 [-0.10]	45 [-0.24]	80 [-1.28]	85 [-0.97]	100 [-0.54]	20	99 [0.85]	78 [0.92]	41 [0.32]	22 [0.15]	77	328

only two transitions on both the heating and cooling cycles. For the first three compounds of this series, the crystallization temperature could not be determined either by DSC or polarized optical microscopy (POM) observations because the crystallization occurred very slowly. Generally, because of their high viscosity, all these samples crystallized very slowly at much lower temperatures than the Cr/Lc temperature transitions.

With the exception of compound **4f**, the stability range of the mesophases, on heating, is reasonably large in the case of the series of compounds **4a**–**f** (between 42 and 87 °C).

The DSC curves of compound **4e** (first heating and first cooling) are illustrated in Fig. 1, as examples. The POM investigations evidenced only the presence of smectic type mesophases. No typical cholesteric oily streaks textures could be observed.
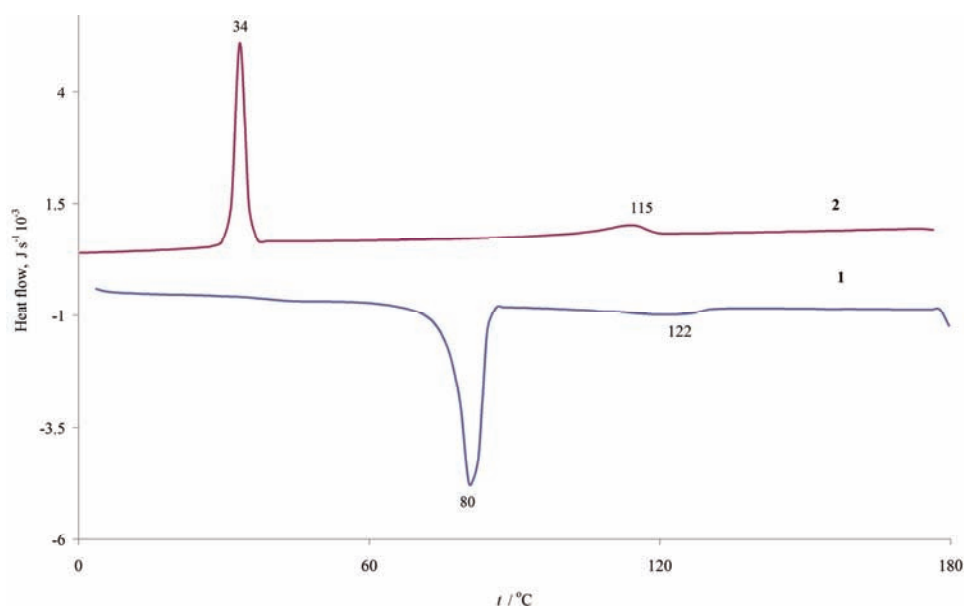
Fig. 1. DSC curves for compound **4e**: 1 – first heating, 2 – first cooling.

In the case of compound **4e**, polarized optical microscopy evidenced a smecticX texture between 80–122 °C during the heating process, (Figs. 2a and 2d). On cooling, smectic textures appeared again between 115–35 °C, (Figs. 2b and 2c).

The compounds of the **5a**–**e** series, obtained by esterification of cholesteryl 6-(3-hydroxyphenoxy)hexanoate with 4-{[4-(alkyloxy)benzoyl]oxy}benzoic acids presented enantiotropic behaviors with the existence of a stability range of mesophases of around 20 °C on heating (Table II). Compounds **5a**–**e** presented a rich polymorphism on heating with several crystalline/crystalline or liquid crystal/li-

quid crystal transitions. On cooling, only two liquid crystal/liquid crystal transitions could be seen for all compounds **5a**–**e** (Table II). As was the case for compounds **4a**–**f**, no typical cholesteric textures could be observed.

(a) (b) (c) (d)
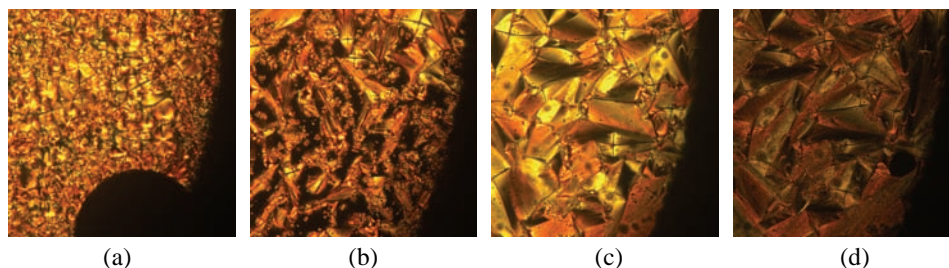
Fig. 2. Microphotographs of the mesophase textures observed for compound **4e**: a) first heating, 104 °C, b) first cooling, 111 °C, c) first cooling, 42 °C, d) second heating, 105 °C.

For the first three compounds of the series, no crystallization temperatures could be observed on the DSC curves on cooling, probably for similar reasons as was the case for compounds **4a**–**c**.

The DSC thermogram of compound **5e**, as a typical example for all the compounds of series **5a**–**e**, is presented in Fig. 3. On the second heating curve, the peaks at 24 and 45 °C corresponded to crystalline/crystalline transitions, while the peaks at 80, 82 and 100 °C corresponded to different smectic liquid crystalline transitions. On cooling, similar transitions at very similar temperatures could be observed on the DSC curves.

Fig. 3. DSC curves for compound **5e**: 1 – first heating, 2 – first cooling.

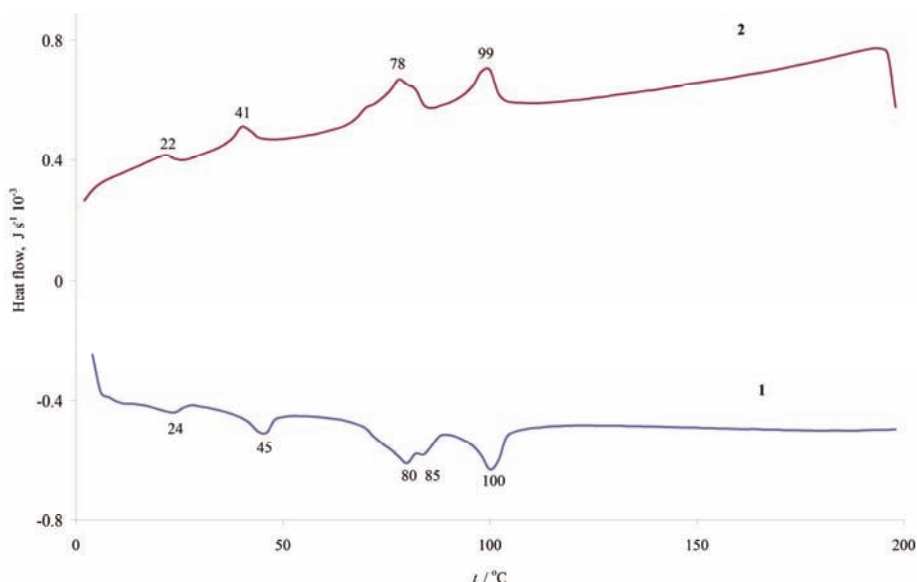Some microphotographs taken during the POM investigations for compound **5e** are presented in Fig. 4.
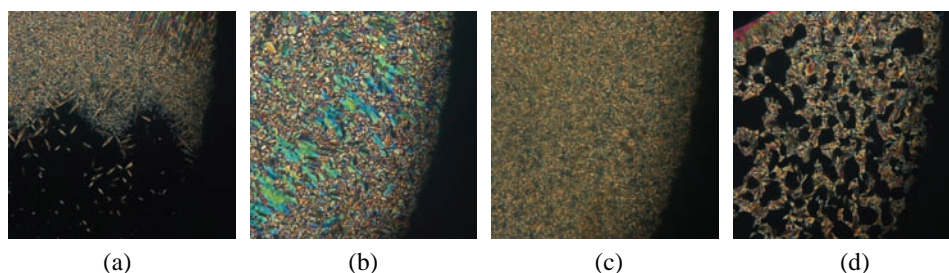

(a) (b) (c) (d)

Fig. 4. Microphotographs of the textures observed for compound **5e**: a) first cooling, 60 °C, b) first cooling, 27 °C, c) second heating, 84 °C, d) second heating, 98 °C.

On both the heating and cooling cycles, smectic type textures were evidenced (Fig. 4). On the first cooling, the smectic type textures appeared at around 100 °C and remained until crystallization (Figs. 4a and 4b) and on the second heating again the same type of mesophases was seen (Figs. 4c and 4d).

CONCLUSIONS

Two new series of bent core liquid crystals based on a resorcinol core and containing a cholesteryl moiety connected to the core *via* a pentamethylen flexible spacer have been synthesized and characterized. The second arm consists of two aromatic rings connected *via* azo or ester groups and containing an alkyloxy terminal chain.

The liquid crystalline properties were investigated by polarized optical microscopy in association with differential scanning calorimetry. All the synthesized compounds presented enantiotropic liquid crystalline properties, with smectic textures. For all synthesized compounds, due to the presence of the cholesteric moiety, both main liquid crystalline transitions (isotropization and isotropic to liquid crystal) are relatively low (between 89 and 146 °C). Due to the presence of the cholesteric moiety, some difficulties were encountered in evidencing the crystallization temperature on cooling, in both the POM and DSC experiments. The largest stability range of the mesophases was met in the case of the compounds **4a**–**f** (between 42 and 87 °C).

The t_{onset} values obtained from thermogravimetric studies evidenced a very good thermal stability for all compounds; the degradation processes beginning more than 150 °C higher than the isotropization temperatures.

SUPPLEMENTARY MATERIAL

Physical and spectral data for the prepared compounds are available electronically from http://www.shd.org.rs/JSCS/, or from the corresponding author on request.

ИЗВОД

НОВИ ТЕЧНИ КРИСТАЛИ КОЈИ САДРЖЕ ХОЛЕСТЕРИЛ-ГРУПУ

COSMIN-CONSTANTIN HUZUM, IRINA CARLESCU, GABRIELA LISA и DAN SCUTARU

Faculty of Chemical Engineering and Environmental Protection, Gheorghe Asachi Technical University of Iasi,71 D. Mangeron St., 700050 – Iasi, Romania

У овом раду приказана је синтеза и мезоморфно понашање две нове серије једи-њења течних кристала базираних на 1,3-дихидроксибензеновом језгру, која садрже холе-стерил 6-оксихексаноатно крило. Две серије су добијене естерификацијом холестерил--6-(3-хидроксифенокси)хексаноатног језгра са 4-{[4-(*n*-алкилокси)фенил]азо}бензоевим киселинама (*n*-алкил = *n*-хексил – *n*-додецил) или 4-{[4-(*n*-алкилокси)бензоил]окси} бензоевим киселинама (*n*-алкил = *n*-хексил – *n*-децил). Реакције естерификације су изведене преко одговарајућих ацил-хлорида или са DCC/DMAP системом. Све синтети-сана једињења су показивала енантиотропне особине течних кристала, са текстурама смектитног типа, приликом испитивања диференцијалном сканирајућом калориметри-јом и поларизованом оптичком микроскопијом. Изотропизација и прелаз из изотропне фазе ка фази течних кристала су биле и на релативно ниским температурама (између 89 и 146 °C). Једињења која садрже азо-ароматичну везујућу групу показују највећи опсег стабилности мезофаза (између 42 и 87 °C). Сва испитивана једињења су термално ста-билна у опсегу у којем постоје мезофазе.

(Примљено 10. августа, ревидирано 3. септембра 2012)

REFERENCES

1. R. Eelkema, B. L. Feringa, *Org. Biomol. Chem.* **4** (2006) 3729
2. A. Y. Bobrovsky, N. I. Boiko, V. P. Shibaev, *Polym. Sci.* **40** (1998) 232
3. P. M. Peter, *Nature* **391** (1998) 745
4. G. Shanker, C. V. Yelamaggad, *J. Phys. Chem.* **115** (2011) 10849
5. F. Renitzer, *Monatsh. Chem.* **9** (1888) 421
6. C. V. Yelamaggad, G. Shanker, U. S. Hiremath, S. K. Prasad, *J. Mater. Chem.* **18** (2008) 2927
7. J. W. Lee, Y. Park, J. Jin, *J. Mater. Chem.* **13** (2003) 1367
8. V. A. Mallia, N. Tamaoki, *Chem. Soc. Rev.* **33** (2004) 76
9. N. Tamaoki, Y. Aoki, M. Moriyama, M. Kidowaki, *Chem. Mater.* **15** (2003) 719
10. T. Ikeda, O. Tsutsumi, *Science* **268** (1995) 1873
11. S. K. Prasad, K. L. Sandhya, G. G. Nair, U. S. Hiremath, C. V. Yelamaggad, *J. Appl. Phys.* **92** (2005) 838
12. V. A. Mallia, N. Tamaoki, *J. Mater. Chem.* **13** (2003) 219
13. H. S. Kitzerow, C. Bahr, *Chirality in liquid crystals*, Springer, New York, USA, 2001, p. 65
14. H. S. Kitzerow, *Chem. Phys. Chem.* **7** (2006) 63
15. C. V. Yelamaggad, N. L. Bonde, A. S. Achalkumar, D. S. Rao, S. K. Prasad, K. Prajapati, *Chem. Mater.* **19** (2007) 2463

16. G. Shanker, C. V. Yelamaggad, *New J. Chem.* **36** (2012) 918
17. C. V. Yelamaggad, S. A. Nagamani, U. S. Hiremath, G. Nair, *Liq. Cryst.* **28** (2001) 1009
18. E. R. Cioanca, E. L. Epure, I. Carlescu, G. Lisa, D. Wilson, N. Hurduc, D. Scutaru, *Mol. Cryst. Liq. Cryst.* **51** (2011) 537
19. N. Gimeno, M. J. Clemente, J. L. Serrano, M. B. Ros, *New J. Chem.* **33** (2009) 2007
20. I. Dierking, *Textures of liquid crystals,* Wiley-VCH, Weinheim, Germany, 2003, p. 188
21. J. Svoboda, V. Novotna, V. Kozmik, M. Glogarova, W. Weissflog, S. Diele, G. Pelzl, *J. Mater. Chem.* **13** (2003) 2104
22. G. Lisa, E. R. Cioanca, N. Tudorachi, I. Carlescu, D. Scutaru, *Thermochim. Acta* **524** (2011) 179.

Journal of the Serbian Chemical Society

SUPPLEMENTARY MATERIAL TO
New cholesteryl-containing bent core liquid crystals

COSMIN-CONSTANTIN HUZUM, IRINA CARLESCU, GABRIELA LISA
and DAN SCUTARU*

Faculty of Chemical Engineering and Environmental Protection, Gheorghe Asachi Technical University of Iasi, 71 D. Mangeron St., 700050 – Iasi, Romania

J. Serb. Chem. Soc. 78 (5) (2013) 669–681

PHYSICAL AND SPECTRAL DATA FOR THE PREPARED COMPOUNDS

*Cholesteryl 6-(3-hydroxyphenoxy)hexanoate (**1**)*. Color: white; Yield: 67.22 % (2.8 g); m.p.: 101 °C; ^{1}H-NMR (400 MHz, CD$_3$COCD$_3$, δ / ppm): 8.24 (1H, *s*, –OH), 7.05 (1H, *m*, Ar-H), 6.42–6.38 (3H, *m*, Ar-H), 5.38 (1H, *d*, *J* = 4.2 Hz, cholesteric), 4.54 (1H, *m*, cholesteric), 3.93 (2H, *t*, *J* = 6.4 Hz, –OCH$_2$–), 2.32––0.73 (51H, complex signals, selected signals: 1.05 (6H, *s*, cholesteric), 0.87 (6H, *dd*, J_1 = 6.6 Hz, J_2 = 1.5 Hz, cholesteric), 0.73 (3H, *s*, cholesteric)); ^{13}C-NMR (101 MHz, CD$_3$COCD$_3$, δ / ppm): 173.05, 161.50, 159.53, 140.82, 130.71, 123.17, 108.54, 106.50, 102.78 (1C, ester, 2C, cholesteric, 6C, aromatic), 74.21 (cholesteric), 68.19 (–OCH$_2$–), 57.64, 57.12, 51.10, 43.17, 40.69, 40.33, 39.02 (7C, cholesteric) , 37.93, 37.43, 37.06, 36.71, 34.95, 32.77, 32.68, 29.80, 29.02 , 28.77, 28.64, 26.39, 25.60 , 25.01 , 24.65 , 23.19 , 22.95 , 21.83 , 19.76 , 19.25 , 12.34 (21C, cholesteric and aliphatic carbon atoms).

*3-{[6-(Cholesteryloxy)-6-oxohexyl]oxy}phenyl 4-{[4-(hexyloxy)phenyl]azo}-benzoate (**4a**)*. Color: orange; Yield: 52.37 % (0.167 g); Liquid crystal: 59 °C (Cr/CL), 146 °C (CL/I), 131 °C (I/CL); FT-IR (KBr, cm^{-1}): 1734 (>C=O, ester); ^{1}H-NMR (400 MHz, CDCl$_3$, δ / ppm): 8.32 (2H, *d*, *J* = 8.5 Hz, Ar-H), 7.96 (4H, *m*, Ar-H), 7.32 (1H, *m*, Ar-H), 7.02 (2H, *d*, *J* = 8.9 Hz, Ar-H), 6.83-6.80 (2H, *m*, Ar-H), 6.80 (1H, *d*, *J* = 2.0 Hz, Ar-H), 5.37 (1H, *d*, *J* = 4.2 Hz, cholesteric), 4.62 (1H, *m*, cholesteric), 4.06 (2H, *t*, *J* = 6.5 Hz, –OCH$_2$–), 3.98 (2H, *t*, *J* = 6.3 Hz, –OCH$_2$–), 2.32–0.67 (62H, complex signals, selected signals: 1.01 (6H, *s*, cholesteric), 0.87 (6H, *dd*, J_1 = 6.6 Hz, J_2=1.5 Hz, cholesteric), 0.67 (3H, *s*, cholesteric)); ^{13}C-NMR (101 MHz, CDCl$_3$, δ / ppm): 172.96, 164.58, 162.44, 160.01, 155.74, 151.83, 146.83, 139.63, 131.15, 130.43, 129.82, 125.27, 122.57, 122.48, 114.79, 113.68, 112.33, 108.17, (2C, ester, 2C, cholesteric, 14C, aromatic), 73.77

* Corresponding author. E-mail: dscutaru@ch.tuiasi.ro

(cholesteric), 68.42 (–OCH$_2$–), 67.84 (–OCH$_2$–), 56.64, 56.10, 49.98, 42.26, 39.68, 39.49, 38.13 (7C, cholesteric), 36.95, 36.54, 36.15, 35.76, 34.53, 31.86, 31.81, 31.54, 29.67, 29.11, 28.81, 28.19, 27.98, 27.79, 25.66, 25.57, 24.74, 24.24, 23.81, 22.57, 22.54, 20.99, 19.28, 18.68, 14.01, 11.82 (26C, cholesteric and aliphatic carbon atoms); MS (CHCl$_3$, *m/z*): 922.25 [M–1+Na]$^+$.

3-{[6-(Cholesteryloxy)-6-oxohexyl]oxy}phenyl 4-{[4-(heptyloxy)phenyl]-azo}benzoate (4b). Color: orange; Yield: 52.17 % (0.169 g); Liquid crystal: 83 °C (Cr/CL), 142 °C (CL/I), 118 °C (I/CL); FT-IR (KBr, cm^{-1}): 1734 (>C=O, ester); ^{1}H-NMR (400 MHz, CDCl$_3$, δ / ppm): 8.32 (2H, *d*, *J* = 8.5 Hz, Ar-H), 7.96 (4H, *m*, Ar-H), 7.32 (1H, *m*, Ar-H), 7.02 (2H, *d*, *J* = 8.9 Hz, Ar-H), 6.83––6.80 (2H, *m*, Ar-H), 6.80 (1H, *d*, *J* = 2.0 Hz, Ar-H), 5.37 (1H, *d*, *J* = 4.1 Hz, cholesteric), 4.62 (1H, *m*, cholesteric), 4.06 (2H, *t*, *J* = 6.6 Hz, –OCH$_2$–), 3.98 (2H, *t*, *J* = 6.3 Hz, –OCH$_2$–), 2.32–0.67 (64H, complex signals, selected signals: 1.01 (6H, *s*, cholesteric), 0.87 (6H, *dd*, *J$_1$* = 6.6 Hz, *J$_2$* = 1.5 Hz, cholesteric), 0.67 (3H, *s*, cholesteric)); ^{13}C-NMR (101 MHz, CDCl$_3$, δ / ppm): 172.99, 164.60, 162.46, 160.03, 155.77, 151.84, 146.85, 139.65, 131.17, 130.44, 129.84, 125.29, 122.59, 122.50, 114.80, 113.70, 112.35, 108.18 (2C, ester, 2C, cholesteric, 14C, Ar-H), 73.78 (cholesteric), 68.44 (–OCH$_2$–), 67.85 (–OCH$_2$–), 56.66, 56.11, 50.00, 42.28, 39.70, 39.50, 38.15 (7C, cholesteric), 36.97, 36.56, 36.17, 35.77, 34.54, 31.87, 31.83, 31.76, 29.69, 29.16, 29.04, 28.83, 28.21, 27.99, 27.81, 25.96, 25.58, 24.76, 24.26, 23.82, 22.81, 22.59, 22.56, 21.00, 19.30, 18.70, 14.08, 11.83 (27C, cholesteric and aliphatic carbon atoms); MS (CHCl$_3$, *m/z*): 936.42 [M–1+Na]$^+$.

3-{[6-(Cholesteryloxy)-6-oxohexyl]oxy}phenyl 4-{[4-(octyloxy)phenyl]azo}-benzoate (4c). Color: Orange; Yield: 49.55 % (0.164 g), Liquid crystal: 77 °C (Cr/CL), 133 °C (CL/I), 130 °C (I/CL); FT-IR (KBr, cm^{-1}): 1734 (>C=O, ester); ^{1}H-NMR (400 MHz, CDCl$_3$, δ / ppm): 8.32 (2H, *d*, *J* = 8.5 Hz, Ar-H), 7.96 (4H, *m*, Ar-H), 7.32 (1H, *m*, Ar-H), 7.02 (2H, *d*, *J* = 8.9 Hz Ar-H), 6.83–6.80 (2H, *m*, Ar-H), 6.79 (1H, *d*, *J* = 2.2 Hz, Ar-H), 5.37 (1H, *d*, *J* = 3.6 Hz, cholesteric), 4.62 (1H, *m*, cholesteric), 4.05 (2H, *t*, *J* = 6.9 Hz,–OCH$_2$–), 3.98 (2H, *t*, *J* = 6.4 Hz, –OCH$_2$–), 2.32–0.67 (66H, complex signals, selected signals: 1.01 (6H, *s*, cholesteric), 0.87 (6H, *dd*, *J$_1$* = 6.6 Hz, *J$_2$* = 1.5 Hz, cholesteric), 0.67 (3H, *s*, cholesteric)); ^{13}C-NMR (101 MHz, CDCl$_3$, δ / ppm): 172.98, 164.59, 162.46, 160.02, 155.76, 151.84, 146.84, 139.65, 131.17, 130.44, 129.83, 125.28, 122.58, 122.50, 114.80, 113.69, 112.34, 108.18 (2C, ester, 2C, cholesteric, 14C, Ar-H), 73.78 (cholesteric), 68.44 (–OCH$_2$–), 67.85 (–OCH$_2$–), 56.65, 56.11, 49.99, 42.27, 39.70, 39.49, 38.14 (7C, cholesteric), 36.96, 36.56, 36.16, 35.77, 34.54, 31.88, 31.82, 29.55, 29.37, 29.30, 29.15, 28.82, 28.20, 27.99, 27.80, 25.99, 25.58, 24.75, 24.25, 23.82, 22.80, 22.66, 22.55, 21.00, 19.29, 18.69, 14.10, 11.83 (28C, cholesteric and aliphatic carbon atoms); MS (CHCl$_3$, *m/z*): 950.29 [M–1+Na]$^+$.

3-{[6-(Cholesteryloxy)-6-oxohexyl]oxy}phenyl 4-{[4-(nonyloxy)phenyl]azo}-benzoate (4d). Color: orange; Yield: 50.72 % (0.169 g); Liquid crystal: 78 °C (Cr/CL), 133 °C (CL/I), 125 °C (I/CL); FT-IR (KBr, cm^{-1}): 1734 (>C=O, ester); ^{1}H-NMR (400 MHz, CDCl$_3$, δ / ppm): 8.32 (2H, *d*, *J* = 8.5 Hz, Ar-H), 7.96 (4H, *m*, Ar-H), 7.32 (1H, *m*, Ar-H), 7.02 (2H, *d*, *J* = 8.9 Hz, Ar-H), 6.83–6.80 (2H, *m*, Ar-H), 6.80 (1H, *d*, *J* = 2.0 Hz, Ar-H), 5.37 (1H, *d*, *J* = 4.1 Hz, cholesteric), 4.62 (1H, *m*, cholesteric), 4.07 (2H, *t*, *J* = 6.6 Hz , –OCH$_2$–), 3.98 (2H, *t*, *J* = 6.3 Hz, –OCH$_2$–), 2.32–0.67 (68H, complex signals, selected signals: 1.01 (6H, *s*, cholesteric), 0.87 (6H, *dd*, *J*$_1$ = 6.6 Hz, *J*$_2$ = 1.5 Hz, cholesteric), 0.67 (3H, *s*, cholesteric)); ^{13}C-NMR (101 MHz, CDCl$_3$, δ / ppm): 172.98, 164.59, 162.46, 160.02, 155.76, 151.84, 146.84, 139.65, 131.17, 130.44, 129.83, 125.28, 122.58, 122.50, 114.80, 113.69, 112.34, 108.18 (2C, ester, 2C, cholesteric, 14C, Ar-H), 73.78 (cholesteric), 68.44 (–OCH$_2$–), 67.85 (–OCH$_2$–), 56.65, 56.11, 49.99, 42.27, 39.70, 39.49, 38.14, (7C, cholesteric) 36.96, 36.56, 36.16, 35.77, 34.54, 31.88, 31.82, 29.55, 29.37, 29.30, 29.15, 28.82, 28.20, 27.99, 27.80, 25.99, 25.58, 24.75, 24.25, 23.82, 22.80, 22.66, 22.55, 21.00, 19.29, 18.69, 14.10, 11.83 (28C, cholesteric and aliphatic carbon atoms); MS (CHCl$_3$, *m/z*): 964.16 [M–1+Na]$^+$.

3-{[6-(Cholesteryloxy)-6-oxohexyl]oxy}phenyl 4-{[4-(decyloxy)phenyl]azo}-benzoate (4e). Yield: 51.45 % (0.174 g); Liquid crystal: 80 °C (Cr/CL), 122 °C (CL/I), 115 °C (I/CL), 8 °C (CL/Cr); FT-IR (KBr, cm^{-1}): 1734 (>C=O, ester); ^{1}H-NMR (400 MHz, CDCl$_3$, δ / ppm): 8.32 (2H, *d*, *J* = 8.6 Hz, Ar-H), 7.96 (4H, *m*, Ar-H), 7.31 (1H, *m*, Ar-H), 7.02 (2H, *d*, *J* = 9.0 Hz, Ar-H), 6.83– 6.80 (2H, *m*, Ar-H), 6.79 (1H, *d*, *J* = 2.0 Hz, Ar-H), 5.37 (1H, *d*, *J* = 4.0 Hz, cholesteric), 4.62 (1H, *m*, cholesteric), 4.06 (2H, *t*, *J* = 6.6 Hz, –OCH$_2$–), 3.98 (2H, *t*, *J* = 6.3 Hz, –OCH$_2$–), 2.32–0.67 (70H, complex signals, selected signals: 1.01 (6H, *s*, cholesteric), 0.87 (6H, *dd*, *J*$_1$ = 6.6 Hz, *J*$_2$ = 1.5 Hz, cholesteric), 0.67 (3H, *s*, cholesteric)); ^{13}C-NMR (101 MHz, CDCl$_3$, δ / ppm): 172.98, 164.59, 162.46, 160.02, 155.76, 151.84, 146.84, 139.65, 131.17, 130.44, 129.83, 125.28, 122.58, 122.50, 114.80, 113.69, 112.34, 108.18 (2C, ester, 2C, cholesteric, 14C, Ar-H), 73.78 (cholesteric), 68.44 (–OCH$_2$–), 67.85 (–OCH$_2$–), 56.65, 56.11, 49.99, 42.27, 39.70, 39.49, 38.14 (7C, cholesteric) 36.96, 36.56, 36.16, 35.77, 34.54, 31.88, 31.82, 29.55, 29.37, 29.30, 29.15, 28.82, 28.20, 27.99, 27.80, 25.99, 25.58, 24.75, 24.25, 23.82, 22.80, 22.66, 22.55, 21.00, 19.29, 18.69, 14.10, 11.83 (28C, cholesteric and aliphatic carbon atoms); MS (CHCl$_3$, *m/z*): 978.03 [M–1+Na]$^+$.

3-{[6-(Cholesteryloxy)-6-oxohexyl]oxy}phenyl 4-{[4-(dodecyloxy)phenyl]-azo}benzoate (4f). Color: orange; Yield: 51.25 % (0.178 g); Liquid crystal: 82 °C (Cr/CL), 97 °C (CL/I), 89 °C (I/CL), 34 °C (CL/Cr); FT-IR (KBr, cm^{-1}): 1734 (>C=O, ester); ^{1}H-NMR (400 MHz, CDCl$_3$, δ / ppm): 8.32 (2H, *d*, *J* = 8.6 Hz, Ar-H), 7.96 (4H, *m*, Ar-H), 7.32 (1H, *m*, Ar-H), 7.02 (2H, *d*, *J* = 9.0 Hz, Ar-H), 6.85–6.80 (2H, *m*, Ar-H), 6.79 (1H, *d*, *J* = 2.1 Hz, Ar-H), 5.37 (1H, *d*, *J* = 4.0 Hz, cholesteric), 4.62 (1H, *m*, cholesteric), 4.06 (2H, *t*, *J* = 6.6 Hz, –OCH$_2$–), 3.98

(2H, t, J = 6.3 Hz, –OCH$_2$–), 2.32–0.67 (74H, complex signals, selected signals: 1.01 (6H, s, cholesteric), 0.87 (6H, dd, J_1 = 6.6 Hz, J_2 = 1.5 Hz, cholesteric), 0.67 (3H, s, cholesteric)); ^{13}C-NMR (101 MHz, CDCl$_3$, δ / ppm): 173.00, 164.61, 162.48, 160.04, 155.77, 151.85, 146.85, 139.67, 131.18, 130.46, 129.85, 125.30, 122.60, 122.50, 114.82, 113.71, 112.36, 108.19 (2C, ester, 2C, cholesteric, 14C, Ar-H), 73.80 (cholesteric), 68.46 (–OCH$_2$–), 67.87 (–OCH$_2$–), 56.67, 56.12, 50.01, 42.29, 39.71, 39.51, 38.15 (7C, cholesteric), 36.98, 36.57, 36.17, 35.78, 34.55, 31.91, 31.88, 31.84, 29.65, 29.63, 29.59, 29.56, 29.37, 29.35, 29.16, 28.84, 28.21, 28.00, 27.81, 26.00, 25.59, 24.77, 24.27, 23.83, 22.81, 22.68, 22.56, 21.01, 19.30, 18.70, 14.11, 11.84 (32C, cholesteric and aliphatic carbon atoms); MS (CHCl$_3$, m/z): 1005.79 [M–1+Na]$^+$.

4-{[3-((6-(Cholesteryloxy)-6-oxohexyl)oxy)phenoxy]carbonyl}phenyl 4-(hexyloxy)benzoate (5a). Color: white; Yield: 53.78 % (0.168 g); Liquid crystal: 33 °C (Cr/Cr), 52 °C (Cr/Cr), 91 °C (Cr/CL), 109 °C(CL/CL), 115 °C (CL/I), 114 °C (I/CL), 107 °C (CL/CL), 91 °C (CL/CL); FT-IR (KBr, cm^{-1}): 1732.07 (>C=O, ester); ^{1}H-NMR (400 MHz, CDCl$_3$, δ / ppm): 8.27 (2H, d, J = 8.6 Hz, Ar-H), 8.15 (2H, d, J = 8.8 Hz, Ar-H), 7.37 (2H, d, J = 8.6 Hz, Ar-H), 7.31 (1H, m, Ar-H), 6.99 (2H, d, J = 8.8 Hz, Ar-H), 6.81 (2H, d, J = 8.3 Hz, Ar-H), 6.77 (1H, d, J = 2.0 Hz, Ar-H), 5.37 (1H, d, J = 4.3 Hz, cholesteric), 4.62 (1H, m, cholesteric), 4.05 (2H, t, J = 6.6 Hz, –OCH$_2$–), 3.97 (2H, t, J = 6.4 Hz, –OCH$_2$–), 2.32–0.67 (62H, complex signals, selected signals: 1.01 (6H, s, cholesteric), 0.87 (6H, dd, J_1 = 6.6 Hz, J_2 = 1.5 Hz, cholesteric), 0.67 (3H, s, cholesteric)); ^{13}C-NMR (101 MHz, CDCl$_3$, δ / ppm): 172.98, 164.34, 164.28, 163.80, 160.01, 155.33, 151.80, 139.66, 132.39, 131.76, 129.81, 126.90, 122.58, 122.05, 120.93, 114.39, 113.70, 112.33, 108.16 (3C, ester, 2C, cholesteric, 14C, Ar-H), 73.77 (cholesteric), 68.36 (–OCH$_2$–), 67.84 (–OCH$_2$–), 56.66, 56.11, 49.99, 42.28, 39.70, 39.49, 38.14 (7C, cholesteric), 36.97, 36.56, 36.16, 35.77, 34.54, 31.87, 31.82, 31.52, 29.03, 28.83, 28.21, 27.99, 27.79, 25.63, 25.58, 24.75, 24.26, 23.81, 22.80, 22.55, 21.00, 19.29, 18.69, 14.01, 11.83 (25C, cholesteric and aliphatic carbon atoms); MS (CHCl$_3$, m/z): 938.37 [M–1+Na]$^+$.

4-{[3-((6-(Cholesteryloxy)-6-oxohexyl)oxy)phenoxy]carbonyl}phenyl 4-(heptyloxy)benzoate (5b). Color: white; Yield: 55.28 % (0.175 g), Liquid crystal: 50 °C (Cr/Cr), 70 °C (Cr/Cr), 87 °C (Cr/CL), 102 °C (CL/CL), 109 °C (CL/I), 108 °C (I/CL), 100 °C (CL/CL), 86 °C (CL/CL); FT-IR (KBr, cm^{-1}): 1735.93 (>C=O, ester); ^{1}H-NMR (400 MHz, CDCl$_3$, δ / ppm): 8.27 (2H, d, J = 8.7 Hz, Ar-H), 8.16 (2H, d, J = 8.8 Hz, Ar-H), 7.37 (2H, d, J = 8.6 Hz, Ar-H), 7.31 (1H, m, Ar-H), 6.99 (2H, d, J = 8.8 Hz, Ar-H), 6.82 (2H, d, J = 8.3Hz, Ar-H), 6.77 (1H, d, J = 2.0 Hz, Ar-H), 5.37 (1H, d, J = 4.1 Hz, cholesteric), 4.62 (1H, m, cholesteric), 4.05 (2H, t, J = 6.6 Hz, –OCH$_2$–), 3.97 (2H, t, J = 6.4 Hz, –OCH$_2$–), 2.32–0.67 (64H, complex signals, selected signals: 1.01 (6H, s, cholesteric), 0.87 (6H, dd, J_1 = 6.6 Hz, J_2 = 1.5 Hz, cholesteric), 0.67 (3H, s, cholesteric)); ^{13}C-NMR

(101 MHz, CDCl$_3$, δ / ppm): 172.98, 164.34, 164.28, 163.80, 160.01, 155.33, 151.80, 139.65, 132.39, 131.76, 129.81, 126.89, 122.58, 122.05, 120.93, 114.39, 113.70, 112.32, 108.16 (3C, ester, 2C, cholesteric, 14C, Ar-H), 73.77 (cholesteric), 68.35 (–OCH$_2$–), 67.83 (–OCH$_2$–), 56.66, 56.11, 49.99, 42.28, 39.70, 39.49, 38.13 (7C, cholesteric), 36.97, 36.56, 36.16, 35.77, 34.53, 31.87, 31.82, 31.73, 29.07, 29.03, 28.83, 28.21, 27.98, 27.79, 25.92, 25.58, 24.75, 24.25, 23.81, 22.80, 22.58, 22.54, 21.00, 19.29, 18.69, 14.06, 11.83 (27C, cholesteric and aliphatic carbon atoms); MS (CHCl$_3$, *m/z*): 952.24 [M–1+Na]$^+$.

4-{[3-((6-(Cholesteryloxy)-6-oxohexyl)oxy)phenoxy]carbonyl}phenyl 4-(octyloxy)benzoate (5c). Color: white; Yield: 54.15 % (0.174 g), Liquid crystal: 78 °C (Cr/Cr), 91 °C (Cr/CL), 102 °C (CL/CL), 110 °C (CL/I), 109 °C (I/CL), 100 °C (CL/CL), 90 °C (CL/CL); FT-IR (KBr, cm^{-1}): 1734 (>C=O, ester); ^{1}H-NMR (400 MHz, CDCl$_3$, δ / ppm): 8.27 (2H, *d*, *J* = 8.7 Hz, Ar-H), 8.16 (2H, *d*, *J* = 8.8 Hz, Ar-H), 7.37 (2H, *d*, *J* = 8.7 Hz, Ar-H), 7.31 (1H, *m*, *J* = 8.2 Hz, Ar-H), 6.99 (2H, *d*, *J* = 8.9 Hz, Ar-H), 6.81 (2H, *d*, *J* = 8.7 Hz, Ar-H), 6.77 (1H, *d*, *J* = 2.0 Hz, Ar-H), 5.38 (1H, *d*, *J* = 4.3 Hz, cholesteric), 4.62 (1H, *m*, cholesteric), 4.05 (2H, *t*, *J* = 6.6 Hz, –OCH$_2$–), 3.97 (2H, *t*, *J* = 6.3 Hz, –OCH$_2$–), 2.32–0.67 (66H, complex signals, selected signals: 1.01 (6H, *s*, cholesteric), 0.87 (6H, *dd*, *J*$_1$ = 6.6 Hz, *J*$_2$ = 1.5 Hz, cholesteric), 0.67 (3H, *s*, cholesteric)); ^{13}C-NMR (101 MHz, CDCl$_3$, δ / ppm): 172.98, 164.34, 16.58, 163.80, 160.01, 155.33, 151.80, 139.66, 132.39, 131.76, 129.81, 126.90, 122.58, 122.05, 120.93, 114.39, 113.70, 112.32, 108.16 (3C, ester, 2C, cholesteric, 14C, Ar-H), 73.77 (cholesteric), 68.36 (–OCH$_2$–), 67.83 (–OCH$_2$–), 56.66, 56.11, 49.99, 42.28, 39.70, 39.49, 38.14 (7C, cholesteric), 36.97, 36.56, 36.16, 35.77, 34.54, 31.87 31.82, 31.78, 29.30, 29.20, 29.07, 28.84, 28.21, 27.99, 27.79, 25.96, 25.58, 24.75, 24.26, 23.81, 22.80, 22.63, 22.55, 21.00, 19.29, 18.69, 14.08, 11.83, (28C, cholesteric and aliphatic carbon atoms); MS (CHCl$_3$, *m/z*): 966.11 [M–1+Na]$^+$.

4-{[3-((6-(Cholesteryloxy)-6-oxohexyl)oxy)phenoxy]carbonyl}phenyl 4-(nonyloxy)benzoate (5d). Color: white; Yield: 49.89 % (0.163 g), Liquid crystal: 20 °C (Cr/Cr), 41 °C (Cr/Cr), 90 °C (Cr/CL), 99 °C (CL/CL), 107 °C (CL/I), 106 °C (I/CL), 97 °C (CL/CL), 90 °C (CL/CL) 18 °C (CL/Cr); FT-IR (KBr, cm^{-1}): 1735.93 (>C=O, ester); ^{1}H-NMR (400 MHz, CDCl$_3$, δ / ppm): 8.27 (2H, *d*, *J* = = 8.6 Hz, Ar-H), 8.15 (2H, *d*, *J* = 8.8 Hz, Ar-H), 7.37 (2H, *d*, *J* = 8.6 Hz, Ar-H), 7.31 (1H, *m*, *J* = 8.2 Hz, Ar-H), 6.99 (2H, *d*, *J* = 8.8 Hz, Ar-H), 6.81 (2H, *d*, *J* = = 8.1 Hz, Ar-H), 6.77 (1H, *d*, *J* = 2.0 Hz, Ar-H), 5.37 (1H, *d*, *J* = 4.4 Hz, cholesteric), 4.62 (1H, *m*, cholesteric), 4.05 (2H, *t*, *J* = 6.5 Hz, –OCH$_2$–), 3.97 (2H, *t*, *J* = 6.3 Hz, –OCH$_2$–), 2.32–0.67 (68H, complex signals, selected signals: 1.01 (6H, *s*, cholesteric), 0.87 (6H, *dd*, *J*$_1$ = 6.6 Hz, *J*$_2$ = 1.5 Hz, cholesteric), 0.67 (3H, *s*, cholesteric)); ^{13}C-NMR (101 MHz, CDCl$_3$, δ / ppm): 172.99, 164.36, 164.30, 163.81, 160.02, 155.34, 151.81, 139.67, 132.40, 131.77, 129.82, 126.90, 122.59, 122.06, 120.94, 114.40, 113.71, 112.34, 108.16 (3C, ester, 2C, chole-

steric, 14C, Ar-H), 73.78 (cholesteric), 68.37 (–OCH$_2$–), 67.84 (–OCH$_2$–), 56.67, 56.11, 50.00, 42.29, 39.71, 39.50, 38.14 (7C, cholesteric), 36.97, 36.57, 36.17, 35.78, 34.55, 31,88, 31,85, 29.50, 29.36, 29.23, 29.07, 28.84, 28.21, 28.00, 27.80, 25.96, 25.59, 24.76, 24.26, 23.82, 22.66, 22.55, 21.01, 19.30, 18.70, 14.10, 11.84 (27C, cholesteric and aliphatic carbon atoms); MS (CHCl$_3$, m/z): 980 [M–1+Na]$^+$.

4-{[3-((6-(Cholesteryloxy)-6-oxohexyl)oxy)phenoxy]carbonyl}phenyl 4-(decyloxy)benzoate (5e). Color: white product; Yield: 53,21 % (0.176 g), Liquid crystal: 24 °C (Cr/Cr), 45 °C (Cr/Cr), 80 °C (Cr/CL), 85 °C (CL/CL), 100 °C (CL/I), 99 °C (I/CL), 78 °C (CL/CL), 41 °C (CL/CL), 22 °C (CL/Cr); FT-IR (KBr, cm^{-1}): 1753.29, 1734, 1728 (>C=O, ester); ^{1}H-NMR (400 MHz, CDCl$_3$, δ / ppm): 8.27 (2H, *d*, *J* = 8.6 Hz, Ar-H), 8.15 (2H, *d*, *J* = 8.8 Hz, Ar-H), 7.36 (2H, *d*, *J* = 8.6 Hz, Ar-H), 7.31 (1H, *m*, Ar-H), 6.99 (2H, *d*, *J* = 8.8 Hz, Ar-H), 6.80 (2H, *d*, *J* = 8.3 Hz, Ar-H), 6.77 (1H, *d*, *J* = 2.0 Hz, Ar-H), 5.37 (1H, *d*, *J* = = 4.3 Hz, cholesteric), 4.62 (1H, *m*, cholesteric), 4.05 (2H, *t*, *J* = 6.5 Hz, –OCH$_2$–), 3.97 (2H, t, *J* = 6.3 Hz, –OCH$_2$–), 2.32–0.67 (70H, complex signals, selected signals: 1.01 (6H, *s*, cholesteric), 0.87 (6H, dd, J_1 = 6.6 Hz, J_2 = 1.5 Hz, cholesteric), 0.67 (3H, *s*, cholesteric)); ^{13}C-NMR (101 MHz, CDCl$_3$, δ / ppm): 173.00, 164.36, 164,30, 163.81, 160.02, 155.34, 151.81, 139.67, 132.40, 131.77, 129.83, 126.91, 122.59, 122.06, 120.94, 114.40, 113.71, 112.34, 108.17 (3C, ester, 2C, cholesteric, 14C, Ar-H), 73.79 (cholesteric), 68.37 (–OCH$_2$–), 67.85 (–OCH$_2$–), 56.67, 56.12, 50.00, 42.29, 39.71, 39.50, 38.14 (7C, cholesteric), 36.98, 36.57, 36.17, 35.78, 34.55, 31.88, 31.84, 29.54, 29,35, 29,30, 29.07, 28.85, 28.22, 28.00, 27.80, 25.97, 25.59, 24.76, 24.27, 23.82, 22.83, 22.67, 22.55, 21.01, 19.31, 18.70, 14.11, 11.84 (28C, cholesteric and aliphatic carbon atoms); MS (CHCl$_3$, m/z): 993.86 [M–1+Na]$^+$.

Ionic strength effect on the deprotonation of *para*-sulfonatocalix[4]arene

MOHAMMAD FARAJI[1]*, ALI FARAJTABAR[2] and FARROKH GHARIB[3]

¹Department of Chemistry, Islamic Azad University, Babol branch, Babol, Iran, ²Department of Chemistry, Islamic Azad University, Jouybar branch, Jouybar, Iran and ³Chemistry Department, Faculty of Sciences, Shahid Beheshti University, Tehran, Evin, Iran

Abstract: The deprotonation of *para*-sulfonatocalix[4]arene was studied by a combination of spectrophotometric and potentiometric methods at 25 °C. The ionic strength of the solutions was kept constant by sodium perchlorate as a background electrolyte at 0.10–4.0 mol dm⁻³. The spectral changes evidenced proton dissociation of only one hydroxyl group of calixarene in the studied pH range of 2–10. The pK_a values were calculated using the STAR program by multivariate curve resolution of the absorbance data. The results indicated that the acid–base behavior of *para*-sulfonatocalix[4]arene varied strongly with increasing ionic strength of the solution. The dependence of the deprotonation constant on ionic strength was explained by means of the Specific Ion Interaction Theory (SIT). The activity coefficients of the species were modeled using a modified SIT approach. The extracted specific ion interaction parameters were associated with the thermodynamic deprotonation constant of *para*-sulfonatocalix[4]arene.

Keywords: deprotonation; sulfonatocalix[4]arene; ionic strength; SIT.

INTRODUCTION

Calix[*n*]arenes are a class of macrocyclic receptors synthesized by the base-induced condensation of formaldehyde with *para*-alkylphenols. The parent structure of calix[*n*]arenes is assembled from several phenolic rings interconnected by methylene bridges, resulting in an electron-rich, hydrophobic cavity. This particular architecture and also the simple derivatization of calixarenes by modification at both the upper and lower rims makes them potential candidates in various fields, such as biological, analytical and supramolecular chemistry.[1–4] *para*-Sulfonatocalix[*n*]arenes, in which the upper rims are functionalized by SO₃⁻ groups, are a water-soluble type of calixarenes with diverse biochemical functions, including enzyme inhibition, antiviral, antibacterial and antithrombotic activities.[4–6]

681

Most of the beneficial effects of these cyclic oligomers arises from their ability as a suitable host molecule to interact with neutral and ionic species through hydrophobic, π–π, cation–π and hydrogen bonding interactions, especially by their lower rim hydroxyl groups.[2,7]

The chemistry of calixarenes is closely related to the nature of their hydroxyl groups at the lower rim. Hydroxyl groups play a major role in conformational flexibility, cavity size and selective binding behavior of calixarenes.[8–10] In addition, lower rim functionalization is one of the most common methodologies applied in the routine synthesis of numerous calixarene derivatives, which is followed by an initial dissociation of hydroxyl groups.[10] Therefore to gain profound insight into the nature of the phenolic hydroxyl groups of *para*-sulfonatocalix[*n*]arenes, an accurate thermodynamics analysis of their acid–base properties seemed necessary. However, the determination of the pK_a values of *para*-sulfonatocalix[*n*]arenes is accompanied by some limitations, such as the complication of proton dissociations and the interference of acidic sulfonato groups. As an initial attempt, the acid–base behavior of *para*-sulfonatocalix[4]arene (SC4), Fig. 1, was studied by Shinkai *et al.*[11] From this study, the first phenolic hydroxyl group of SC4 was found to be extremely acidic (pK_a < 1). Although later studies confirmed that the first deprotonation of SC4 occurs at relatively high acidic pH value, a much larger pK_a value was determined when the strong acid dissociation of sulfonic acid groups were considered in the calculation.[12–14]
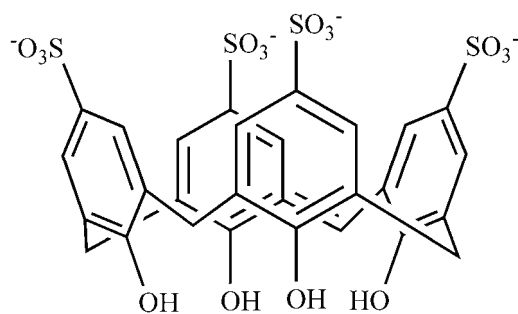
Fig. 1. Chemical structure of *para*-sulfonatocalix[4]arene.

Unfortunately, not only are there a few data for the pK_a value of SC4 in the literature, but also their determinations were performed under different experimental conditions (ionic media and ionic strength), which makes the prediction and modeling of the chemical speciation of SC4 in aqueous solutions difficult.[12–14] With the aim of extracting the thermodynamics standard state for pK_a, the deprotonation of SC4 was studied in the present work by a combination of spectroscopic and potentiometric methods over a wide range of ionic strengths, $0.10 \leq I$ (mol dm^{-3}) ≤ 4.0, in a NaClO$_4$ electrolyte at 25 °C. The dependence of deprotonation constant on ionic strength and ionic interaction parameters were evaluated by the Specific Ion Interaction Theory (SIT).[15–19]

EXPERIMENTAL

The *para*-sulfonatocalix[4]arene sodium salt was obtained from Sigma-Aldrich. NaOH and $HClO_4$ were purchased from Merck. Double-distilled water with a conductivity of 1.3 ± 0.1 $\mu\Omega^{-1}$ cm^{-1} was used. Sodium perchlorate was supplied by Merck as an analytical reagent grade material and was used without further purification.

Potentiometric measurements were performed in a double-walled thermostated reaction vessel at 25 °C. A model 3520 Jenway research potentiometer with a combined pH electrode was used for the *emf* measurement in the potentiometric titrations of the acidic mixture solutions.

The spectrophotometric measurements were performed on a Shimadzu 2100 UV–Vis spectrophotometer with a Pentium 4 computer and using thermostated matched 10 mm quartz cells. A flow measurement cell was used. A peristaltic pump allowed the circulation of the solution under study from the potentiometric cell to the spectrophotometric cell, so the absorbance and the *emf* of the solution could be measured simultaneously. To exclude carbon dioxide from the system, a stream of purified nitrogen was passed through a sodium hydroxide solution and then bubbled slowly through the reaction solution.

Prior to each spectrophotometric titration, the potentiometric cell was calibrated to obtain formal electrode potential $E°_{cell}$ at each ionic strength.[20-22] Approximately 20 mL of solutions of $HClO_4$ in constant ionic strength of $NaClO_4$ were titrated by the stepwise addition of NaOH solution. The equilibrium *emf* values of the cell were recorded after allowing potential stabilization. The $E°_{cell}$ values were computed from the Nernst equation knowing the exact concentration of H^+ in all titration points. In the next section, 25 mL of an acidic solution of SC4 was titrated with a sodium hydroxide solution (0.1 mol dm^{-3}). The absorbance data were recorded in the interval of 200–400 nm after reading the *emf* values of the potentiometric cell. Then spectroscopic titration data were introduced into the STAR program[23] to calculate the pK_a values of SC4.

RESULTS AND DISCUSSION

Calibration of potentiometric cell for each ionic strength

According to the Nernst equation, the potential of a potentiometric cell equipped by a glass electrode can be presented as:

$$E_{cell} = E°_{cell} + k\log [H^+] + k\log \gamma_{H+} + E_{LJ} \qquad (1)$$

where E_{LJ} is the liquid junction potential, $k = 2.303RT/F$ in which R, T and F have their usual meaning and γ_{H+} is the activity coefficient of hydrogen ion. As the ionic strength of the solution was kept constant for each experiment, the activity coefficient of hydrogen ion was also constant. The non-ideality of solutions is then included in k_a (the specific constant of the potentiometric cell in acidic region), and thus:

$$E_{cell} = k_a + k \log [H^+] \qquad (2)$$

with k_a being $E°_{cell} + k \log \gamma_{H+} + E_{LJ}$. The hydrogen ion concentration can be easily calculated by:

$$[H^+] = (M_H V_0 - M_{OH} V_1) / (V_0 + V_1) \qquad (3)$$

where M_H and M_{OH} are the molarities of acid and base, respectively, and V_0 and V_1 are the initial volume of acid and the added volume of sodium hydroxide solution, respectively. The k_a values were calculated from measured *emf* and known concentration of solvated proton in every titration point by linear regression analysis. For each experiment at constant ionic strength, the slopes obtained from least squares analysis were close to the theoretical Nernst value (59.167 mV at 25 °C) with correlation coefficients of nearly $r^2 = 0.99$. Accordingly, the pH values could be properly measured at each constant ionic strength by:

$$p_cH = (k_a - E_{cell}) / k \qquad (4)$$

Computing the protonation constants

Typical spectral changes of SC4 at a constant ionic strength of 3 mol dm^{-3} NaClO$_4$ are shown in Fig. 2.
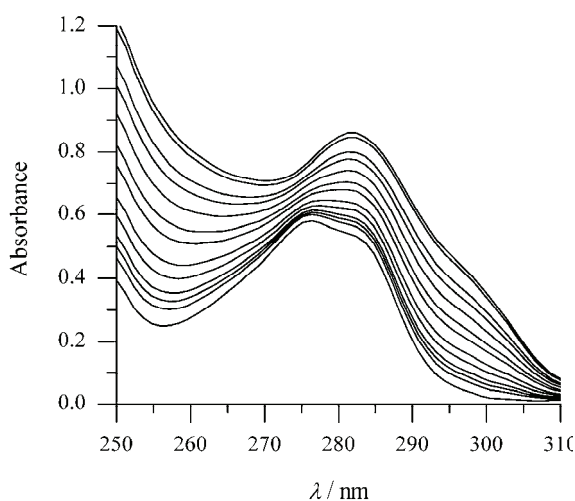
Fig. 2. Spectral change of *para*-sulfonatocalix[4]arene (1.45×10^{-4} mol dm^{-3}) with increasing pH at an ionic strength of 3 mol dm^{-3} NaClO$_4$.

To analyze mathematically the deprotonation equilibria, the absorbance data gathered from solutions of different pH values were used to construct a matrix **R** of size $m\times n$ where m is the number of different pH values in which absorbance was determined in n wavelengths at one nm intervals. According to the Beer law, a least squares analysis was performed in STAR program environment to decompose the data matrix **R** into a matrix of pure concentration, *C*, and a matrix of pure spectral profiles, **S**, with the optimal residual error matrix **E**.

$$\mathbf{R} = \mathbf{CS} + \mathbf{E} \qquad (5)$$

In iterative cycles, those matrices **C** and **S** were determined which best represent the original matrix **R**. The matrix of pure concentration profiles is related to protonation constant and total concentration of the compounds. Under suitable constraints, the nonlinear least-squares fitting continues until best set of

parameters (pK_a and molar absorptivities of the species) that result in a minimum of **E** is found.

The optimal fitting between theoretical and experimental absorbance data was achieved when only one of four possible deprotonation equilibria of SC4 was considered in the calculation. Therefore, the gradual spectral shift of SC4 to longer wavelength in the studied pH range is attributed to the first deprotonation of its phenolic hydroxyl groups that can be represented by:

$$H_4L^{4-} \rightleftharpoons H^+ + H_3L^{5-} \tag{6}$$

It seems that further proton dissociation may be observed at pH > 11. This explanation is in good qualitative agreement with previous studies by other groups.[12–14] The pK_a values of SC4 calculated by the STAR program in different ionic strengths are reported in Table I in the molar and molal concentration scale.

Ionic strength effect

According to Eq. (6), the first deprotonation constant of SC4 can be given by:

$$K_a^T = \frac{[H^+][H_3L^{5-}]}{[H_4L^{4-}]} \frac{\gamma_{H^+} \gamma_{H_3L^{5-}}}{\gamma_{H_4L^{4-}}} = K_a \frac{\gamma_{H^+} \gamma_{H_3L^{5-}}}{\gamma_{H_4L^{4-}}} \tag{7}$$

where γ_i is activity coefficient of species i; K_a^T represents thermodynamic deprotonation constant of SC4, and K_a stands for stoichiometric constant determined at each ionic strength. By taking the negative logarithm on Eq. (7):

$$pK_a = pK_a^T + \log\gamma_{H^+} + \log\gamma_{H_3L^{5-}} - \log\gamma_{H_4L^{4-}} \tag{8}$$

The dependence of the pK_a values on ionic strength may be analyzed by considering the well-known Specific Ion Interaction Theory (SIT).[15–19] In the original SIT model, the activity coefficient of ion i with charge z_i in a solution of ionic strength I (on the molal scale) at 25 °C can be expressed by the equation:

$$\log\gamma_i = -z_i^2 \frac{0.51\sqrt{I}}{1+1.5\sqrt{I}} + \sum_j \varepsilon_{ij} m_i \tag{9}$$

The ion interaction coefficient, ε_{ij}, usually called the SIT parameter, interprets the specific short-range interactions of ion i with ion j in its molal concentration m_j. The SIT model assumes that interaction coefficient is zero for two electrically like sign ions or neutral species. Although SIT parameters are considered to be approximately constant for some ionic media in the range $0.50 \leq I$ (mol kg^{-1}) ≤ 3.50, literature data indicate that they are function of I at lower and higher ionic strengths.[24] An expertise group in Italy modified the SIT model and introduced the concentration dependency of ε by the term:[25,26]

$$\varepsilon = \varepsilon_\infty + \frac{\varepsilon_0 - \varepsilon_\infty}{1 + I} \qquad (10)$$

By considering the modified SIT model for the calculation of activity coefficients of species, Eq. (8) can be reformulated as follows:

$$pK_a = pK_a^T - z * \frac{0.51\sqrt{I}}{1 + \sqrt{I}} + \Delta\varepsilon I \qquad (11)$$

where

$$z* = \sum(\text{charges})^2_{\text{products}} - \sum(\text{charges})^2_{\text{reactants}} \qquad (12)$$

$$\Delta\varepsilon = \varepsilon_{H_3L^{5-},Na^+} + \varepsilon_{H^+,ClO_4^-} - \varepsilon_{H_4L^{4-},Na^+} \qquad (13)$$

It should be noted that the pK_a and I values are in the molal concentration scale; in addition, all SIT parameters were defined concentration-dependent by the use of Eq. (10).

The experimental pK_a values from Table I were fitted into Eq. (11) as a function of ionic strength by least squares regression analysis. The results were $pK_a^T = 4.13 \pm 0.05$, $\Delta\varepsilon_0 = 1.79 \pm 0.13$ and $\Delta\varepsilon_\infty = 0.20 \pm 0.02$. The goodness of fit of the SIT model was judged by the excellent square correlation coefficient $R^2 = 0.97$, associated with low values of the standard deviation obtained for each of regression coefficients. This is illustrated better in Fig. 3, where the experimental pK_a values together with modeled values from SIT approach, Eq. (11), are depicted as a function of the square root of the molal ionic strength.

TABLE I. The pK_a values of SC4 in different ionic strength of NaClO$_4$ at 25 °C

I		pK_a	
mol kg^{-1}	mol kg^{-1}	mol dm^{-3}	mol kg^{-1}
0.10	0.10	3.24 ± 0.02	3.24
0.25	0.25	3.05 ± 0.01	3.05
0.50	0.51	2.93 ± 0.03	2.92
0.75	0.78	3.01 ± 0.01	2.99
1.00	1.05	3.14 ± 0.02	3.12
1.50	1.62	3.26 ± 0.05	3.23
2.00	2.21	3.39 ± 0.02	3.35
3.00	3.50	3.65 ± 0.02	3.58
4.00	4.95	3.90 ± 0.04	3.81

CONCLUSIONS

The acid–base properties of SC4 were investigated at 25 °C by an accurate spectroscopic method over a wide range of ionic strengths, supplied by sodium perchlorate. Spectral analysis indicates that only one of the four hydroxyl groups of SC4 dissociates in pH range 2–10. The pK_a values assigned for first depro-
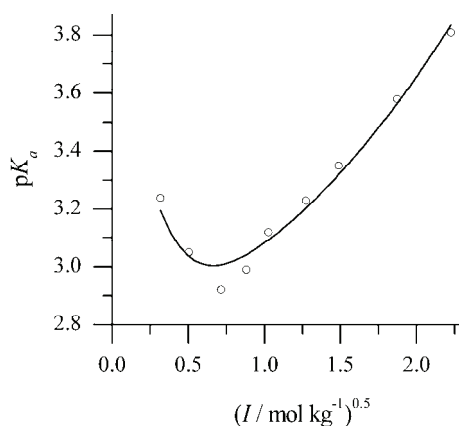
Fig. 3. pK_a values of *para*-sulfonatocalix-[4]arene *vs*. the square root of the ionic strength of the solution. Symbols refer to experimental data, while the solid line represents the value calculated according to the SIT model.

tonation equilibrium were calculated by multivariate curve fitting implemented in the STAR program. The results showed that, as a regular trend, the pK_a of SC4 first decreased sharply to its minimum value at an ionic strength of around 0.5 mol kg^{-1} and then increased in a relatively linear manner. The SIT theory was applied successfully to describe the ionic strength dependency of the pK_a values. The thermodynamic deprotonation constant at infinite ionic strength was calculated together with the overall specific ion interaction coefficients.

ИЗВОД

УТИЦАЈ ЈОНСКЕ ЈАЧИНЕ НА ДЕПРОТОНАЦИЈУ
para-СУЛФОНАТОКАЛИКС[4]АРЕНА

MOHAMMAD FARAJI[1], ALI FARAJTABAR[2] и FARROKH GHARIB[3]

[1] *Department of Chemistry, Islamic Azad University, Babol branch, Babol, Iran,* [2] *Department of Chemistry, Islamic Azad University, Jouybar branch, Jouybar, Iran* и [3] *Chemistry Department, Faculty of Sciences, Shahid Beheshti University, Tehran, Evin, Iran*

Депротонација *para*-сулфонатокаликс[4]арена је проучавана комбиновањем спектрофотометријских и потенциометријских метода на 25 °C. Јонска јачина раствора је одржавана константном помоћу натријум-перхлората на 0,10 до 4,0 mol dm^{-3}. Спектралне промене показују да долази до дисоцијације протона са само једне хидроксилне групе каликсарена у испитиваном опсегу pH од 2–10. pK_a вредности су израчунате коришћењем STAR софтвера за мултиваријантну анализу апсорпционих података. Резултати указују да кисело–базно понашање *para*-сулфонатокаликс[4]арена јако варира са порастом јонске јачине раствора. Зависност депротонационих константи од јонске јачине је објашњена коришћењем теорије специфичних јонских интеракција (SIT). Коефицијенти активности испитиваних врста су моделовани модификованим SIT приступом. Параметри специфичне јонске интеракције су добијени са термодинамичком депротонационом константом за *para*-сулфонатокаликс[4]арен.

REFERENCES

1. Z. Asfari, V. Bohmer, J. Harrowfield, J. Vicens, M. Saadioui, *Calixarenes 2001*, Kluwer Academic Pub., Dordrecht, 2001
2. A. F. D. de Namor, R. M. Cleverley, M. L. Zapata Ormachea, *Chem. Rev*. **98** (1998) 2495
3. E. Makrlik, J. Budka, P. Vanura, P. Selucky, *J. Serb. Chem. Soc*. **73** (2008) 1181
4. F. Perret, A. N. Lazar, A. W. Coleman, *Chem. Commun*. (2006) 2425
5. E. Da Silva, D. Ficheux, A. W. Coleman, *J. Inclusion Phenom. Macrocyclic Chem.* **52** (2005) 201
6. G. Droogmans, C. Maertens, J. Prenen, B. Nilius, *Br. J. Pharmacol*. **128** (1999) 35
7. J. Cui, V. D. Uzunova, D. S. Guo, K. Wang, W. M. Nau, Y. Liu, *Eur. J. Org. Chem*. (2010) 1704
8. L. Wang, X. F. Shi, Z. L. Zhu, *Spectrochim. Acta, A* **67** (2007) 789
9. E. B. Brouwer, K. A. Udachin, G. D. Enright, J. A. Ripmeester, *Chem. Commun*. (2000) 1905
10. C. D. Gutsche, *Calixarenes Revisited*, in *Monographs in Supramolecular Chemistry*, J. F. Stoddart, Ed., The Royal Society of Chemistry, Cambridge, U.K., 1998
11. S. Shinkai, K. Araki, H. Koreoshi, T. Tsubaki, O. Manabe, *Chem. Lett*. (1986) 1351
12. I. Yoshida, N. Yamato, F. Sagara, D. lshii, K. Ueno, S. Shinkai, *Bull. Chem. Soc. Jpn*. **65** (1992) 1012
13. G. Arena, R. Cali, G. O. Lombardo, E. Rizzarelli, D. Sciotto, R. Ungaro, A. Casnati, *Supramol. Chem*. **1** (1992) 19
14. H. Matsumiya, Y. Terazono, N. Iki, S. Miyano, *J. Chem. Soc., Perkin Trans. 2* (2002) 1166
15. J. N. Bronsted, *J. Am. Chem. Soc*. **44** (1922) 877
16. E. A. Guggenheim, J. C. Turgeon, *Trans. Faraday Soc*. **51** (1955) 747
17. C. Bretti, C. De Stefano, C. Foti, S. Sammartano, G. Vianelli, *J. Chem. Thermodyn*. **44** (2012) 154
18. I. Grenhe, J. Fuger, R. J. M. Konings, R. J. Lemire, A. B. Muller, C. Nguyen-Trung, H. Wanner, *Chemical Thermodynamics of Uranium*, Elsevier Science Publishers, Amsterdam, The Netherlands, 1992
19. F. Gharib, M. Jabbari, A. Farajtabar, *J. Mol. Liq*. **144** (2009) 5
20. F. Gharib, A. Farajtabar, *J. Mol. Liq*. **135** (2007) 27
21. G. Gran, *Acta Chem. Scand*. **4** (1950) 559
22. G. Gran, *Analyst* **77** (1952) 661
23. M. Faraji, A. Farajtabar, F. Gharib, H. Ghasemnejad-Borsa, *J. Serb. Chem. Soc*. **76** (2011) 1455
24. J. L. Beltran, R. Codony, M. D. Prat, *Anal. Chim. Acta* **276** (1993) 441
25. K. S. Pitzer, *Activity Coefficients in Electrolyte Solutions*, 2nd ed., CRC Press, Boca Raton, FL, 1991
26. C. De Stefano, D. Milea, A. Pettignano, S. Sammartano, *Biophys. Chem*. **121** (2006) 121
27. C. Bretti, C. Foti, N. Porcino, S. Sammartano, *J. Solution Chem*. **35** (2006) 1401.

Ni–MoO2 composite cathodes for hydrogen evolution in alkaline solution. Effect of aging of the electrolyte for their electrodeposition

VLADIMIR D. JOVIĆ[1*#], UROŠ Č. LAČNJEVAC[1#], BORKA M. JOVIĆ[1#],
LJILJANA M. GAJIĆ-KRSTAJIĆ[2#] and NEDELJKO V. KRSTAJIĆ[3]

[1]*Institute for Multidisciplinary Research, University of Belgrade, 11030 Belgrade, P. O. Box 33, Serbia,* [2]*Institute of Technical Sciences SASA, Knez Mihajlova 35, 11000 Belgrade, Serbia and* [3]*Faculty of Technology and Metallurgy, University of Belgrade, 11000 Belgrade, Karnegijeva 4, Serbia*

Abstract: In this work, the effect of aging of the electrolyte in the electrodeposition of Ni–MoO2 composite coatings on their morphology (scanning electron microscopy), chemical composition (energy-dispersive X-ray spectroscopy), polarization characteristics and "service life", tested for the hydrogen evolution reaction (HER) in 32 mass % NaOH at 90 °C, was investigated. Polarization characteristics and results of the "service life" test of Ni–MoO2 composite coatings obtained after different aging periods of the electrolyte for deposition (suspension of MoO2 powder particles in a solution containing 2 M NH4Cl + + 0.2 M NiCl2) were compared with that recorded for the commercial De Nora's Ni+RuO2 cathode coating (DN). It was shown that aging of the electrolyte did not influence the morphology and chemical composition of Ni–MoO2 composite coatings electrodeposited under conditions simulating their industrial production, while the polarization characteristics for the HER were influenced. The best coating, obtained after 180 days of electrolyte aging, showed a completely different (layered) structure of the deposit and significantly better performance than the commercial DN electrode during the "service life" test.

Keywords: Ni–MoO2 composite coating; hydrogen evolution; "service life" test.

INTRODUCTION

In the process of chlor–alkali electrolysis for chlorine production in the membrane cells,[1–3] an ion-exchange membrane separates the anode and the cathode compartments and gaseous hydrogen is produced in the cathode compartment from 30–32 mass % caustic soda solution at a typical operating tempe-

---

rature of 90 °C. The efficiency of the cathodes is an important issue in this process, since the overvoltage for the hydrogen evolution reaction (HER) in the cathode compartment contributes significantly to the overall power consumption.[3] The efficiency of the cathodes is the result of a combination of certain activities and stability at the high current densities (3–6 kA m^{-2}) normally used in technological applications. The main reason for the loss of activity and stability of the cathodes during long-term operation is the so-called "polarity inversion" of the electrodes, which occurs during replacement of old electrodes of an electrolyzer with new ones in the zero–gap cells. During this operation, the anodes and cathodes are short-circuited, causing a reverse current flow that may damage the cathodes and negatively affect their activity for the HER.[4] Manufacturers can predict how often in a certain period such an operation should be performed and accordingly designed an appropriate accelerated "service life" test for cathodes.[5,6]

As explained in previous papers,[6–8] Ni–MoO$_2$ composite coatings could be electrodeposited from a suspension of MoO$_2$ powder particles in an electrolyte containing 2M NH$_4$Cl + 0.2 M NiCl$_2$ and their overvoltage for the HER could be lower than that on a commercial De Nora's Ni+RuO$_2$ cathode obtained under similar conditions of electrolyte circulation and mixing by bubbling gas through the pipes placed on the bottom of the electrolyzer tank.[7] As was shown,[7] the optimal content of MoO$_2$ powder in the electrolyte was 3 g dm^{-3}, while the optimal deposition current density was –0.3 A cm^{-2}. To obtain good quality coating with low overvoltage for the HER, it was necessary to perform the electrodeposition after at least 24 h of conditioning of the prepared suspension, since the suspension needed a certain period to stabilize.[7]

In this work the effect of aging of the electrolyte for electrodeposition of Ni–MoO$_2$ composite coatings on their morphology, chemical composition, polarization characteristics and "service life" test performance for the HER was investigated and the obtained results were compared with that recorded for the commercial De Nora Ni+RuO$_2$ cathode coating (DN).

EXPERIMENTAL

HER Investigations

All experiments were performed with extra pure UV water (Smart2PureUV, TKA) and p.a. chemicals in a three compartment electrochemical cell with two Pt mesh counter electrodes placed parallel (in separate compartments) to the working electrode and a saturated calomel electrode (SCE), connected to the working electrode (in the central compartment) by means of a Luggin capillary, as the reference electrode,.

a) Polarization curve measurements. The electrodes were first submitted to hydrogen evolution at a constant current density of j = –0.3 A cm^{-2} for 0.5 h in 32 mass % NaOH at 90 °C and after such pre-electrolysis, the polarization curves were recorded using a potentiostat Reference 600 and PHE 200 or DC 105 Software (Gamry Instruments). The starting potential was –1.35 V and potential was changed in steps of 0.01 V towards less negative values, up to

the open circuit potential. At each potential, the current response was recorded for 500 s and the value recorded at the end was used to produce the polarization curve. Electrochemical impedance spectroscopy (EIS) measurements were performed at certain potentials in the frequency range from 30 kHz to 1 Hz (*ac* amplitude 0.01 V, EIS 300 Software) and the ohmic resistance (R_Ω) was determined from the high–frequency intercept on the Z' axis (the value of R_Ω was constant). Each applied potential was corrected for the IR_Ω drop and the corresponding polarization curves were plotted.

b) "Service life" test. The experiments were performed in the following way: the electrode was kept at $j = -0.3$ A cm^{-2} for 0.5 h and the corresponding potential response was recorded. Subsequently, the electrode was cycled (5 cycles) in the potential range from –1.25 V to 0.5 V at a sweep rate of 0.05 V s^{-1}. In the next step the electrode was again kept at $j = -0.3$ A cm^{-2} for 500 s and the corresponding potential response was recorded. This procedure was repeated 5 times, until the number of cycles reached 25. The potential response measured at $j = -0.3$ A cm^{-2} for 500 s was corrected for IR_Ω drop using the value of ohmic resistance (R_Ω) obtained from the EIS measurements. For this test the Ni–MoO$_2$ coatings (deposited onto Ni 40 mesh) with the best polarization characteristics were used (sample 1 and 5C) and compared with that recorded for the commercial DN electrode under the same conditions (commercial De Nora Ni+RuO$_2$ coating was originally deposited onto Ni 40 mesh).

Electrodeposition of the Ni–MoO$_2$ composite coatings

The MoO$_2$ powder was synthesized by a rheological phase reaction route.[7,9] All samples were deposited onto Ni 40 mesh from a suspension of MoO$_2$ powder particles (3 g dm^{-3}) in an electrolyte containing 2 M NH$_4$Cl + 0.2 M NiCl$_2$ (pH 3.8) in a pilot plant cell for the deposition of approximately 20 dm^{-3} (Fig. 1). The electrolyte was circulated with a pump, while the flow rate (20 dm^3 min^{-1}) was measured with a flow meter. Additional mixing of the electrolyte was provided by an airflow of 10 dm^3 min^{-1} through two pipes with small openings facing the bottom of the cell in order to remove eventually precipitated molybdenum oxide particles from the bottom of the cell and force the particles to float and circulate with the electrolyte. The temperature of the electrolyte was kept constant by a thermocouple, heater and control unit (as shown in Fig. 1a). The 40-mesh Ni cathode (dimensions 5×6 cm^2), connected to a Ni holder (frame, Figs. 1b and 1c), was placed between two Ni anode plates (18×22 cm^2). A home made power supply, with the ripple smaller than 1 %, was used for applying the necessary current/voltage.[7] In order to examine the influence of electrolyte aging on the morphology, chemical composition and electrochemical properties of the cathodes, samples were deposited from the same electrolyte after 1, 10, 30, 90 and 180 days. Between use, the electrolyte was cycled and mixed every day for at least 1 h.

All Ni 40 mesh substrates were etched only shortly in a 1:3 mixture of H$_2$O:HNO$_3$ and washed with distilled water before the deposition of the Ni–MoO$_2$ composite coatings.

SEM and EDS analysis of the Ni–MoO$_2$ composite coatings

The appearance of coated surfaces and the cross-sections of the coatings were investigated by scanning electron microscope (SEM) Tescan, VEGA TS 5130 MM equipped with an energy dispersive X–ray spectroscopy (EDS), INCAPentaFET–x3, Oxford Instruments.

Particle size analysis of the suspension containing MoO$_2$ powder

The average size of MoO$_2$ powder particles was determined with Brookhaven Instruments light-scattering system equipped with a BI-200SM goniometer, a BI-9000AT correlator, a temperature controller and a Coherent INNOVA 70C argon-ion laser. Dynamic light scattering measurements were performed using 135 mW laser excitation at 514.5 nm at a 90° detection angle.
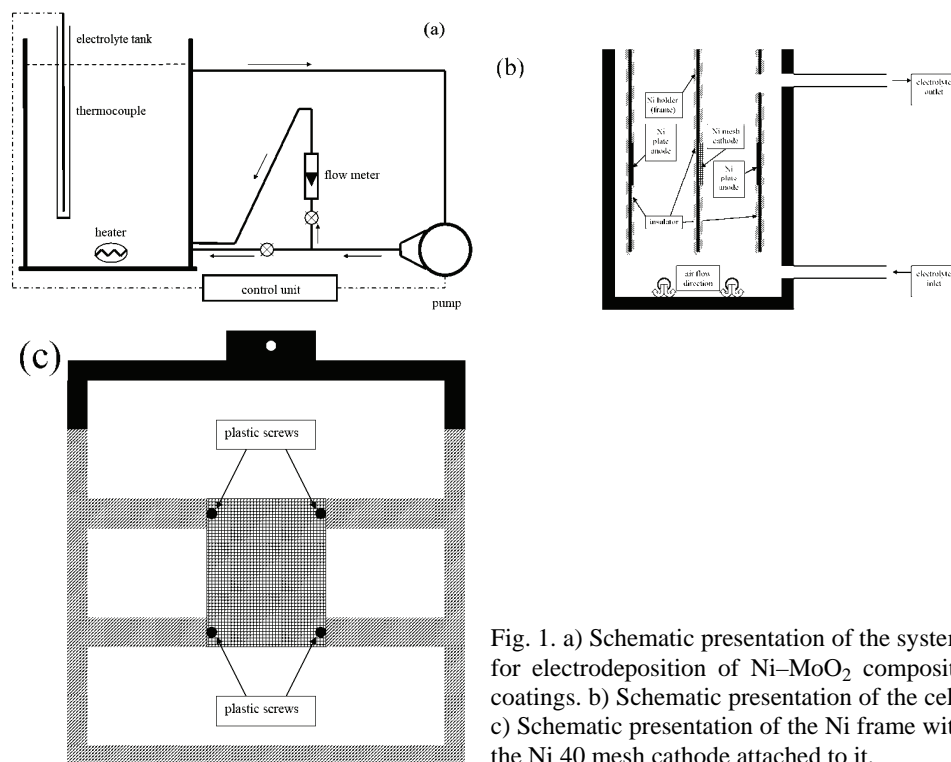
Fig. 1. a) Schematic presentation of the system for electrodeposition of Ni–MoO$_2$ composite coatings. b) Schematic presentation of the cell. c) Schematic presentation of the Ni frame with the Ni 40 mesh cathode attached to it.

RESULTS AND DISCUSSION

Polarization curves for the HER onto Ni–MoO$_2$ electrodes

As shown in a previous paper,[7] the best polarization characteristics were obtained for the sample deposited at –0.3 A cm^{-2} (sample 1). The polarization curves for the HER onto Ni–MoO$_2$ electrodes obtained after different aging periods (samples 1, 2, 3, 4, 5A, 5B and 5C, see Table I) recorded in 32 mass % NaOH at 90 °C are presented in Fig. 2. All polarization curves are characterized with two slopes: curves 1–3 with –0.031 V dec^{-1} in the range of current densities lower than 0.1 A cm^{-2} and –0.13 V dec^{-1} in the range of current densities higher than 0.1 A cm^{-2}; curve 4 with – 0.038 V dec^{-1} in the range of current densities lower than 0.1 A cm^{-2} and –0.14 V dec^{-1} in the range of current densities higher than 0.1 A cm^{-2} and sample 5A with –0.058 V dec^{-1} in the range of current densities lower than 0.1 A cm^{-2} and –0.14 V dec^{-1} in the range of current densities higher than 0.1 A cm^{-2} (Fig. 2). Such a shape of the polarization curves indicates true catalysis of the HER.[10–17] Kinetic parameters for the HER, as well as the contribution of surface roughness to the catalytic activity, were evaluated using the EIS technique.[8] Based on the presented theoretical model for the faradic impedance of the HER,[10–17] the rate constants of the individual steps

were determined by simulating both the polarization and EIS experimental data. It was found that the reaction proceeded equally *via* the Volmer–Heyrovsky and the Volmer–Tafel routes at lower overpotentials, while at higher overpotentials, the Volmer–Heyrovsky pathway dominated the process with the Heyrovsky step being the rate determining step (rds).[8] A comparison of the intrinsic activities of the Ni–MoO$_2$ composite and a flat Ni electrode proved that the combination of Ni and MoO$_2$ produced a true catalytic effect for the HER.[8]

TABLE I. Conditions of samples deposition and their average chemical compositions obtained by EDS analysis of their cross-sections

Sample deposited afer days	Sample No.	j_{dep} A cm^{-2}	τ_{dep} min	d_{av}[a] μm	Position	Composition, at. %		
						O	Ni	Mo
1	1	–0.3	24	56	Average	5	87	8
10	2	–0.3	24	57	Average	5	87	8
30	3	–0.3	24	55	Average	5	87	8
90	4	–0.3	24	54	Average	5	86	9
180	5A	–0.3	24	53	Average	5	84	11
	5B	–0.1	10	15	Mo rich	71	9	20
					Ni rich	4	89	7
	5C	–0.062	15	23	Mo rich	71	9	20
					Ni rich	4	86	10

[a]Average thickness was estimated from the SEM cross-sections

As can be seen from Fig. 2, during the first 30 days of electrolyte aging (samples 1–3), no change in the polarization characteristics for the HER could be observed. Simultaneously, practically no change was observed in the thicknesses and compositions of the coatings, Table I. After 90 days of electrolyte aging, the polarization curve for the HER changed, showing more positive potential values in the range of low current densities and slightly higher slope at high current densities (Fig. 2, curve 4) in comparison with samples 1, 2 and 3. A significant change in the activity for the HER was recorded for the sample deposited from the same electrolyte (under the same conditions, deposition current density –0.3 A cm^{-2}) after an aging period of 180 days (sample 5A) at current densities higher than 0.03 A cm^{-2}. Although the chemical composition and thickness, as well as the appearance of the coating surface, did not change, the overvoltage for the HER increased by about 50 mV. Such an effect could be the consequence of agglomeration of the MoO$_2$ powder particles. The morphology of sample 5A is presented in Fig. 3. The same morphologies were obtained for samples 1–4. As can be seen on the back–scatter SEM of the cross-section of sample 5A (Fig. 3b), the coating is characterized with gray and white areas, the former corresponding to Ni-richer deposits and the latter corresponding to the Mo-richer deposits.[6–8] Unfortunately, agglomerates in the composite coating were not detectable. The agglomeration of MoO$_2$ powder particles was confirmed by particle size analysis

Fig. 2. Polarization curves for the HER on Ni–MoO$_2$ cathode coatings recorded in a solution of 32 mass % NaOH at 90 °C. The Ni–MoO$_2$ coatings were deposited from a suspension containing 3 g dm^{-3} MoO$_2$ powder particles in 2 M NH$_4$Cl + 0.2 M NiCl$_2$ electrolyte, pH 3.8, after different times of electrolyte aging: 1 – after 1 day (□); 2 – after 10 days (□); 3 – after 30 days (□); 4 – after 90 days (○) and 5A – after 180 days (△).

(see Experimental). For samples deposited after 1, 10 and 30 days, average particles size in the electrolyte was about 200 nm, while in the electrolyte used for deposition after 180 days, average particles size was about 500 nm. It appears that with increasing size of the MoO$_2$ powder particles (due to agglomeration), the applied current density of –0.3 A cm^{-2} for sample deposition was not the optimal one and that for a given hydrodynamics an optimal value of the deposition current density should be defined by additional experiments. Accordingly, two samples, 5B and 5C, were deposited at lower current densities of –0.1 A cm^{-2} and –0.062 A cm^{-2}, respectively. Polarization curves for HER for samples 5A–5C are presented in Fig. 4 together with that for the commercial DN electrode. As can be seen, a significant decrease in the overvoltage for HER was achieved with the decreases in the deposition current density. The potential for the HER recorded at –0.3 A cm^{-2} (current density in industrial electrolysis) amounted to: –1.34 V for sample 5A, –1.27 V for sample 5B and –1.20 V for sample 5C (for the DN electrode this value was –1.23 V). Hence, it appears that sample 5C required a lower overvoltage for the HER by about 30 mV compared to that that for the commercial DN electrode. By the SEM and EDS analysis of the surfaces and the cross-sections of the samples 5A, 5B and 5C, it was discovered that their surfaces and the cross-sections were different. The morphology and chemical composition of the sur-

Fig. 3. Surfaces of the Ni–MoO$_2$ composite coatings for sample 5A (a and c). The cross-sections of the Ni–MoO$_2$ composite coatings for sample 5A (b).

face of sample 5A was identical to those for samples 1–4 (Figs. 3a and 3c). The cross–section analysis also showed practically the same results (Fig. 3b and Table I). In the case of sample 5B, the SEM analysis of its surface showed the presence of small number of cracks, while EDS analysis confirmed that the surface was composed of a Ni-rich coating. The cross–section analysis showed a layered structure, Fig. 5b, with the top layer being rich in Ni and the bottom layer of the coating being rich in Mo. Average chemical compositions of these layers are given in Table I. In the case of sample 5C, the surface was characterized by the presence of larger number of cracks, Fig. 6a. Simultaneously, the surface was rougher than those for samples 1–4, 5A and 5B (Fig. 3c), as shown in Fig. 6c. EDS analysis of the surface of 5C showed that the top layer was rich in Mo. Its cross-section analysis also showed a layered structure with a much lower number of thicker layers, only three Mo-rich and three Ni-rich layers (Fig. 6b). In this case, the top layer was rich in Mo, while the bottom layer was rich in Ni. Taking into account that coatings richer in Mo are better catalysts for the HER, it is quite clear why its polarization curve showed a lower overvoltage for the HER for

about 70 mV than that for the sample 5B at the same current density usually used in industrial electrolysis ($j = -0.3$ A cm^{-2}).
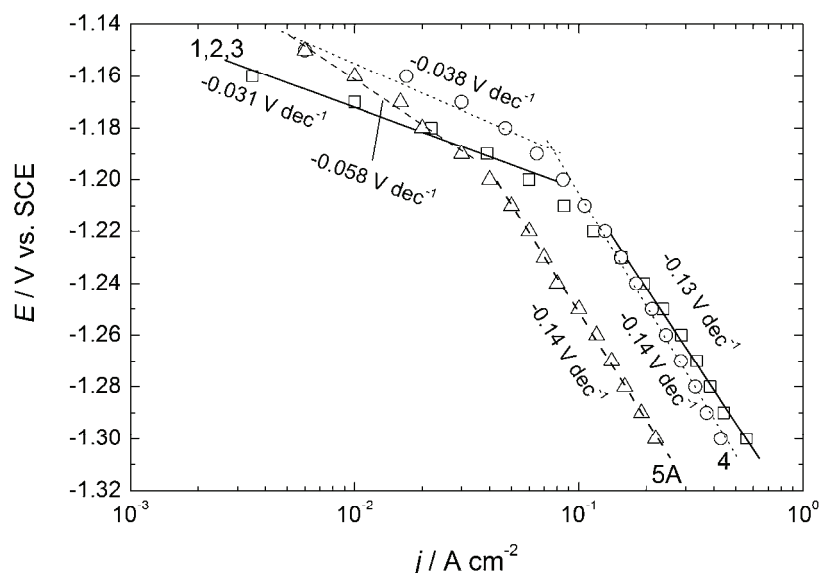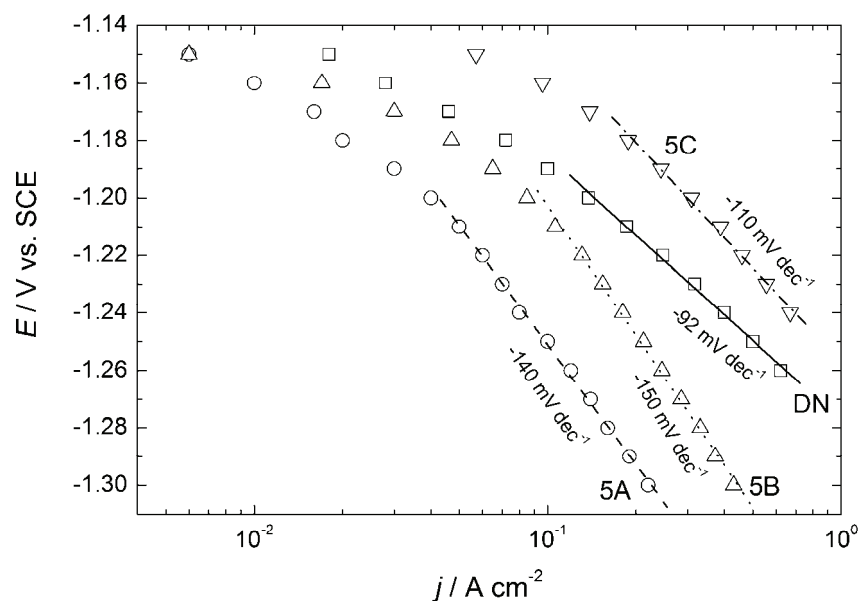

Fig. 4. Polarization curves for the HER on Ni–MoO$_2$ cathode coatings recorded in a solution of 32 mass % NaOH at 90 °C. The Ni–MoO$_2$ coatings were deposited from a suspension containing 3 g dm^{-3} MoO$_2$ powder particles in 2 M NH$_4$Cl + 0.2 M NiCl$_2$ electrolyte, pH 3.8, after 180 days of electrolyte aging: (○) 5A – j_{dep} = –0.3 A cm^{-2}; (△) 5B – j_{dep} = –0.1 A cm^{-2}; and (▽) 5C – j_{dep} = –0.062 A cm^{-2}. For comparison, the polarization curve for the commercial De Nora electrode (DN – □), recorded under the same conditions, is presented.
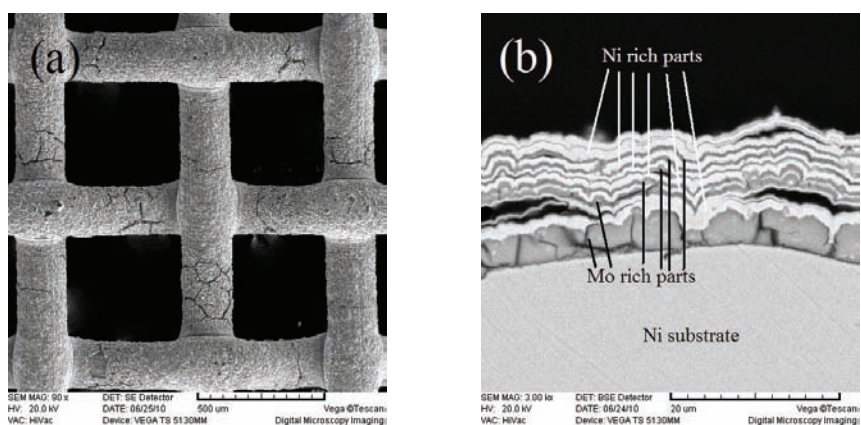
Fig. 5. Surface (a) and cross-section (b) of the Ni–MoO$_2$ composite coating for sample 5B (SEM). The average chemical compositions of the Ni-rich and Mo-rich layers (EDS) are given in Table I.
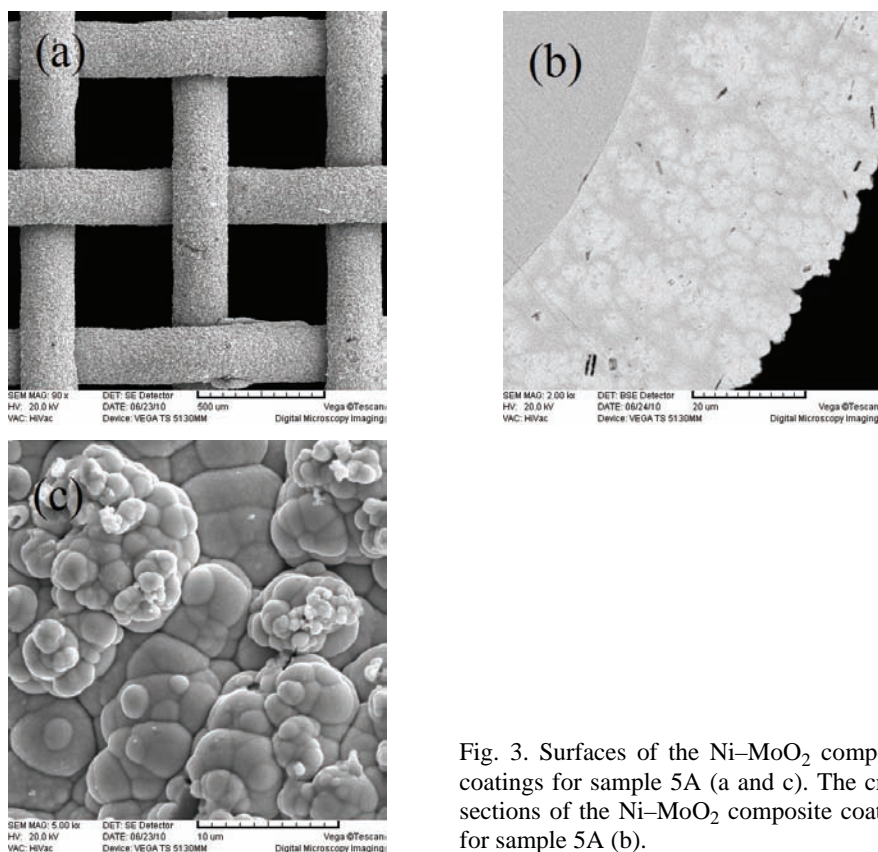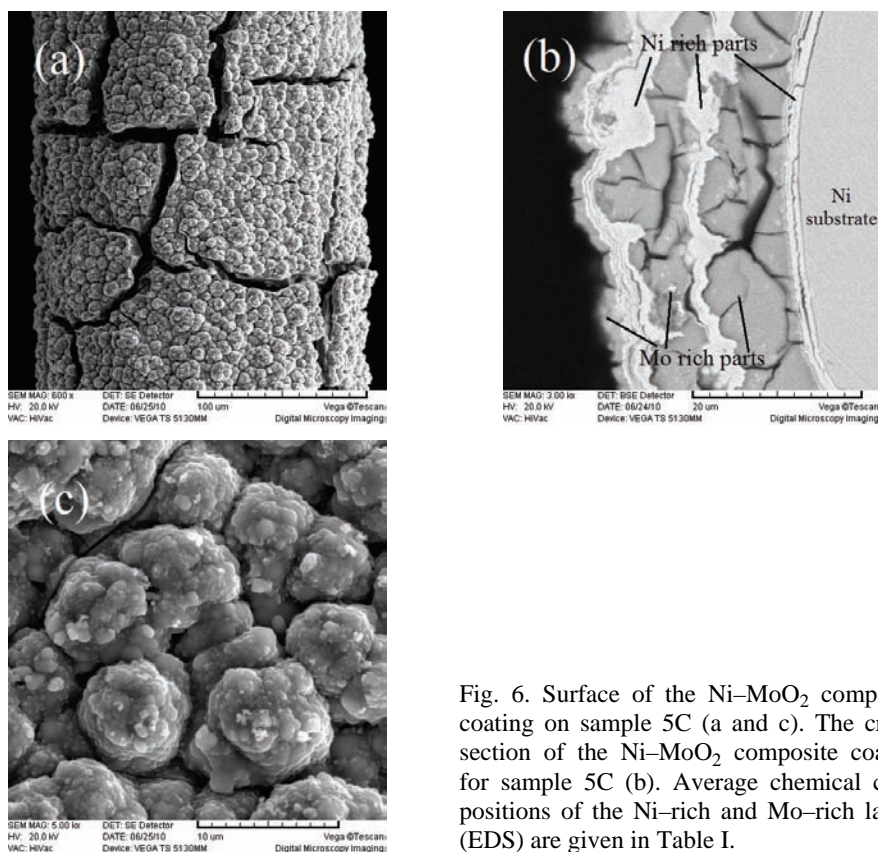
Fig. 6. Surface of the Ni–MoO$_2$ composite coating on sample 5C (a and c). The cross-section of the Ni–MoO$_2$ composite coating for sample 5C (b). Average chemical compositions of the Ni–rich and Mo–rich layers (EDS) are given in Table I.

"Service life" test

After recording the polarization curves, the electrodes 1, 5C and DN were subjected to the "service life" test, as explained in the Experimental section. Since in most industrial plants, automatic cathodic protection of cathodes is switched on during shut–downs, the "service life" test is designed to estimate the efficiency of cathodes during so–called "polarity inversion" which occurs during the replacement of old electrodes of an electrolyzer with new ones in the zero-gap cells (see Introduction). In a previous paper,[6] it was shown that the activity of Ni–MoO$_2$ and DN electrodes at the end of the "service life" test dropped to approximately 54 % of the initial value, being comparable with the results obtained for Pt–based cathodes.[5] The SEM–EDS analysis of the Ni–MoO$_2$ electrode (sample 1) after the "service life" test showed that parts of their surfaces rich in Mo had peeled off during the cycling treatment of this electrode. It was concluded that the dissolution of MoO$_2$-rich parts of the coating occurred at anodic potentials, causing the loss of their activity for the HER.[6]

The results of the "service life" test for electrodes 1, 5C and DN are presented in Fig. 7. The potentials for the HER, recorded at $j = -0.3$ A cm^{-2}, before and after a certain period of cycling the electrodes (from -1.25 to 0.5 V at a sweep rate of 0.05 V s^{-1}), indicate that sample 1 and DN behaved in a similar manner. With increasing number of cycles, the potential response changed to more negative values, starting from about -1.21 V and finishing at about -1.24 V. In the case of sample 5C, the starting potential was more positive, about -1.20 V, and had not changed after 10 cycles. With further increase of the number of cycles, the potential decreased to about -1.21 V after 25 cycles. Hence, it appeared that the most stable electrode during the "service life" test was sample 5C. Considering its structure (cross–section analysis) and the fact that practically no changes on the electrode surface before and after the "service life" test could be detected by SEM analysis (contrary to the sample 1), it is most likely that the second layer from the top of the coating, rich in Ni (Fig. 6b) protected further decomposition of the coating (after the first layer, rich in Mo, has been dissolved during oxygen evolution at anodic potentials, as it was the case with the sample 1 in a previous study[6]), causing much better stability of this coating during the "service life" test.
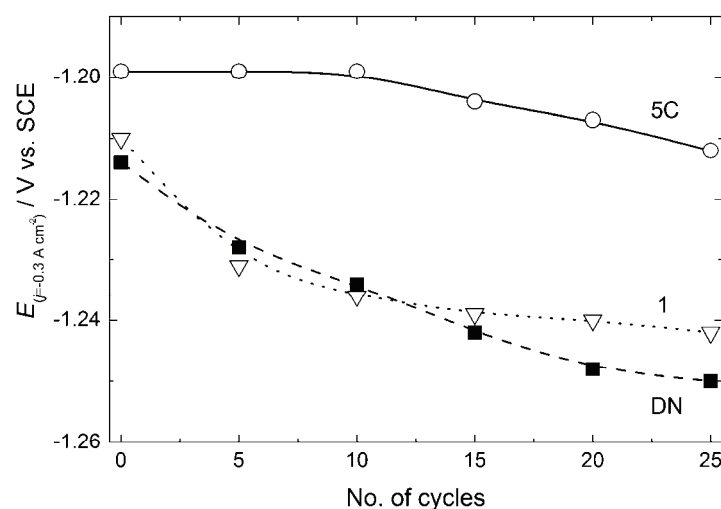
Fig. 7. Potentials for the HER corrected for the IR_Ω drop, recorded at $j = -0.3$ A cm^{-2}, as a function of the number of cycles performed in the potential range from -1.25 to 0.5 V at a sweep rate of 0.05 V s^{-1}, for samples 1 and 5C and the commercial DN electrode ("service life" test).

CONCLUSIONS

From the results presented in this study, it could be concluded that the morphology and chemical composition of the Ni–MoO$_2$ coatings deposited under the

same conditions (current density and hydrodynamics) remained practically constant after 180 days of aging of the electrolyte for their deposition, although agglomeration of the MoO$_2$ powder particles was found to occur. Contrarily, the polarization curves for the HER on these coatings were different, showing an increase in the overvoltage with aging time. After 180 days of electrolyte aging and significant agglomeration of MoO$_2$ powder particles, a different morphology and chemical composition of the coatings were obtained at lower deposition current densities. The overvoltage for the HER on these coatings decreased due to the change in the morphology and chemical composition. The "service life" test for the electrode with the best polarization characteristics showed that this electrode would be more stable during industrial application than the commercial De Nora Ni+RuO$_2$ electrode.

И З В О Д

КОМПОЗИТНЕ Ni–MoO$_2$ КАТОДЕ ЗА ИЗДВАЈАЊЕ ВОДОНИКА ИЗ АЛКАЛНИХ РАСТВОРА. ЕФЕКАТ СТАРЕЊА ЕЛЕКТРОЛИТА ЗА ЊИХОВО ТАЛОЖЕЊЕ

ВЛАДИМИР Д. ЈОВИЋ[1], УРОШ Ч. ЛАЧЊЕВАЦ[1], БОРКА М. ЈОВИЋ[1], ЉИЉАНА М. ГАЈИЋ-КРСТАЈИЋ[2] и НЕДЕЉКО В. КРСТАЈИЋ[3]

[1]*Институт за мултидисциплинарна истраживања, Универзитет у Београду, п. пр. 33, 11030 Београд,* [2]*Институт техничких наука САНУ, Кнез Михајлова 35, 11000 Београд и* [3]*Технолошко–металуршки факултет, Универзитет у Београду, Карнегијева 4, 11000 Београд*

У овом раду испитиван је утицај старења електролита за електрохемијско таложење Ni–MoO$_2$ композитних превлака на њихову морфологију (скенирајућа електронска микроскопија), хемијски састав (енергетско-дисперзиона анализа X-зрацима), поларизационе карактеристике и тест стабилности у условима индустријске примене за издвајање водоника у раствору 32 мас. % NaOH на 90 °C. Остварени резултати су упоређени са резултатима за комерцијалну катоду Ni+RuO$_2$, произвођача "De Nora". Показано је да старење електролита (суспензија MoO$_2$ честица у електролиту састава 2 M NH$_4$Cl + 0,2 M NiCl$_2$) не утиче на морфологију и хемијски састав Ni–MoO$_2$ композитних превлака исталожених у условима њихове индустријске производње иако долази до агломерације честица MoO$_2$, али значајно утиче на поларизационе карактеристике за реакцију издвајања водоника. Електрода са најбољим поларизационим карактеристикама за реакцију издвајања водоника, исталожена из електролита старог 180 дана при мањим густинама струје од оптималне за свеж електролит, показала је значајно боље перформансе (бољу стабилност) од комерцијалне катоде при испитивању теста стабилности у условима индустријске примене.

(Примљено 31. августа, ревидирано 17. октобар 2012)

REFERENCES

1. M. Nagamura, H. Ukihashi, O. Shiragami, in *Modern Chlor–Alkali Technology*, Vol. 2, C. Jackson, Ed., Ellis Horwood, Chichester, UK, 1983, p. 61
2. D. E. Grove, in *Modern Chlor–Alkali Technology*, vol. 3, K. Wall, Ed., Ellis Horwood, Chichester, UK, 1986, p. 250
3. S. Trasatti, *Electrocatalysis of Hydrogen Evolution: Progress in Cathode Activation*, in *Advances in Electrochemical Science and Engineering*, vol. 2, H. Gerischer, C. W. Tobias, Eds., VCH, Weinheim, Germany, 1992, pp. 1–85
4. C. Iwakura, M. Tanaka, S. Nakamatsu, H. Noue, M. Matsuoka, N. Furukawa, *Electrochim. Acta* **40** (1995) 977
5. A. L. Antozzi, C. Bargioni, L. Jacopetti, M. Musiani, L. Vazquez-Gomez, *Electrochim. Acta* **53** (2008) 7410
6. V. D. Jović, U. Lačnjevac, B. M. Jović, N. V. Krstajić, *Electrochim. Acta* **63** (2012) 124
7. N. V. Krstajić, U. Lačnjevac, B. M. Jović, S. Mora, V. D. Jović, *Int. J. Hydrogen Energy* **36** (2011) 6450
8. U. Č. Lačnjevac, B. M. Jović, V. D. Jović, N. V. Krstajić, *J. Electroanal. Chem.* **677**–**680** (2012) 31
9. Y. Liang, S. Yang, Z. Yi, X. Lei, J. Sun, Y. Zhou, *Mat. Sci. Eng., B* **121** (2005) 152
10. J. Niedbala, A. Budniok, E. Lagiewka, *Thin Solid Films* **516** (2008) 6191
11. Q. Han, S. Cui, N. Pu, J. Chen, K. Liu, X. Wei, *Int. J. Hydrogen Energy* **35** (2010) 5194
12. I. Herraiz-Cardona, E. Ortega, V. Pérez-Herranz, *Electrochim. Acta* **56** (2011) 1308
13. F. Rosalbino, D. Maccio, A. Saccone, E. Angelini, S. Delfino, *Int. J. Hydrogen Energy* **36** (2011) 1965
14. M. Wang, Z. Wang, Z. Guo, Z. Li, *Int. J. Hydrogen Energy* **36** (2011) 3305
15. H. Dong, T. Lei, Y. He, N. Xu, B. Huang, C. T. Liu, *Int. J. Hydrogen Energy* **36** (2011) 12112
16. B. M. Jović, U. Č. Lačnjevac, V. D. Jović, Lj. M. Gajić-Krstajić, N. V. Krstajić, *J. Serb. Chem. Soc.* **77** (2012) 211
17. J. Kubisztal, A. Budniok, A. Lasia, *Int. J. Hydrogen Energy* **32** (2007) 1211.

Electrochemical determination of hydrogen peroxide at a glassy carbon electrode modified with palladium nanoparticles

SHIMELES ADDISU KITTE, BIRHANU DESALEGN ASSRESAHEGN
and TESFAYE REFERA SORETA*

Department of Chemistry, College of Natural Sciences, Jimma University, Ethiopia

Abstract: Herein the modifications of a glassy carbon electrode (GCE) with palladium nanoparticles and a palladium film are reported. The response to hydrogen peroxide on the modified electrode was examined using cyclic voltammetry and amperometry (at –0.2 V *vs.* Ag/AgCl reference electrode in the phosphate buffer solution, pH 7.4). The palladium film and palladium nanoparticle-modified GCE showed a linear response to hydrogen peroxide in the concentration range 10 µM to 14 mM and 1 µM to 14 mM with detection limit of 6.79 and 0.33 µM, respectively.

Keywords: palladium; nanoparticles; hydrogen peroxide; glassy carbon electrode.

INTRODUCTION

Nanotechnology has recently become one of the most exciting forefront fields in analytical chemistry.[1–3] A wide variety of nanomaterials, especially nanoparticles (NPs) with different properties, have found broad application in many kinds of analytical methods.[1–3] Accordingly, electrode development has concentrated more on surface modification of electrodes with nanotubes or nanoparticles.[2,3] Nanoelectrochemistry plays a significant role in the fabrication of various nanomaterials and devices for detecting molecules at very low concentrations.

Electrochemical deposition approaches are often reported as the methods of choice for simple and low cost nanostructuring and nanopatterning of electrode surfaces.[4] The fabrication of metal NPs modified electrodes by electrochemical techniques is advantageous because it is a single-step process involving reduction of the metal salt at an applied potential, which is a convenient, fast and low-cost method.[5–7]

701

The introduction of NPs with catalytic properties into electrochemical sensors and biosensors can decrease overpotentials[8] of many analytically important electrochemical reactions, and even realize the reversibility[8] of some redox reactions that are irreversible at common unmodified electrodes. For instance, a sensitive NO microsensor was developed through the modification of a platinum microelectrode with gold NPs in which the gold NPs catalyzed the electrochemical oxidation of NO with an overpotential decrease of about 250 mV.[9]

Palladium is a well-known catalyst for many reactions, such as the electrocatalytic oxidation of hydrazine[10] and formaldehyde,[11,12] hydrogenation of unsaturated hydrocarbons,[13–15] for the reduction of oxygen,[16] the oxidation of alcohols,[17,18] the oxidation of hydrogen to hydrogen peroxide,[19] and is routinely used in the automobile industry in catalytic converters to reduce the amounts of nitrogen oxides, carbon monoxide, unburned hydrocarbons.[20]

Hydrogen peroxide has wide applications in environmental, pharmaceutical, clinical, and industrial research. It is also a by-product of reactions catalyzed by a large number of oxidase enzymes. Therefore, the detection of hydrogen peroxide is important in biomedical and environmental applications.[21]

Glassy carbon electrode (GCE) is a useful electrode material because of its high electrical conductivity, impermeability to gases, high chemical resistance, reasonable mechanical and dimensional stability and widest potential range of all carbonaceous electrodes.[22] Many attempts have been made to improve the electrochemical properties of glassy carbon electrodes by chemical modifications, such as the addition of a variety of molecular catalysts and mediators to the electrode surface by adsorption, covalent bonding of electroactive catalysts, and entrapment of metals within an affixed polymer film and vapour or electro-deposition of metals directly onto the electrode.[22] It is also known that a GCE is a convenient material for surface modification with metals, *e.g.*, mercury[23] and bismuth.[24]

EXPERIMENTAL

Chemicals

Palladium dichloride (PdCl$_2$, 99.9 %, Aldrich), sodium perchlorate (NaClO$_4$, 98 %, Sigma), potassium hydroxide (KOH, BDH), citric acid (99.5 %, Wardel Chemicals), HCl (37 %, Riedel de Haen), NaCl (99.8 %, Riedel de Haen), potassium hexacyanoferrate (97 %, Labmark Chemicals), potassium hydrogen phosphate (K$_2$HPO$_4$, 98 % (Finkem), potassium dihydrogen phosphate (KH$_2$PO$_4$), potassium iodide (KI, 99 %, Riedel de Haen), sulphuric acid (98 %, Riedel de Haen) and sodium thiosulphate (Na$_2$S$_2$O$_3$, Riedel de Haen) were used as received without any treatment.

Instrumentation

The cyclic voltammetry and amperometric experiments were realized using a BASi Epsilon EC-Version 1.40.67 voltammetric analyzer (Bio-analytical Systems, USA), controlled with basic Epsilon software. A conventional three-electrode setup was used with a

glassy carbon electrode (3 mm diameter, BASi, MF 2012) as the working electrode and a platinum wire counter electrode (BASi, MW 1032). An Ag/AgCl electrode (BASi, MF 2079) served as the reference electrode. All potentials are reported with respect to this reference electrode. A magnetic stirrer (BASi C3 Cell stand at 500 rms) was used for stirring.

Methods

Solution preparation. A 7.5 mM $PdCl_2$ deposition bath was prepared by dissolving, 6.65 mg of $PdCl_2$ in 50 mL, pH 2, citrate buffer and left overnight in the dark, after which period a clear solution was obtained. Finally, the pH of the solution was adjusted to 3 by the addition of dilute KOH.

Hydrogen peroxide was standardized by iodimetric titration.[25] A stock standard solution containing H_2O_2 was prepared freshly each day. Working standard solutions of lower concentrations were prepared immediately before use. Double distilled water was used to prepare all aqueous electrolyte solutions throughout the analysis.

Electrode preparation. Glassy carbon rods (Bioanalytical Systems, BASi, USA) with a diameter of 3 mm were used. The electrode surface was polished with 0.3 μm alumina slurry (BASi). After polishing, the electrodes were carefully rinsed with double distilled water and electrochemically conditioned by potential scanning from –1.1 to 1.4 V in 0.1 M $NaClO_4$ for at least five complete scans at 50 mV s^{-1}, during which the high background current due to glassy carbon oxidation diminished and a reproducible cyclic voltammograms was obtained.[26] The background current of the bare electrode was measured by cyclic voltammetry within the potential window of 0 to 0.7 V. Electrodes with a high background current above a selected reference were excluded. The electrodes were used immediately following the cleaning and conditioning steps.

Fabrication of Pd film and Pd nanoparticles-modified GCE. Palladium film and nano-modified electrodes were prepared by potentiostatic deposition of Pd on the cleaned GCEs from the Pd deposition bath. To fabricate Pd film-modified electrode, palladium was electrochemically deposited in the solution of $PdCl_2$ by stepping the potential from the rest potential of 1.10 V for 1 s to the deposition potential of 0 V for 30 s. In the case of the Pd nano-modified GCE, the same potentials were used except the deposition potential was applied from 1 to 5 s.[27] The modified GCEs were rinsed with double distilled water and immediately used for electrochemical determination of hydrogen peroxide.

Real sample preparation and analysis. For real sample analysis, hair colouring cream (Crust Hair Dye Lotion, Thai-meko Co., Ltd.; Bangkok, Thailand) which contains H_2O_2 solution was used. The concentration of H_2O_2 in the hair colouring cream was determined by titration.[25] Amperometric determination of H_2O_2 at the modified GCEs was realized by the standard addition method. Thus, 1 mL of sample solution was diluted to 100 fold and 0.5 mL of this solution was spiked into 10 mL of the buffer and successive ejection of 1, 2, 3, 4 and 5 mL of 10^{-5} M H_2O_2 standard solution was added to the spiked buffer.

Chronoamperometric measurements. Amperometric experiments were performed in a stirred system under the optimized experimental conditions for the working electrodes and the addition of freshly prepared H_2O_2 standard solution to the PBS buffer. Current-time data were recorded after steady state current had been achieved.

RESULTS AND DISCUSSION

Voltammetric analysis of Pd in the deposition path using GCEs was performed to obtain the appropriate reduction potentials for Pd. The voltammogram

recorded was in good agreement with the experimental results reported by Soreta, *et al.*[26] A deposition potential of 0 V was selected. In the same manner, palladium film and palladium NP electrodeposition procedure was based on the work of Soreta *et al.*[26,27] It was reported[27] that for 1 s deposition time, the estimated Pd NPs diameter was within the range of 48±25 nm, and for 3 s deposition, it was 85±58 nm. Hence, short deposition times caused nucleation of Pd NPs. On extension of the deposition time, the nuclei centres became bigger and bigger, nearby nuclei centres merged and finally a Pd film was formed.[26]

Optimization of the parameters for H_2O_2 detection

The cyclic voltammograms of H_2O_2 at the bare, Pd NPs-modified and Pd film-modified electrodes over a wide range of potentials are depicted in Fig. 1. It is evident that the voltammograms of Pd NPs and Pd film modified electrodes differed substantially from that of the bare electrode. There was no obvious peak corresponding to the reduction and oxidation of hydrogen peroxide (0–25 mM) in phosphate buffer at the bare GCE within the studied potential window. This is in line with experimental results reported by Compton *et al.*[28], where no reduction or oxidation peak for hydrogen peroxide was seen at a bare glassy carbon electrode.
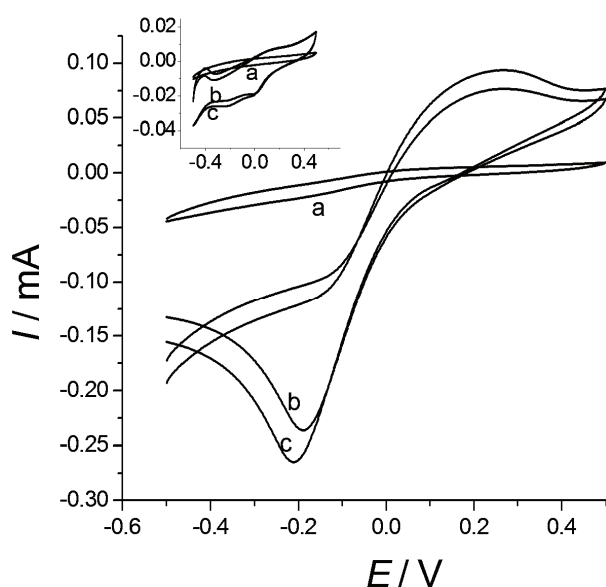
Fig. 1. Cyclic voltammograms of 0.01 M H_2O_2 in pH 7.4 PBS (0.1 mol L^{-1}) at a) bare glassy carbon electrode, b) Pd film-modified glassy carbon electrode and c) Pd NPs-modified glassy carbon electrode. Inset: the corresponding voltammograms in blank phosphate buffer. All the voltammograms were recorded at a scan rate of 50 mV s^{-1}.

From the voltammograms, the reduction potential of –0.2 V was selected for chronoamperometric studies as at this potential reduction of H_2O_2 occurred at a higher magnitude and the selected potential was safe to avoid unwanted side reactions at the working electrode, such as reduction of hydrogen ions.

The pH of the electrolyte was also an important parameter that could influence the response of the electrode in the electroanalysis of H_2O_2. The effect of the pH of the supporting electrolyte on the electrode response was studied in the range 5.8–7.6. Study on effect of pH below 5.8 was purposefully excluded by anticipating that palladium may adsorb hydrogen on its surface at higher concentrations of hydrogen ions and may interfere with the analyte of interest. With increasing buffer pH within the studied range, the voltammetric response for the reduction of H_2O_2 at the modified electrodes increased until pH 7.4. Further increase in pH of the buffer led to a decrease in the response, possibly due to instability of palladium under these conditions where it can form stable hydroxo complexes.[26] Therefore, pH 7.4 was taken as the optimal pH for the electroanalysis of H_2O_2 in PBS, which is in close agreement with previous reports.[28] In addition to the working potential and pH, the deposition time for both the NPs and film were optimized. For the deposition of Pd NP the optimization starts from 1 s and it was found that the CV response of the modified GCE increased up to 5 s deposition of particles (Fig. 2), after which a further increase in the deposition time led to a decline in the response. Therefore, Pd NPs were deposited on the GCE for 5 s and electrodes prepared under this condition are referred to as Pd NPs modified GCE.
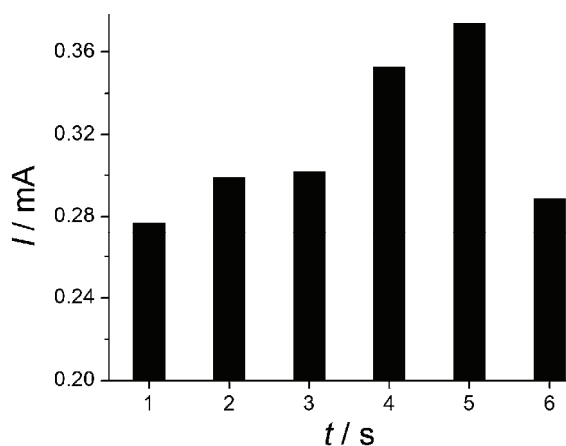
Fig. 2. Effect of Pd NPs deposition time on the electrode voltammetric response for 0.01 M H_2O_2 (cyclic voltammetry run at a scan rate of 50 mV s^{-1} in PBS (0.1 M, pH 7.4)).

For the deposition of a palladium film, the optimization for the deposition time started from 10 s and the CV response of the modified GCE towards the analyte continued to increase until a time of 30 s (Fig. 3). Further increase of the deposition time led to a decrease in the response. The electrode prepared by deposition of Pd for 30 s on GCE is referred to as Pd film-modified GCE.

The electrochemical parameters were optimized to obtain maximum sensitivity for the modified electrode towards H_2O_2 and values for the optimized parameters are summarized in Table I.
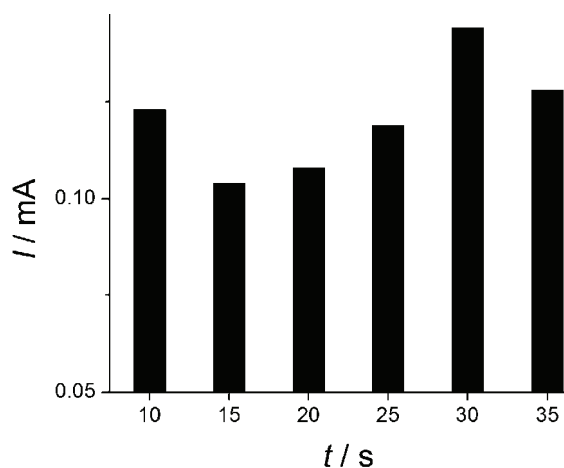
Fig. 3. Effect of Pd film deposition time on the electrode voltammetric response of 0.01 M H_2O_2 (cyclic voltammetry run at a scan rate of 50 mV s^{-1} in PBS (0.1 M, pH 7.4)).

TABLE I. The optimized experimental parameters and their values

Parameter	Value
Working potential	–0.2 V
Working pH	7.4
Pd NP deposition time	5 s
Pd Film deposition time	30 s

Determination of H_2O_2 amperometrically

Since amperometry under stirred condition is much more sensitive than cyclic voltammetry, this method is usually employed for the determination of lower concentrations of analytes.[29] In this work, amperometric measurements were performed for the determination of H_2O_2 at the modified electrodes and their analytical performance was compared with respect to that of a bare GCE. The current-time responses of the Pd NPs and Pd film-modified GCE with successive injection of hydrogen peroxide at an applied potential of –0.20 V are displayed in Fig. 4.

The amperometric response of both the Pd NPs and Pd film modified GCE for successive additions of H_2O_2 increased stepwise with each additions of hydrogen peroxide. In addition, the GCE modified with Pd NPs exhibited better amperometric response to H_2O_2 than the Pd film modified GCE. This signal enhancement was believed to be attributable to the unique reactivity and electrocatalytic activity of the Pd NPs as compared to those of the Pd film. The size effect (higher surface area to volume ratio) of the NPs is the main reason for the observed high reactivity of H_2O_2 at the Pd NPs modified GCE than at the Pd film-modified GCE.

The calibration plots in Fig. 4 are the amperometric responses of the Pd NPs modified GCE and the Pd film at –0.20 V (*vs*. Ag/AgCl) in 0.1 M PBS (pH 7.4)

with varying concentration of hydrogen peroxide, ranging from 1 µM to 13 mM for the former and 10 µM to 13 mM for the latter.
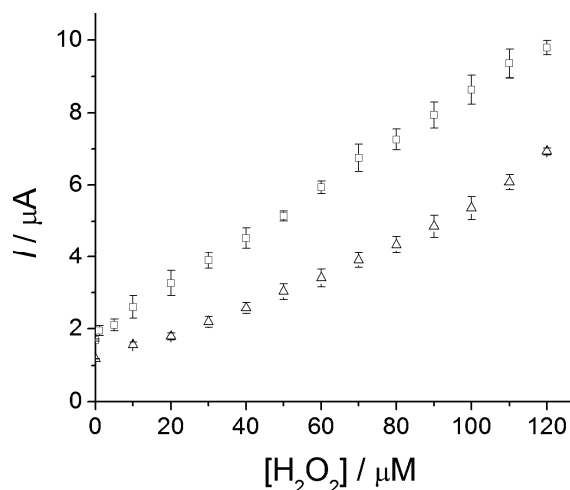
Fig. 4. Calibration curves for the determination of H_2O_2 with amperometric measurements using: ( ) Pd NP-modified GCE; (Δ) Pd film-modified GCE for the determination of hydrogen peroxide.

As depicted in Fig. 4, there is an obvious linear relationship between the current and the concentration of hydrogen peroxide in the studied concentration ranges. The sensitivity for determination of hydrogen peroxide as determined from the slope of the calibration curves for the three electrodes is in the order of Pd NPs > Pd film >> bare GCE. The values clearly demonstrate substantial improvements of the sensitivity of the measurements as a result of GCE surface modification with Pd NPs and Pd film.

The detection limits for the modified electrodes were found to be 0.33 and 6.79 µM for the Pd NPs and Pd film modified GCE, respectively. The detection limit was calculated as the concentration equivalent to three times the standard deviation for five blanks and fitted to the calibration curve. Comparisons of the detection limit of the developed sensor with those previously reported works were also made and the values are summarized in Table II. Therefore, the hydrogen peroxide sensor reported herein could be a good candidate for H_2O_2 analysis.

Inter-electrode reproducibility and stability

The inter-electrode reproducibility was investigated both for Pd NPs and Pd film modified GCEs by preparing three electrodes under the same deposition conditions. Triplicate determination of 0.1 mM H_2O_2 with each electrode was used to estimate the reproducibility. The reproducibility expressed in relative standard deviation was found to be 3.52 % for the Pd NPs modified GCE. In the same manner, a relative standard deviation of 4.31 % was obtained for the Pd film-modified GCE. The results showed good reproducibility of the electrode modification.

TABLE II. Comparison of the developed sensor with previously reported modified electrodes for the determination of H_2O_2

Electrode	Detection limit, μM	Ref.
Gold nanoelectrode ensembles (NEE)	4	31
Pd NPs/onion-like mesoporous carbon vesicle (MCV)	0.079	21
Multi walled carbon nanotubes (MWCNTs)–Pd NPs on a modified GCE	0.3	30
Immobilization of horseradish peroxidase in chitosan matrix cross-linked with glyoxal	8	32
Pd NPs-modified GCE	0.33	This work

The modified electrode showed low stability. The current response of the Pd NPs-modified GCE declined for the determination made on the same electrode on consecutive days. The current response had decreased by about 29 % on the second day of the experiment. On the 4th, 6th, 8th and 10th day of the experiment, the current response had decreased by 49, 55, 62 and 71 %, respectively. This could be due to the high surface reactivity of Pd NPs. It is recommended that a fresh surface be prepared prior to each experiment.

Interference study

The ability of the electrochemical sensors developed to withstand potential interferents was studied by chronoamperometric measurements. The effect of common interfering electroactive substances, such as uric acid (UA), ascorbic acid (AA) and glucose were assessed. The amperometric response of the Pd NPs modified GCE for the subsequent injection of 5.0 mM glucose, 0.15 mM AA, 0.5 mM UA and 1.0 mM H_2O_2 at –0.2 V are depicted in Fig. 5. These concentrations were selected because the level of endogenous AA, glucose, and UA is, respectively, about 0.125 mM, 4.4–6.6 mM and 0.33 mM in the blood sample.[30]
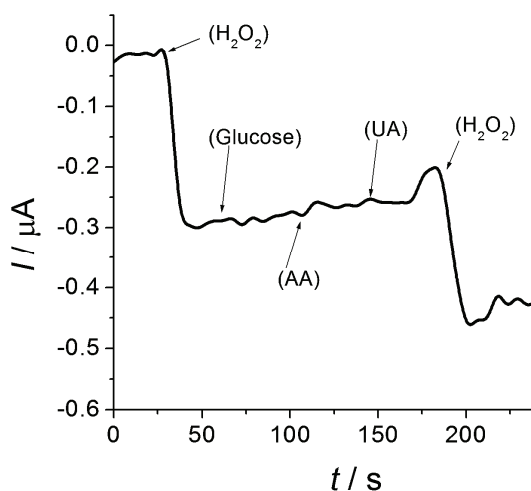
Fig 5. Amperometric response of the Pd NPs-modified GCE upon addition of 1.0 mM H_2O_2, 0.15 mM ascorbic acid, 5.0 mM glucose, 0.5 mM uric acid and 1.0 mM H_2O_2. Applied potential: –0.2 V.

The current response of AA, glucose and UA were much smaller than those of H_2O_2. The influence of the species tested on the H_2O_2 response was negligible, indicating high selectivity of the palladium modified electrodes for H_2O_2.

Real sample analysis

In order to demonstrate the applicability of the modified electrode for real sample analysis, hair colouring cream containing H_2O_2 solution was analysed. The bulk concentration of H_2O_2 in the hair colouring cream was first determined by titration. The concentration of H_2O_2 obtained was 1.49 ± 0.012 M. Thus, the 1.49 M solution was diluted 100 fold and spiked into the buffer and the successive ejection of 0.01 mM H_2O_2 standard solution into the spiked buffer. Finally the concentration was determined by the standard addition method using the bare and modified GCEs. The results are given in Table III.

TABLE III. Concentration of H_2O_2 detected in a real sample

Working electrode	Concentration of H_2O_2 detected
Bare GCE	Not detected
GCE modified with Pd NPs	0.015 ± 0.0015 mM
GCE modified with Pd film	0.018 ± 0.0047 mM

Pd modified GCEs were able to detect lower concentrations of H_2O_2 in the hair colouring cream. The amounts of hydrogen peroxide detected by the modified electrodes were in good agreement with the actual value determined by the standard method. The relative error for Pd NPs and film modified GCE were 0.67 and 21 %, respectively. The Pd NPs modified GCE was found to be more accurate than the Pd film modified GCE under the studied conditions.

CONCLUSIONS

In this work, the amperometric determination of H_2O_2 using Pd NPs and Pd film modified GCE was studied. The electrodes were modified by electrochemical deposition of palladium from Pd deposition bath at different deposition times. The developed sensor exhibited higher sensitivity for H_2O_2 than unmodified GCEs. The catalytic properties of Pd NPs and Pd film gave enhanced electrochemical responses for hydrogen peroxide. The improved analytical performance makes Pd NPs and film modified GCE promising amperometric sensor for hydrogen peroxide. Remarkable electrocatalytic activity and significantly lower detection limits were achieved with these modified electrodes that could be favourably compared to unmodified and other enzyme modified electrodes reported in the literature. Furthermore, the demonstrated modification procedure is less expensive and more convenient than previously reported sensors. The analytical performances of the modified electrodes indicate that they could be used as sensitive amperometric detectors for the determination of lower concentrations of

hydrogen peroxide as compared to the bare GCE. In this study, determination of H_2O_2 in more a complex matrix, such as blood samples, was not investigated. Further study need to be performed on the employment of these electrodes for the electroanalysis of H_2O_2 in biological samples.

И З В О Д

ЕЛЕКТРОХЕМИЈСКО ОДРЕЂИВАЊЕ ВОДОНИК-ПЕРОКСИДА НА ЕЛЕКТРОДИ ОД СТАКЛАСТОГ УГЉЕНИКА МОДИФИКОВАНОЈ НАНОЧЕСТИЦАМА ПАЛАДИЈУМА

SHIMELES ADDISU KITTE, BIRHANU DESALEGN ASSRESAHEGN и TESFAYE REFERA SORETA

Department of Chemistry, College of Natural Sciences, Jimma University, Ethiopia

У раду је приказана модификација стакластог угљеника наночестицама паладијума и филмом паладијума. Активност модификованих електрода у присуству водоник-пероксида је испитивана цикличном волтаметријом и амперометријом (на −0,2 V према Ag/AgCl референтној електроди у фосфатном пуферу, pH 7,4). Електроде модификоване филмом паладијума и наночестицама паладијума показале су линеарну зависност струје редукције водоник-пероксида у опсегу концентрација 10 μM–14 mM и 1 μM–14 mM уз границу детекције од 6,79 и 0,33 μM, редом.

(Примљено 19. јуна, ревидирано 3. новембра 2012)

REFERENCES

1. S. G. Penn, L. He, M. J. Natan, *Chem. Biol.* **7** (2003) 609
2. C. E. Banks, T. J. Davies, G. G. Wildgoose, R. G. Compton, *Chem. Commun.* **7** (2005) 829
3. X. Dai, O. Nekrassova, M. E. Hyde, R. G. Compton, *Anal. Chem.* **76** (2004) 5924
4. E. Budevski, G. Staikov, W. J. Lorenz, *Electrochim. Acta* **45** (2000) 2559
5. K. Shimazu, D. Weisshaar. T. Kuwana, *J. Electroanal. Chem. Interfacial Electrochem.* **223** (1987) 223
6. D. Crotty, *Met. Finish.* **94** (1996) 54
7. Y. Okinaka, M. Hoshino, *Gold Bull.* **31** (1998) 3
8. X. Luo, A. Morrin, A. J. Killard, M. R. Smyth, *Electroanalysis* **18** (2006) 319
9. M. Zhu, M. Liu, G. Shi, F. Xu, X. Ye, J. Chen, L. Chen, J. Jin, *Anal. Chim. Acta* **455** (2002) 199
10. K. H. Lubert, M. Guttmann, L. Beyer, K. Kalcher, *Electrochem. Commun.* **3** (2001) 102
11. G. Y. Gao, D. J. Guo, H. L. Li, *J. Power Sources* **162** (2006) 1094
12. A. Safavi, N. Maleki, F. Farjami, E. Farjami, *J. Electroanal. Chem.* **626** (2009) 75
13. D. Teschner, E. Vass, M. Hävecker, S. Zafeiratos, P. S. Schnörch, H., A. Knop Gericke, R. Schlögl, M. Chamam, A. Wootsch, A. S. Canning, J. J. Gamman, S. D. Jackson, J. McGregor, L. F. Gladden, *J. Catal.* **242** (2006) 26
14. O. Trapp, S. K. Weber, S. B. Bauch, T. W. Hofstadt, B. Spliethoff, *Chem. Eur. J.* **14** (2008) 4657
15. D. Mukherjee, *J. Nanopart. Res.* **10** (2008) 429

16. C.-C. Yang, A. S. Kumar, J.-M. Zen, *Electroanalysis* **18** (2006) 64
17. J. Chen, Q. Zhang. Y. Wang. H. Wan., *Adv. Synth. Catal.* **350** (2008) 453
18. C. L. Bianchi, P. Canton, N. Dimitratos, F. Porta, L. Prati, *Catal. Today* **102**–**103** (2005) 203
19. V. R. Choudhary, C. Samanta, *J. Catal.* **238** (2006) 28
20. Y. Nishihata, J. Mizuki, T. Akao, H. Tanaka, M. Uenishi, M. Kimura, T. Okamoto, N. Hamada, *Nature* **418** (2002) 164
21. X. Bo, J. Bia, J. Ju, L. Guo, *Anal. Chim. Acta* **675** (2010) 29
22. N. L. Pocard, D. C. Alsmeyer, R. L. McCreery, T. X. Neenan, M. R. Callstrom, *Chem-Inform* **23** (1992) 50
23. T. M. Florence, *Anal. Chim. Acta* **119** (1980) 217
24. J. Wang, J. Lu, S. B. Hocevar, P. A. M. Farias, B. Ogorevc, *Anal. Chem.* **72** (2000) 3218.

EXTENDED ABSTRACT
Plasma electrolytic oxidation of metals[•]

STEVAN STOJADINOVIĆ

University of Belgrade, Faculty of Physics, Studentski trg 12, 11000 Belgrade, Serbia

Abstract: The results of investigation of the plasma electrolytic oxidation (PEO) process on some metals (aluminum, titanium, tantalum, magnesium and zirconium) were presented. The whole process involves anodizing metals above the dielectric breakdown voltage, when numerous micro-discharges are generated continuously over the coating surface. For characterization of the PEO process, optical emission spectroscopy and real-time imaging were used. These investigations enabled the determination of electron temperature, electron number density, spatial density of micro-discharges, the active surface covered by micro-discharges, and the dimensional distribution of the micro-discharges at various stages of the PEO process. Special attention was focused on the results of a study of the morphology, and the chemical and phase composition of oxide layers obtained in the PEO process on aluminum, tantalum and titanium in electrolytes containing tungsten. Physicochemical methods: atomic force microscopy (AFM), scanning electron microscopy (SEM-EDS), X-ray diffraction (XRD) analysis, X-ray photoelectron spectroscopy (XPS) and Raman spectroscopy served as tools for examining the obtained oxide coatings. In addition, the application of the obtained oxide coatings, especially the application of TiO_2/WO_3 coatings, in photocatalysis was discussed.

Keywords: plasma electrolytic oxidation; micro-arc oxidation; micro-discharges; oxide coatings; optical emission spectroscopy.

Plasma electrolytic oxidation (PEO), also called micro-arc oxidation (MAO) or anodic spark deposition (ASD), is an economic, efficient, and environmentally benign technology capable of producing a stable oxide coating on the surface of lightweight metals (aluminum, magnesium, zirconium, titanium, tantalum, *etc*.) or metal alloys.[1,2] The oxide coatings have controllable morphology and composition, excellent bonding strength with the substrate, good electrical and ther-

---

713

mal properties, high microhardness, and high-quality wear and corrosion resistance.

The PEO process is coupled with the formation of plasma, as indicated by the presence of micro-discharges on the metal surface, accompanied by gas evolution.[3,4] Various processes, including chemical, electrochemical, thermodynamic, and plasma-chemical reactions, occur at the discharge sites, due to increased local temperature (10^3 to 10^4 K) and pressure ($\approx 10^2$ MPa). These processes are responsible for modifying the structure, composition, and morphology of obtained oxide coatings. The oxide coatings formed by the PEO process usually contain crystalline and amorphous phases with constituent species originating from both the metal and electrolyte.

Micro-discharge phenomena are important characteristics of the PEO process. Given the liquid environment, optical emission spectroscopy (OES) is the most convenient technique for characterization of the micro-discharges appearing during the PEO process. OES in the visible and near UV spectral region was not only used for identification of species present in the investigated systems, but also for determination of important parameters of these systems.[5–11] The results of relative line intensity measurements of species originating in the substrate or in the electrolyte were employed to determine the electron temperature.[5,6,8] Spectral line shape analysis of the hydrogen Balmer lines was used to estimate the electron number density.[5,9] The molecular vibrational temperature was determined from the $B^2\Sigma^+ - X^2\Sigma^+$ emission transition of AlO,[10] and the $B^1\Sigma^+ - X^1\Sigma^+$ emission transition of MgO.[11] Real-time imaging showed that the spatial density of micro-dischargers was the highest in the early stage of the PEO process, while the percentage of oxide coatings area covered by active discharge sites decreases with PEO time.[7,9,12]

The results of an investigation of the PEO process on aluminum, titanium, and tantalum in tungstate electrolytes (12-tungstosilicic acid, 12-tungstophosphoric acid, and sodium tungstate) were presented in the lecture,[12–16] because tungsten-containing oxide layers have extensive catalytic, semiconducting, and corrosion-resistant properties. It was shown that the outer layer of oxide coatings formed by PEO in tungstate electrolytes was tungsten bronze. In addition, it was shown that PEO of titanium in 12-tungstosilicic acid is an economic and efficient process for forming TiO_2/WO_3 coatings with enhanced photocatalytic activity, compared to that of pure TiO_2.[16]

И З В О Д

ПЛАЗМА ЕЛЕКТРОЛИТИЧКА ОКСИДАЦИЈА МЕТАЛА

СТЕВАН СТОЈАДИНОВИЋ

Универзитет у Београду, Физички факултет, Студентски трг 12, 11000 Београд

У овом предавању су приказани резултати истраживања плазма електролитичке оксидације (PEO) метала (алуминијума, титана, тантала, магнезијума и цирконијума). Процес се заснива на анодизацији метала изнад напона диелектричног пробоја оксидног слоја и карактерише га појава микропражњења на целој површини метала. Представљени су резултати истраживања феномена PEO методама оптичке емисионе спектроскопије и праћењем догађаја у реалном времену. Овим истраживањима је омогућено одређивање електронске температуре плазме формиране на местима микропражњења, електронске густине плазме, просторне густине микропражњења, активне површине обухваћене микропражњењима и димензионалне дистрибуције величина микропражњења у различитим етапама PEO процеса. Посебна пажња је фокусирана на резултате истраживања морфологије, хемијског и фазног састава оксидних слојева добијених PEO процесом на алуминијуму, танталу и титану у електролитима који садрже волфрам. Карактеризација добијених површина је вршена физичко хемијским методама: AFM микроскопијом, SEM–EDS микроскопијом, рентгенском структурном анализом, фотоелектронском и Рамановом спектроскопијом. Дискутована је и примена добијених оксидних структура, нарочито примена TiO_2/WO_3 структура у фотокатализи.

(Примљено 26. новембра 2012)

REFERENCES

1. A. L. Yerokhin, X. Nie, A. Leyland, A. Matthews, S. J. Dowey, *Surf. Coat. Technol.* **122** (1999) 73
2. S. Stojadinović, R. Vasilić, I. Belča, M. Petković, B. Kasalica, Z. Nedić, Lj. Zeković, *Corros. Sci.* **52** (2010) 3258
3. S. Stojadinović, R. Vasilić, M. Petković, I. Belča, B. Kasalica, M. Perić, Lj. Zeković, *Electrochim. Acta* **59** (2012) 354
4. S. Stojadinović, R. Vasilić, M. Petković, I. Belča, B. Kasalica, M. Perić, Lj. Zeković, *Electrochim. Acta* **79** (2012) 133
5. S. Stojadinović, R. Vasilić, M. Petković, B. Kasalica, I. Belča, A. Žekić, Lj. Zeković, *Appl. Surf. Sci.* **265** (2013) 226
6. J. Jovović, S. Stojadinović, N. M. Šišović, N. Konjević, *J. Quant. Spectrosc. Radiat. Transfer* **113** (2012) 1928
7. S. Stojadinović, J. Jovović, M. Petković, R. Vasilić, N. Konjević, *Surf. Coat. Technol.* **205** (2011) 5406
8. J. Jovović, S. Stojadinović, N. M. Šišović, N. Konjević, *Surf. Coat. Technol.* **206** (2011) 24
9. S. Stojadinović, R. Vasilić, M. Petković, Lj. Zeković, *Surf. Coat. Technol.* **206** (2011) 575
10. S. Stojadinović. M. Perić, M. Petković, R. Vasilić, B. Kasalica, I. Belča, J. Radić-Perić, *Electrochim. Acta* **56** (2011) 10122
11. S. Stojadinović, M. Perić, J. Radić-Perić, R. Vasilić, M. Petković, Lj. Zeković, *Surf. Coat. Technol.* **206** (2012) 2905

12. M. Petković, S. Stojadinović, R. Vasilić, I. Belča, Z. Nedić, B. Kasalica, U. B. Mioč, *Appl. Surf. Sci.* **257** (2011) 9555
13. M. Petković, S. Stojadinović, R. Vasilić, Lj. Zeković, *Appl. Surf. Sci.* **257** (2011) 10590
14. U. Mioč, S. Stojadinović, Z. Nedić, *Materials* **3** (2010) 110
15. S. Stojadinović, R. Vasilić, M. Petković, Z. Nedić, B. Kasalica, I. Belča, Lj. Zeković, *Electrochim. Acta* **55** (2010) 3857
16. S. Stojadinović, N. Radić, R. Vasilić, M. Petković, P. Stefanov, Lj. Zeković, B. Grbić, *Appl. Catal., B* **126** (2012) 334.

Journal of the Serbian Chemical Society

Trace and selective determination of cobalt(II) in water and salt samples using cathodic adsorptive stripping voltammetry in the presence of Pyrogallol Red

FOROOZAN HASANPOUR[1], HOSSEIN TEIMORI[2], MASOUD FOULADGAR[3]*
and MASOUMEH TAEI[1]

[1]Chemistry Department, Payame Noor University, 19395-4697 Tehran, Iran, [2]Cellular and Molecular Research Center, School of Medicine, Shahrekord University of Medical Sciences, Shahrekord, Iran and [3]Department of Biochemistry, Falavarjan Branch, Islamic Azad University, Falavarjan, Iran

Abstract: A sensitive and selective procedure is presented for the voltammetric determination of cobalt. The procedure involves an adsorptive accumulation of cobalt Pyrogallol Red (PGR) complex on a stationary mercury drop electrode, followed by cathodic stripping voltammetry measurement of the reduction current of the adsorbed complex at -1.17 V (*vs.* Ag/AgCl). The optimum conditions for the determination of cobalt include pH 11.0, 35 μM Pyrogallol Red, an accumulation potential of -0.9 V (*vs.* Ag/AgCl) and scan rate 80 mV s^{-1}. The peak current is proportional to the concentration of cobalt over the concentration range 5.0 to 280 ng mL^{-1} with a detection limit of 1 ng mL^{-1} and an accumulation time of 140 s. The method was applied to the determination of cobalt in analytical grade NaCl and water samples.

Keywords: adsorptive cathodic stripping voltammetry, Pyrogallol Red, Co(II) determination.

INTRODUCTION

Cobalt is an essential trace element, a component of vitamin B$_{12}$ and it is non-specific activator of several enzymes. However, cobalt toxicity causes different diseases. including asthma, contact dermatitis, lung cancer and bronchitis.[1,2] Cobalt(II) compounds can cause mutagenic effect in plants and mammal cells.[3] Due to insufficient data, the allowed concentration level of cobalt in drink water has not been reported but in fresh water for aquatic life, the recommended maximum concentration of total cobalt is 110 μg L^{-1}.[4] The concentrations of cobalt in drinking water are generally in the range of 0.1–5.0 μg L^{-1}.[5]

There are several methods for the determination of cobalt ions. The two most frequently used methods are flame atomic absorption spectrometry and electrothermal atomic absorption spectrometry.[6–8] However, to decrease the detection limit of these methods, usually pre-concentration methods, such as liquid and solid phase extraction,[9,10] cloud point extraction,[11–14] adsorption,[15,16] membrane filtration,[17] *etc.*, are used.

A rather simple method for the determination of heavy metals is based on adsorptive accumulation. Stripping adsorptive accumulation of metal chelates is a widely accepted analytical tool because of its high sensitivity, selectivity and inexpensive instrumentation. Adsorption of surface-active complexes, prior to the reduction step in adsorptive cathodic stripping voltammetry (ACSV), causes the formation of a monomolecular layer of complex species on the surface of the electrode. This is followed by electrochemical reduction either of the element or the ligand in the complex.[18] Due to the accumulation of most of the analyte in a mercury drop, the reduction current will be increased and the detection limit of the methods will be reduced.

Pyrogallol Red is well known as a complexing agent for some heavy metal ions.[19] It forms a selective and stable complex with cobalt(II).[20]

In this study, a simple adsorptive cathodic stripping voltammetry method was developed for trace determination of cobalt based on the effective accumulation of the cobalt(II)–Pyrogallol Red complex (Co(II)–PGR) on a stationary mercury drop electrode. The adsorbed complex was reduced through cathodic differential pulse polarography.

EXPERIMENTAL

Reagents

All employed chemicals were of analytical reagent grade (Merck, Fluka). Doubly distilled water was used throughout.

A fresh stock solution of Pyrogallol Red (Merck) in water (2×10^{-3} mol L^{-1}) was prepared every three days. A stock solution of cobalt(II) (1000 µg mL^{-1}) was prepared by dissolving cobalt nitrate hexahydrate in water and diluting to 250 mL; dilute solutions were prepared by diluting this solution with distilled water. Ammonia buffer (0.5 mol L^{-1}) was prepared by dissolving an appropriate volume of ammonia in water and diluting to 1.0 L. The pH of the solution was adjusted to 11.0 with hydrochloric acid solution (0.5 mol L^{-1}).

Apparatus

The electrochemical measurements realized using a computer driven µAUTOLAB type II analyzer equipped with a Metrohm VA STAND 663 and GPES ver. 4.9 software. The medium drop size was selected. A three-electrode arrangement with an Ag/AgCl, 3 mol L^{-1} KCl reference electrode, a platinum wire counter electrode and a multi-mode mercury drop electrode were used. The pH values were controlled by a Metrohm 691 pH meter.

Procedure

About 5 mL of sample solution containing 1–800 ng cobalt was pipetted into a 10 mL volumetric flask and pH was adjusted to 11.0 by addition of the ammonia buffer (pH 11.0).

PGR solution (180 µL, 2×10^{-3} mol L^{-1}) was added and the volume was adjusted to 10 mL with distilled water. The solution was transferred to the voltammetric cell. The stirrer was switched on and the solution was purged with argon gas for 5 min. A new drop was formed and accumulation was effected for 140 s at –0.9 V whilst stirring the solution. Then the stirrer was switched off, and the potential was scanned in a negative direction. When further volume of cobalt or PGR was added to the cell, the solution was deoxygenated with argon gas for 1 min.

Preparation of water and salt samples

Water samples were filtered using a 0.45 µm pore size membrane filter to remove suspended particles. A Metrohm UV-digester 705 with a temperature control was used.10 mL water sample was irradiated and decomposed for 2 h at 90 °C. The pH value was adjusted to 11.0 with ammonia buffer. Then the cobalt was determined using the recommended procedure.

One mL of a 0.5 mol L^{-1} NaCl salt (analytical grade) was transferred to the voltammetric cell and the pH was adjusted to 11.0 with ammonia buffer. Then the cobalt was determined using the recommended procedure.

RESULTS AND DISCUSSION

Adsorptive and voltammetric characteristics of the Co(II)–PGR complex

Preliminary experiments were performed to identify the general features that characterize the behavior of the C(II)–PGR complex at a dropping mercury electrode. No peak was found on cyclic voltammogram in a solution containing 1×10^{-4} mol L^{-1} PGR in ammonia buffer solution at pH 11.0 in the potential range 0 to –1 V.

The adsorption voltammograms of a solution of ammonia buffer at pH 11.0 containing PGR and after addition of Co(II) ions are shown in Fig. 1 as curve A and curves B–H, respectively. The peak potential of the reduction of adsorbed Co(II)–PGR in the ammonia buffer was –1.17 V. Cyclic voltammetry was used to investigate the electrode reaction. The Co(II)/Co(Hg) system showed irreversible behavior. This behavior was unchanged after the addition of PGR. The peak current of Co(II)–PGR *vs*. scan rate in the cyclic voltammetric mode was linear. This feature is characteristic of a reaction in which the reactant is adsorbed on the surface.[21]

The peak height increased with increasing deposition time. Cyclic voltammograms of the system between 0 to –1.5 V (*vs*. Ag/AgCl), after 0 and 60 s were obtained on a SMDE. The response increased dramatically when the accumulation period increased.

The apparent transfer coefficient could be estimated from the peak half-width, $W_{1/2}$, according to the Laviron Equation:[22]

$$\alpha n = \frac{2.44RT}{W_{1/2}F} = \frac{62.5}{W_{1/2}} \tag{1}$$

The average peak half-widths for more than 10 measurements were 60.05±±0.04 mV. From this value, an *αn* value of 1.04 was obtained. If the value of *α* was assumed to be 0.5, then a value for *n* of 2 was obtained. Therefore, the oxidation state of Co in the complex was 2. This result could be expected by comparison of the redox peak potential of Co(II)–PGR and Co(II)/Co(Hg) in Fig. 2. The peak height of Co(II)–PGR was found to depend on the PGR concentration as well as on cobalt concentration, the solution pH, the collection potential and the collection period.
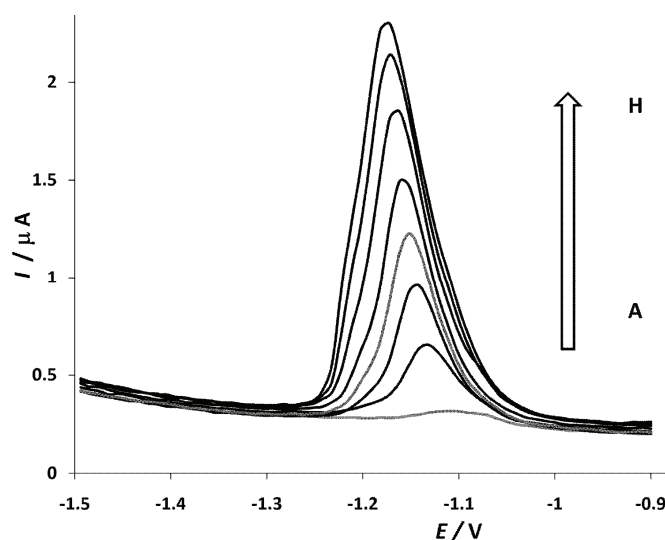
Fig. 1. Effect of Co(II) concentration on peak height of Ads voltammograms in ammonia buffer solution pH 11.0. Concentration of Co(II): A) 0.0; B) 32; C) 65; D) 139; E) 176; F) 201; G) 250; H) 265 ng mL^{-1}. [PGR] = 100 μmol L^{-1}; E_{acc} = –0.9 V; pulse height =100 mV.

Optimization of the parameters

Several parameters, *i.e.*, pH, scan rate, PGR concentration, and accumulation potential and time had to be optimized to achieve maximum sensitivity in the determination of the cobalt concentration.

Effect of pH. The influence of pH on the stripping peak current was studied in the pH range 7–12. As can be seen in Fig. 3, the peak height was small when the pH value was lower than 9.0, and the peak current was approximately independent of pH when the pH value exceeded 10.5. The reason for decreasing peak height could be attributed to the weak complexing ability of PGR at pH values lower than 9.0. An optimum value of pH 11.0 was selected for the further experiments.

Effect of the accumulation potential. The effect of accumulation potential on the stripping peak current of the complex was examined over the potential range

of 0.1 to –1.1 V. The peak current increased with increasing accumulation potential from 0.1 to –1.0 V. A potential of –0.9 V was selected as the optimized accumulation potential.
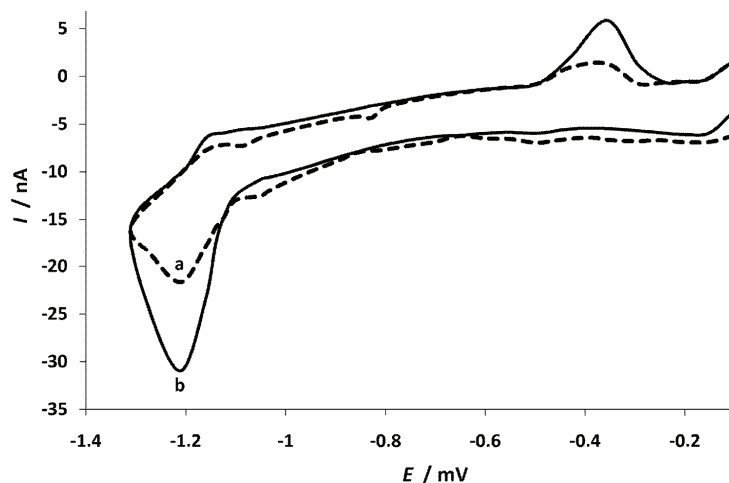
Fig. 2. Cyclic voltammograms of Hg electrode in the solution containing 50 ng mL^{-1} Co(II) for comparison of peak potential of a) Co(II)/Co(Hg) and b) Co(II)–PGR in 100 μmol L^{-1} PGR.
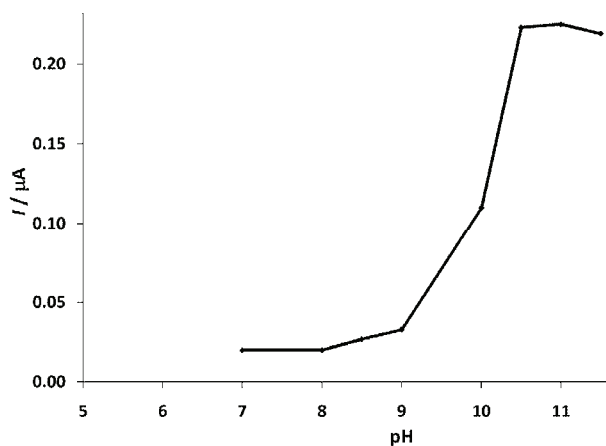
Fig. 3. Effect of pH on the cathodic peak current, after 80 s accumulation at –0.9 V, for 50 ng mL^{-1} of cobalt and 100 μmol L^{-1} PGR.

Effect of accumulation time. The effect of accumulation time on the peak current was also studied. The peak current increased with increasing accumulation time up to 140 s and then starts to level off at longer accumulation times. Therefore, 140 s was selected as the optimum accumulation time.

Effect of the PGR concentration. The peak current for cobalt increased with increasing PGR concentration up to 32 μmol L^{-1} PGR, and leveled off at higher concentrations. An optimum PGR concentration of 35 μmol L^{-1} was selected for the further experiments.

Effect of scan rate. The effect of scan rate on the peak current was studied in the range 10–120 mV s^{-1}. When the scan rate was increased from 10–80 mV s^{-1} (in the differential pulse mode), the peak current increased. However, at scan rates faster than 80 mV s^{-1}, there was no increase in the peak current height.

It was found that the peak current, I_p, of the complex varied linearly with potential scan rate ν (in the cyclic voltammetric mode). There was a linear relation between log I_p and log ν in the range 100 to 800 mV s^{-1}, with the a slope of 0.906, which indicates the target in the electrochemical process was adsorbed on the electrode surface.

Linear range, detection limit and reproducibility

Under the optimum experimental conditions, the calibration curve was linear over the range of 5.0 to 280 ng mL^{-1} at pH = 11.0 (ammonia buffer), 35 µmol L^{-1} PGR, accumulation potential of –0.9 V and accumulation time of 140 s, v = 80 mV s^{-1}. The detection limit $Y_{LOD} = \bar{X}_B + 3S_B$ (where Y_{LOD} is the signal for the detection limit, $\bar{X}_B$ is the mean of the blank signal and S_B is the standard deviation of the blank signal) was obtained as 1 ng mL^{-1}. The precision for seven determinations of 50 ng mL^{-1} of Co(II) was calculated to be 4 %.

Effect of foreign ions on the determination of cobalt

Possible interference by cations, anions and some surfactants were investigated in the adsorptive stripping voltammetric determination of cobalt by the addition of the interfering ion to a solution containing 50 ng mL^{-1} of cobalt using the optimized experimental conditions. The results of this study are given in Table I.

TABLE I. Maximum tolerable concentration of interfering species for a cobalt concentration of 50 ng mL^{-1}

Foreign ions and surfactant	Tolerance limit, mole ratio [interferent]/[sample]
Alkaline and alkaline earth metals, Mn^{2+}, Cu^{2+}, Se^{4+}, Cd^{2+} ,Al^{3+}, Tl^+, In^{3+}, Fe^{2+}	800
Ce^{3+}, Pb^{2+}, Ni^{2+}, CO_3^{2-}, Br^-, Cl^- ,NO_3^-, HCO_3^-, SO_4^{2-}	500
Ce^{3+}, Tl^{3+}, Cr^{3+}, Ag^+, Hg^{2+}, CH_3COO^-, CN^-	200
V^{4+}, La^{3+}, UO_2^{2+}, Zr^{4+},CPC	100
TritonX-305	50
TritonX-100	10

Application of the method for the determination of cobalt in real samples

The utility of developed method was tested by determining cobalt in analytical grade NaCl and water samples (Tables II and III, respectively), using the recommended procedure. The data obtained for samples spiked with cobalt showed good recoveries.

TABLE II. Determination of Co in NaCl salt in pH 11.0 ammonia buffer

Concentration of cobalt, ng mL^{-1}		Recovery, %
NaCl added	Total found	
0	5.74	–
8	13.2	96
11	16.48	98
14	19	96
17.8	23.98	101.8

TABLE III. Determination of Co in water samples

Concentration of cobalt, ng mL^{-1}		Recovery, %
Added	Found	
0.0	25.1	–
20.0	48.3	107.1
40.0	62.4	95.8
50.0	70.6	94.0
80.0	108.7	103.4

CONCLUSIONS

The applicability of the proposed method using adsorptive cathodic stripping voltammetry (ACSV) for trace determination of cobalt(II) ions, based on the accumulation of Co(II)–PGR on a stationary mercury drop and using differential pulse polarography for striping the mercury drop, was confirmed. This method has good selectivity for the determination of cobalt(II) in the presence of some other heavy metals and it was successfully employed for the analysis of water and NaCl salt samples. In addition, it has advantages, such as simplicity, rapidity and low detection limit, over some other methods.

ИЗВОД

СЕЛЕКТИВНО ОДРЕЂИВАЊЕ ТРАГОВА КОБАЛТА(II) У ВОДИ И УЗОРЦИМА СОЛИ ПРИМЕНОМ КАТОДНЕ АДСОРПЦИОНЕ СТРИПИНГ ВОЛТАМЕТРИЈЕ У ПРИСУСТВУ ПИРОГАЛОЛ ЦРВЕНОГ

FOROOZAN HASANPOUR[1], HOSSEIN TEIMORI[2], MASOUD FOULADGAR[3] и MASOUMEH TAEI[1]

[1]Chemistry Department, Payame Noor University, 19395-4697 Tehran, Iran, [2]Cellular and Molecular Research Center, School of Medicine, Shahrekord University of Medical Sciences, Shahrekord, Iran и [3]Department of Biochemistry, Falavarjan Branch, Islamic Azad University, Falavarjan, Iran

У овом раду је описан осетљив и селективан поступак за волтаметријско одређивање кобалта. Поступак укључује адсорпцију комплекса кобалт–пирогалол црвеног (PGC) на стационарној капљућој живиној електроди, чему следи мерење струје редукције адсорбованог комплекса катодном стрипинг волтаметријом на 1,17 V (према Ag/AgCl). Оптимални услови за одређивање комплекса су: pH 11,0, концентрација пирогалол црвеног од 35 μM, потенцијал адсорпције од −0,9 V (према Ag/AgCl) и брзина промене потенцијала од 80 mV s^{-1}. Струја пика је пропорционална концентрацији кобалта у опсегу 5,0–280 ng mL^{-1}, са границом детекције од 1 ng mL^{-1} и временом ад-

сорпције од 140 s. Метода је примењена за одређивање кобалта у NaCl аналитичког степена чистоће и узорцима вода.

REFERENCES

1. M. De Boeck, M. Kirsch-Volders, D. Lison, *Mutat. Res.* **533** (2003) 135
2. V. Verougstraete, A. Mallants, J. P. Buchet, B. Swennen, D. Lison, *Am. J. Res. Crit. Care Med.* **170** (2004) 162
3. D. Beyersmann, A. Hartwig, *Toxicol. Appl. Pharm.* **115** (1992) 137
4. http://www.env.gov.bc.ca/wat/wq/BCguidelines/cobalt/cobalt_over.html, (accessed on 3 Feb, 2012)
5. C. Rojas, V. Arancibia, M. Góme, E. Nagles, *Int. J. Electrochem. Sci.* **7** (2012) 979
6. Y. Cai, G. Jiang, J. Liu, *Talanta* **57** (2002) 1173
7. S. Cerutti, S. Moyano, J. A. Gásquez, J. Stripeikis, R. A. Olsina, L. D. Martinez, *Spect. Chim. Acta, B* **58** *(*2003) 2015
8. Y. Wang, X. Luo, J. Tang, X. Hu, Q. Xu, C. Yang, *Anal. Chim. Acta* **713** (2012) 92
9. P. Berton, E. M. Martinis, L. D. Martinez, R. G. Wuilloud, *Anal. Chim. Acta* **713** (2012) 56
10. R. S. Praveen, S. Daniel, T. P. Rao, *Talanta* **66** (2005) 513
11. D. Citak, M. Tuzen, *Food Chem. Toxicol.* **48** (2010) 1399
12. M. Ghaedi, A. Shokrollahi, F. Ahmadi, H. R. Rajabi, M. Soylak, *J. Hazard. Mater.* **150** (2008) 533
13. G. L. Donati, C. C. Nascentes, A. A. Nogueira, M. A. Z. Arruda, J. A. Nóbrega, *Microchem. J.* **82** (2006*)* 189
14. J. Chen, K. Chuan Teo, *Anal. Chim. Acta* **434** (2001) 325
15. H. Minamisawa, H. Iwanami, N. Arai, T. Okutani, *Anal. Chim. Acta* **378** (1999) 279
16. X. Liu, Z. Fang, *Anal Chim. Acta* **316** (1995) 329
17. I. Narin, M. Soylak, *Anal. Chim. Acta* **493** (2003) 205
18. Y. Li, Y.-H. Xie, F. Zhou, H. Guo, *Electroanalysis* **18** (2006) 976
19. T. Korenaga, S. Motomizu, K. Tôei, *Anal. Chim. Acta* **104** (1979) 369
20. A. A. Ensafi, A. Aboutalebi, *Sensors Actuators, B* **105** (2005) 479
21. A. J. Bard, L. R. Faulkner, *Electrochemical methods – Fundamentals and Applications*, Wiley, New York, USA, 1980, p. 179
22. E. Laviron, *J. Electroanal. Chem.* **52** (1974) 355.

A solidification/stabilization process for wastewater treatment sludge from a primary copper smelter

DRAGANA IVŠIĆ-BAJČETA[1]*, ŽELJKO KAMBEROVIĆ[2], MARIJA KORAĆ[1] and MILORAD GAVRILOVSKI[1]

[1]*Innovation Center of the Faculty of Technology and Metallurgy in Belgrade, University of Belgrade, Karnegijeva 4, 11000 Belgrade, Serbia and* [2]*Faculty of Technology and Metallurgy, University of Belgrade, Karnegijeva 4, 11000 Belgrade, Serbia*

Abstract: Wastewater treatment sludge from a primary copper smelter is characterized as hazardous waste that requires treatment prior to disposal due to its significant contents of heavy metals and arsenic. The aim of the presented study was to investigate the feasibility and the effectiveness of a solidification/stabilization process of the sludge using fly ash and lime as binders. The effectiveness of the process was evaluated by Unconfined Compressive Strength (UCS) testing, leaching tests (EN 12457-4 and Toxicity Characteristic Leaching Procedure (TCLP)) and Acid Neutralization Capacity (ANC) tests. All the samples reached the target UCS value of 0.35 MPa. The calcium to silicon concentration ratio (c_{Ca}/c_{Si}), determined by X-ray fluorescence analysis, was identified as main factor governing strength development. Inductively coupled plasma-optical emission spectrometry analyses of solutions after leaching tests showed excellent stabilization of Cu, Ni, Pb and Zn (above 99 %) and arsenic (above 90 %) in samples with high $Ca(OH)_2$ content. Results of the ANC test indicated that the buffering capacity of solidified material linearly depended on Ca concentration in FA and lime. Samples with 20 % of binder having 50 % of FA and 50 % of lime met all the requirements for safe disposal.

Keywords: fly ash; lime; heavy metals; unconfined compressive strength; leaching tests.

INTRODUCTION

Wastewaters produced during gas cleaning and cooling processes and electrolytic refining in the Copper Smelter RTB Bor in Serbia are currently discharged without previous treatment. These wastewaters, the amount of which occasionally have reached several hundred cubic meters per hour, represent a major environmental problem for the western Balkans and the Danube Basin.[1]

725

The construction of a wastewater treatment (WWT) plant is planned during Bor Copper Smelter – Acid Plant Modernization Project in next few years. Generation of WWT sludge, bearing significant amount of heavy metals and arsenic, is estimated at 11.2 t h^{-1}.[2] This copper WWT sludge is characterized as hazardous waste in the Waste Catalogue (also adopted in Serbian law[3]) by the code 19 02 05*, and must be chemically and physically treated prior to disposal in order to prevent secondary pollution. The aim of presented study was to investigate the feasibility and the effectiveness of a solidification/stabilization (S/S) process of future copper WWT sludge as an addendum to the ongoing project.

An S/S process is recognized as "the best demonstrated available technology" for treatment of industrial waste containing heavy metals.[4,5] It involves mixing a binding reagent with contaminated media or waste, changing the chemical and physical properties of hazardous materials to make it suitable for land disposal. Cement is the most frequently used binder for S/S treatment of hazardous waste.[5] In order to improve economic and environmental effects of the process, nowadays, cement is increasingly replaced by fly ash (FA), which is an excellent example of a cost effective utilization of a waste product.[6] In Serbia alone, about 5 million tons of ash is generated annually during coal combustion in thermal power plants.[7] Besides benefits in the use of waste materials such as FA, compared to other more expensive binders in S/S processes, FA increases the pH region for heavy metals immobilization and improves the mechanical properties of the treated waste.[6] In the S/S treatment of heavy metals- and arsenic-bearing waste, FA as a binder is usually used individually[8,9] or in mixtures with Portland cement and lime.[4,10]

The quality of an S/S process is determined by the compressive strength and leaching resistance of the treated material. Development of strength and immobilization of metal ions in waste primarily depend on the products of hydration reaction of pozzolanic components in FA (SiO_2, Al_2O_3, CaO and Fe_2O_3).[11] The optimum amounts of pozzolans present in waste, or their addition, can lead to better mechanical properties of a material.[12,13] The hydration reaction is influenced by the nature and relative quantity of the waste.[14] It is generally believed that heavy metals ions present in the waste can affect the pozzolanic reaction by precipitation of insoluble Ca–heavy metals[15] and Ca–As[16,17] salts on the new formed hydrates. Precipitated salts can prevent further hydration and inhibit the development of the hydrated structure.[18,19]

The leaching behavior of stabilized waste is pH dependent and it is mainly controlled by the alkaline nature and acid buffering capacity of the S/S matrix. pH value of leachates should be within the range of the minimum solubility of the metals,[20,21] although Polat *et al.*[22] and Srivastava *et al.*[23] reported excellent stabilization behavior of FA over a wide pH range. For each individual waste stream, it is necessary to provide an integrated approach for the proper selection

of binder that would ensure stabilization of the pollutants and prevent their migration into the environment.

The presented study investigates the possibility of employment of an S/S process on the sludge from the WWT plant in the future modernized RTB Bor Copper Smelter – Acid Plant using FA and mixture of FA and lime as binders. Process optimization was achieved by varying content and composition of the binder. UCS Testing and the standardized leaching tests: EN 12457-4, TCLP and ANC tests were used to determine the effect of the binder on strength development and heavy metals/arsenic ion immobilization. The results provide a novel clarification of the effect of pozzolans on the quality of the S/S process.

EXPERIMENTAL

The experiments were conducted on synthesized sludge that chemically and physically corresponded to the future WWT sludge defined by the Modernization Project with 50.67 mass % water content and a density of 1.55 kg dm^{-3}. Basic materials for the synthesis of WWT sludge were systematically collected dusts from the electro-filters of the reactor and converter in the Bor Copper Smelter. The synthesis of the sludge under laboratory conditions was described in detail previously.[24]

FA from the Bor heating plant, Serbia was used as the sole binder and in mixtures with commercial grade hydrated lime ("Nexe", Jelen Do). The FA originated from the combustion of lignite coal from the Kolubara mines in Serbia. Due to conditions of storage and transport, the FA had to be dried at 105 °C for 24 h and sieved in order to obtain <100 µm fraction for the further experiments.

The chemical composition of the sludge, FA and lime, and the mineralogical composition of the sludge were determined by X-Ray fluorescence (XRF) and X-Ray diffraction (XRD) analyses, respectively. The pollution potentials of the sludge and FA were evaluated by EN 12457-4 and TCLP tests. These two leaching tests have both been adopted into Serbian Law[3] for the testing of the hazardous characteristics of waste and are described below.

In order to optimize the composition of the S/S mixture, eight series of experiments with different additions and compositions of binder were prepared. The compositions of the S/S mixtures are presented in Table I.

TABLE I. Compositions of the S/S mixtures, mass %

| Sample | Binder composition | | Sludge:binder |
	FA	Lime	
S95F100	100	–	95:5
S90F100	100	–	90:10
S85F100	100	–	85:15
S80F100	100	–	80:20
S75F100	100	–	75:25
S80F90L10	90	10	80:20
S80F75L25	75	25	80:20
S80F50L50	50	50	80:20

The sludge, fly ash and lime were thoroughly mixed for 10 min with a mechanical mixer at room temperature to form a homogeneous paste. The paste was cast in two portions into

plastic molds dimensions 5×5×5 cm^3 and vibrated in order to remove entrapped air and excess water. The specimens were cured according to the ASTM C109 Standard:[25] 24 h under wet towels to meet the requirement of 99 % moisture; after 3 days, the samples were removed from the mold and left to cure in air.

The UCS test provides basic information on material stabilization. According to the U.S. Environmental Protection Agency (USEPA), 0.35 MPa is the minimum compressive strength required for the safe disposal of stabilized waste.[5] The UCS values of the samples were determined after 7, 14 and 28 days of curing using a servo hydraulic testing machine type Instron 1332-retrofitted Fast track 8800 with a maximum load of 100 kN. The presented results are the mean measurements of three samples.

Leaching procedures allow the characterization of the environmental behavior of wastes and S/S products using the solubility and/or availability of pollutants as limits. TCLP[26] and EN 12457-4[27] are very common tests, standardized and accepted in the USA and the EU for evaluating the pollution potential of materials. The EN 12457-4 test was conducted after 28 days of curing to simulate long-term leaching processes at disposal sites. Distilled water was used as the extraction fluid at a liquid to solid (L/S) ratio of 10. Crushed samples (<10 mm, 100 g) were leached by rotating for 24 h in polyethylene bottles. TCLP tests, simulating the worst-case scenario, were conducted after curing the samples for 180 days. For this purpose, 50 g of ground samples (<10 mm) were placed in polyethylene bottle together with 1.0 dm^3 of extraction fluid (L/S 20). A solution of glacial acetic acid having a pH value of 2.88±0.05 was used as the extraction fluid. The mixture was agitated for 18±2 h. After the leaching tests, the solutions were filtered through a blue ribbon filter paper. The metal concentrations in the solutions were determined by atomic absorption spectroscopy (AAS) (after the EN 12457-4 test) and by inductively coupled plasma-optical emission spectrometry (ICP-OES) (after the TCLP test).

The ANC test provides information on the buffering (acid neutralization) capacity of S/S materials and thus their resistance to various environmental conditions at landfills. The ANC test was adapted from the Environment Canada procedure described by Stegemann and Cote.[28] The test consists of a series of batch extractions with increasing additions of nitric acid, ranging from distilled water to 2.0 M HNO$_3$ over 11 equal increments. The samples cured for 180 days were crushed, sieved to <125 μm and dried at 60 °C to constant weight. Samples of 3 g were placed in 50 cm^3 polyethylene bottles together with distilled water and 1 M HNO$_3$ to give an L/S ratio of 10 and the desired acid addition. The bottles were sealed and rotated for 48 h prior to centrifugation and measurement of the pH. Measured pH values were plotted against the equivalent mass of acid added per kg of dried material, eq. kg^{-1}, for each individual mixture.

In order to determine the chemical composition of the S/S samples and its influence on the compressive strength and leaching resistance of the waste, XRF analysis was performed using a Niton XRF instrument.

The redox potential (*Eh*) and pH values of each filtrated solution after the leaching tests were measured. These data were used to determine ions species in aqueous solutions from *Eh*–pH diagrams. The *Eh*–pH diagrams were designed in the Outokumpu HSC Chemistry ver. 4 (HSC4) software package based on the concentrations of metals ions obtained by ICP-OES analysis of the solutions.

RESULTS AND DISCUSSION

Chemical composition of the sludge, FA and lime, determined by XRF analysis, are presented in Table II. The metals in the sludge were in the form of sulfates and hydroxides and in FA in the form of oxides. By its chemical composition, the employed FA belonged to class F according to the ASTM C618 standard.[29] XRD Analysis of the sludge, Fig. 1, revealed that the main mineral phase was gypsum ($CaSO_4 \cdot 2H_2O$).

TABLE II. Chemical composition of the sludge, FA and lime, mass %; n.d. – not detected

Element	Sludge	FA	Lime
Fe	13.38	8.02	0.02
Ca	12.49	10.68	54.09
S	10.81	2.14	0.12
Zn	5.15	0.02	n.d.
Cu	4.04	0.13	n.d.
Pb	0.86	0.03	n.d.
As	0.65	0.01	n.d.
K	0.12	0.56	n.d.
Mn	0.09	0.08	n.d.
Ni	0.08	0.01	n.d.
Se	0.02	n.d.	n.d.
Si	1.95	17.16	0.14
Al	n.d.	7.06	0.03
Sb	0.89	n.d.	n.d.
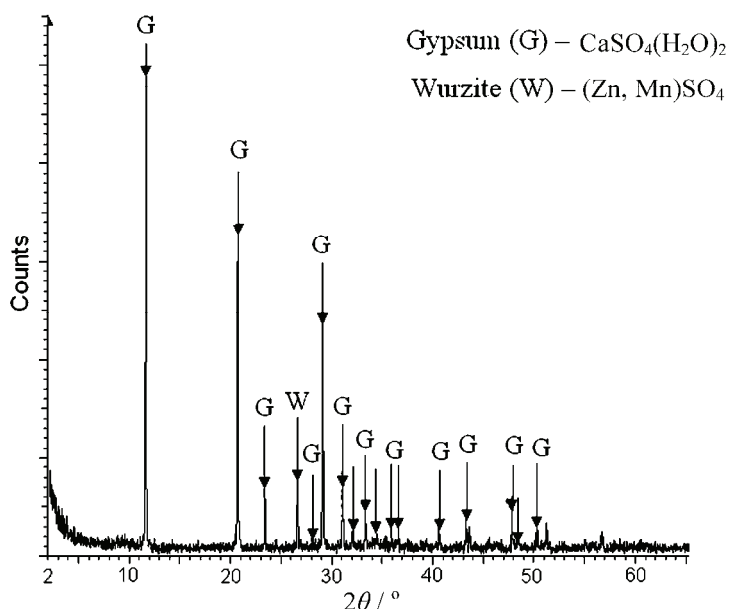
Fig. 1. XRD Analysis of the sludge.

The pollution potentials of the sludge and FA, evaluated by the EN 12457-4 and TCLP tests, are presented in Table III. The EN 12457-4 test showed leaching of Zn and Sb and the TCLP test showed leaching of Zn and Cu above the regulation limits.

TABLE III. Pollution potential of the sludge and FA compared with national legislative for non-hazardous waste

Metal	EN 12457-4, mg 100 g^{-1} dried material			TCLP, mg dm^{-3}		
	Sludge	FA	Limit	Sludge	FA	Limit
Fe	<0.1	<0.1	–	3.9	<0.1	–
Ca	604.2	638.9	–	951.4	1784.7	–
Zn	16.0	0.1	5	1232.6	0.05	250
Cu	<0.1	<0.1	5	26.2	<0.1	25
Pb	<0.3	<0.3	1	3.45	<0.3	5
As	0.14	<0.1	2	2.6	<0.1	5
Ni	0.42	<0.2	1	7.4	<0.2	20
Sb	0.27	<0.1	0.07	3.1	<0.1	15

The main metal constituents of the solidified material, as determined by XRF analysis and presented in Table IV, were Fe, Ca, Zn, Cu and Si, which were expected considering the nature of the sludge and FA.

TABLE IV. Concentrations of metals in the solidified samples, *c* / mass %

Sample	Fe	Ca	Zn	Cu	Si	Pb	As	Ni	Mn
S95F100	13.06	10.06	5.61	4.60	2.71	0.90	0.69	0.08	0.08
S90F100	11.79	9.40	4.44	3.93	3.47	0.75	0.58	0.07	0.06
S85F100	12.03	8.59	4.07	3.67	4.23	0.69	0.53	0.05	0.07
S80F100	10.64	8.66	3.38	2.90	4.99	0.58	0.45	0.06	0.07
S75F100	11.53	10.74	3.23	2.80	5.75	0.57	0.44	0.05	0.07
S80F90L10	10.94	11.03	3.49	3.13	4.65	0.61	0.46	0.05	0.06
S80F75L25	10.06	13.03	3.77	3.18	4.14	0.61	0.50	0.05	0.06
S80F50L50	8.00	13.53	3.57	2.81	3.28	0.57	0.47	0.05	0.05

The results of the testing after 7, 14 and 28 days for systems of different compositions are given in Table V.

All samples, with a few exceptions for systems with a high lime content, exceeded the required value of 0.35 MPa for UCS even after 7 days of curing. In systems with FA as binder, the UCS increased with increasing binder content from 5 to 20 %, but decreased in the sample with 25 % of the binder. The reason for this was optimal water to solid ratio, which was considered to be between 0.6–0.4.[5] Water was introduced into the system within the sludge (50.67 mass % water content). Insufficient amount of water for the hydration reaction, below 0.4, as was the case was with 25 % added binder, resulted in a low value of UCS.

TABLE V. Results of UCS testing after 7, 14 and 28 days

Sample	UCS / MPa		
	7th day	14th day	28th day
S95F100	0.40	0.45	0.57
S90F100	0.39	0.57	0.66
S85F100	0.40	0.66	0.78
S80F100	0.40	0.79	1.00
S75F100	0.40	0.58	0.84
S80F90L10	0.51	0.67	0.73
S80F75L25	0.35	0.47	0.64
S80F50L50	0.32	0.73	0.55

Addition of lime resulted in a decrease in the UCS after 28 days of curing. In the work performed by Antiohos and Tsimas, this was explained by insufficient silica present in the samples to react completely with the excess of hydrated lime.[12] The remaining unreacted $Ca(OH)_2$ exerted a negative affect on the strength development and possibly some durability properties.[30] The assumption about more than the optimum amount of $Ca(OH)_2$ for the pozzolanic reaction was confirmed by calculating the Ca to Si concentration ratio (c_{Ca}/c_{Si}) in the samples determined by XRF analysis. This ratio provides information of the available pozzolans for the formation of cementious phases in the waste. The correlation between the UCS, developed after 28 days of curing, and the corresponding c_{Ca}/c_{Si} ratio is presented in Fig. 2. An increase in the c_{Ca}/c_{Si} ratio in the system resulted in a reduction of the UCS due to higher amount of unreacted $Ca(OH)_2$. The highest compressive strength was achieved for a c_{Ca}/c_{Si} ratio of 1.73 (sample S80F100), which was the lowest one. The ratios of the Ca concentration with the concentration of others elements were also analyzed but there was no agreement with the results of the UCS. This confirmed the major role of the silica concentration in governing the development of the UCS in waste samples.[31]

The results of leaching tests are presented in Table VI. After the EN 12457-4 test, the concentrations of Cu, Fe, Ni, Pb and Zn were below the detection limits for AAS analysis. Concentrations of As were in the range from 0.10 to 0.18 mg 100 g^{-1} dried material, and Sb concentration from 0.10 to 0.29 mg 100 g^{-1} dried material, Table VI. Variations in the results could be considered as errors of the measuring instrument due to the very low concentrations. Unlike EN 12457-4 test, the results of the TCLP tests, Table VI, showed the presence of heavy metals ions in the leachates due to the more aggressive leaching conditions. The addition of 25 % FA as binder resulted in reductions in the leaching by 84.5 % Cu, 73.4 % Ni, 90.7 % Pb and 87.9 % Zn compared to the untreated sludge (Table III). The addition of lime resulted even higher reductions in the leaching of heavy metals. For the sample with 50 % lime in the binder, the concentrations of Cu, Ni, Pb and Zn were reduced by 99.6, 99.7, 99.7 and 99.8 %, respectively. The concentrations

of As in the treated samples were very similar and the results evidenced no corre-lation between As leaching and FA/lime addition, although it was reduced by over 90 % compared to the leaching from the untreated sludge. The concentra-tions of Sb were below the detection limit for most samples.
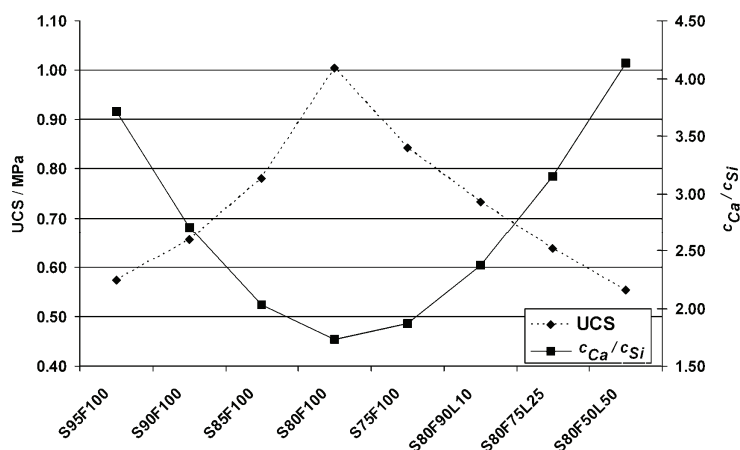
Fig. 2. UCS Values after 28 days and the corresponding Ca to Si concentration ratios (c_{Ca}/c_{Si}) in the solidified samples, determined by XRF analysis.

Although both tests are accepted in the National Law, the results of the EN 12457-4 and TCLP tests gave different toxicological characterization of the same waste. The Zn concentrations in the solutions after the EN 12457-4 tests were below 0.1 mg 100 g^{-1} dried material for all samples and the S/S waste could be characterized as non-hazardous. However, according to the TCLP results, samples S95F100, S90F100, S85F100 and S80F100 had Zn leached concentrations above the concentration limits defining non-hazardous waste. The pH value of the ex-traction fluid was the main parameter governing the leaching of pollutants. The aggressive extraction fluid in the TCLP test can neutralize all alkalinity in an S/S sample and lead to much higher leaching of metals. The alkalinity of S/S waste samples depends on the content of CaO and Ca(OH)$_2$ derived from FA and lime. The Ca concentration in samples in the form of CaO and Ca(OH)$_2$ can be cal-culated according to FA and lime additions (Ca concentration in the binder). The influence of the alkalinity (presented as the Ca concentration in the binder, c_{Ca} / / mass %) on heavy metals leaching during the TCLP tests is presented in Fig. 3. A larger amount of Ca in the form of CaO and Ca(OH)$_2$ in the samples resulted in a reduction of heavy metals leaching.

The *Eh* and pH values of each filtrated solution after leaching were measured. These data were used for metal ions speciation in *Eh*–pH diagrams. Diagrams were realized in the HSC4 software package as combined diagrams in metal–Ca–

TABLE VI. Results of EN 12457-4 test, mg 100 g^{-1} of dried material and TCLP test, mg dm^{-3}

Test	As	Sb	Cu	Fe	Ni	Pb	Zn
			S95F100				
EN 12457-4	0.11	0.12	<0.10	<0.10	<0.20	<0.30	<0.10
TCLP	0.12	<0.10	14.85	0.06	4.34	1.58	621.00
			S90F100				
EN 12457-4	0.18	0.16	<0.10	<0.10	<0.20	<0.30	<0.10
TCLP	0.18	<0.10	10.60	0.03	3.46	1.34	405.70
			S85F100				
EN 12457-4	0.17	0.19	<0.10	<0.10	<0.20	<0.30	<0.10
TCLP	0.33	<0.10	8.52	0.01	3.13	0.96	385.60
			S80F100				
EN 12457-4	0.15	0.24	<0.10	<0.10	<0.20	<0.30	<0.10
TCLP	0.30	0.50	7.05	0.06	2.76	0.87	279.30
			S75F100				
EN 12457-4	<0.10	0.29	<0.10	<0.10	<0.20	<0.30	<0.10
TCLP	0.19	0.20	4.07	0.01	1.97	0.32	148.90
			S80F90L10				
EN 12457-4	<0.10	0.14	<0.10	<0.10	<0.20	<0.30	<0.10
TCLP	0.20	0.27	2.00	0.01	1.30	0.20	71.46
			S80F75L25				
EN 12457-4	0.17	<0.10	<0.10	<0.10	<0.20	<0.30	<0.10
TCLP	0.25	<0.10	0.78	0.01	0.43	0.12	43.44
			S80F50L50				
EN 12457-4	0.11	<0.10	<0.10	<0.10	<0.20	<0.30	<0.10
TCLP	0.20	<0.10	0.09	0.24	0.02	0.01	1.79
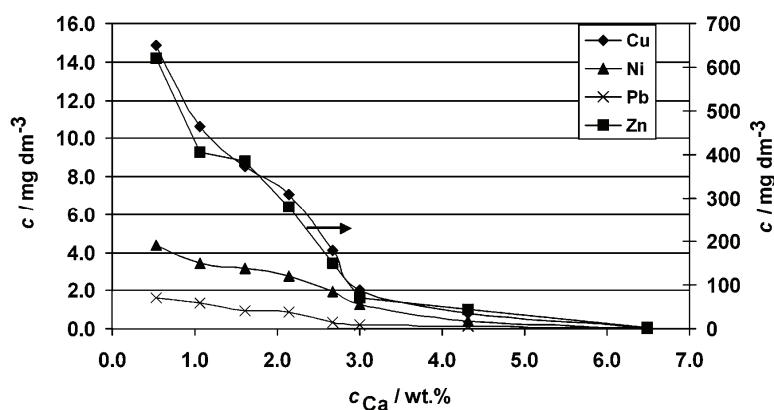
Fig. 3. Dependence of the concentrations of heavy metals, c, in solutions after leaching on the Ca concentration in the binder, c_{Ca}.

–S–H$_2$O system based on different ion concentrations in the solutions after TCLP leaching. Zinc and arsenic were selected due to their very different behavior

during leaching: the As concentrations remained almost constant while the Zn concentrations were reduced by 99 % with the addition of lime. The *Eh*–pH diagram of As and Zn are shown in Fig. 4, combined with their concentrations in solution after leaching, c / mg dm^{-3}. Different additions and compositions of binder did not effect arsenic leaching. In all systems, As remained in the soluble form as $HAsO_3^-$. Concentrations of As were in the range from 0.1 to 0.3 mg dm^{-3} in solutions after the TCLP leaching test of stabilized waste. The As concentration was ten times reduced compared to its concentration in solution of untreated sludge although in the same area of $HAsO_3^-$. This implies that, beside the formation of insoluble Ca–As salts, the binder effects the stabilization of As ions by increasing the pH value of the matrix and, possibly, by other physicochemical interactions. In contrast to arsenic, different amounts and composition of binder affected Zn leaching. The addition of FA caused an increase in the pH value of the material and zinc transformed from its soluble form into insoluble oxides. The Zn concentration in the S75F100 solution was reduced to below the regulation limits (200 mg dm^{-3}). Lime addition resulted in better Zn stabilization and in sample with 50 % of $Ca(OH)_2$ in binder (S80F50L50), zinc leaching was reduced by 99.8 %.
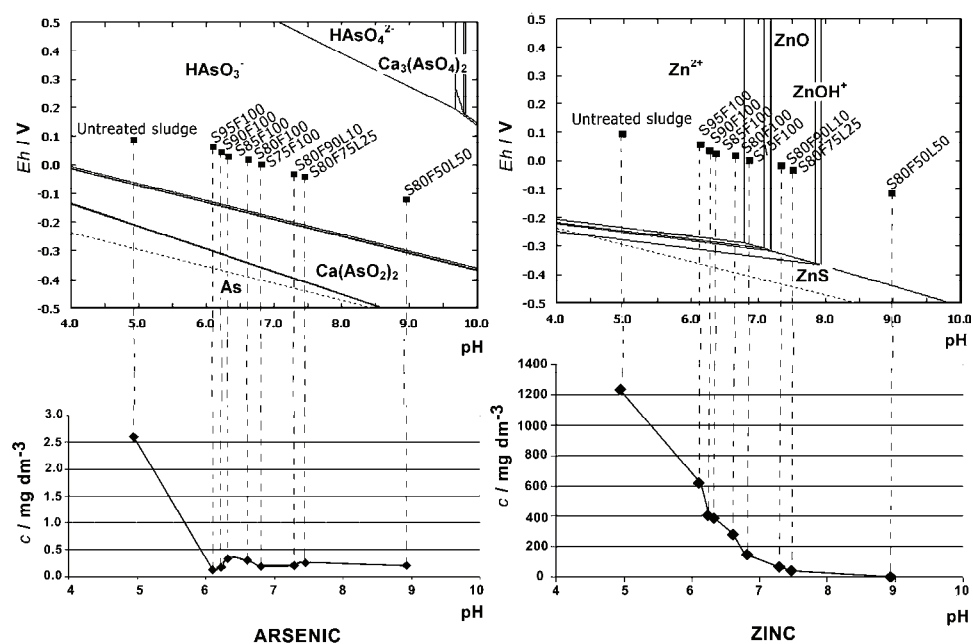
Fig. 4. *Eh*–pH diagrams of As and Zn for the systems metal–Ca–S–H_2O at 25 °C with their concentration in solution after leaching, *c*.

The ANC test was conducted for determining the buffering capacity of the S/S samples. Since the S/S process is pH-dependent, sufficient acid neutralizing capacity is necessary to stabilize the heavy metals. The ANC test results presented in Fig. 5 show the pH value of leachates as a function of added equivalents of nitric acid per kilogram of dried sample, ANC in eq. kg^{-1}. These figures are known as titration curves and a plateau at a defined pH describes the waste buffer capacity. A material has a larger buffering capacity if it can neutralize more equivalents of acid.
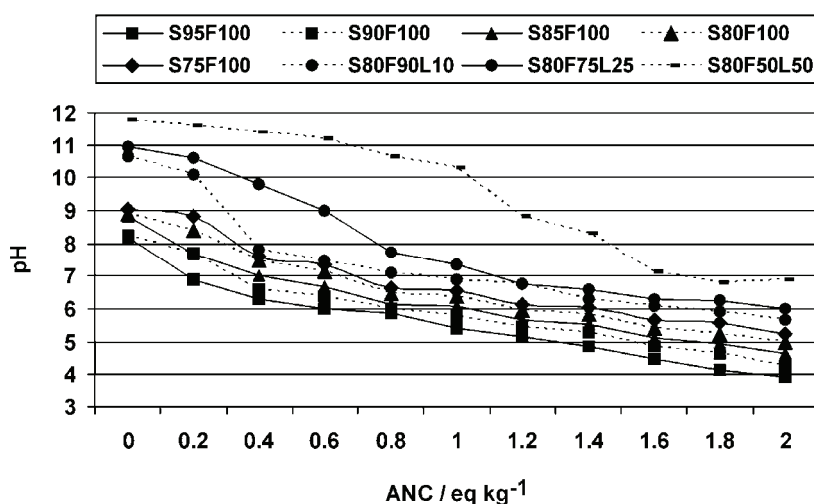
Fig. 5. ANC Test results.

Samples with FA as binder had initial pH values between 8 and 9, and a lower decrease at around pH 6. The reason for this was, primarily, the presence of gypsum and other sulfates with a buffering capacity around pH 5–6,[32] and a significant content of iron and zinc in the WWT sludge having a buffering capacity also around pH 5–6.[33] The amount of acid that a stabilized material could neutralize (at pH 7) increased with the amount of FA in the samples, from 5 to 25 %. The samples with added lime had greater buffering capacities. The acid neutralization capacity, ANC, depends on the amount of alkaline reagents in the S/S waste, while pozzolanic agents have negative effects on the buffering capacity with nitric acid, due to the substitution of basic reagents by acidic oxides.[34] In addition, alkalis in FA are combined in the glassy phase and the amorphous silica in FA might react with the alkalis rendering them less available.[21] In the literature, the ANC was found to be a function of the calcium containing compounds in the binder,[35,36] which was also confirmed in present study. Buffering capacity of stabilized waste (at pH 7) linearly depended on the concentration of calcium in the FA and lime (Ca concentration in binder, c_{Ca} / mass %), Fig. 6.
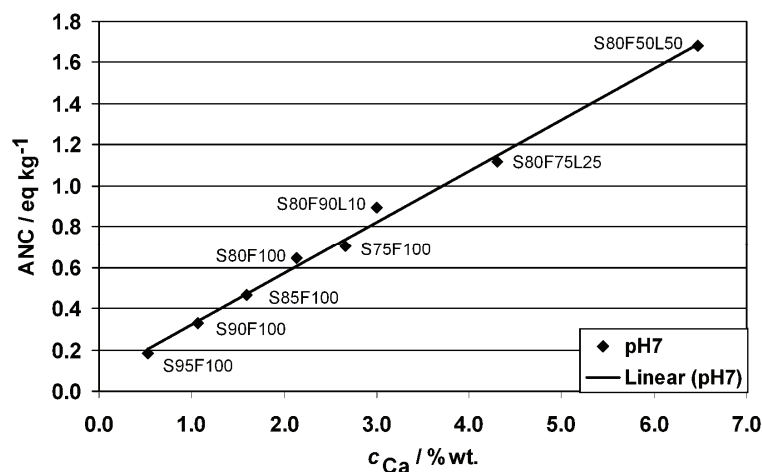
Fig. 6. *ANC* at pH 7 as a function of the Ca concentration in the binder, c_{Ca}.

Stegemann and Cote proposed that the S/S product should have an *ANC* greater than 1 eq. kg^{-1} before reaching pH 9 in order to be disposed at a segregated landfill.[37] Only sample S80F50L50 met this condition. The reasons why the other samples did not fulfill this condition were primarily the chemical composition of the WWT sludge and the use of FA as the main binder.

CONCLUSIONS

In the presented study, it was observed that solidification and stabilization of WWT sludge from a Copper Smelter bearing high amounts of heavy metals and arsenic was possible using FA in mixtures with lime. All samples with different addition and composition of binder had *UCS* above the required 0.35 MPa after 28 days of curing. The c_{Ca}/c_{Si} ratio was found to be the main factor governing strength development. With addition of lime, there was not enough silica present in waste to react with the surplus of Ca(OH)$_2$. Unreacted Ca(OH)$_2$ caused a decrease in the *UCS* values. In the leachates after the EN 12457-4 test, the concentration of Zn and Ni were under 0.1 and 0.2 mg 100 g^{-1} dried material, respectively. Different additions and compositions of binder had no influence on the leaching As and Sb. On the other hand, the results of the TCLP tests revealed stabilization of Cu, Ni, Pb and Zn by over 99 % and As by over 90 % with addition of 50 % of lime to the FA. Heavy metals leaching was reduced with increasing calcium concentration in the form of CaO and Ca(OH)$_2$ (Ca concentration in binder), probably due to the formation of insoluble Ca–heavy metals salts and by increasing the pH value of the waste. The difference in the extraction fluids employed in the EN 12457-4 and TCLP leaching tests resulted in different toxicity characterization of the same waste. Acid neutralization (buffering) capacity, *ANC*, of waste increased with addition of FA and more with the addition of lime.

The results showed a linear dependence of the buffering capacity on the Ca concentration in the form of CaO and Ca(OH)$_2$. However, only the sample with 50 % of lime added to the FA had an *ANC* value above required one. The reasons for this were the high gypsum and heavy metals concentrations in the WWT sludge and employment of FA as the binding agent. Sample with optimal addition of 20 % of binder containing 50 % of lime mixed with FA met all the requirements for safe disposal. Although the addition of lime to FA decreased the *UCS*, it was necessary for a better stabilization of the heavy metals and an increase in *ANC* value. Results of conducted tests indicate that the optimum amount of pozzolans present in the material could lead to the successful solidification/stabilization of WWT sludge bearing high amounts of heavy metals and arsenic.

ИЗВОД

ПРОЦЕС СОЛИДИФИКАЦИЈЕ/СТАБИЛИЗАЦИЈЕ ЗА ТРЕТМАН ОТПАДНИХ ВОДА МУЉА ИЗ ПРИМАРНЕ ТОПИОНИЦЕ БАКРА

ДРАГАНА ИВШИЋ-БАЈЧЕТА[1], ЖЕЉКО КАМБЕРОВИЋ[2], МАРИЈА КОРАЋ[1] и МИЛОРАД ГАВРИЛОВСКИ[1]

[1]*Иновациони центар Технолошко–металуршког факултета у Београду, Универзитет у Београду, Карнегијева 4, 11000 Београд и* [2]*Технолошко–металуршки Факултет, Универзитет у Београду, Карнегијева 4, 11000 Београд*

Муљ који настаје третманом отпадне воде из примарне топинице бакра представља опасан отпад који се мора третирати пре одлагања услед високог садржаја тешких метала и арсена. Циљ презентованог рада је испитивање изводљивости и ефикасности процеса солидификације/стабилизације овог муља коришћењем летећег пепела и хидратисаног креча као агенса за стабилизацију. Ефикасност процеса се одређивала мерењем притисне чврстоће (УЦС) солидификата, тестовима лужења (EN 12457-4 и *Toxicity Characteristic Leaching Procedure* (TCLP)) и тестом капацитета за неутрализацију киселине (ANC test). Сви испитивани узорци су имали притисну чврстоћу изнад захтеваних 0,35 MPa. Однос концентрација калцијума и силицијума (c_{Ca}/c_{Si}) у узорцима, одређен рендгенско–флуоресцентном анализом, је идентификован као главни фактор развоја притисне чврстоће. Оптичка емисиона спектрометријска анализа са индуковано спрегнутом плазмом раствора након тестова лужења је показала одличну стабилизацију Cu, Ni, Pb и Zn (изнад 99 %) и арсена (изнад 90 %) у узорцима са високим садржајем Ca(OH)$_2$. Резултати ANC теста указују на то да пуферски капацитет солидификованог материјала линеарно зависи од концентрације Ca у летећем пепелу и кречу. Узорак са 20 % везива састава 50 % летећи пепео и 50 % хидратисани креч испуњава све захтеване услове да буде безбедно одложен.

(Примљено 16. јула, ревидирано 19. новембра 2012)

REFERENCES

1. M. Korać, Ž. Kamberović, *Metalurgija – J. Metallurgy* **13** (2007) 41
2. Environmental impact assessment, New Smelter and Sulphuric Acid Plant RTB Bor, http://www.rtb.rs/media/dokumenti/nt/EIA_Volume_1.pdf (accessed 23.03.2012).

3. *Regulation on categories, testing and classification of waste*, Official Gazette of the Republic of Serbia, No. 56/10 (in Serbian)
4. T. S. Singh, K. K. Pant, *J. Hazard. Mater.* **131** (2006) 29
5. R. Malviya, R. Chaudhary, *J. Hazard. Mater.* **137** (2006) 267
6. D. Dermatas, X. Meng, *Eng. Geol.* **70** (2003) 377
7. M. Komljenović, Z. Baščarević, V. Bradić, *J. Hazard. Mater.* **181** (2010) 35
8. L. M. Camacho, S. H. Munson-McGee, *J. Hazard. Mater.* **137** (2006) 144
9. D. H. Moon, D. Dermatas, *J. Hazard. Mater.* **141** (2007) 388
10. M. Erdem, A. Özverdi, *Hydrometallurgy* **105** (2011) 270
11. M. Ahmaruzzaman, *Prog. Energ. Combust.* **36** (2010) 327
12. S. K. Antiohos, S. Tsimas, *Cement Concrete Res*. **34** (2004) 769
13. S. Lim, W. Jeon, J. Lee, K. Lee, N. Kim, *Water Res.* **36** (2002) 4177
14. J. N. Diet, P. Moszkowicz, D. Sorrentino, *Waste Manage.* **18** (1998) 17
15. X. C. Qiao, C. S. Poon, C. R. Cheeseman, *J. Hazard. Mater.* **139** (2007) 238
16. W. H. Choi, S. R. Lee, J. Y. Park, *Waste Manage.* **29** (2009) 1766
17. C. Sullivan, M. Tyrer, C.R. Cheeseman, N. J. D. Graham, *Sci. Total Environ.* **408** (2010) 1770
18. A. K. Minocha, N. Jain, C. L. Verma, *Cement Concrete Res.* **33** (2003) 1695
19. M. F. M. Zain, M. N. Islam, S. S. Radin, S. G. Yap, *Cement Concrete Comp.* **26** (2004) 845
20. C. F. Pereira, M. Rodríguez-Piñero, J. Vale, *J. Hazard. Mater.* **82** (2001) 183
21. X. D. Li, C. S. Poon, H. Sun, I. M. C. Lo, D. W. Kirk, *J. Hazard. Mater.* **82** (2001) 215
22. M. Polat, E. Guler, E. Lederman, H. Cohen, *Waste Manage.* **27** (2007) 482
23. S. Srivastava, R. Chaudhary, D. Khale, *J. Hazard. Mater.* **153** (2008) 1103
24. D. Ivšić-Bajčeta, Ž. Kamberović, M. Korać, B. Anđelić, V. Trujić, in *Proceedings of the XIX International Scientific and Professional Meeting "Ecological Truth, EcoIst 11"*, Bor, Serbia, 2011, p. 420
25. American Society for Testing and Materials, *ASTM C109: Standard test method for compressive strength of hydraulic cement mortars (using 2-in. or [50-mm] cube specimens), Annual Book of ASTM Standards,* 2001, p. 83
26. United States Environmental Protection Agency (USEPA), *Test Methods for Evaluating Solid Waste, SW- 846, Method 1311: Toxicity Characteristic Leaching Procedure (TCLP)*, 1992
27. European Committee of Standardization, *EN 12457-4: Characterization of waste - Leaching - Compliance test for leaching of granular waste materials and sludges - Part 4: One stage batch test at a liquid to solid ratio of 10 l/kg for materials with particle size below 10 mm (without or with size reduction), CEN/TC 292*, 2002, p. 28
28. J. A. Stegemann, P. L. Cote, *Waste Manage.* **10** (1990) 41
29. American Society for Testing and Materials, *ASTM C618: Standard specification for coal fly ash and raw or calcined natural pozzolan for use in concrete, Annual Book of ASTM Standards*, 2005
30. M. S. Konsta-Gdoutos, S. P. Shah, *Cement Concrete Res.* **3** (2003) 1269
31. S. K. Antiohos, V. G. Papadakis, E. Chaniotakis, S. Tsimas, *Cement Concrete Res.* **37** (2007) 877
32. Q. Y. Chen, M. Tyrer, C. D. Hills, X. M. Yang, P. Carey, *Waste Manage.* **29** (2009) 390
33. A. Coz, A. Andrés, S. Soriano, J. R. Viguri, M. C. Ruiz, J. A. Irabien, *J. Hazard. Mater.* **164** (2009) 755

34. A. Coz, A. Andrés, S. Soriano, Á. Irabien, *J. Hazard. Mater.* **109** (2004) 95
35. A. G. Kim, *Fuel* **85** (2006) 1403
36. C. S. Poon, K. W. Lio, *Waste Manage.* **17** (1997) 15
37. J. A. Stegemann, P. L. Cote, *Sci Total Environ.* **178** (1996) 103.

Discovery of uranium mineralizations in the rhyolite–granite complex in the Jabal Eghei area of southern Libya

JOVAN KOVAČEVIĆ[1], MEHDI BASHIR TEREESH[2], MIRJANA B. RADENKOVIĆ[3]
and ŠĆEPAN S. MILJANIĆ[4*]

[1]*Geological Institute of Serbia, P. O. Box 42, 11000 Belgrade, Serbia,* [2]*Tajoura Nuclear Research Centre. P. O. Box 30878, Tajoura, Libya,* [3]*University of Belgrade, Vinča Institute of Nuclear Sciences, P. O. Box 522, 11001 Belgrade, Serbia and* [4]*University of Belgrade, Faculty of Physical Chemistry, P. O. Box 47, 11158 Belgrade 118, Serbia*

Abstract: During an investigation of the Jabal Eghei area in southern Libya and the production of geological maps on a scale of 1:250 000 (Tibesti sector, sheet Wadi Eghei NF 34-1 and NF 34-2), regional prospecting for mineral raw materials was performed. A radiometric survey of the observed targets at the sites indicated two significant uranium mineralizations in rhyolites, and some smaller ones in granites that are in close contact with rhyolites. Rhyolites are located in the central part of the investigated region. They cut through granite rocks. The first mineralization is in the central part of the rhyolite region, which is mostly composed of silificated rhyolites. The second one was discovered near the granite–rhyolite contact zone, characterized by the presence of silicified breccia rocks. These findings were confirmed by laboratory measurements of more than seventy samples collected in the area, using high-resolution gamma-ray spectrometry. The concentrations of uranium in these mineralizations were found to range from approx. 50 mg kg^{-1} to more than 600 mg kg^{-1}. The latter value is about 240 times above the Earth's average. Besides uranium, these measurements have also given concentrations of thorium and potassium. Additional geochemical analysis was performed on samples taken from locations where uranium anomalies were discovered using the ICP-MS technique, in which the concentrations of more than forty elements were determined. The uranium mineralizations are accompanied by increased contents of silver (up to 17 times), arsenic (up to 8 times), molybdenum (up to 50 times), mercury (up to 9 times), and lead (up to 14 times), with regards to the Clark values. These results warrant a continued investigation of this region because of potential interest in the discovery of nuclear mineral raw materials.

Keywords: terrestrial radioactivity; Jabal Eghei; gamma-ray spectrometry; uranium; mineralization; geological map.

741

INTRODUCTION

Studies of naturally occurring radioactive materials (NORM) are of great interest to many fields of human activity. They usually involve the determination of the uranium, thorium and potassium contents in rocks and soil, since their natural radioactive isotopes are among the most abundant on Earth. Their radioactivity is dependent on three natural radioactive series: the *uranium series* originating with ^{238}U, the thorium series originating with ^{232}Th, and the actino–uranium series originating with ^{235}U, as well as on the singly occurring potassium isotope ^{40}K. As the ratio of natural uranium isotopes ^{235}U to ^{238}U is very low (0.007), the contribution of ^{235}U to environmental radioactivity is negligible. In terms of their abundances, potassium is considered a major element, having crustal abundance with a Clarke value of 2.5 %, while U and Th occur as trace elements with Clarke values of 2.50 and 13 mg kg^{-1}, respectively.[1]

Natural environmental radiation mainly depends on the content of radionuclides in the outcropping rock. Igneous rocks, especially granites, exhibit higher radioactivity, due to geochemical behavior of the above elements during geogenesis. From a practical point of view, uranium is the most important among them. Granitic rocks can serve as uranium source rocks for secondary areas of uranium enrichment that occurs by movement of groundwater through fractures in these rocks or through porous zones within rocks adjacent to the granitic rocks. It dissolves uranium and transports it to a place favorable for its deposition.

The history of geological investigations of the Tibesti Massif and its surroundings is relatively long. The first explorers reached the Massif in the mid-1860s. The remoteness and general inaccessibility of the area made these investigations much slower and more complicated than those in other parts of Libya. After almost half a century of inactivity, French and Italian military experts produced the first sketches and rough topographic maps of Tibesti in the early 1900s. Significant changes in the approach to geological investigations began when the Industrial Research Center (IRC) of Libya was founded in 1970. As the official institution for systematic geological and mining investigations, the IRC commissioned the production of geologic maps at a scale of 1:250,000. The area of direct interest was essentially not hitherto investigated. This lack of previous data, as well as some significant uranium anomalies indicated by preliminary measurements at the site, makes this renewed investigation particularly important. These measurements at Jabal Eghei were performed in order to detect nuclear mineral resources while collecting geological samples. The radiometric survey of the observed targets was realized using portable instruments.

The main objectives of this work were to: 1) investigate the radioactivity of rhyolite–granitoide rocks in the area of Jabal Eghei – Kangara Massif that originates from uranium, thorium and potassium, 2) advance knowledge of the mining potential of this interesting region, especially regarding uranium and 3) contri-

bute to the establishment of a baseline map of environmental radioactivity levels.[2] With these goals in mind, attention was focused on measurements of the radioactivity of ^{238}U, ^{232}Th and ^{40}K isotopes. They are commonly used to determine contents of the corresponding elements in investigated objects. During the course of this work, however, unusual anomalies in uranium-based radioactivity of the terrain were discovered, and accordingly investigations were extended to several other elements, as well as to the recognition of the rock types and corresponding geological aspects of the area, including the production of a geological map, all based on measurements of numerous geological samples collected during the regional geological mapping of Jabal Eghei (Tibesti sector, sheet Wadi Eghei NF 34-1 and NF 34-2).

The data obtained from gamma spectroscopy measurements was also employed to assess the radiological risk in this area,[2] by calculating the corresponding radiation hazard indices and related quantities, in a way analogous to that recently applied in some similar cases.[3,4]

A combination of terrain work (sample collection and preliminary investigation on site), laboratory measurements (determination of contents of elements), and data analysis and interpretation was applied. It was expected to gather necessary data about geological composition, structure, magmatism, mineralization control factors, geochemical and geophysical characteristics. Based on these data, a rough interpretation of the conditions and characteristics of the mineralization environment could be made. High-resolution gamma-ray spectrometry was used to measure the radioactivity of all the collected samples. From the obtained data, contents of the corresponding elements were calculated. They were additionally checked by ICP-MS (Inductively Coupled Plasma Mass Spectroscopy) analysis for comparison. Same method was used to determine concentrations of about forty other elements appearing in minerals. In the case of potassium, the X-ray fluorescence (XRF) method was used for some samples, in addition to the above techniques.

EXPERIMENTAL

Study area

The investigated area of Jabal Eghei is located in the farthest southeastern part of Libya, near the border with Chad. The area is a part of the Tibesti Mountains massif, which is the largest massif in the Sahara. In a morphological sense, the investigated region belongs to rocky deserts at altitudes between 720 and 1120 m. The main geomorphologic feature of the terrain is a rhyolite mass in its central part. The photograph given in Fig. 1 shows the typical appearance of the mass. The area composed of granitoide rocks is mostly flattened due to Eolian erosion, but there are large prominent ridges made of quartzite, gneiss or scorn. There are also large wades in the northern part, which are most favorable for the movement of field vehicles. The investigated region is characterized by a desert climate, with almost no precipitation. There are no inhabited places in the area or in the wider surroundings of approxi-

mately five hundred kilometers in diameter. The investigated area is about 12 km long and 5 km wide.

Fig. 1. Photograph of the rhyolite region in Jabal Eghei exhibiting anomalous radioactivity.

Sample collection and preparation

A total of 110 samples were collected by geological experts in the second half of 2010, from numerous locations in the specified area (Kangara Massif rhyolite, Jabal Eghei). The quantity of each sample was ≈1 kg. Some samples were rocky, while some were mixtures of rocks and sand. The samples were of different geological composition, including granite, rhyolite, granitoide, silification rhyolite and apilite, depending on the type of the natural stretcher of the area. The collecting of the samples was complicated by the desert environment, lack of communications and the general remoteness of the investigated area.

Radiometric surveys of observed spots on the entire massif of rhyolites (about 60 square kilometers), which lie over granitoide rocks, were realized using either a GR-110 scintillation counter or a portable γ-spectrometer GR-130-minispec (with a sodium iodide detector), both made by Exploranium, Canada. The measured profiles were at a distance of about 1 km from each other, for cases without lithologic changes or radioactive anomalies. Radioactive anomalies were registered at two sites in rhyolites. One of them was an area of 100 m×100 m, the other one the area of 50 m×20 m. At these locations, the sampling points were closer to each other: on average, one sample was analyzed per area of 10 m×10 m.

A selection of about seventy samples, based on a preliminary radiometric survey of observed targets at the sites, was subjected to laboratory measurements. Samples were ground in a ball mill, sieved through the 0.2-mm mesh, dried at a temperature slightly above 100 °C to a constant weight, and then homogenized. Each sample was placed in the standard 450 mL Marinelli beaker, sealed hermetically and stored for at least four weeks before counting, to allow the in-growth of uranium and thorium decay products, and achievement of equilibrium between ^{238}U and ^{232}Th and their respective progeny, *i.e.*, to ensure secular equilibrium between ^{226}Ra and its products.

Counting and radioactivity analysis

Radioactivity was measured using standard gamma spectrometry[5,6] to determine the concentrations of ^{238}U, ^{232}Th and ^{40}K isotopes in the samples. Measurements were performed using a gamma spectrometry system with a high-purity germanium (HPGe) detector (Canberra), having a relative efficiency of 23 % and a resolution of 1.8 keV at the 1332.5 keV ^{60}Co gamma line.

The efficiency calibration was performed using a certified standard reference soil material (MIX-OMH-SZ, National Office of Measures, Budapest), spiked with ^{22}Na, ^{57}Co, ^{60}Co, ^{89}Y, ^{133}Ba and ^{137}Cs in the cylindrical Marinelli beaker geometry.

Other utilized methods

As a rule, gamma spectrometry measurements are very selective and highly reliable for the determination of both isotope concentrations and abundances of the corresponding elements. However, in order to check the results obtained by the radioactivity measurements, these results were compared with those obtained by ICP-MS analysis of all samples for U and Th, and also by XRF analysis of some samples for K, because the ICP-MS method is not at all a reliable for the analysis of potassium. X-Ray fluorescence (XRF) is a method of non-destructive elemental analysis based on the emission of characteristic fluorescent X-rays from a sample excited by high-energy X-rays. The spectral line used for the analysis of potassium was $K\alpha_{1,2}$ at 0.3742 nm. The ICP-MS method was also used for geochemical analysis and characterization of samples exhibiting high uranium concentrations through the contents of more than forty micro elements appearing in them, because the ICP-MS is widely accepted as the most powerful method for the analysis and quantification of trace elements, especially metals. It is based on ionizing the sample with inductively coupled plasma and then using a mass spectrometer to separate and measure those ions. Due to this, its sensitivity is of the order of ng kg^{-1}. It is now commonly used in both environmental analyses and geological applications.

RESULTS AND DISCUSSION

General geological characteristics of the investigated area

During the field investigation of the basement in the Jabal Eghei area, the following types of rocks were recognized: amphibolites, metavulcanites, mica-schists, phyllites, calc-silicates, marbles, graphite-schists, quartz–sericite–chlorite schists, quartz–biotite–garnet–staurolite–muskovite schists, hornblende–plagioclase–epidote schists, quartzites, gneisses, serpentinites and other metamorphic rocks.

The identified mineral associations represent metamorphism of rocks of the Lower Tibestian as a regional metamorphism in the interval from the upper greenschist to the lower amphibolite facies. Contact alterations in the zones of contact between granitoids and metamorphites make the geological setting of the research area even more complicated (schists with wollastonite–idocrase–calcite––diopside association and similar rocks). During the syntectonic intrusion of magmatic rocks, partial mixing of metamorphites and granitoids occurred, which resulted in the formation of the parts of the basement in which metamorphic rocks cannot be distinguished from intrusives. Large masses of gneiss rocks occur frequently in these areas. There are also areas in the peripheral parts of the large post-tectonic granitoid intrusions, where foliation in metamorphic rocks is concordant with contacts between granites and metamorphites.

Magmatic rocks. Constituent parts of the consolidated basement are petrolgically different intrusive magmatic rocks, mostly of granitoid affinity. Synchro-

nous with the collisional events, large plutonic bodies of syntectonic igneous rocks were intruded and shaped. Large post-collisional granitoid intrusives were formed at the end of the Proterozoic and during the Lower Paleozoic.[7] Intrusive magmatic rocks constitute the largest part of the basement. They are spatially related to the central and eastern parts of the area made of metamorphic and magmatic rocks.

Granite. Granite is the most common magmatic rock of the basement. These rocks make discontinuous NNE–SSW-striking zones. Granite has largest extension in the investigation area. In the large granitic bodies, the syntectonic character of the magmatites is reflected by well-developed secondary ruptures, along which shearing occurred. These ruptures are echelons arranged in plan view. Macroscopically, these are leucocratic medium-grained to coarse-grained rocks made of orthoclase, albite, quartz and biotite. Frequent and significant variations in the granite mineral composition, mostly in the peripheral parts of large intrusives, which results in changes in the rock type; thus transitions toward granodiorite and diorite are often noticed.

Rhyolite. Large occurrences of rhyolite were noticed in the central part of sheet NF 34-1. The rhyolite lies above metamorphic and igneous rocks of the basement. As resistant rocks, rhyolites make morphologically conspicuous relief forms. Petrologically, these rocks are rhyolites (and porphyrites) of pinkish, reddish and red–brown color. Scarce phenocrysts of potassium feldspars and spherical grains of quartz lie in a matrix composed of microcrystalline quartz and feldspars.

Based on the identified types of rocks (a description of these rocks was left out due to space shortage), the geological map of the area was constructed.[8] The map is given in Fig. 2.

Gamma-ray measurements and specific activity determinations

The background radiation and the samples were counted for 60,000 seconds. The 63.28 keV ^{234}Th gamma ray line and the 1001.03 ^{234m}Pa gamma ray line were used to determine the ^{238}U activity concentration, although the latter one, which is very weak, could only be used for uranium-rich samples. The ^{232}Th activity concentration was determined using the 338.42 and 911.07 keV ^{228}Ac gamma lines. The activities of ^{40}K were determined directly from the 1460.8 gamma line.

After completion of the measurement, the peak areas in the spectrum were calculated. Following the spectrum analysis, count rates for each detected photopeak and the activity per sample mass (specific activity) for each of the detected nuclides were calculated. The specific activity A (Bq kg^{-1}) of a radionuclide is calculated using the following equation:

$$A = \frac{I(E_\gamma)}{mtP_\gamma(E_\gamma)\varepsilon(E_\gamma)} \qquad (1)$$

where $I(E_\gamma)$ is the number of counts in a given peak area, corrected for background peaks of a peak at energy E, t is the counting time (s), m is the mass of the sample (kg), $P_\gamma(E_\gamma)$ is the probability of disintegration with E_γ (transition probability) and $\varepsilon(E_\gamma)$ is the detection efficiency for energy E_γ. Obtained specific activities of ^{238}U, ^{232}Th and ^{40}K are given in Table I.
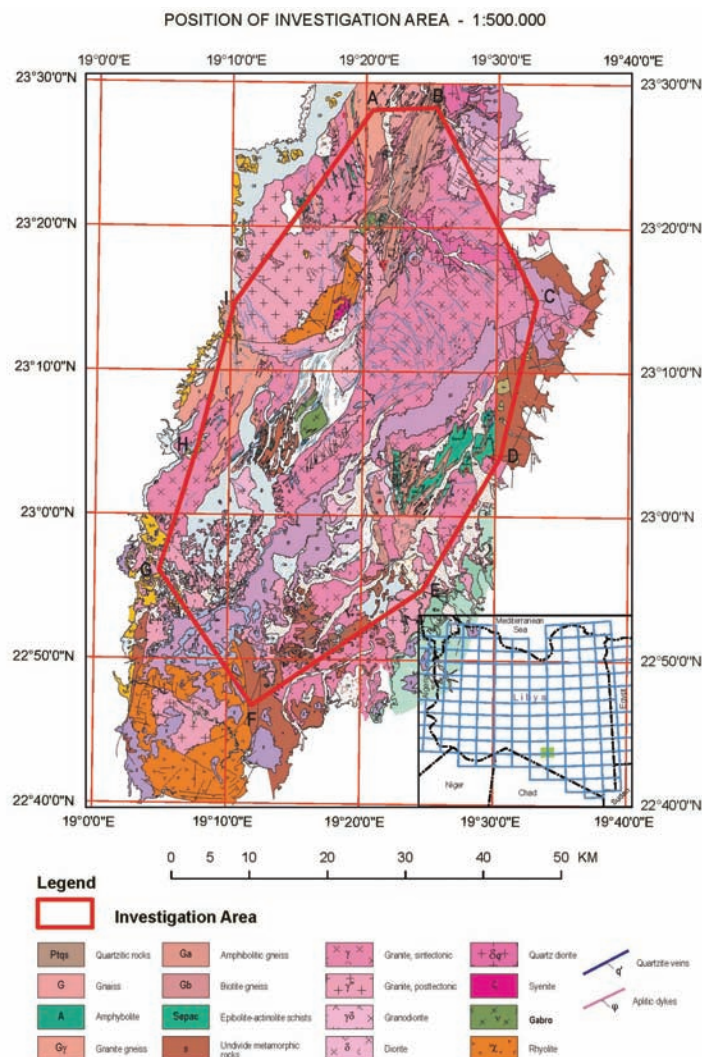
Fig. 2. Geological map of the Jabal Eghei area and the map of Libya with the investigated area highlighted in green.

TABLE I. Specific activities (A / Bq kg^{-1}) of ^{238}U, ^{232}Th and ^{40}K in samples from Jabal Eghei, obtained from gamma spectrometric measurements (values in bold show anomalous radio-activity with regards to the local background level for uranium)

Sample		^{238}U	^{232}Th	^{40}K	Rock type
No	Code				
1	186	81±15	53±4	1261±76	Rhyolite
2	187	74±10	60±6	1281±86	Rhyolite
3	188	83±12	64±6	1433±94	Rhyolite
4	191	154±21	88±7	1386±86	Granitoide
5	193	125±20	88±7	1462±91	Contact zone q-vein/rhyolite
6	194	64±15	55±5	790±55	q-vein
7	198	91±15	54±5	1170±76	Rhyolite
8	200	87±16	50±5	1157±75	Silificated rhyolite
9	201	99±17	32±4	1763±111	Silificated rhyolite
10	202	177±23	83±7	1591±99	Silificated rhyolite, fault zone
11	203	146±17	147±12	1546±104	Silificated rhyolite
12	205	130±13	101±8	1245±82	Granite
13	207	123±14	96±8	1597±104	Breccia silificated
14	208	180±20	91±8	1749±118	Silificated rhyolite
15	209	377±37	122±9	1155±75	Granite
16	210	173±22	93±7	1513±93	Contact rhyolite–granite
17	211	98±19	81±6	1512±94	Contact rhyolite–granite
18	212	63±13	73±6	1383±86	Rhyolite
19	213	119±19	75±6	1485±94	Rhyolite
20	214	140±13	92±8	1576±100	Rhyolite
21	215	184±24	78±7	1401±89	Rhyolite
22	216	139±16	101±9	1495±99	Silificated rhyolite
23	217	122±14	101±9	1651±109	Contact rhyolite–granite
24	219	140±20	82±7	1067±69	q-breccia
25	220	67±11	129±10	2304±145	Rhyolite
26	222	104±12	71±6	1551±101	Rhyolite
27	223	104±17	80±7	1545±96	Breccia silificated
28	225	69±12	57±5	890±59	Rhyolite
29	226	101±12	82±7	1240±82	Silificated rhyolite
30	227	92±11	85±7	1729±112	Silificated rhyolite
31	230	–	–	–	Rhyolite-breccia
32	231	–	–	–	Rhyolite-breccia
33	234	114±18	59±5	1092±72	Fault zone
34	235	171±23	88±7	1447±92	Rhyolite
35	237	140±14	58±6	561±45	q-breccia
36	238	66±11	24±3	322±25	q-breccia (fault zone)
37	239	98±13	37±3	877±57	Tuff
38	240	284±32	150±11	1517±95	Aplite vein
39	241	448±48	221±15	1210±78	Aplite
40	242	62±14	81±7	1533±97	Silificated rhyolite
41	243	122±18	93±7	1350±86	Silificated rhyolite
42	**244**	**1176±78**	63±7	875±65	Rhyolite
43	**245**	**3097±185**	68±9	529±47	Rhyolite

TABLE I. Continued

Sample		^{238}U	^{232}Th	^{40}K	Rock type
No	Code				
44	**246**	**3272±194**	64±9	593±50	Rhyolite
45	248	151±14	55±5	995±68	Silificated rhyolite
46	249	62±8	58±5	1048±72	Silificated rhyolite
47	267	64±9	61±6	1148±79	Gabbro
48	268	112±11	55±5	1044±70	Rhyolite
49	269	104±16	43±4	1284±85	Rhyolite
50	270	16±5	11±1	256±20	Silificated rhyolite
51	271	0	14±2	132±13	Silificated rocks
52	272	73±13	62±5	1131±73	Contact rhyolite–granite
53	273	111±16	66±6	1204±78	Amphipolite pyritized
54	274	68±14	64±5	1123±72	Schistose rhyolite
55	275	0	72±7	1120±76	Silificated rhyolite
56	**620**	**1515±98**	26±3	893±67	Rhyolite
57	**621**	**2788±168**	61±9	983±74	Rhyolite
58	**622**	**3570±229**	62±7	750±53	Rhyolite
59	**624**	**7477±458**	0	140±20	q-breccia
60	701	111±13	60±5	1374±88	Rhyolite
61	702	126±14	104±8	1251±76	Granite
62	706	332±33	136±9	1333±83	Granite
63	707	103±12	61±5	1468±94	Rhyolite
64	708	51±8	39±4	777±54	Granite
65	709	182±22	70±6	1296±82	Granite
66	710	184±21	68±6	1288±81	Rhyolite
67	712d	62±12	39±4	1742±106	Granite
68	713	104±16	64±5	1774±108	Rhyolite
69	2775	73±11	63±5	1242±77	Granite
70	2776d	82±15	59±5	1342±83	Rhyolite
71	2778d	147±19	80±6	1451±90	Rhyolite

Concentrations of uranium, thorium and potassium in the samples

Specific activities of radioisotopes given in the above table were converted into concentrations of corresponding elements, according to the following expression:

$$F_\mathrm{E} = A_\mathrm{I} \frac{M_\mathrm{I}}{\lambda_\mathrm{I} N_\mathrm{A} f_\mathrm{I}} C \tag{2}$$

where F_E is the fraction of element E in the sample, A_I is the measured specific activity of the isotope I (Bq kg^{-1}), M_I, λ_I, and f_I are the atomic mass (kg mol^{-1}), the decay constant (s^{-1}), and the fractional atomic abundance in nature, respectively, of the radioisotope considered, N_A is Avogadro's number, while C is a constant with a value of 10^6 for U and Th and 10^2 for K. In this way, elemental concentrations are expressed as mg kg^{-1} for uranium and thorium, and as percen-

tages (%) for potassium. For inter-comparison, these data, together with the results of ICP-MS analysis, and XRF analysis for some samples, were collected and are given in Table II.

TABLE II. Concentrations (*F*) of U, Th and K in samples collected in the Jabal Eghei area

Sample		U concentration, mg kg⁻¹			Th concentration, mg kg⁻¹			K concentration, %	
No	Code	Gamma	ICP-MS	XRF	Gamma	ICP-MS	XRF	Gamma	XRF
1	186	6.5±1.2	1.86		13.0±1.1	11.7		4.16±0.25	
2	187	6.0±0.8	2.38		14.8±1.4	13.3		4.22±0.28	
3	188	6.7±1.0	2.45		15.7±1.5	15.4		4.73±0.31	
4	191	12.4±1.7	6.37		21.8±1.7	22.4		4.57±0.28	
5	193	10.1±1.6	6.12		21.6±1.7	22.9		4.82±0.30	
6	194	5.2±1.2	1.45		13.4±1.2	12.3		2.60±0.18	
7	198	7.3±1.2	2.89		13.4±1.2	11		3.86±0.25	
8	200	7.1±1.3	3.69		12.3±1.1	12.6		3.81±0.25	
9	201	8.0±1.4	0.99		8.0±0.9	5.1		5.82±0.37	
10	202	14.3±1.8	6.29		20.5±1.7	22.7		5.25±0.33	4.7
11	203	11.8±1.4	7.75		36.2±2.9	32.8		5.10±0.34	
12	205	10.6±1.1	4.62		24.9±2.0	21.5		4.10±0.27	
13	207	10.0±1.1	1.63		23.6±2.0	17.5		5.27±0.34	
14	208	14.6±1.6	9.7		22.5±2.1	18.2		5.77±0.39	
15	209	30.6±3.0	21.8		30.1±2.2	28.9		3.81±0.25	3.6
16	210	14.0±1.8	4.21		22.9±1.8	23.5		4.99±0.31	
17	211	7.9±1.5	1.56		19.9±1.6	16.7		4.99±0.31	4.6
18	212	5.1±1.1	1.16		18.0±1.4	17.8		4.56±0.29	
19	213	9.7±1.5	2.14		18.5±1.5	18.2		4.90±0.31	
20	214	11.3±1.1	4.7		22.6±1.9	19.8		5.20±0.33	
21	215	14.9±1.9	7.06		19.3±1.6	16.2		4.62±0.29	
22	216	11.3±1.3	3.67		25.0±2.2	17.1		4.93±0.33	
23	217	9.9±1.1	2.02		24.9±2.2	17.3		5.45±0.36	
24	219	11.3±1.7	2.41		20.3±1.6	14.8		3.52±0.23	
25	220	5.4±0.9	4.7		31.9±2.6	15.7		7.60±0.48	
26	222	8.4±0.9	4.16		17.4±1.6	15.1		5.11±0.33	
27	223	8.4±1.4	1.25		19.6±1.6	13.1		5.10±0.32	
28	225	5.6±1.0	1.55		13.9±1.2	11.3		2.94±0.20	
29	226	8.2±1.0	1.15		20.2±1.8	9.1		4.09±0.27	
30	227	7.4±0.9	3.87		21.1±1.8	5.4		5.70±0.37	
31	230	–	175.5		–	1.43		–	
32	231	–	40.9		–	0.23		–	
33	234	9.2±1.5	4.87		14.6±1.3	18.1		3.60±0.24	
34	235	13.8±1.9	1.6		21.6±1.8	10.7		4.77±0.30	
35	237	11.3±1.2	3.77		14.4±1.5	9.6		1.85±0.15	
36	238	5.4±0.9	1.48		5.9±0.6	4.6		1.06±0.08	
37	239	8.0±1.0	1.11		9.1±0.8	8.5		2.89±0.19	
38	240	23.0±2.6	14.1		36.9±2.7	38.7		5.00±0.31	4.5
39	241	36.3±3.9	21.2		54.5±3.7	72.8		3.99±0.26	3.6
40	242	5.0±1.1	0.12		19.9±1.6	1.4		5.06±0.32	

TABLE II. Continued

Sample		U concentration, mg kg^{-1}			Th concentration, mg kg^{-1}			K concentration, %	
No	Code	Gamma	ICP-MS	XRF	Gamma	ICP-MS	XRF	Gamma	XRF
41	243	9.9±1.5	4.54		22.9±1.8	23.2		4.45±0.28	
42	**244**	**95.3±6.3**	**50.1**	**71.5**	15.5±1.7	10.7	13	2.89±0.21	2.2
43	**245**	**250.9±15.0**	**214**	**208.9**	16.7±2.3	11.6	9.6	1.74±0.15	1.1
44	**246**	**265.0±15.7**	**204**	**208.6**	15.9±2.1	11	8.6	1.96±0.16	1.5
45	248	12.2±1.2	4.69		13.5±1.3	10.5		3.28±0.22	
46	249	5.0±0.7	1.49		14.3±1.3	9.9		3.46±0.24	
47	267	5.2±0.8	2.31		14.9±1.5	12.6		3.79±0.26	
48	268	9.1±0.9	2.52		13.4±1.2	12.3		3.44±0.23	
49	269	8.4±1.3	1		10.5±1.1	7.9		4.23±0.28	
50	270	1.3±0.4	0.44		2.7±0.4	2.7		0.84±0.07	
51	271	0.0±0.0	0.25		3.4±0.5	1.9		0.44±0.04	
52	272	6.0±1.1	1.62		15.4±1.3	14.7		3.73±0.24	
53	273	9.0±1.3	1.6		16.2±1.4	14.2		3.97±0.26	
54	274	5.5±1.1	0.91		15.7±1.3	13		3.71±0.24	
55	275	0.0±0.0	0.45		17.8±1.6	5.7		3.69±0.25	
56	**620**	**122.7±7.9**	**74.2**	**105.8**	6.5±0.7	10.4	10.3	2.95±0.22	2.2
57	**621**	**225.8±13.6**	**149**	**187**	15.1±2.3	11.6	11.2	3.24±0.24	2.2
58	**622**	**289.2±18.5**	**232**	**225.1**	15.3±1.8	12.1	10.4	2.47±0.18	1.9
59	**624**	**605.7±37.1**	**356**	**294.2**	0.00±0.0	2.9	3.1	0.46±0.07	0.1
60	701	9.0±1.0	3.16		14.7±1.4	12.3		4.53±0.29	
61	702	10.2±1.1	10.6		25.6±2.0	56.7		4.13±0.25	
62	706	26.9±2.7	19.95		33.5±2.3	48.1		4.40±0.27	
63	707	8.4±1.0	2.93		15.0±1.3	14.5		4.84±0.31	
64	708	4.2±0.6	1.56		9.7±1.0	12.4		2.56±0.18	
65	709	14.7±1.8	12.4		17.2±1.4	53.9		4.28±0.27	
66	710	14.9±1.7	2.57		16.8±1.4	8.8		4.25±0.27	
67	712d	5.0±1.0	2.08		9.7±0.9	15.1		5.75±0.35	
68	713	8.4±1.3	2.91		15.8±1.3	17.9		5.85±0.36	
69	2775	5.9±0.9	–		15.5±1.2	–		4.09±0.26	
70	2776d	6.7±1.2	–		14.5±1.2	–		4.42±0.27	
71	2778d	11.9±1.6	4.25		19.8±1.5	15.4		4.79±0.30	

Table II is a good illustration of the reliability of the different methods used to determine the elemental concentrations. Undoubtedly, the most reliable among them is gamma spectrometry. The table shows that ICP-MS analysis is in very good agreement with radioactivity measurements for thorium (most results are within 15 %), and in moderately good agreement for uranium; most results are within 60 %, with the ICP values always being lower than the radioactivity ones. However, for potassium, there was almost no agreement at all. This discrepancy was expected, as the relatively low ionization potential of potassium causes its ionization to occur early at the entrance into the plasma. Thus, it is forced by radial electric field on its way through plasma to migrate from the central zone, which means that its concentration in that zone is much lower than the true

concentration. This behavior has an impact on the measurement of potassium concentration. Potassium is not unique among the elements in this behavior in ICP. For this reason, XRF analysis was used to prove undoubtedly the previously obtained results for potassium from gamma spectrometry measurements.

Moreover, it can be notice that the thorium and potassium concentrations given in Tables I and II are, on average, within the background levels, while uranium in some samples (620−622, 624, 244−246; these numbers are given in bold in Tables I and II) is remarkably increased.

As mentioned earlier, a radiometric survey of the observed targets at the sites was performed while collecting the samples. At the same time, the local average background values in cps (counts per second) for different types of rocks were established and are given in Table III. Typically, several thousand measurements, sometimes up to five thousand, were performed for each value of background given in the Table. This survey was the first indication of increased radioactivity of rhyolites through the increased background value. Further laboratory measurements fully proved these findings and it was shown that they come from uranium.

TABLE III. Average background values for various types of rocks in the region of Jabal Eghei, obtained from a radiometric survey of the observed targets at the sites

Rock type	Local background, cps
Granitoide	120
Rhyolite	160
Syenite	125
Quartzite	35
Skarn	40
Amphipolite	45

This survey indicated two significant uranium anomalies in the rhyolites, as well as some smaller ones in granites that are in close contact with rhyolites. These field findings were subsequently confirmed by laboratory measurements.

The rhyolites are located in the central part of the investigated region, covering an area of about 60 square kilometers. They cut through granite rocks. From the viewpoint of nuclear mineral raw materials, rhyolites are always considered as rocks of highest significance.

Anomaly I is located in the central part of the rhyolite region (23°14' 23.2"; 19°17' 04"), which is mostly composed of silificated rhyolites. In an area of size 60 m × 40 m counts from about 500 to above 2400 cps were registered, *i.e.*, significantly above the background level. Those values correspond to sample codes 244–246 and 620–622 (Table II). Using the portable GR-130 γ-spectrometer it was proved that this anomaly could exclusively be attributed to uranium, because corresponding numbers of counts for Th and K were within the back-

ground values for this type of rocks. Experience with this instrument and the way of running the measurements enabled the investigators to estimate roughly the concentration of uranium in mg kg^{-1} from the number of counts per second. The estimations obtained in this manner were substantiated by the three applied laboratory methods. Conclusively, all methods gave very similar results, which clearly confirmed that the studied area is enriched in uranium, if compared to the local background. In some cases, the enrichment was up to two orders of magnitude.

Geochemical analysis

As mentioned above, ICP-MS method was employed in this work in addition to radiological techniques. It was used for geochemical analysis of a limited number of samples from locations where uranium mineralizations (anomaly I) were registered, not only to compare the contents of uranium or thorium with those obtained by gamma spectrometry, but also to determine the concentrations of about forty other elements appearing in the examined minerals. These elements are important for understanding the entire geological context regarding uranium. The obtained results are presented in Table I-S of the Supplementary material to this paper, together with the corresponding Clark values.

Formation of uranium mineralizations is directly related to its geochemical properties and behavior in different geological media. The discovered uranium mineralizations in Jabal Eghei are spatially and genetically connected to granitoid rocks cut through by rhyolites. Based on the geological and structural characteristics of the area, as well as the locations of these uranium mineralizations, and bearing in mind the results of the geochemical analyses (Table I-S – increased contents of As a P), it could be concluded that a hydrothermal stage occurred in their formation. In the initial phase, uranium was bonded mostly with petrogenetic minerals of granitoids (feldspar and biotite). Although the concentration of uranium in these minerals is relatively low, the total amount of uranium bound in the rocks in this way is large, because of the great amounts of these rocks and the carrier mineral within them. Beside traces of uranium in the petrogenetic minerals of magmatic rocks, uranium in them also appears in the form of independent minerals, cationic substitutes in the accessory minerals of granitoid complexes and vulcanites. In waters with pH between 4 and 7.5, complexes of the uranyl ion with $KAsO_4^{2-}$ and SiO_3^{2-} may be, and probably were, formed. In the presence of Na^+, K^+, Ca^{2+}, Mg^{2+} and Fe^{2+}, the solubility of uranyl complexes is decreased. This leads to the formation of more favorable conditions for uranium mineralization. Some of these minerals are insoluble (such as their compounds with PO_4^{3-}, AsO_4^{3-}, SiO_2, *etc*.), thus they appear accompanied with uranium at a location, while the others easily move to the solution.[10]

Anomaly II was discovered near the granite–rhyolite contact zone (23°13'42"; 19°16'05"). This zone is connected with a noticeable tectonic zone.

The azimuth of the zone is 160° and dip 85°. It is characterized by the presence of silicified breccia rocks. Counting in the field gave values from 400 to above 3000 cps. From these measurements, it was estimated that concentrations of uranium were higher than those of the first anomaly. This estimation was further confirmed by laboratory measurements (sample codes 230, 231 and 624) using the already described methods. Simultaneously, the thorium concentrations in these samples were negligible. From the location where this uranium anomaly was registered, three samples were taken for further geochemical analysis for significant elements, similarly to the anomaly 1. The results of the analyses are given in Table II-S of the Supplementary material to this paper.

The results of chemical analysis indicate that the registered uranium mineralizations are accompanied with anomal contents of silver, arsenic, molybdenum, mercury and lead.

Taking into account the location and manner of appearance of these uranium anomalies, the following could be concluded. Uranium was probably deposited from mineralized solutions circulating through granites and rhyolites, especially through the fault zones in them, where geochemical conditions were favorable (clay- and iron-abundant regions). Both types of minerals are known as exceptional absorbers of uranium in nature. Significant concentrations of these minerals, especially limonite, were discovered just in the open structure. Some additional uranium anomalies of lower countings (300 to 500 cps) were discovered within the granitoide massif, very close to rhyolites. They are certainly not of economic interest, but could serve as evidence that the main primary source of uranium mineralization was connected with granitoides. It is to be ascertained why the rocks with increased concentrations of uranium do not contain more thorium than the average background. This could be an indication of preferable deposition of uranium to its washing at such points.

Thorium appearances. In the investigated area, the greater part with increased contents of thorium (30 to 72 mg kg^{-1}) were found in granitoide rocks, very close to the granitoide–rhyolite contact zone, on the western side of rhyolites. They are not of interest because of the very low intensities of mineralization.

Potassium. Taking into account that the average concentration of potassium in the Earth's crust is about 2.5 % and in magmatic rocks 3.3 %, the results shown in Table II give an indication of increased contents of this element in the Jabal Eghei rhyolites and granitoide rocks. The most important carriers of uranium are primary calc-alkaline and alkaline acidic magmas, in which potassium prevails over sodium. Uranium concentrations are decreased going toward more alkaline and calcium–magnesium types of granitoide complexes.

A simple genetic model for uranium mineralization in the Jabal Eghei region

The main primary sources of uranium mineralization are granitoides. Uranium is mobilized from them mostly through cold solutions and deposited in favorable geochemical environments, such as contact zones with rhyolites, fault structures filled with clay, ferrous oxides *etc*. During the phase of magma differentiation, uranium was predominantly bonded to petrogenic minerals, such as feldspars and biotites.[11] Although the uranium concentration in these minerals is relatively low (*e.g*., in feldspars, the average concentration is 10^{-6} %), the total amount of uranium in these rocks is large, due to their great masses. On the other hand, concentrations of uranium in micas (which are basically biotites) are about five times higher than the average ones in magmatic rocks. This could also be of importance for the ore deposits. Besides the presence of uranium traces in petrogenetic minerals of magmatic rocks, uranium is also present in the form of independent minerals, as well as on the surfaces of crystals.

Regarding the genesis of the ore deposits and the possibilities of the formation of economically interesting uranium concentrations, which are spatially and genetically related to acidic and intermediate magmatic complexes, the leaching of uranium is of particular interest. It is connected with the possibilities of uranium mobilization from primary sources and its concentration in media to be transported to locations of mineralization. Under favorable physicochemical and geochemical conditions, theoretically about 40 % of total uranium could be mobilized from granitoide complexes. In aqueous solutions, uranium can be often found in the form of sulfate, carbonate, phosphate, chloride and fluoride complexes. The chemical stability of these species predominately depends on the pH and *Eh* values, temperature and the physicochemical properties of the ore-bearing fluids. Numerous factors could have had an impact on the uranium mineralization from ore-bearing solutions and the appearance of its mineralization in the rhyolite massif, such as changes in its chemical composition, or the degassing of solutions in chemical reactions with rock complexes while traveling through rhyolites. The most important factors that lead to the uranium mineralization are changes in pH and *Eh* values, as well as changes in the CO_2 concentration along the route of the ore-bearing solutions from granite to rhyolites.

Bearing in mind all the collected data, connection between uranium mineralization and tecto–magmatic (*i.e*., tecto–volcanic) structures, or more specifically – effusive, volcanic and sub-volcanic structures could be assumed. This further means that the possibility of volcanic uranium mineralization should not be excluded. Uranium mineralization is spatially and genetically related to the volcanic complexes (rhyolites). Some interesting data about the Tibesti massif generally, as well as about Jabal Eghei area, related to this issue have already been published in the scientific literature.[12,13] The spatial position of the postorogen magmatism, which is at the same time the lithologic control factor of the

mineralization position, is controlled by the locations of deep fault zone cross sections. The forms of the ore bodies depend on the structural and lithologic control factor. The uranium ore bodies in anomaly I were probably in the form of a pillar (column). The main ore material was pitchblende, although the presence of uranitite, coffinite and uranium titanite could not be excluded. A full explanation of the genesis of these uranium mineralizations could be obtained from detailed geological investigations.

The possible positions and forms of the ore bodies, as well as a model of the formation of uranium mineralizations are shown in Fig. 3.
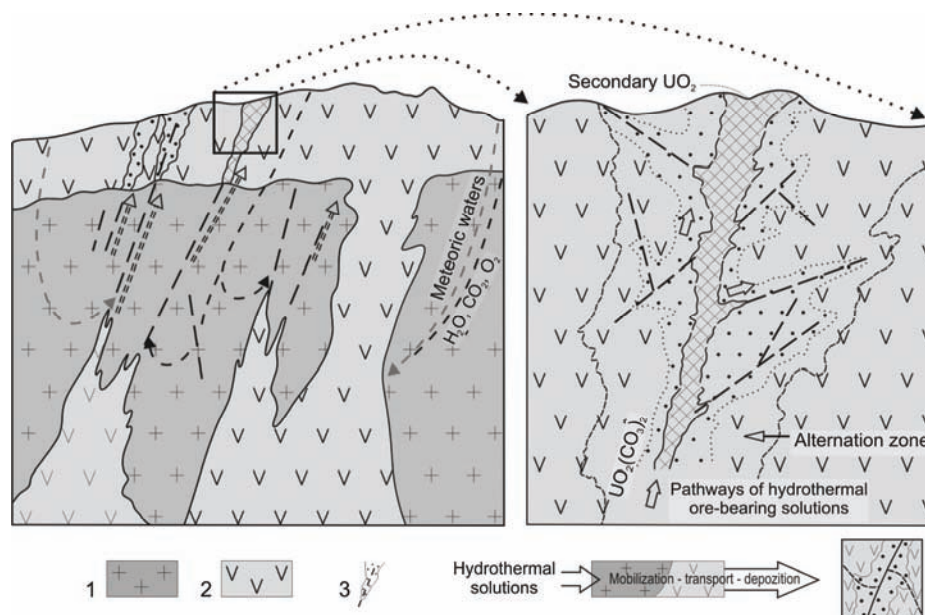
Fig. 3. Schematic representation of the genetic model of uranium mineralization in rhyolites in the Jabal Eghei region: 1 – granitoide rocks; 2 – rhyolites; 3 – uranium mineralization.[7] The side length of the square is 300 m.

CONCLUSIONS

This investigation of the terrain of Jabal Eghei in southern Libya represents the first systematic sampling and radioactivity measurements, and the first determinations of concentrations of some important elements.

Two significant uranium anomalies-mineralizations were discovered in the area, while thorium and potassium were found to be at the average background level, except in a minor number of slightly increased samples.

Geochemical analysis of some samples, taken from places where uranium anomalies were discovered, for more than forty elements was realized using the ICP-MS technique, for a better insight into these anomalies.

Based on all investigations of Jabal Eghei, a detailed geological map of the area was drawn.

In our opinion, investigation of this interesting region, primarily its part made of rhyolites, should be continued, because that might be of interest for the discovery of nuclear mineral raw materials.

SUPPLEMENTARY MATERIAL

Results of geochemical (ICP-MS) analysis of rhyolites exhibiting increased ura¬nium values – anomalies I and II, are available electronically from http://www.shd.org.rs/JSCS/, or from the corresponding author on request.

ИЗВОД

ОТКРИЋЕ УРАНИЈУМСКИХ МИНЕРАЛИЗАЦИЈА У РИОЛИТСКО-ГРАНИТСКОМ КОМПЛЕКСУ У ОБЛАСТИ *JABAL EGHEI* У ЈУЖНОЈ ЛИБИЈИ

ЈОВАН КОВАЧЕВИЋ[1], МЕХДИ БАШИР ТЕРЕШ[2], МИРЈАНА Б. РАДЕНКОВИЋ[3] и ШЋЕПАН С. МИЉАНИЋ[4]

[1]*Геолошки институт Србије, п.пр. 42, 11000 Београд,* [2]*Tajoura Nuclear Research Centre, P. O. Box 30878, Tajoura, Libya,* [3]*Универзитет у Београду, Институт за нуклеарне науке „Винча“, п.пр. 522, 11001 Београд и* [4]*Универзитет у Београду, Факултет за физичку хемију, п.п. 47, 11158 Београд*

Током истраживања подручја *Jabal Eghei* у јужној Либији и прављења геолошких мапа размере 1:250.000 (сектор Тибести, лист Вади Еги НФ 34-1 и НФ 34-2), урађена је регионална проспекција за минералне сировине. Радиометријски преглед појединих тачака на терену указао је на две значајне уранијумске минерализације у риолитима, као и на неколико мањих у гранитима који су у блиском контакту с риолитима. Риолити су лоцирани у централном делу истраживаног подручја. Они пробијају гранитне стене. Прва минерализација је у средишњем делу риолитске области, која се углавном састоји од силификованих риолита. Друга је откривена близу контактне зоне гранити–риолити, коју карактерише присуство силификованог бреча. Ови су налази потврђени лабораторијским мерењима на више од седамдесет узорака прикупљених у овој области, коришћењем гама спектрометрије високе резолуције. Нађено је да се концентрације уранијума у овим минерализацијама крећу од око 50 mg kg^{-1} до више од 600 mg kg^{-1}. Потоња вредност је око 240 пута већа од средње вредности на Земљи. Поред уранијума, ова мерења су дала концентрације торијума и калијума. Додатне геохемијске анализе су урађене на узорцима са локација на којима су откривене уранијумске аномалије коришћењем технике ICP-MS, у којима су одређене концентрације више од четрдесет елемената. Уранијумске минерализације су праћене повећаним садржајима сребра (до 17 пута), арсена (до 8 пута), молибдена (до 50 пута), живе (до 9 пута) и олова (до 14 пута), у односу на Кларкове вредности. Добијени резултати заслужују да се настави истраживање ове области, зато што постоји могућност да се овде открију нуклеарне минералне сировине.

(Примљено 19. септембра, ревидирано 12.новембра 2012)

REFERENCES

1. V. I. Vernadskiĭ, *Ocherki geohimii*, Nauka, Moskva, Russia, 1983 (In Russian)
2. M. B. Tereesh, M. B. Radenkovic, J. Kovacevic, S. S. Miljanic, *J. Radiat. Prot. Dosim.* **153** (2013) 475
3. R. O. Bastos, C. R. Appoloni, *Radioactivity of rocks from the geological formations belonging to the Tibagi River hydrographic Basin*, in *2009 International Nuclear Atlantic Conference – INAC*, Rio de Janeiro, Brazil, 2009
4. R. C. Ramola, V. M. Choubey, G. Prasad, G. S. Gusain, Z. Tosheva, A. Kies, *Curr. Sci.* **100** (2011) 906
5. G. R. Gilmore, *Practical Gamma-Ray Spectrometry*, 2nd ed., Wiley, Warrington, UK, 2008
6. G. E. Knoll, *Radiation Detection and Measurement*, 3rd ed., Wiley, New York, USA, 2000
7. A. A. Makhrouf, *Geology, petrology, geochemistry, and geochronology of Eghei (Nugay) batholith alkali rich granites, NE Tibesti, Libya*, University of North Carolina at Chapel Hill, Chapel Hill, USA, 1984
8. M. Toljić, J. Kovačević, *Geological map of Libya 1:250,000; Sheet Wadi Eghei NF 34-1*, in *General Report (Mineral raw materials)*, Industrial Research Center, Tripoli, Libya and the Geological Institute of Serbia, Belgrade, Serbia, 2010, p. 264
9. A. A. Beus, S. V. Grigorian, *Geochemical exploration methods for mineral deposits*, Applied Publishing, Wilmette, USA, 1977
10. S. M. Romberger, *Transport and deposition of uranium in hydrothermal systems at temperatures up to 300 °C: Geological implications*, in *Uranium geochemistry, mineralogy, geology, exploration and resources*, B. De Vivo, Ed., The Institution of Mining and Metallurgy, London, UK, 1984, pp. 12−17
11. M. Moreau, *L'uranium et les granitoides−essai d'interpretation (in French)*, in *Geology, mining, and extractive processing of uranium*, M. J. Jones, Ed., Institution of Mining Metallurgy, London, UK, 1977, pp. 83−102.
12. I. B. Suayah, J. S. Miller, B. V. Miller, T. M. Bayer, J. J. W. Rogers, *Afr. Earth. Sci.* **44** (2006) 561
13. A. A. Makkrouf, *J. Afr. Earth. Sci. (and the Middle East)* **7** (1988) 945.

Journal of the Serbian Chemical Society

Discovery of uranium mineralizations in the rhyolite–granite complex in the Jabal Eghei area of southern Libya

JOVAN KOVAČEVIĆ[1], MEHDI BASHIR TEREESH[2], MIRJANA B. RADENKOVIĆ[3] and ŠĆEPAN S. MILJANIĆ[4*]

[1]*Geological Institute of Serbia, P. O. Box 42, 11000 Belgrade, Serbia,* [2]*Tajoura Nuclear Research Centre. P. O. Box 30878, Tajoura, Libya,* [3]*University of Belgrade, Vinča Institute of Nuclear Sciences, P. O. Box 522, 11001 Belgrade, Serbia and* [4]*University of Belgrade, Faculty of Physical Chemistry, P. O. Box 47, 11158 Belgrade 118, Serbia*

TABLE I-S. Results of geochemical (ICP-MS) analysis of rhyolites exhibiting increased uranium values – anomaly I. The concentrations are given in mg kg^{-1}. The values in bold show anomalous concentrations of the corresponding elements with regard to the Clark values[9]

Sample code		244	245	246	620	621	622	3177[1]
Element	Clarke	Rhyolite-silification			Rhyolite			
Au	0.0043	<0.2	<0.2	<0.2	<0.2	<0.2	<0.2	<0.005
Ag	0.07	0.09	0.03	0.11	0.08	0.09	0.12	0.13
As	1.7	**16.8**	**12.2**	**21.9**	**19.1**	**20.7**	**21.4**	**36.6**
Ba	650	340	320	330	260	410	300	240
Be	38	0.39	0.7	0.44	0.42	0.32	0.52	0.41
Bi	0.009	0.06	0.06	0.09	0.15	0.27	0.24	0.1
Cd	0.13	0.15	0.21	0.16	0.16	0.07	0.21	0.14
Ce	70	71.8	59.8	56	64.2	80.3	67.9	57
Co	18	29.2	18	30.9	15.2	15.7	15.7	26.7
Cr	83	18	10	15	31	30	18	26
Cs	3.7	6.57	1.55	3.33	5.02	7.32	3.24	3.67
Cu	47	36.9	4.5	12.3	18.2	10	14.8	19.2
Ga	19	10.45	5.25	8.1	9.63	10.7	7.51	8.03
Ge	1.4	0.18	0.14	0.16	0.12	0.12	0.1	0.1
Hf	1	1.32	0.82	1.43	1.04	1.08	0.75	0.83
Hg	0.083	0.07	0.08	0.07	0.02	0.02	0.02	0.01
In	0.25	0.045	0.018	0.022	0.031	0.035	0.024	0.022
La	29	35.6	28.7	27.3	29.5	38.7	33	29.5
Li	32	52.3	17.6	34.4	36.6	44.2	31.7	32.4
Mn	1000	548	501	477	684	535	463	701
Mo	1.1	1.15	1.44	2.64	2.49	3.55	3.75	20

* Corresponding author. E-mail: epan@ffh.bg.ac.rs

TABLE I-S. Continued

Sample code		244	245	246	620	621	622	3177[a]
Element	Clarke	Rhyolite-silification			Rhyolite			
Nb	20	0.68	1.58	1.22	0.66	0.56	1.43	0.86
Ni	58	9.9	5.6	9.2	13	11.5	8.6	18.9
P	930	**1090**	**1280**	**1060**	**1120**	**1170**	**1180**	**1060**
Pb	16	11	26.6	29.7	16.6	28.3	32.7	27.3
Rb	150	100.5	23.3	71	79.4	100.5	61.2	72.2
Re	0.001	0.001	<0.001	0.001	<0.001	0.001	0.001	0.001
Sb	0.5	0.81	0.94	0.95	1.11	1.14	1.19	1.03
Sc	10	9.4	2.5	4.1	6.2	8.1	4	4.3
Se	0.05	0.4	0.5	0.6	0.4	0.5	0.5	0.4
Sn	2.5	2.2	2.7	2.5	2.9	2.9	3.7	1.8
Sr	340	42	53.3	46.8	49.4	35.4	68.6	51.3
Ta	2.5	0.01	0.01	0.01	0.01	0.01	0.01	0.01
Te	0.002	<0.01	<0.01	<0.01	0.01	0.01	0.01	0.01
Th	13	10.7	11.6	11	10.4	11.6	12.1	8.8
Tl	1	0.81	0.25	0.82	0.65	0.97	0.68	0.86
U	2.5	**50.1**	**214**	**204**	**74.2**	**149**	**232**	**152.5**
V	90	55	17	35	41	51	27	34
W	1.3	84	64.9	69.1	2.16	1.63	1.08	0.6
Y	29	12.45	13.05	14.7	11.55	14.45	14.15	10.15
Zn	83	61	33	57	52	75	48	67
Zr	170	42.8	33.6	49.5	39.7	44.5	34.9	28.2

[a]The radioactivity of this sample was not measured. The concentrations of uranium and all other elements here were obtained by ICP-MS analyses

TABLE II-S. Results of geochemical (ICP-MS) analysis of rhyolites exhibiting increased uranium values – anomaly II. The concentrations are given in mg kg^{-1}. The values in bold show anomalous concentrations of the corresponding elements with regard to the Clark values[9]

Sample code		230	231	624
Rock type		Rhyiolite-breccia		
Element	Clarke			
Au	0.0043	<0.2	<0.2	<0.2
Ag	0.07	**1.2**	**0.62**	**1.18**
As	1.7	13.1	9.5	14.5
Ba	650	**2800**	**2270**	**2420**
Be	38	1.56	1.44	1.16
Bi	0.009	0.43	0.17	2.63
Cd	0.13	0.61	0.42	0.64
Ce	70	31.7	17.45	19.4
Co	18	4.3	23.6	2
Cr	83	18	12	20
Cs	3.7	0.7	0.43	0.55
Cu	47	22	20.1	18.1
Ga	19	3.14	1.78	1.92
Ge	1.4	0.09	0.05	<0.05

KOVAČEVIĆ et al.

TABLE II-S. Continued

Sample code		230	231	624
Rock type			Rhyiolite-breccia	
Element	Clarke			
Hf	1	0.44	0.21	0.34
Hg	0.083	**0.18**	**0. 22**	**0.72**
In	0.25	0.067	0.044	0.153
La	29	14.1	4.1	5.7
Li	32	1.8	1	1
Mn	1000	774	493	267
Mo	1.1	**32.4**	**52.6**	**44.7**
Nb	20	0.23	0.12	0.23
Ni	58	5.4	5.6	6.8
P	930	200	250	282
Pb	16	**77.9**	**88.4**	**231**
Rb	150	4.6	2.5	3.3
Re	0.001	<0.001	0.003	0.001
Sb	0.5	4.44	4.05	6.78
Sc	10	4.2	3.6	2.2
Se	0.05	0.8	0.3	1
Sn	2.5	1.9	1.8	1.7
Sr	340	78.9	57.3	69.6
Ta	2.5	<0.01	0.01	0.01
Te	0.002	<0.01	0.01	0.06
Th	13	3.9	1.6	2.9
Tl	1	1.43	0.23	0.1
U	2.5	**175.5**	**40.9**	**356**
V	90	14	10	6
W	1.3	3.15	183	5.54
Y	29	25.3	9.63	28
Zn	83	93	91	109
Zr	170	19.6	9.3	18.4